THE ELECTRICAL AND OPTICAL PROPERTIES OF DOPED YTTRIUM ALUMINUM GARNETS

by

Jimmy Kuo-Wei Chen

M.S., Materials Science & Engineering, University of California, Berkeley (1987)
B.S., Electrical Engineering & Computer Science and Materials Science &
Engineering University of California, Berkeley (1985)

Submitted to the Department of Materials Science and Engineering
in Partial Fulfillment of the Requirements of
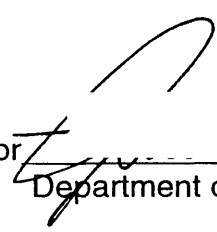the Degree of Doctor of Philosophy
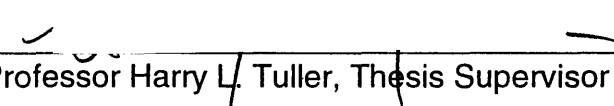
at the

Massachusetts Institute of Technology

April, 1994
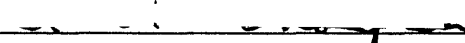
© Massachusetts Institute of Technology, 1994

Signature of Author_____
Department of Materials Science and Engineering
April 29, 1994

Certified by_____
Professor Harry L. Tuller, Thesis Supervisor

Accepted by_____
Carl V. Thompson II
Professor Electronic Materials
Chair, Departmental Committee on Graduate Students

THE ELECTRICAL AND OPTICAL PROPERTIES OF DOPED YTTRIUM ALUMINUM GARNETS

by

Jimmy Kuo-Wei Chen

Submitted to the Department of Materials Science and Engineering
on April 29, 1994 in Partial Fulfillment of the
Requirements for the Degree of Doctor of Philosophy

ABSTRACT

The electrical and optical properties of YAG, Nd:YAG, Ti:YAG, and Zr:YAG were studied and quantitatively correlated to determine defect models for the defect structure of these systems. Correlations of these independent measurements were essential, as defect models derived from electrical or optical measurements alone were inconclusive. The correlated defect model provided a new interpretation for the electrical and optical properties of Ti:YAG. This defect model was then tested by checking its predicted dependence of Ti:YAG's optical properties with PO_2. This prediction was experimentally verified.

Most of the systems were found to have a defect structure controlled by inadvertent background acceptors compensated by oxygen vacancies. This structure led to a characteristic conductivity isotherm where the conductivity varied as $PO_2^{-1/4}$ for reduced PO_2's, and approached PO_2 independence for oxidizing PO_2's. Only for a heavily doped Zr:YAG sample was a new defect structure encountered. For this sample, an *extrinsically* compensated defect structure was detected, with the Zr^{+4} ions compensating the background acceptors. The conductivity isotherm for this sample had a n-type like component that varied as $PO_2^{-1/6}$.

Quantitative correlations of the electrical and optical properties also provided a deep insight into the nature of the optical properties, and how these properties change as a function of oxidizing and reducing anneals. Correlations of this type were used to locate the energy level positions of Fe^{+2}, Ti^{+3}, Zr^{+3}, and $V_o^{\bullet\bullet}$ in the YAG bandgap.

Thesis Supervisor: Dr. Harry L. Tuller

      Title: Sumitomo Electric Industries Professor of
Ceramics and Electronic Materials

Table of Contents

6

11

List of Tables

ACKNOWLEDGMENTS

Dedicated

to my wife

Wen-Ching (Audrey),

whose enduring optimism and faith re-defined

my perception

of the impossible, as well as my understanding of love.

Without

her support and constant encouragement,

this thesis could not have been written.

CHAPTER 1: INTRODUCTION

The properties of a material depend on its structure, composition, and its processing. To engineer desired properties into a material, one must first establish how the processing affects the structure, and then understand why these structural changes result in the observed properties. For many functional ceramics, the electrical, optical, or magnetic properties usually depend on their defect structure, as reflected in the ceramic's electronic and ionic defects. This defect structure can vary dramatically with doping and/or changes in stoichiometry, leading to major changes in their properties. For example, the ionic conductivity of $Y_2(Ti_{1-x}Zr_x)_2O_7$ can vary over four orders of magnitude as x varies from zero to one.[1,2] Similarly, up to 1% of chromium can be substituted for aluminum to give colorless sapphire the deep red color of ruby.[3]

Unfortunately, the defect structures of functional ceramics are not easy to determine, and often more than one defect structure model is consistent with the experimental results. To distinguish between competing models, experimental measurements of an independent nature are extremely useful. Electrical and optical measurements are an example of such complementary measurements. One of the main objectives of this thesis is to demonstrate how one may quantitatively correlate electrical and optical measurements for the purpose of identifying the defect structure of a material. Once this defect structure has been determined, one can then study the effect of processing on this defect structure, and on the resulting properties. The next step is to understand these properties in terms of the defect structure changes. Finally, from an understanding of these structure-property-processing relationships, one can estimate the range of defect structure variations the system is capable of, the

range of properties that are accessible, and the processing steps necessary to obtain the desired defect structure and accompanying material properties.

We chose yttrium aluminum garnet ($Y_3Al_5O_{12}$) as the prototype material system to demonstrate this concept of correlating electrical and optical measurements. Yttrium aluminum garnet or YAG, as it is commonly referred to has a number of properties that make it suitable for such a study. It is an optical material system of technological interest, e.g. Nd:YAG is a high power solid-state laser system. It has been studied for a number of years, so that data regarding many of its properties are readily available. And finally, standard techniques for growing large single crystals exist, so samples can be readily obtained.

Stan Rotman, a former student in our research group, demonstrated in his PhD thesis that correlations of electrical and optical measurements were extremely useful in determining the defect structure of YAG.[4] His qualitative correlations revealed that most YAG samples, both doped and undoped, had defect structures consistent with a model based on background acceptors controlling the defect structure. We sought to expand on his work in two primary ways. First, we sought to extend the technique to *quantitative* correlations of electrical and optical properties. As we will show, quantitative correlations will allow us to estimate the positions of energy levels in the bandgap, as well as allow us to discriminate between defect models which are qualitatively consistent with both electrical and optical measurements. Second, we sought to explore defect structures controlled by donors. We chose Zr and Ti as the donors. Both these ions are commonly found in the +4 valence in oxides, consequently they would indeed function as donors in this valence. Furthermore, in the +3 valence, both of these ions have only one d-electron. Consequently their optical properties would be much simpler to analyze. Finally, previous studies suggested that solubilities of these ions approached 1%, suggesting that one

16

could obtain samples with donor concentrations high enough to overwhelm background impurity effects.[5,6]

We began our investigation by attempting to fabricate transparent polycrystalline YAG ceramics. Such a process, if successful, would have technological implications. Polycrystalline ceramics have a number of advantages over single crystals: a) they tend to be more uniform, b) dopant concentrations are easier to control, c) they are amenable to processing in various shapes, and d) they are cheaper to process. We were somewhat successful in our attempts, fabricating translucent polycrystalline ceramics with >99% density. However, densities in excess of 99% proved difficult to achieve, and probably could have constituted a thesis in itself. Unfortunately these translucent ceramic samples weren't suitable for optical measurements. Samples thin enough to obtain an optical signal from were generally too thin to see any effects from the dopants. Consequently we looked for alternative ways to make samples.

Toshihiro Kotani, a scientist from Sumitomo Electric who is currently visiting us, employed John Haggerty's laser heated floating zone technique to grow single crystal fibers from our dense ceramic samples. By using these ceramic samples as feed rods, he grew single crystal fibers suitable for electrical and optical measurements. A number of Ti:YAG and Zr:YAG fibers were grown in this manner. We were also fortunate enough to obtain some large single crystals of YAG grown by the Czochralski process to study and compare with our fibers. John Haggerty of MIT donated some YAG and Nd:YAG crystals, while Milan Kokta of Union Carbide donated some Ti:YAG crystals.

With these samples, we intend to fulfill the two primary objectives of this thesis: a) to develop a technique for quantitatively correlating the electrical and optical measurements of YAG, and b) to determine the defect structure of donor

doped YAG. As seen in the following thesis, these objectives were largely met. The next chapter, Chapter 2, covers some general background material, and Chapter 3 is a short literature review of previous work. Chapter 4 covers the experimental details, and Chapters 5, 6, & 7 cover the experimental results of YAG & Nd:YAG, Ti:YAG, and Zr:YAG respectively. Finally, we summarize all of our results in Chapter 8, the conclusion.

CHAPTER 2: BACKGROUND

2.1: OPTICAL PROPERTIES OF OXIDES

2.1.1: Energy Levels in Atoms & Solids:

Any discussion of the optical properties of a material must begin with a discussion of the electron energy levels of the material, since the optical properties typically involve electronic transitions between these levels. In the case of the simplest system, the hydrogen atom, these levels can be determined exactly by applying Schrodinger's equation to the central field problem of the electrostatic attraction between the proton and the electron.[7-9] The electron orbitals derived from this calculation are characterized by three quantum numbers, n, l, and m_l, which describe the orbital energy, the orbital angular momentum and shape, and the z-component of the angular momentum respectively. All these quantum numbers must be integers, with n=1,2,3..., l=0,1,2...n-1, and m_l=-l,-l+1,...0,...l-1,l. The l quantum numbers are often labeled with letters, with s,p,d,f,g,h,l,.... for l=0,1,2... A fourth quantum number $m_s=\pm\frac{1}{2}$ describes the spin of the electron occupying a certain orbital, and these four quantum numbers fully specify the electronic structure of the hydrogen atom, or hydrogen-like atoms that have only one electron. For a give n shell, all of the orbitals are degenerate in energy, with E=-13.6 eV/n^2.[10]

For multi-electron atoms, two additional forces become relevant, the electrostatic electron-electron repulsion, and the magnetic spin-orbit coupling between the magnetic moments of the electron spin and the orbit it occupies. These additional forces dramatically complicate the calculations for the atomic orbitals, such that exact solutions are no longer possible.[11] These forces also split the energy degeneracy, so much so that inversion of energy levels may occur, with for example the 4s levels being lower in energy that the 3d levels.[7]

These levels are filled starting with the lowest energy level according to the Pauli Exclusion Principle, no more than two electrons per electron orbital. Because the levels are no longer degenerate within a given n shell, the different electronic structures within a given n shell will have different energies. To distinguish, label, and describe these different structures, term symbols are used. The term symbol designation is $^{2S+1}L_{2J+1}$ all in capital letters to designate that we are describing the electronic structure of the whole atom, and not the atomic orbital of a particular electron, which we designated by lower case letters.[7] The notation is consistent and converges for the hydrogen atom where we have only one electron. The relation between s and S, l and L, and j and J for the term symbol is as follows:

$$L = \sum m_{l_i} = 0,1,2,3,4,5.... \quad ; \qquad S = \sum s_i \quad ; \qquad J = L+S, L+S-1, ... L-S$$
$$= S, P, D, F, G, H....$$

The atomic orbital calculations are greatly simplified for the limiting cases, where the electrostatic electron-electron repulsion is either much greater or much smaller than the magnetic spin-orbital coupling. Russell-Sanders coupling designates the former case, and is valid when the atomic number, z ≤40. The inverse case is referred to as j-j coupling, and is valid for the heavy atoms, z>40.[7] In both cases the ground state is determined by Hund's rules of maximum multiplicity.[7,9]

When atoms are brought close together, the outer valence electrons of the atoms interact, and molecular orbitals incorporating this interaction are formed. These molecular orbitals tend to split the energy of the corresponding atomic orbitals, so that one is lower in energy than the atomic orbital (bonding molecular orbital), and one is higher in energy (anti-bonding molecular orbital).[9,11] As more and more atoms are added as in a solid, the number of

these molecular orbitals increase until bands of orbitals in energy space are formed. The width of the band depends on the nature of the atomic orbitals contributing to the molecular orbital. S and p states tend to have broad bands while d and f states tend to have narrow bands. If the fermi energy (the energy above which all the electronic states are empty and below which they are filled at $T=0°K$) lies in one of these energy bands, the material is a metal. If the fermi energy lies between these bands, the material is an insulator or semiconductor, depending on the magnitude of the bandgap. Large bandgap materials with bandgaps of $\geq \approx 3$ eV are typically insulators.

2.1.2: Energy Levels in Large Bandgap Oxides:

In an oxide, the valence band, the highest occupied energy band of "molecular orbitals" below the fermi energy, is typically the oxygen 2p band, and the conduction band, the lowest energy band of "molecular orbitals" above the fermi energy, is typically the empty cation band. In YAG for example, the conduction band is presumably the 4d band of yttrium. If the oxide was perfect, then no energy levels would be present between the valence and conduction band. At higher temperatures, entropic forces induce defects such as atomic vacancies or interstitials, and these defects often create energy levels within the bandgap. Another source of levels within the bandgap are impurities. Transition metal and rare earth impurities often have energy levels within the bandgap of oxides. These levels are typically due to the d and f electron orbitals, respectively.

The effect of the oxide lattice on these free ion orbitals can be very dramatic, especially for the d orbitals which extend farther out into the host lattice and can interact more strongly with the electrons of the host atoms.[11] Two related theories have been developed to describe these interactions

quantitatively. The simpler theory, known as crystal field theory, models the oxide lattice interaction as point negative charges arranged in the symmetry of the site occupied by the impurity. These point negative charges perturb the free ion orbitals with their electrostatic fields, and new orbitals are calculated accordingly.[11,12] Since these new orbitals are critically dependent upon the symmetry of these point charges, which represent the symmetry of the site, group theory notation is used to describe these orbitals. The magnitude of the crystal field is often labeled 10Dq or Δ, and is of the order of a few eV for most oxides.[11] The related but more complicated ligand field theory fully models the complete interaction of the impurity atom's orbitals with its nearest neighbor's orbitals, to generate molecular orbitals for the "molecule." Group theory notation is also used for these orbitals.[12,13] Clearly crystal field theory is more suitable for describing ionic bonds between the impurity atom and its host, whereas ligand field theory is needed if significant covalent bond nature is present. Crystal field theory has been used with remarkable success for a number of oxides.[11]

Crystal field calculations are simplest to do for Ti^{+3}, since it involves only one d-electron, and is consequently hydrogen-like in nature. Such calculations reveal that the five degenerate d-electron orbitals for a free ion are split into two degenerate sets in an octahedral field, the triply degenerate t_{2g} ground state orbitals, and the doubly degenerate e_g excited state orbitals, as shown in Figure 2.1.[3] Other site symmetries are also shown. Note in particular that the tetrahedral symmetry is qualitatively the inverse of the octahedral symmetry. This inversion stems from the fact that six negative charges at the faces of a cube is qualitatively the same as four positive charges placed at alternate cube vertices. Also note that qualitatively the cubic field splitting is the same as the
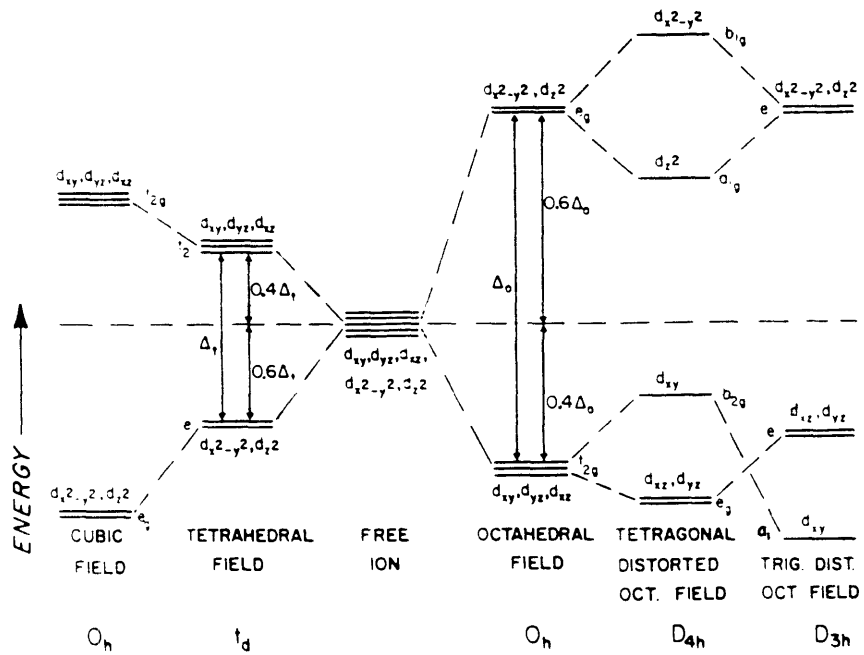
Figure 2.1. Splitting of five d orbitals in various types of crystal fields. [3]

tetrahedral field splitting. Quantitatively, for the same strength ligands and interionic distance, the magnitude of the splitting follows the relation: $\Delta_{oct}=9/4\Delta_{tet}=9/8\Delta_{cubic}$.[11]

These orbitals are then the starting base for atoms with more than one d-electron. Similar to the hydrogen atom, when more than one d-electron is filled into these orbitals, we have to factor in the electron-electron repulsion of the d-electrons into our calculations.[11] These calculations were made by Tanabe and Sugano, and their results are shown in Figure 2.2 as a function of the crystal field strength for octahedral sites.[14-16] As in the free atom case discussed above, consideration of the electron-electron repulsion of the d-electrons gives rise to additional terms. Also in analogy to the free atom case, the ground state is dictated by Hund's maximum multiplicity rules. In these Tanabe-Sugano diagrams, the spin-orbit energy is assumed to be much less than the crystal field energy, as is the case for transition metals in the first row.[14-16] Both coordinates are normalized against the Racah parameter B, which is a measure of the interelectronic repulsion. As seen in the Tanabe-Sugano diagrams, when 10Dq gets very large, Hund's maximum multiplicity relations break down, and a lower spin state then becomes the ground state.

Another process by which energy levels in the band gap can be split is the Jahn-Teller effect. For orbitally degenerate electronic states, any distortions of a non-linear molecule which will split the states and create lower energy states thereby lowering the overall energy of the system, will spontaneously occur.[11,12,17] For example, Ti^{+3} in a number of octahedral complexes is observed to have a double band in absorption as shown in Figure 2.3 for Ti:sapphire, whereas crystal field theory predicts only one band, the T_{2g} to E_g transition.[18] This double band can be understood by a tetragonal distortion of the octahedral site by Jahn-Teller splitting, which splits both the triply degenerate
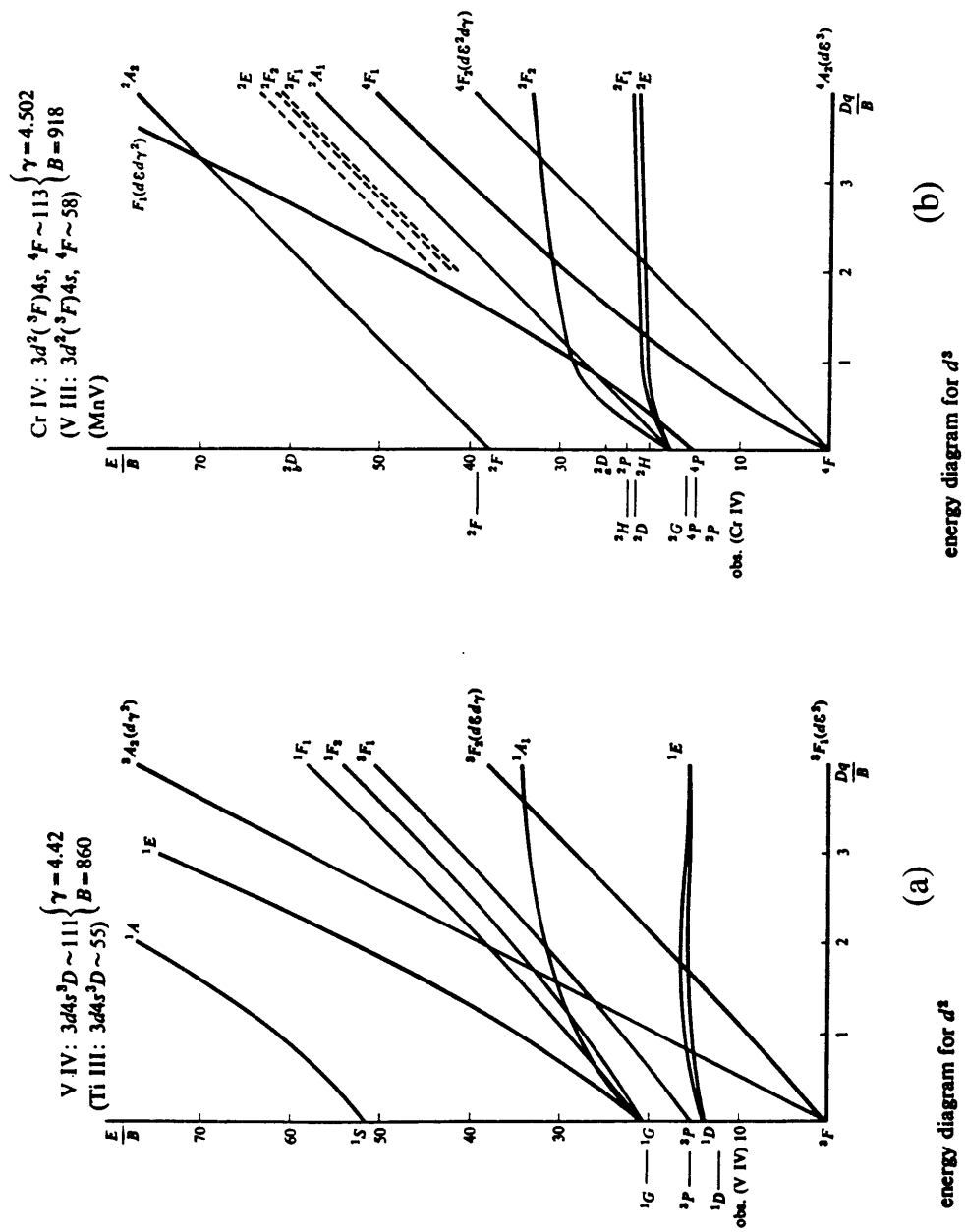
Figure 2.2 Tanabe-Sugano diagrams for configurations d2 (a) and d3 (b). [14]
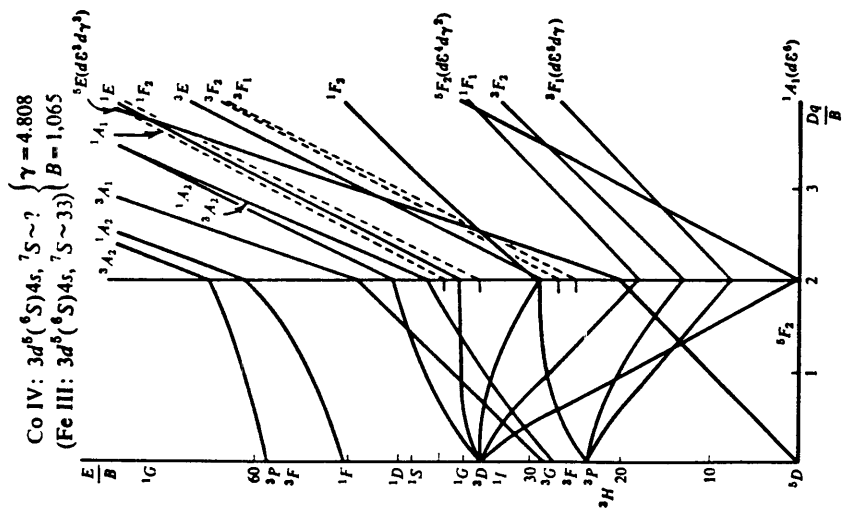
Figure 2.2 Tanabe-Sugano diagrams for configurations d^4 (c) and d^5 (d). [14]
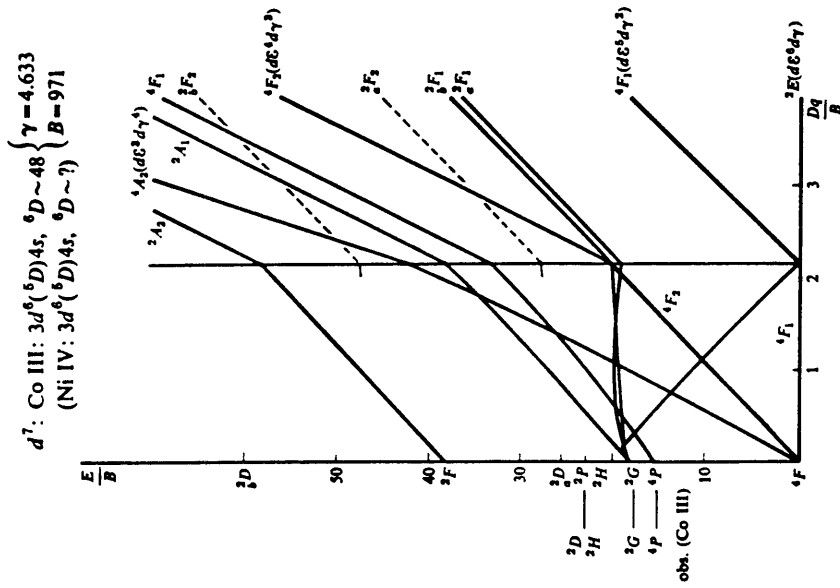
Figure 2.2 Tanabe-Sugano diagrams for configurations d6 (e) and d7 (f). [14]

energy diagram for d^8 (g)
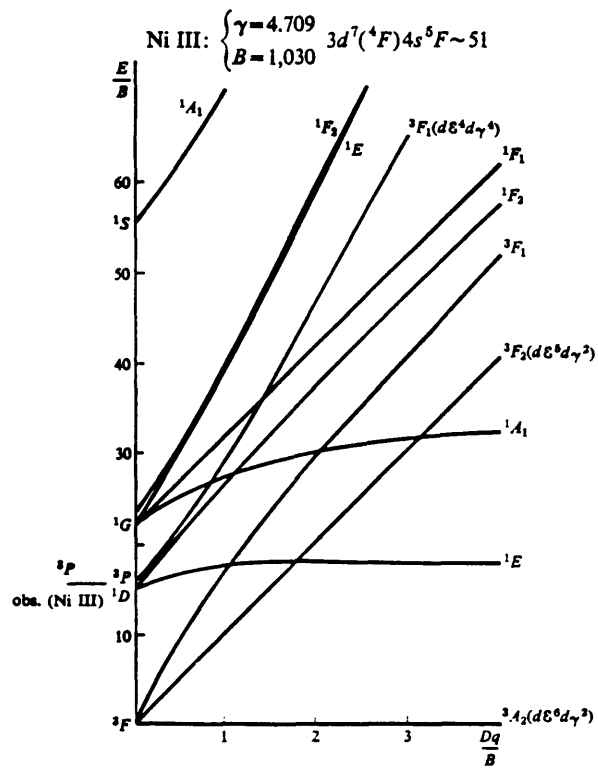
Figure 2.2 Tanabe-Sugano diagram for configuration d^8 (g). [14]

28
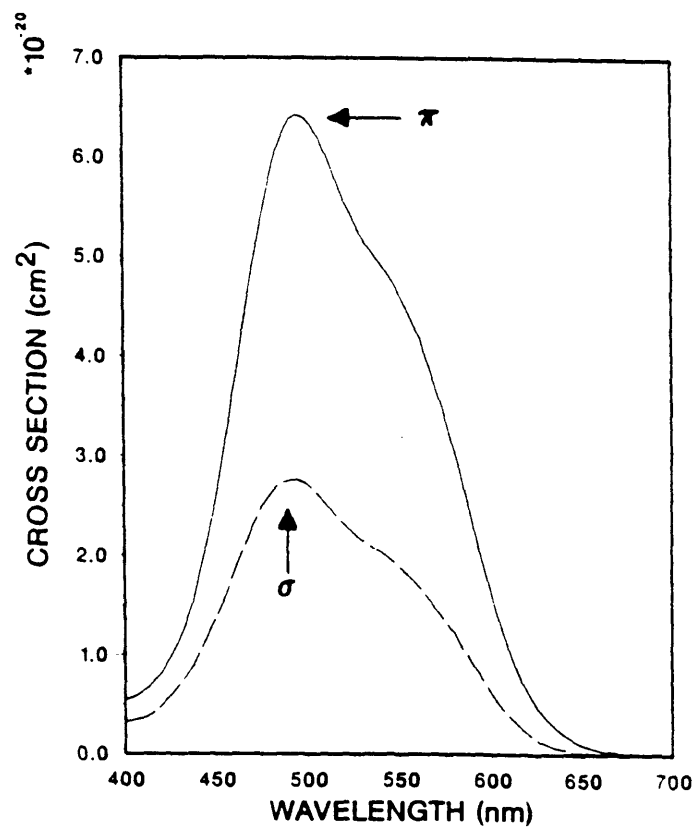
Figure 2.3. Polarized absorption cross sections for the $T_{2g} \rightarrow E_g$ transition in Ti:Al$_2$O$_3$.[18]

ground state T_{2g} and the doubly degenerate E_g levels. However, the T_{2g} levelsare split only slightly, so we observe two peaks in absorption at room temperature.[17,18] It is important to realize that because of the Jahn-Teller effect and other crystal lattice interactions (e.g. magnetic coupling between electron spins), a perfect cubic symmetry is seldom found for any site. These crystal field considerations plus spin-orbital coupling means that few crystal field states are degenerate in the absolute sense, even for the case of only one d-electron.[11]

2.1.3: Line Shapes & Peak Heights:

The lineshapes of an optical absorption or emission peak is ultimately determined by the mechanism that has the widest peak. Mechanisms can be classified into two categories, homogeneous mechanisms which affect every atom the same way, and inhomogeneous mechanisms which affect each atom differently.[19] Homogeneous mechanisms include 1) lifetime broadening, which is caused by the decay mechanisms of the atomic system, 2) dipolar broadening, which is caused by interactions between the magnetic or electric dipolar fields of neighboring atoms; and 3) thermal broadening, which is caused by the effect of phonons on atomic transitions. Homogeneous mechanisms lead to a Lorentzian lineshape:[19,20]

$$g(v) = \frac{\Delta v / 2\pi}{(v - v_0)^2 + (\Delta v / 2)^2}$$

where Δv is the full width at half maximum, and v_0 is the central frequency of the peak. Inhomogeneous mechanisms include 1) doppler broadening, and 2) crystal inhomogeneities such as dislocations and oxygen vacancies. Inhomogeneous mechanisms lead to a Gaussian lineshape:[19,20]

$$g(v) = \frac{2}{\Delta v}\left(\frac{\ln 2}{\pi}\right)^{1/2} \exp\left[-\left(\frac{v - v_0}{\Delta v / 2}\right)^2 \ln 2\right]$$

Inhomogeneous mechanisms generally have a wider peak with the result that most lineshapes are gaussian.[11,21]

Many optical transitions are found to follow the Beer-Lambert Law:[10]

$$I_f = I_o e^{-\varepsilon' cl}$$

where I_o is the incident light intensity, I_f the exiting light intensity, ε' the absorption strength parameter, c the molar concentration of the absorbing species, and l the sample thickness in cm. The same law in base 10 defines the molar extinction coefficient ε:

$$I_f = I_o 10^{-\varepsilon cl}$$

where the other parameters are the same as before. Clearly, the larger the maximum molar extinction coefficient ε_{max} is, the stronger the transition. However, the absolute absorption intensity depends on the total area under an absorption curve, not just its peak height. This quantity is termed the oscillator strength f:

$$f = 4.32 x 10^{-9} \int \varepsilon \, dv \approx 4.6 x 10^{-9} \varepsilon_{max} \, \Delta v$$

where Δv is the full width at half maximum of the peak in units of cm^{-1}, and ε_{max} is the molar extinction coefficient at the central frequency in units of [liters/mole-cm].

Consequently, both ε_{max} and f are a direct measure of the intensity of the transition, which ultimately reflects to what extent the transition is allowed. Whether a transition is allowed or forbidden depends on the selection rules for that transition. For an electric-dipole transition of a free ion, these selection rules are: [11]

$$\Delta S = 0, \qquad \Delta L = 0,\pm 1, \qquad \Delta J = 0,\pm 1, \text{ but not } J = 0 \text{ to } J = 0$$

Allowed transitions of this type are extremely intense, ε_{max}=10^3-10^6, f≈0.1.[11,12] The mixture of atomic states by a crystal field allows these rules to be broken, although the less rules are broken, the stronger the transition will be. Typical

transitions between octahedrally split crystal field states that are spin-allowed have $\varepsilon_{max} \approx 1$, $f \approx 10^{-5}$.[11,12] If the symmetry of the site does not possess an inversion center as in the case of a tetrahedral site, the intensity of the transition is generally stronger by ten to a hundred times.[11,12] This arises because the non-centrosymmetric crystal field removes the centrosymmetric nature of the original atomic orbitals, allowing electric-dipole transitions to occur.

Another common way by which atomic states are mixed and transition intensities increased is by temporarily removing the center of symmetry with a phonon.[12,22] Such vibronically-coupled transitions are especially common when the transitions are between bonding and non-bonding or anti-bonding orbitals, and involve a change in the equilibrium interatomic distance.[11] Vibronically-coupled transitions typically have $\varepsilon_{max} \approx 10\text{-}100$, $f \approx 10^{-4}$.[11,12] Rare earth f-electron transitions are weakly perturbed by crystal field or vibrational interaction. Consequently their transitions typically have $f \approx 10^{-6}\text{-}10^{-7}$.[11]

As a final note, transitions between atoms are also possible. Such charge transfer processes are fully allowed and consequently extremely intense, with $\varepsilon_{max} \approx 10^3\text{-}10^6$ and $f \approx 0.1$.[11] For example, the charge transfer spectra of an electron from oxygen to Fe^{+3} in sapphire is shown in Figure 2.4.[23]

2.2: DEFECT STRUCTURE OF OXIDES

As we stated in Section 2.1.2, entropic forces will induce the formation of defects at any $T > 0°K$, and these defects can often be detected optically because of the energy levels they create in the bandgap. We will employ Kroger-Vink notation to describe these defects, and a primer on this notation can be found in
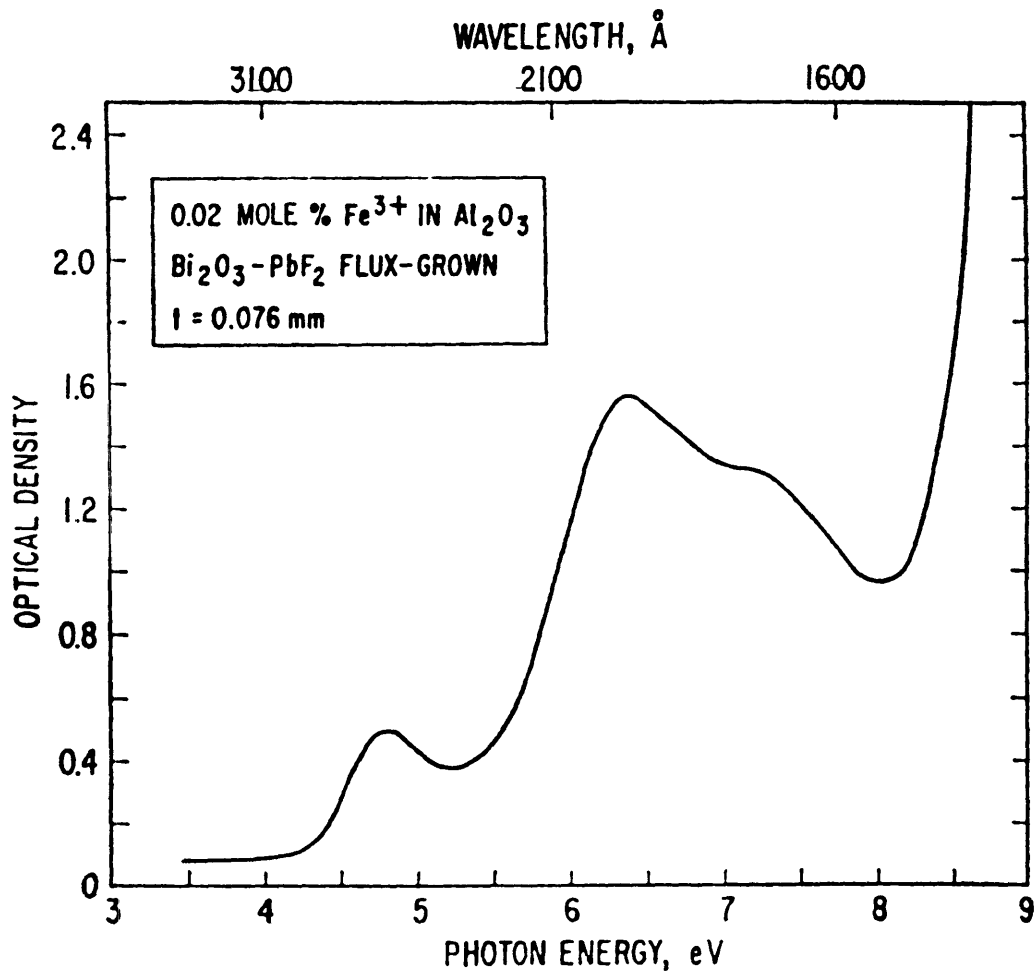
Figure 2.4 Absorption Spectrum of Fe^{+3} in Al_2O_3.[23]

reference 24. Alternative ways to induce defects in an oxide is a) by doping, and b) by changing the oxide stoichiometry.

Doping is typically achieved by doping the oxide melt directly, or by diffusing in desired dopants, usually at high temperatures. In addition, aliovalent dopants will generate additional charge compensating defects. For example, calcium in sapphire could generate the compensating ionic defects of a oxygen vacancy or metal interstitial, or the compensating electronic defect of a hole, as shown below:

$$2CaO \xrightarrow{Al_2O_3} 2Ca'_{Al} + 2O_o + V_o^{\bullet\bullet} \qquad K_1 = \left[Ca'_{Al}\right]^2 \left[V_o^{\bullet\bullet}\right] = K_1^{\ o} e^{\left(\frac{-\Delta H_1^{\ o}}{kT}\right)}$$

$$Ca \xrightarrow{Al_2O_3} Ca_i^{\bullet\bullet} + 2e' \qquad K_2 = \left[Ca_i^{\bullet\bullet}\right]n^2 = K_2^{\ o} e^{\left(\frac{-\Delta H_2^{\ o}}{kT}\right)}$$

$$2CaO + \frac{1}{2}O_2 \xrightarrow{Al_2O_3} 2Ca'_{Al} + 3O_o + 2h^{\bullet} \qquad K_2 = \frac{\left[Ca'_{Al}\right]^2 p^2}{PO_2^{\ 1/2}} = K_3^{\ o} e^{\left(\frac{-\Delta H_3^{\ o}}{kT}\right)}$$
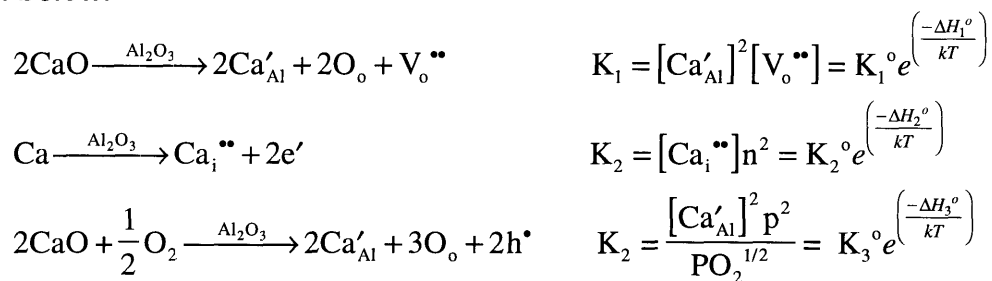
for conditions when Al_2O_3 is in equilibrium with pure CaO or Ca. Which of these compensating defects will actually occur depends on their respective energies. The defect with the lowest energy will compensate the calcium.

Changing the oxide stoichiometry is usually achieved by annealing the oxide in a gas with an excess or depletion of one of its components, typically oxygen. These anneals will then remove or incorporate the component, generating defects in the process. For example, a reducing anneal could remove oxygen from the oxide by the following reaction:

$$O_o \longrightarrow V_o^{\bullet\bullet} + 2e' + \frac{1}{2}O_2 \qquad K_r = \left[V_o^{\bullet\bullet}\right]n^2 PO_2^{\ 1/2}$$
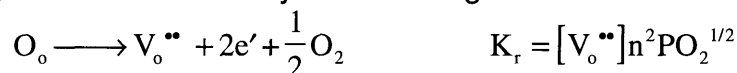
and generate oxygen vacancies in the process.

Consequently the equilibrium defect structure of an oxide is a function of many things, among them temperature, oxygen partial pressure (PO_2), and dopants. In principle, we could quantitatively predict the functional dependence of this defect structure if we knew certain parameters, e.g. the free energy

change associated with the various defect reactions, the effective density of states for the conduction band, the concentration level of the impurities, etc. Without this data, we can still make certain assumptions and model the functional dependence of the defect structure based on these assumptions.

For example, let us model an ideally pure YAG, and assume that the Schottky mechanism is the only relevant intrinsic defect reaction for the ionic defects (i.e. no interstitials). Then,

$$\varnothing \rightarrow 3V_Y''' + 5V_{Al}''' + 12V_O^{\bullet\bullet} \qquad K_s = \left[V_Y'''\right]^3 \left[V_{Al}'''\right]^5 \left[V_O^{\bullet\bullet}\right]^{12}$$

If we further assume for simplicity that the aluminum and yttrium vacancies are identical, and represented by a generalized metal vacancy V_M''', then:

$$K_s = \left[V_M'''\right]^8 \left[V_O^{\bullet\bullet}\right]^{12}$$

Other relevant defect reactions are the redox reaction for oxygen, and the electronic excitation across the bandgap.

$$O_o \longrightarrow V_o^{\bullet\bullet} + 2e' + \frac{1}{2}O_2 \qquad K_r = \left[V_o^{\bullet\bullet}\right]n^2 PO_2^{1/2}$$

$$\varnothing \longrightarrow e' + h^{\bullet} \qquad K_e = np$$
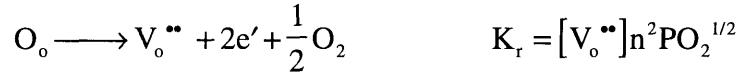
Finally, the overall electroneutrality relation would be:

$$3\left[V_M'''\right] + n = p + 2\left[V_O^{\bullet\bullet}\right]$$

A second assumption we will make is that the formation energy for the Schottky reaction is much less than the formation energy for the electron-hole pairs, i.e. $\Delta H_e = E_g >> \Delta H_s$, where E_g is the bandgap. Thus the number of ionic defects should greatly outnumber the electronic defects, and the electroneutrality relation at the stoichiometric PO_2 is primarily:

$$3\left[V_M'''\right] = 2\left[V_O^{\bullet\bullet}\right]$$

$$\therefore \quad K_s = \left[V_M'''\right]^8 \left[V_O^{\bullet\bullet}\right]^{12} = \left(\frac{3}{2}\right)^{12} \left[V_M'''\right]^{20}$$

Thus the concentration of cation vacancies is independent of PO_2 over the PO_2 range where the above electroneutrality is valid. The PO_2 and temperature

dependence of the other components are shown in regime (b) of Table 2.1.

Under heavily reduced conditions, we would move away from the ideal cation to

anion stoichiometry and generate more and more oxygen vacancies, until these

oxygen vacancies and their accompanying electrons exceed those generated by

the Schottky mechanism. For this case, the electroneutrality relation becomes

$n=2[V_o^{\bullet\bullet}]$ and the temperature and PO_2 dependence of the various defects are

shown in regime (a) of Table 2.1. Under extremely oxidizing conditions, oxygen

is added to the lattice via the crystal surface. This process actually builds up the

lattice, reducing the oxygen vacancy concentration and increasing the cation

vacancy concentration. The resulting electroneutrality relation then becomes:

$$3[V_M''] = p$$

The resulting temperature and PO_2 dependencies of the defects are shown in

regime (c) of Table 2.1. An isothermal diagram of the defect concentration as a

function of PO_2 is shown in Figure 2.5 for the three regimes.

Similar diagrams and tables can be derived for acceptor and donor doped

YAG. Schuh performed a number of theoretical calculations of defect energies

in YAG, and concluded that Schottky vacancies are the favored intrinsic defect,

with an average energy of 5.3 eV per vacancy.[25,26] He also concluded that

interstitials, both cation and anion interstitials had very high formation energies,

and consequently were unlikely in the tightly packed YAG structure.[25] Geller

arrived at similar conclusions.[27] Thus the most likely compensating defects for

acceptor or donor doped YAG are ionic vacancies or electronic defects.

A defect model based on acceptor doped YAG compensated by doubly

charged oxygen vacancies is shown in Figure 2.6, with corresponding

temperature and PO_2 dependencies in Table 2.2. [A'] stands for the

concentration of negatively charged acceptors, which is constant for a given

sample. For simplicity, we again assume that the formation energies of the

36

Defect Model for Intrinsic YAG

Figure 2.5 Schematic representation of the defect concentrations as a function of PO_2 for the defect model of intrinsic YAG.

Temperature & PO₂ Dependence for Intrinsic YAG

Defect	Regime (a) $n = 2[V_o^{\bullet\bullet}]$		Regime (b) $2[V_o^{\bullet\bullet}] = 3[V_M''']$		Regime (c) $p = 3[V_M''']$	
	PO₂ Dependence	Activation Energy	PO₂ Dependence	Activation Energy	PO₂ Dependence	Activation Energy
$[V_{Al}''']$	$PO_2^{1/4}$	$\frac{\Delta H_r}{2} - \frac{\Delta H_s}{8}$	None	$-\frac{\Delta H_s}{20}$	$PO_2^{3/16}$	$\frac{3\Delta H_r}{8} - \frac{\Delta H_s}{32} - \frac{3E_g}{4}$
$[V_Y''']$	$PO_2^{1/4}$	$\frac{\Delta H_r}{2} - \frac{\Delta H_s}{8}$	None	$-\frac{\Delta H_s}{20}$	$PO_2^{3/16}$	$\frac{3\Delta H_r}{8} - \frac{\Delta H_s}{32} - \frac{3E_g}{4}$
$[V_o^{\bullet\bullet}]$	$PO_2^{-1/6}$	$-\frac{\Delta H_r}{3}$	None	$-\frac{\Delta H_s}{20}$	$PO_2^{-1/8}$	$-\frac{\Delta H_r}{4} - \frac{\Delta H_s}{16} - \frac{E_g}{2}$
n	$PO_2^{-1/6}$	$-\frac{\Delta H_r}{3}$	$PO_2^{-1/4}$	$\frac{\Delta H_s}{40} + \frac{-\Delta H_r}{2}$	$PO_2^{-3/16}$	$-\frac{3\Delta H_r}{8} - \frac{\Delta H_s}{32} - \frac{E_g}{4}$
p	$PO_2^{1/6}$	$\frac{\Delta H_r}{3} - E_g$	$PO_2^{1/4}$	$-\frac{\Delta H_s}{40} + \frac{\Delta H_r}{2} - E_g$	$PO_2^{3/16}$	$\frac{3\Delta H_r}{8} + \frac{\Delta H_s}{32} - \frac{3E_g}{4}$

Table 2.1. Temperature and PO2 dependence of defects for the defect model of intrinsic YAG in Figure 2.5.

Defect Model for Fixed Valence Acceptor Doped YAG

(a) $n=2[V_o^{..}]$

(b) $[A']=2[V_o^{..}]$

(c) $[A']=p$

(d) $p=3[V_M^{''''}]$

n
p
$[V_o^{..}]$
$[V_{Al}^{'''}]$
$3[V_Y^{'''}]$
$[A']$
$\log_{10}\sigma$

log concentration (au)

log PO_2 (au)

40   20   0   -20   -40   -60   -80   -100

-200   -100   0   100   200
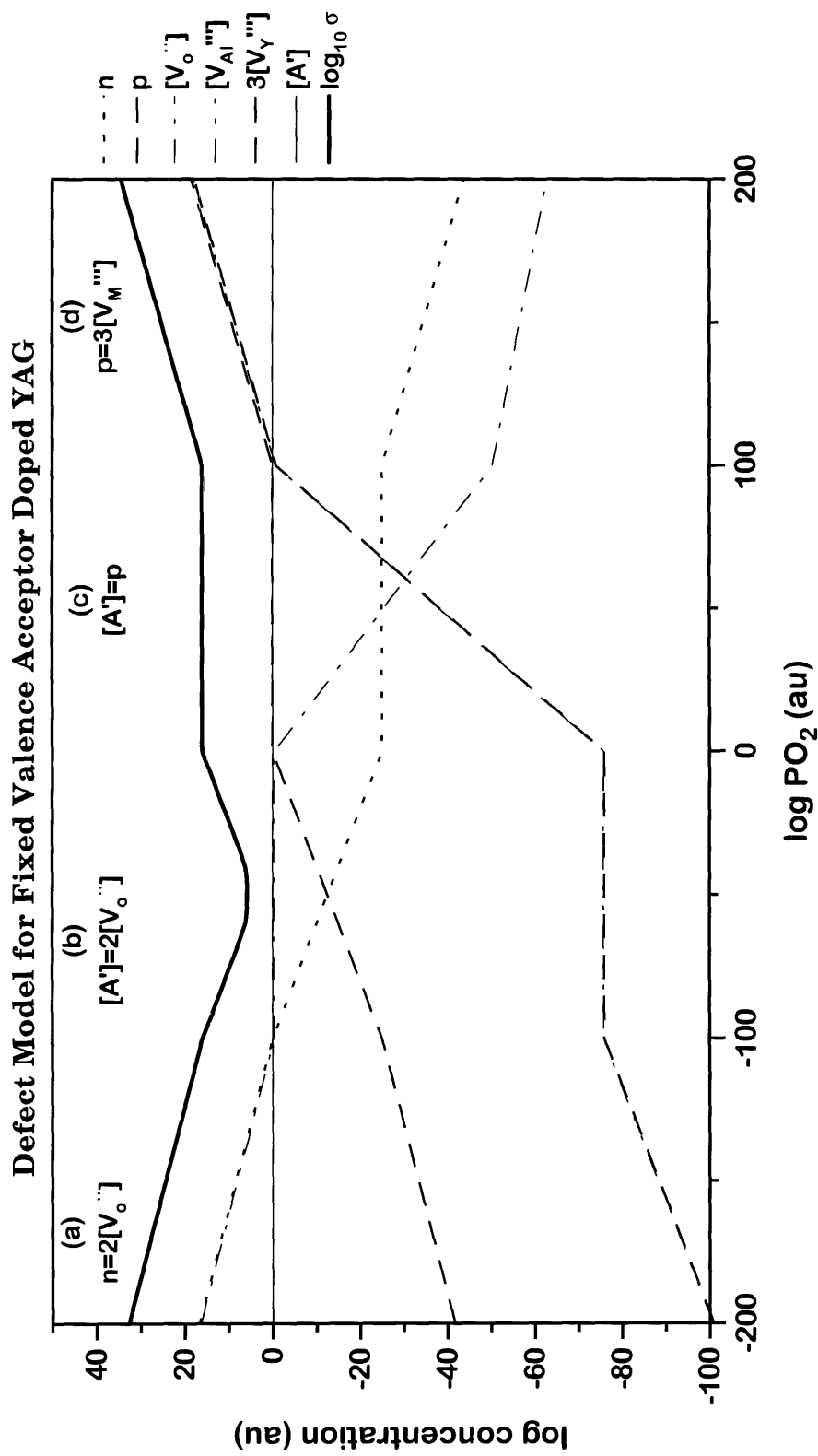
Figure 2.6 Schematic representation of the defect concentrations as a function of PO_2 for the defect model of a fixed valence acceptor doped YAG.

Temperature & PO$_2$ Dependence for Acceptor Doped YAG

Defect	Regime (a) $n=2[V_o^{\bullet\bullet}]$		Regime (b) $[A']=2[V_o^{\bullet\bullet}]$		Regime (c) $[A']=p$		Regime (d) $p=3[V_M''']$	
	PO$_2$ Dep.	Activation Energy	PO$_2$ Dep.	Activation Energy	PO$_2$ Dep.	Activation Energy	PO$_2$ Dep.	Activation Energy
$[V_{Al}''']$	$PO_2^{1/4}$	$\frac{\Delta H_r}{2}-\frac{\Delta H_s}{8}$	None	$-\frac{\Delta H_s}{8}$	$PO_2^{3/4}$	$\frac{3\Delta H_r}{2}-3E_g-\frac{\Delta H_s}{8}$	$PO_2^{3/16}$	$\frac{3\Delta H_r}{8}-\frac{\Delta H_s}{32}-\frac{3E_g}{4}$
$[V_Y''']$	$PO_2^{1/4}$	$\frac{\Delta H_r}{2}-\frac{\Delta H_s}{8}$	None	$-\frac{\Delta H_s}{8}$	$PO_2^{3/4}$	$\frac{3\Delta H_r}{2}-3E_g-\frac{\Delta H_s}{8}$	$PO_2^{3/16}$	$\frac{3\Delta H_r}{8}-\frac{\Delta H_s}{32}-\frac{3E_g}{4}$
$[V_o^{\bullet\bullet}]$	$PO_2^{-1/6}$	$-\frac{\Delta H_r}{3}$	None	None	$PO_2^{-1/2}$	$2E_g-\Delta H_r$	$PO_2^{-1/8}$	$-\frac{\Delta H_r}{4}-\frac{\Delta H_s}{16}-\frac{E_g}{2}$
n	$PO_2^{-1/6}$	$-\frac{\Delta H_r}{3}$	$PO_2^{-1/4}$	$-\frac{\Delta H_r}{2}$	None	$-E_g$	$PO_2^{-3/16}$	$-\frac{3\Delta H_r}{8}+\frac{\Delta H_s}{32}-\frac{E_g}{4}$
p	$PO_2^{1/6}$	$\frac{\Delta H_r}{3}-E_g$	$PO_2^{1/4}$	$+\frac{\Delta H_r}{2}-E_g$	None	None	$PO_2^{3/16}$	$+\frac{3\Delta H_r}{8}-\frac{\Delta H_s}{32}-\frac{3E_g}{4}$

Table 2.2. Temperature and PO$_2$ dependence of defects for the defect model of a fixed valence acceptor doped YAG in Figure 2.6.

aluminum and yttrium vacancies are the same, that the Schottky mechanism is the primary intrinsic defect mechanism for ionic defects, and that the formation energy for the Schottky reaction is much less than the formation energy for the electron-hole pairs. Note regime (b) in particular, where p and n vary as $PO_2^{\pm 1/4}$ respectively, and the oxygen vacancy concentration is PO_2 independent. We will refer to this regime later in the thesis.

A defect model based on donor doped YAG compensated by cation vacancies is shown in Figure 2.7, with the corresponding temperature and PO_2 dependencies in Table 2.3. [D$^\bullet$] stands for the concentration of positively charged donors, which is constant for a given sample. Again we assume that the formation energies of the aluminum and yttrium vacancies are the same. Note that regime (c) in this figure also has a PO_2 independent ionic regime with p and n varying as $PO_2^{\pm 1/4}$ respectively, just as in regime (b) of Figure 2.6. One way of distinguishing between these two regimes is by varying the donor and acceptor concentration. Increasing the donor concentration in acceptor doped YAG will decrease the concentration of the oxygen vacancies, whereas it will increase the cation vacancy in donor doped YAG.

A related defect model is shown in Figure 2.8, where the valence of the donor changes over the measured PO_2 range. In this model, the valence of the donor is +4 in regime (d), and +3 in regime (c). Notice that over the PO_2 range where the donor changes its valence, the conductivity isotherm has a very peculiar shape. The temperature and PO_2 dependencies of the various components in this model is listed in Table 2.4. The optical properties of acceptor and donor doped YAG will depend in general on both the acceptor and donor ions themselves, acting as optical centers, as well as the compensating defects these dopants generate, e.g. V and F color centers in alkali halides.[28]

41
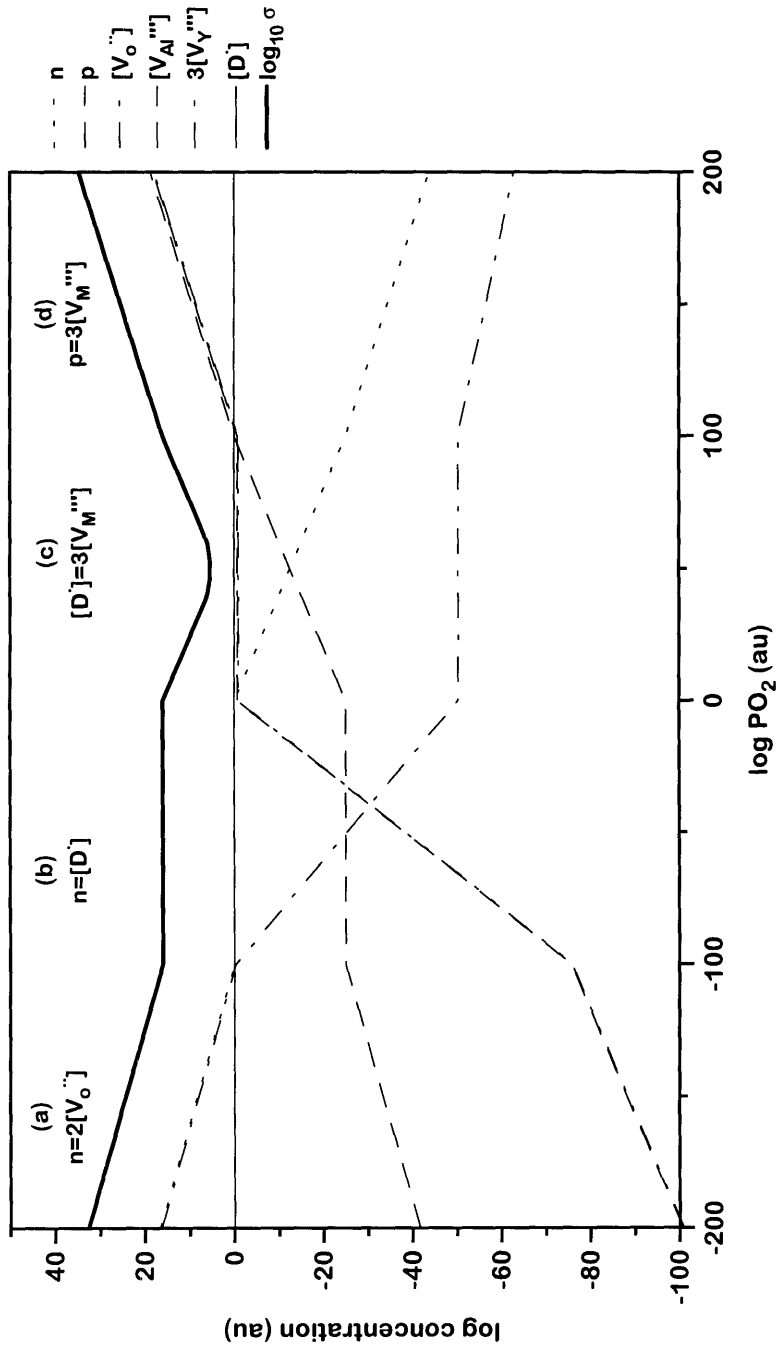
Figure 2.7 Schematic representation of the defect concentrations as a function of PO_2 for the defect model of a fixed valence donor doped YAG.

Temperature & PO₂ Dependence for Donor Doped YAG

Defect	Regime (a) $n = 2[V_o^{\bullet\bullet}]$		Regime (b) $[D^\bullet] = n$		Regime (c) $[D^\bullet] = 3[V_M''']$		Regime (d) $p = 3[V_M''']$	
	PO₂ Dep.	Activation Energy	PO₂ Dep.	Activation Energy	PO₂ Dep.	Activation Energy	PO₂ Dep.	Activation Energy
$[V_{Al}''']$	$PO_2^{1/4}$	$\frac{\Delta H_r}{2} - \frac{\Delta H_s}{8}$	$PO_2^{3/4}$	$\frac{3\Delta H_r}{2} - \frac{\Delta H_s}{8}$	None	None	$PO_2^{3/16}$	$\frac{3\Delta H_r}{8} - \frac{\Delta H_s}{32} - \frac{3E_g}{4}$
$[V_Y''']$	$PO_2^{1/4}$	$\frac{\Delta H_r}{2} - \frac{\Delta H_s}{8}$	$PO_2^{3/4}$	$\frac{3\Delta H_r}{2} - \frac{\Delta H_s}{8}$	None	None	$PO_2^{3/16}$	$\frac{3\Delta H_r}{8} - \frac{\Delta H_s}{32} - \frac{3E_g}{4}$
$[V_o^{\bullet\bullet}]$	$PO_2^{-1/6}$	$-\frac{\Delta H_r}{3}$	$PO_2^{-1/2}$	$-\Delta H_r$	None	$-\frac{\Delta H_s}{12}$	$PO_2^{-1/8}$	$-\frac{\Delta H_r}{4} - \frac{\Delta H_s}{16} - \frac{E_g}{2}$
n	$PO_2^{-1/6}$	$-\frac{\Delta H_r}{3}$	None	None	$PO_2^{-1/4}$	$-\frac{\Delta H_r}{2} + \frac{\Delta H_s}{24}$	$PO_2^{-3/16}$	$-\frac{3\Delta H_r}{8} + \frac{\Delta H_s}{32} - \frac{E_g}{4}$
p	$PO_2^{1/6}$	$\frac{\Delta H_r}{3} - E_g$	None	$-E_g$	$PO_2^{1/4}$	$\frac{\Delta H_r}{2} - \frac{\Delta H_s}{24} - E_g$	$PO_2^{3/16}$	$\frac{3\Delta H_r}{8} - \frac{\Delta H_s}{32} - \frac{3E_g}{4}$

Table 2.3. Temperature and PO₂ dependence of defects for the defect model of a fixed valence donor doped YAG in Figure 2.7.
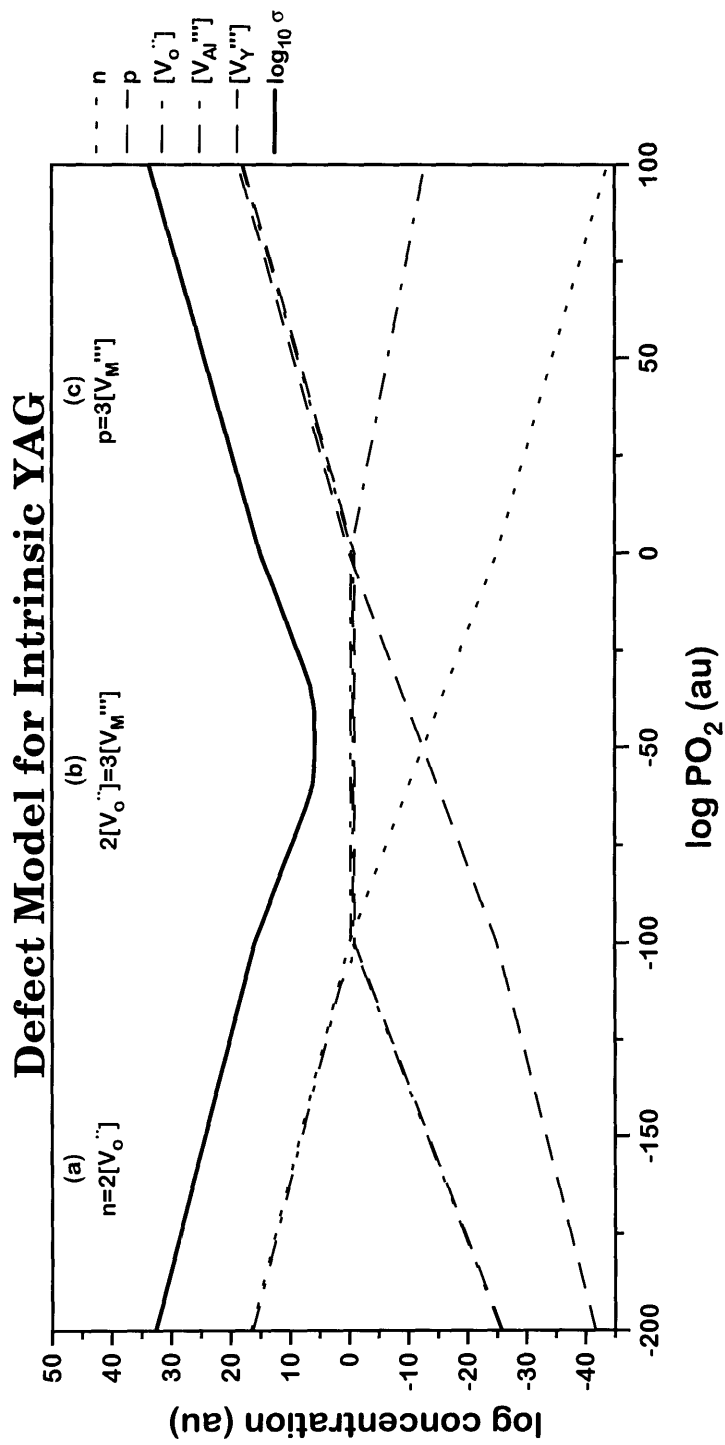
Figure 2.8 Schematic representation of the defect concentrations as a function of PO_2 for the defect model of a variable valence donor doped YAG.

Temperature & PO2 Dependence for Variable Valence Donor

Defect	Regime (a) $n=2[V_O^{••}]$		Regime (b) $2[V_O^{••}]=3[V_M''']$		Regime (c) $[Ti^•_{Al}]=3[V_M''']$ $[Ti^x_{Al}]=[Ti_{Al}]_{total}$	
	PO2 Dep.	Activation Energy	PO2 Dep.	Activation Energy	PO2 Dep.	Activation Energy
$[V_{Al}''']$	$PO_2^{1/4}$	$\dfrac{\Delta H_r}{2} - \dfrac{\Delta H_s}{8}$	None	$-\dfrac{\Delta H_s}{20}$	$PO_2^{3/16}$	$\dfrac{-\Delta H_s}{32} + \dfrac{-3\Delta H_i}{4} + \dfrac{3\Delta H_r}{8}$
$[V_Y''']$	$PO_2^{1/4}$	$\dfrac{\Delta H_r}{2} - \dfrac{\Delta H_s}{8}$	None	$-\dfrac{\Delta H_s}{20}$	$PO_2^{3/16}$	$\dfrac{-\Delta H_s}{32} + \dfrac{-3\Delta H_i}{4} + \dfrac{3\Delta H_r}{8}$
$[V_O^{••}]$	$PO_2^{-1/6}$	$-\dfrac{\Delta H_r}{3}$	None	$-\dfrac{\Delta H_s}{20}$	$PO_2^{-1/8}$	$\dfrac{-\Delta H_s}{16} + \dfrac{\Delta H_i}{2} + \dfrac{-\Delta H_r}{4}$
n	$PO_2^{-1/6}$	$-\dfrac{\Delta H_r}{3}$	$PO_2^{-1/4}$	$\dfrac{\Delta H_s}{40} + \dfrac{-\Delta H_r}{2}$	$PO_2^{-3/16}$	$\dfrac{\Delta H_s}{32} + \dfrac{-\Delta H_i}{4} + \dfrac{-3\Delta H_r}{8}$
p	$PO_2^{1/6}$	$\dfrac{\Delta H_r}{3} - E_g$	$PO_2^{1/4}$	$\dfrac{-\Delta H_s}{40} + \dfrac{\Delta H_r}{2} - E_g$	$PO_2^{3/16}$	$\dfrac{-\Delta H_s}{32} + \dfrac{\Delta H_i}{4} + \dfrac{3\Delta H_r}{8} - E_g$
$[Ti^•_{Al}]$	$PO_2^{1/6}$	$\dfrac{\Delta H_r}{3} - \Delta H_i$	$PO_2^{1/4}$	$\dfrac{-\Delta H_s}{40} + \dfrac{\Delta H_r}{2} - \Delta H_i$	$PO_2^{3/16}$	$\dfrac{-\Delta H_s}{32} + \dfrac{-3\Delta H_i}{4} + \dfrac{3\Delta H_r}{8}$
$[Ti^x_{Al}]$	None	None	None	None	None	None

Regime (d)
$$[Ti_{Al}^{\bullet}] = 3[V_M''']$$
$$[Ti_{Al}^{\bullet}] = [Ti_{Al}]_{total}$$

Regime (e)
$$p = 3[V_M''']$$

Defect	Regime (d) PO₂ Dependence	Regime (d) Activation Energy	Regime (e) PO₂ Dep.	Regime (e) Activation Energy
$[V_{Al}''']$	None	None	$PO_2^{3/16}$	$\frac{3\Delta H_r}{8} - \frac{\Delta H_s}{32} - \frac{3E_g}{4}$
$[V_Y''']$	None	None	$PO_2^{3/16}$	$\frac{3\Delta H_r}{8} - \frac{\Delta H_s}{32} - \frac{3E_g}{4}$
$[V_o^{\bullet\bullet}]$	None	$\frac{-\Delta H_s}{12}$	$PO_2^{-1/8}$	$-\frac{\Delta H_r}{4} - \frac{\Delta H_s}{16} - \frac{E_g}{2}$
n	$PO_2^{-1/4}$	$\frac{\Delta H_s}{24} + \frac{-\Delta H_r}{2}$	$PO_2^{-3/16}$	$-\frac{3\Delta H_r}{8} + \frac{\Delta H_s}{32} - \frac{E_g}{4}$
p	$PO_2^{1/4}$	$\frac{-\Delta H_s}{24} + \frac{\Delta H_r}{2} - E_g$	$PO_2^{3/16}$	$+\frac{3\Delta H_r}{8} - \frac{\Delta H_s}{32} - \frac{3E_g}{4}$
$[Ti_{Al}^{\bullet}]$	None	None	None	None
$[Ti_{Al}^x]$	$PO_2^{-1/4}$	$\Delta H_i + \frac{\Delta H_s}{24} + \frac{-\Delta H_r}{2}$	$PO_2^{-3/16}$	$-\Delta H_i + \frac{\Delta H_s}{32} + \frac{-3\Delta H_r}{8} - \frac{E_g}{4}$

Table 2.4. Temperature and PO₂ dependence of defects for the defect model of a variable valence donor doped YAG in Figure 2.8.

46

2.3: ELECTRICAL PROPERTIES IN OXIDES:

The defects described above will not only affect the optical properties of the oxide, but also the electrical properties. For example, because of compensating oxygen vacancies, the acceptor doped YAG in Figure 2.6 should have a higher ionic conductivity than the undoped YAG in Figure 2.5, due to its higher concentration of mobile oxygen vacancies. Electrical measurements thus provide a means of monitoring the change in defect concentration of the majority species, as long as the difference in defect concentration between the majority and minority species overwhelm any differences in their mobility. Electronic mobilities are typically orders of magnitude larger than ionic mobilities, so the electrical properties of an oxide can in fact change with the concentration of the electronic defects, even when they are the minority species, as long as they make a significant contribution to the total conductivity:

$$\sigma_{tot} = \sum_j \sigma_j = \sum_j c_j e z_j \mu_j$$

where c_j is the concentration of the jth species, $e z_j$ is the charge of the jth species, and μ_j is the mobility of the jth species.

Electrical measurements of oxides are typically done at high temperatures so that defect reactions are equilibrated within a reasonable time, and the defect concentrations and mobilities are large enough to bring the sample resistance within the measurement range of the instrumentation. The relation between the resistance, defect concentration, and mobility is shown below:

$$R = \frac{l}{A\sigma_{tot}} = \frac{l}{A\sum_j c_j e z_j \mu_j}$$

where l is the length of the sample, and A its cross-sectional area. Standard two probe dc current-voltage measurements often include significant contributions from electrode polarization. Two probe ac measurements can be used to isolate

the electrode contribution, provided the time constant for the electrical relaxation process of the electrode is significantly different from that for the sample.

The ac response of many oxide materials can be modeled by a parallel RC circuit as shown in Figure 2.9, where the resistive and reactive response of the sample is modeled by a resistor and capacitor.[30] The impedance plot of a parallel RC circuit is a semicircle as shown in Figure 2.10, where the imaginary axis is inverted so that the semicircle sits in the first quadrant. The intersection of the semicircle with the real axis gives us the value of R, the resistance for the RC circuit which occurs at small values of the frequency $\omega \rightarrow 0$. The apex of the semicircle occurs at the resonance frequency, $\omega/2\pi=1/\tau=1/(RC)$, the inverse of the electrical relaxation time constant τ. Similarly, the electrode and grain boundary (if the sample is polycrystalline) impedance can be modeled by additional parallel RC circuits in series with the RC circuit for the bulk, as shown in Figure 2.11. If the RC time constants of the sample, electrode, and grain boundary are very different, ≥ 100, then the three semicircles belonging to the three RC circuits can be clearly resolved, as shown in Figure 2.12 for the pyrochlore $Gd_2(Zr_{0.6}Ti_{0.4})_2O_7$.[29] Careful measurements using different electrodes and electrode areas can be used to determine which semicircle belongs to the sample and which to the electrode.

A series of such measurements at different temperature and PO_2 are then used to construct conductivity isotherms as shown in Figure 2.13 for Ce:YAG.[31] Such isotherms yield a great deal of information about the defect structure of the sample. These isotherms are used to construct a defect model for the sample, one which can explain the various features of the isotherm. When comparing defect models with measured isotherms, it is important to remember that the measured isotherms represent the total conductivity. Thus a defect model such as that shown in Figure 2.6 should be mentally multiplied by a mobility factor
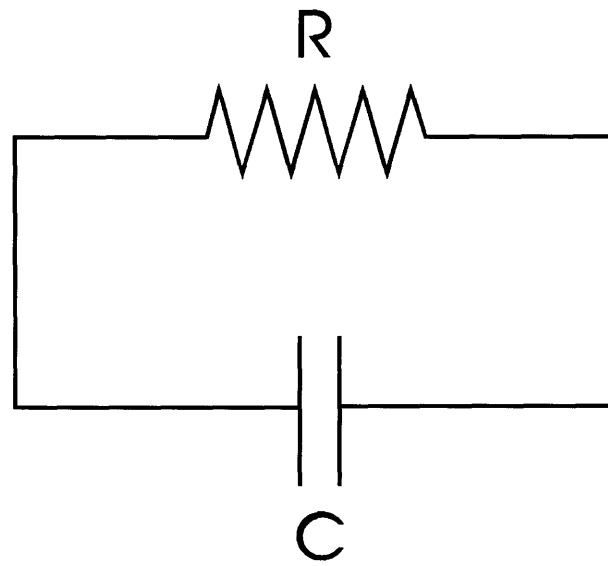
Figure 2.9 Equivalent Circuit Model for a single crystal oxide ceramic.[30]
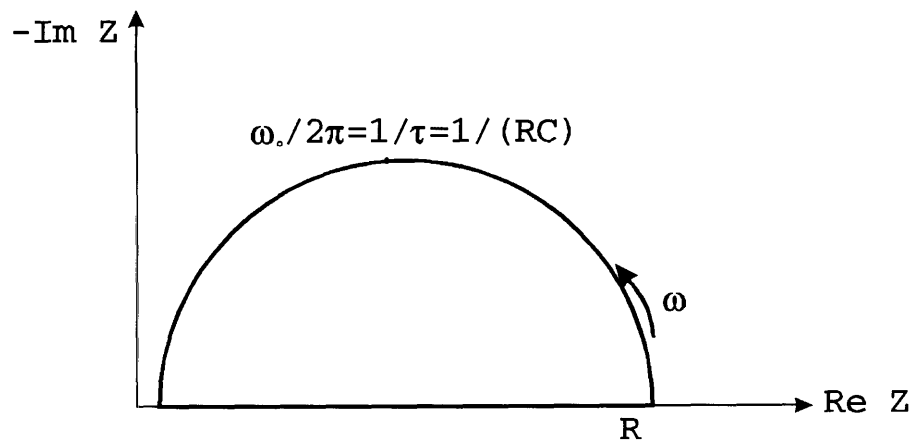
Figure 2.10 Schematic complex impedance plot of the equivalent
circuit in Figure 2.9.
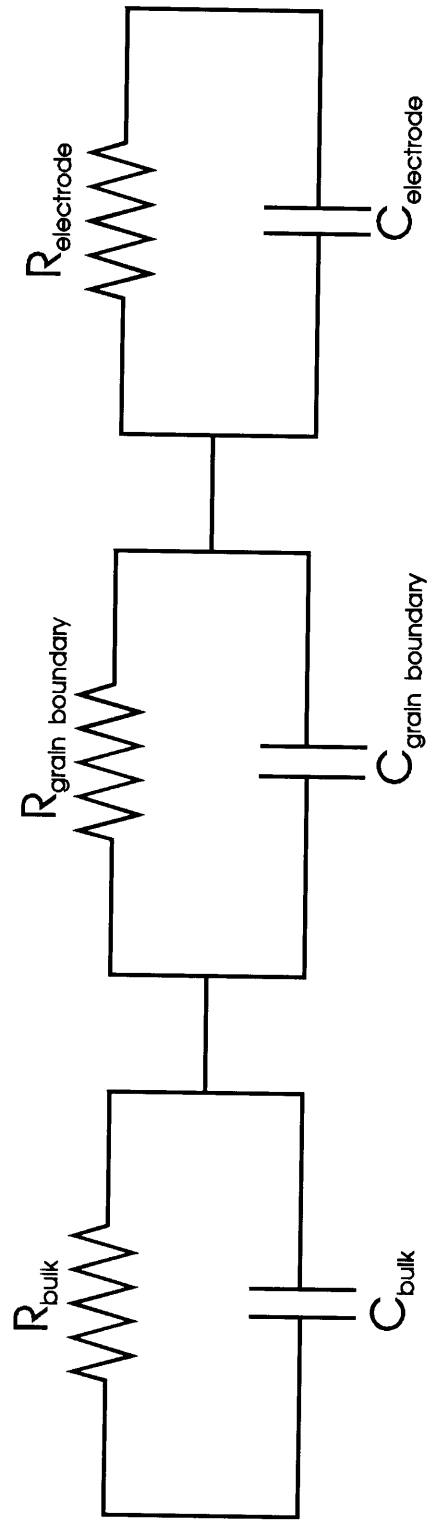
Figure 2.11 Equivalent Circuit Model for a polycrystalline oxide ceramic.[30]

51
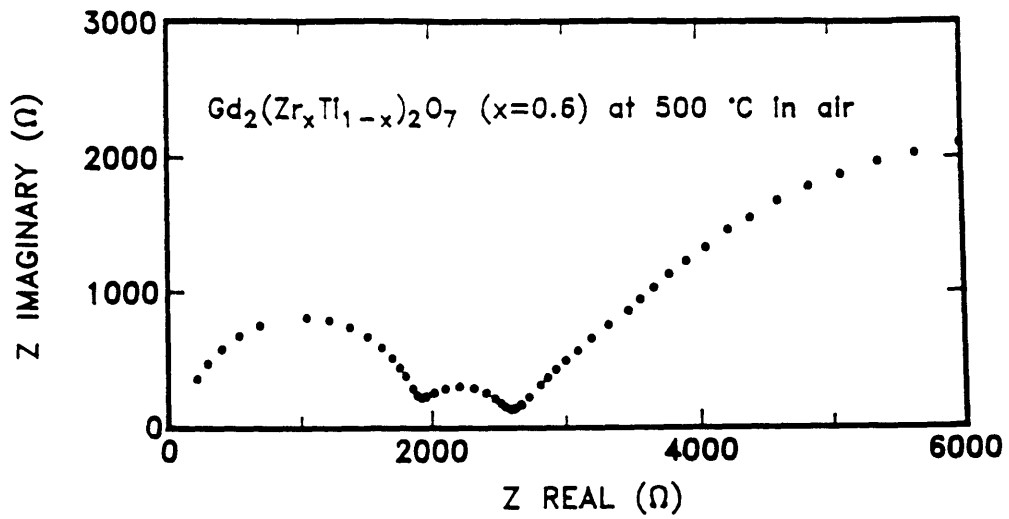
Figure 2.12 Complex impedance plot for $Gd_2(Zr_{0.6}Ti_{0.4})_2O_7$ at 500°C in air showing the bulk, grain boundary, and electrode impedances.[29]
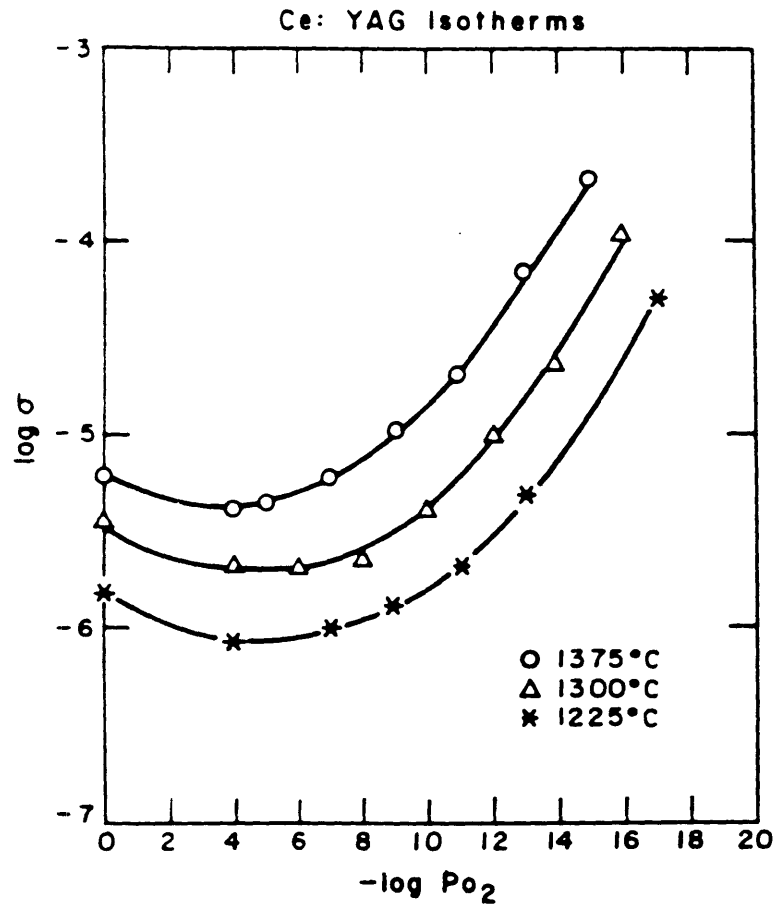
Figure 2.13 AC conductivity isotherms for Ce:YAG as a function of PO_2.[31]

for the various components and then all the conductivity components added together to generate a predicted conductivity isotherm, as seen in Figures 2.5-2.8.

For example, Ce:YAG isotherms in Figure 2.13 were modeled as being acceptor doped, with the defect model of Figure 2.6.[4,31] The PO_2 range of the isotherm in Figure 2.13 corresponds to regime (b) in Figure 2.6, where the conductivity increase under oxidizing and reducing conditions is interpreted in terms of increases in the hole and electron concentration respectively. Even though the hole and electron concentration is much smaller than the oxygen vacancy concentration, the higher mobilities of these electronic carriers make them a significant part of the total conductivity. The deconvolution of the Ce:YAG isotherm into a PO_2 dependent and PO_2 independent part is shown in Figure 2.14.[31] As seen in regime (b) of Figure 2.6, the defect model's prediction of a 1/4 power law dependence with PO_2 for the concentration of electronic carriers is consistent with the de-convoluted PO_2 dependence of the measured conductivity isotherm.[4,31] The defect model also allows us to ascribe defect reaction energies to the measured activation energies of the conductivity isotherms. For example, the activation energies of the components of the Ce:YAG isotherms are shown in Figure 2.15.[31] If the activation energies for the electronic mobilities are assumed to be negligible (large polaron), then the activation energies for the n and p branches are primarily associated with defect generation and recombination processes, and from regime (b) of Table 2.2, we see that they correspond to:[31]

$$\frac{E_r}{2} = 3.9 \text{ eV} \qquad \text{(n branch)}$$

$$E_g - \frac{E_r}{2} = 2.2 \text{ eV} \qquad \text{(p branch)}$$

$$\implies E_g = 6.1 \text{ eV}$$

54
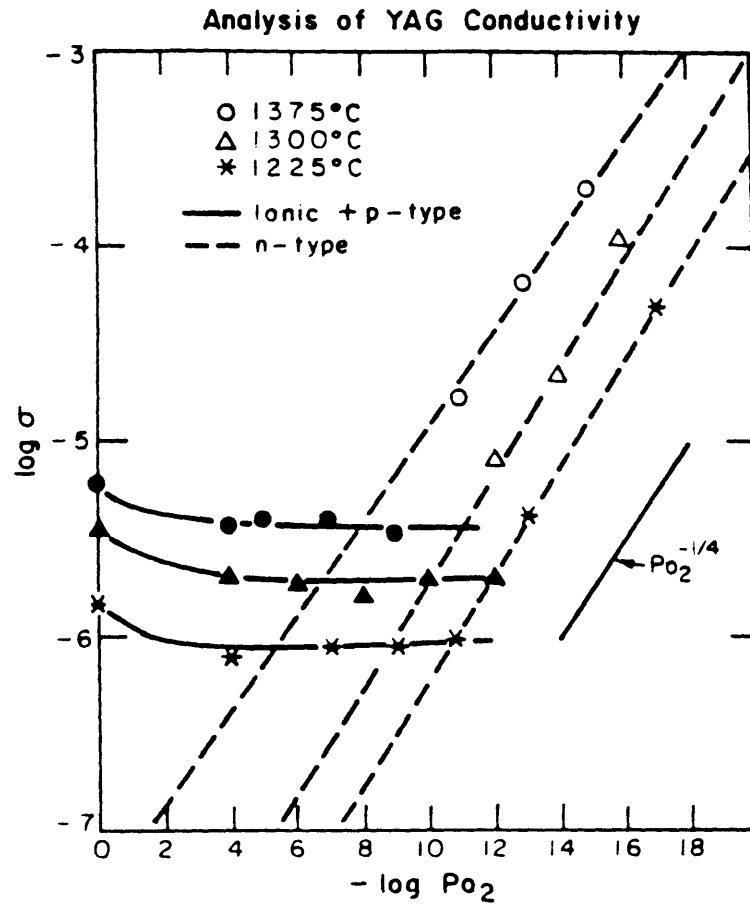
Figure 2.14 AC conductivity isotherms for Ce:YAG separated into n-type and ionic components, as a function of PO_2.[31]
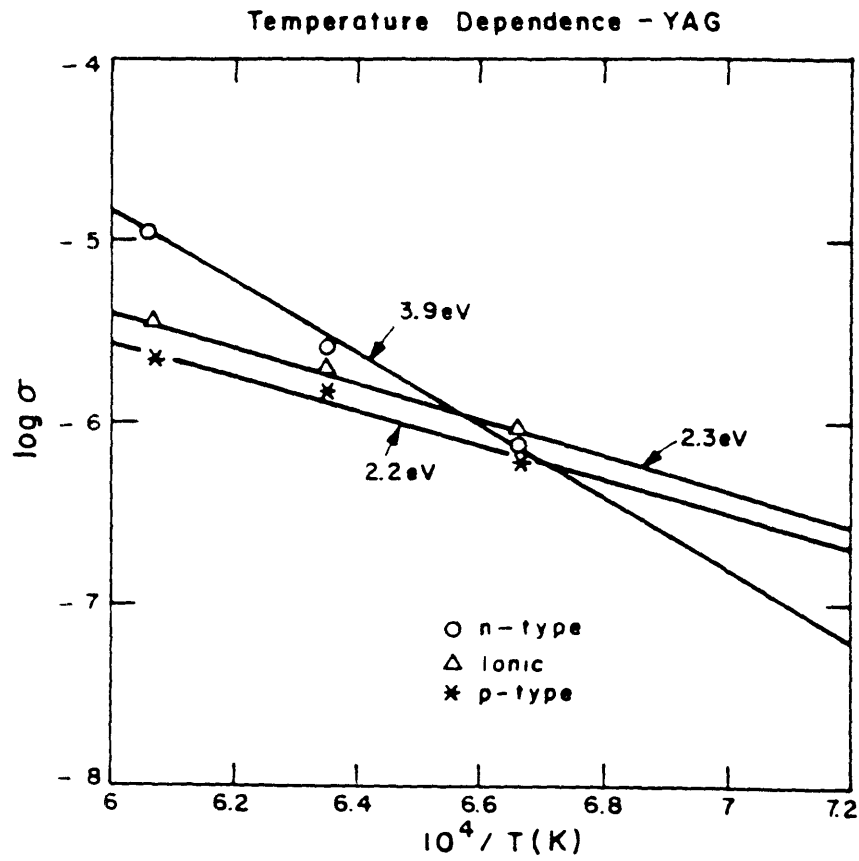
Figure 2.15 Temperature dependence of p-type, n-type, and ionic conductivity of
Ce:YAG.[31]

The optical bandgap has been reported to be ≈ 6 eV,[32] in close agreement with the value derived from electrical measurements, supporting the defect model and its associated assumptions.

In constructing defect models from conductivity isotherms, it is immensely helpful to know what fraction of the total conductivity is ionic, and what fraction electronic. To this end, ionic transference measurements are often employed. Ionic transference measurements enable one to establish the degree of ionic conductivity at a given temperature and PO_2 by measuring the voltage induced across a cell in which the sample serves as an electrolyte between two chambers of different oxygen partial pressure. If we define the transference number t_i to be the ratio of the ionic conductivity to the total conductivity, the voltage E generated across the transference cell is approximated by

$$E = \langle t_i \rangle \frac{kT}{4q} \ln \frac{PO_2^{\ I}}{PO_2^{\ II}}$$

where $\langle t_i \rangle$ is the average ionic transference number within that PO_2 gradient, k is Boltzmann's constant, q is the charge of an electron, and $PO_2^{\ I}$ and $PO_2^{\ II}$ correspond to the partial pressures of oxygen on either side of the crystal. Ionic transference measurements of Ce:YAG are shown in Figure 2.16.[4,31] These measurements reveal that Ce:YAG is a mixed ionic electronic conductor, further supporting the acceptor doped defect model of Figure 2.6.

2.4: CRYSTAL STRUCTURE OF YAG

YAG is a member of the garnet crystal system, a crystal system found in many natural minerals. Garnets have a chemical formula $A_3B_2C_3O_{12}$, with eight formula units per unit cell, and the cubic space group Ia3d.[27,33-35] The A cations occupy the 8-fold dodecahedral site, a distorted cube polyhedron with a local symmetry of D_2. The B cations occupy the 6-fold octahedral site with a local symmetry of $\bar{3}$. The C cations occupy the 4-fold tetrahedral site with a
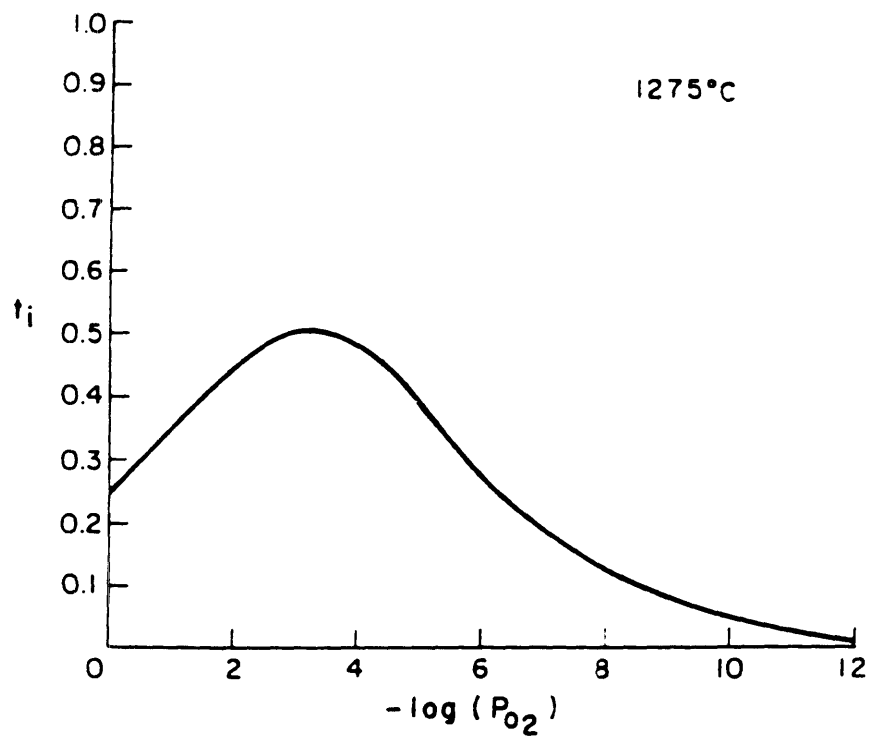
Figure 2.16 Ionic transference number t_i in Ce:YAG as a function of PO_2.[31]

local symmetry of $\bar{4}$.[27,33-35] Drawings of these polyhedra are seen in Figure 2.17.[35] The 8-fold site is the largest, occupying the space group position 24c, followed by the six-fold site in position 16a, and the smallest 4-fold site in position 24d. All three of these space group positions are "special positions" in that they occur at an intersection of symmetry elements of the space group, and consequently have symmetrical constraints on the types of distortions that the coordination polyhedra can have. The oxygen anion in contrast, occupies the "general" space group position 96h, and consequently has no symmetrical constraints on its position. Thus the exact position of the anion is flexible, and can change so as to best accommodate the distortions permitted by the cation special positions above. This flexibility is a primary reason why garnets occur in so many natural minerals, and why synthetic garnets have been developed with most of the first row transition metals, as well as most of the rare earths.[27,33-35]

The garnet crystal system can be built up from these cation coordination polyhedra using a variety of schemes. One scheme is to form two linearly repetitive chains, a) chains of alternating dodecahedra and tetrahedra along [001] with shared edges, and b) chains of octahedra sharing corners along [111]. Dodecahedra are also situated at the point of closest approach between adjacent chains.[33] Drawings of these polyhedra in the garnet structure are seen in Figure 2.18 & 2.19.[34,36] Each tetrahedron shares two edges with dodecahedra, and each octahedron shares six edges with dedecahedra. The dodecahedron has three types of shared edges. Each dodecahedron shares two edges with tetrahedra, four edges with octahedra, and four edges with other dodecahedra. Tetrahedra share only corners with octahedra.[35] The different edges for the polyhedra tend to distort along Pauling's rules, the shared edges of each polyhedra tend to be shorter than the unshared edges.[33,34] Consequently all the polyhedra are distorted from regular polyhedra. Two non-equivalent
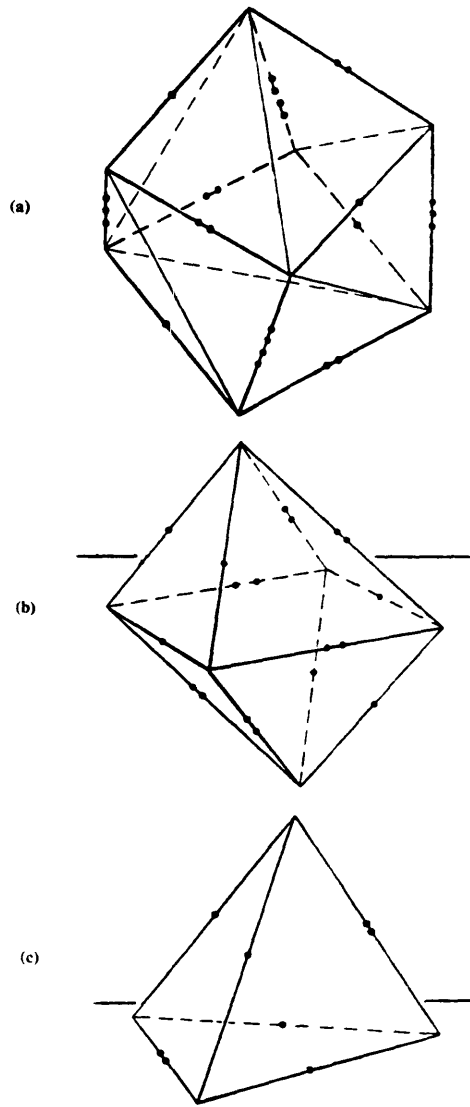
Figure 2.17 Anion polyhedra in YAG. (a) dodecahedron, (b) octahedron,
(c) tetrahedron.[35]
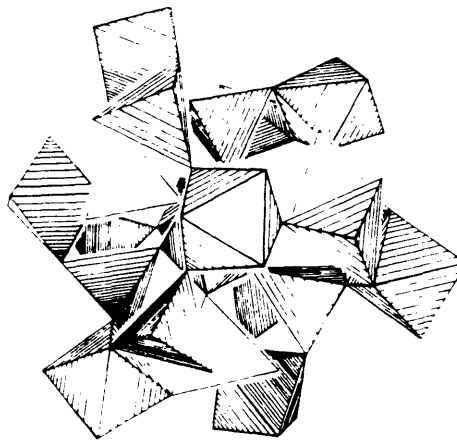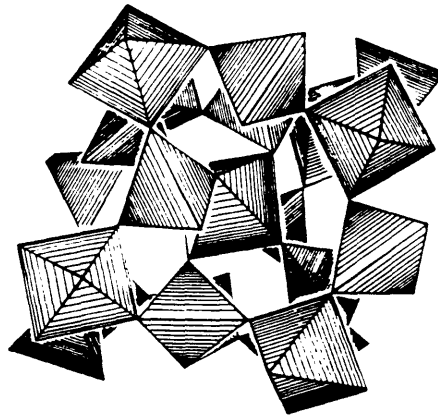
Figure 2.18 Drawings of the octahedral and tetrahedral polyhedra in YAG
viewed down $\bar{3}$ (a) and along z (b). Dodecahedral polyhedra have
been ommitted for clarity, and polyhedra may have been displaced
slightly to avoid superposition.[34]

61
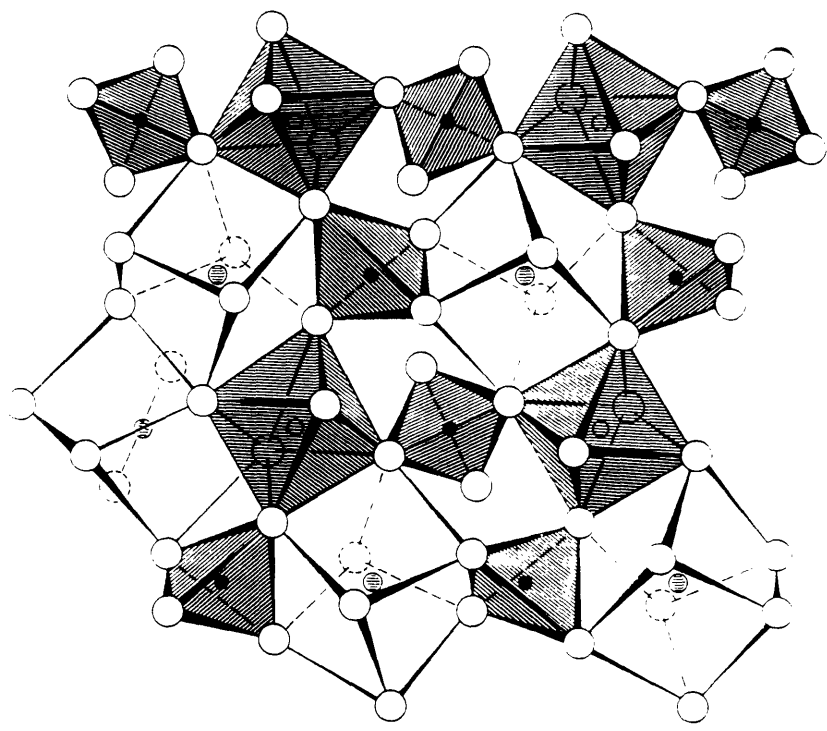
Figure 2.19 Drawing of the garnet structure projected down z.[36]

octahedral sites and six non-equivalent dedecahedral sites result from these distortions for yttrium iron garnet.[35] Note that the site symmetry of these non-equivalent sites is still the same, $\bar{3}$ and D_2 respectively, so optical measurements of crystal field states in these sites would be insensitive to their inequivalency, whereas magnetic measurements like paramagnetic resonance would detect these inequivalencies. Representative inter-atomic distances are shown in Figure 2.20 for the garnet andradite, $Ca_3Fe_2Si_3O_{12}$, which has a lattice parameter of a_o=1.2058 nm.[34]

In YAG, yttrium occupies the 8-fold site while aluminum occupies both the 6-fold and 4-fold sites.[27,33] YAG's lattice parameter is a_o=1.0220 nm, and interionic distances are shown in Figure 2.21.[27,33] These interionic distances should be compared with the ionic radii of the matrix ions, as well as the ionic radii of some potential impurities and dopants as seen in Table 2.5.[37,38] In garnets, site preference of impurities or dopants depend primarily on relative ionic sizes.[27,34-35] The large dopants tend to go into the large 8-fold dodecahedral site, whereas the smallest dopants tend to go into the small 4-fold tetrahedral site. Thus Nd^{+3} with its large ionic radius of 1.12 angstroms goes into the dodecahedral sites exclusively.[27] A secondary but important factor for site preference is the crystal field stabilization energy (CFSE), the reduction in ground state energy of the incorporated ion relative to that of the free ion due to crystal field splitting of the degenerate electronic states. Differences in CFSE for the octahedral and tetrahedral sites have been used successfully in the past to explain site occupancy of transition metals in normal and inverted spinels.[39] An extrapolation of these results to garnets helped explain some anomalous results with respect to the ionic size criterion. For example, Cr^{+3} substitutions in yttrium iron garnet (YIG) and yttrium gallium garnet were found to enter the octahedral site exclusively, despite its smaller size with respect to Fe^{+3} and Ga^{+3}, as seen
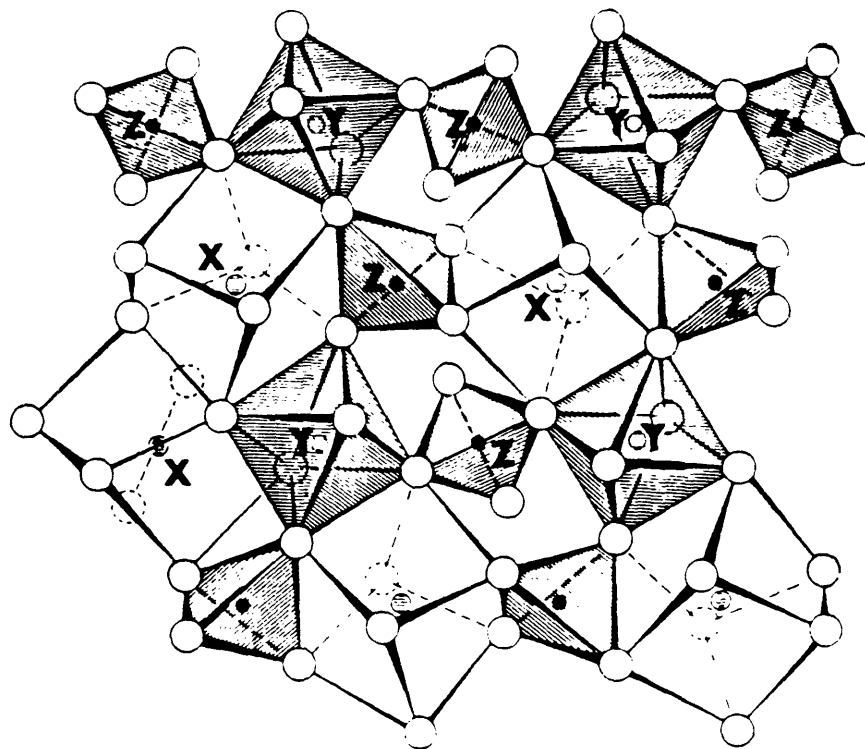
Z-O	0.1643 nm	average
Y-O	0.2024 nm	average
X-O	0.2433 nm	average
X-Y	0.3370 nm	edge-shared XO_8 and YO_6
X-Z	0.3692 nm	edge-shared XO_8 and ZO_4
X-Z	0.3015 nm	edge-shared XO_8 and ZO_4
X-X	0.3692 nm	edge-shared XO_8
Y-Z	0.3370 nm	corner-shared YO_6 and ZO_4

Figure 2.20 Garnet structure projected down z with interatomic distances for andradite, $Ca_3Fe_2Si_3O_{12}$.[34]

Figure 2.21 (a) Arrangement of the anion polyhedra in garnets.[33]
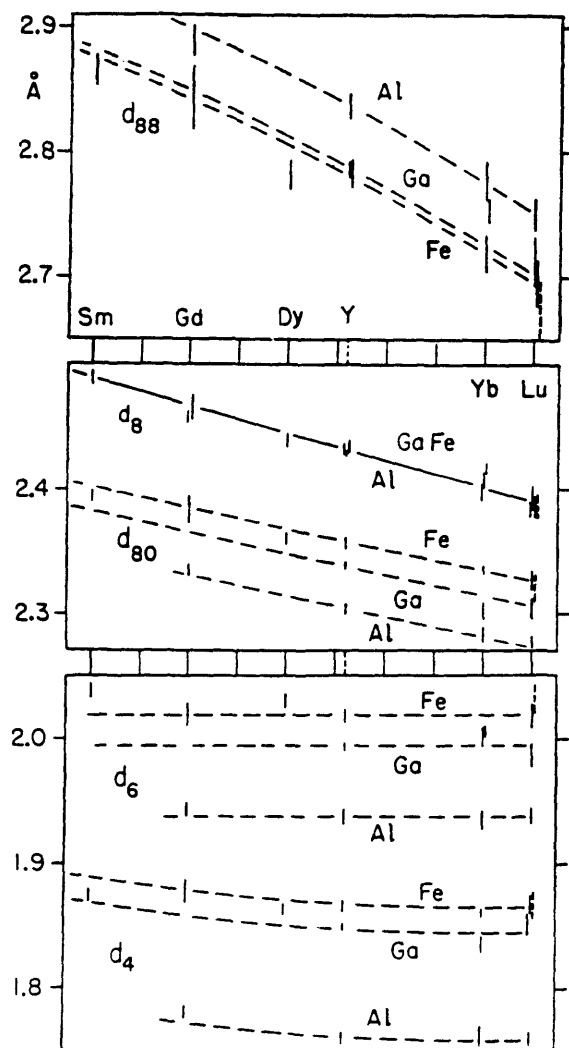
Figure 2.21(b) Interatomic distances in rare-earth garnets $R_3M_5O_{12}$ as a function of the atomic number of the rare-earths. Notation refers to Figure 2.21(a).[33]

Ionic Radii* vs. Cation Valence / Coordination Number

Cation:	VIII	VI	IV
Y^{+3}	1.019	0.90	
Nd^{+3}	1.12	0.98	
Zr^{+4}	0.84	0.72	0.59
Al^{+3}		0.54	0.39
Ti^{+4}		0.61	0.42
Ti^{+3}		0.67	
Ti^{+2}		0.86	
Fe^{+2}		0.61 (LS) 0.78 (HS)	0.63 (HS)
Fe^{+3}		0.55 (LS) 0.65 (HS)	0.49 (HS)
Cr^{+2}		0.73 (LS) 0.82 (HS)	
Cr^{+3}		0.62	
O^{-2}	1.42	1.40	1.38

----
*(in Angstroms)   LS: Low Spin   HS: High Spin

Table 2.5. Ionic radii vs. cation valence and coordination number.[37,38]

in Table 2.5.[27,37-38] This result can be understood in terms of the octahedral site preference energy, the difference between the CFSE for the octahedral and tetrahedral sites. In spinels, this preference energy is 2.0 eV/atom for Cr^{+3}, and 0 eV for Fe^{+3} as shown in Table 2.6.[39]

From both size and CFSE considerations, (see Table 2.5 & 2.6) we see that Ti^{+3} should enter the octahedral site in YAG. In fact, Ti^{+3} has been found in octahedral sites in a large number of hosts including YAG, as evidenced by the spectroscopic data of Ti^{+3} in octahedrally split crystal field states.[11,18,40-42] No evidence for Ti^{+3} entering the dodecahedra site in garnets has been found, and would be unexpected from size considerations. Ti^{+4} on the other hand, has no CFSE, and its ionic radii is very close to Al^{+3} for 4-fold coordination as seen in Table 2.6.[37,38] Thus, Ti^{+4} may enter the tetrahedral sites, and has been found to do so in YIG and YGaG, as evidenced by crystallographic and magnetic data.[43,44]

From size considerations, we would expect Zr^{+4} to enter the dodecahedral or octahedral site in YAG, its ionic radii being a bit small for the dodecahedral site, and a bit large for the octahedral site. See Table 2.5. Zr^{+4} has been found in both types of sites in other oxides. For example, in pyrochlores such as $Gd_2(Zr_xTi_{1-x})_2O_7$, Zr^{+4} occupies an 8-fold-like site,[45] while in perovskites such as $Pb(Zr,Ti)O_3$, Zr^{+4} occupies a 6-fold site.[46] Similarly, Zr^{+4} has been found in both types of sites in garnets, in the dodecahedral site for $Ca_{2.5}Zr_{2.5}Ga_3O_{12}$, and the octahedral site for $Ca_3Zr_2(V_{0.5}Ga_{2.5})O_{12}$, as evidenced by both crystallographic and magnetic data.[47,48] If Zr^{+4} were to be reduced to a +3 valence state however, it would have a significantly larger ionic radii, and consequently be expected to occupy the dodecahedral site exclusively. Zr^{+3} occupying the dodecahedral site exclusively has been observed in Zr:YAG from electron spin resonance data.[5]

Number of d-electrons	Ion	Free ion ground state	Octahedral field ground state	Tetrahedral field ground state	Dq cm^{-1} oct.	Dq cm^{-1} tetr.	Stabilization, kcal oct.	Stabilization, kcal tetr.	Oct. site preference energy kcal/mole
1	Ti^{+++}	^2D	$^2T_{2g}$	^2E_g	2030	900	23·1	15·4	7·7
2	•V^{+++}	^3F	$^3T_{1g}$	$^3A_{2g}$	1800	840	30·7	28·7	2·0
3	V^{++}	^4F	$^4A_{2g}$	$^4T_{1g}$	1180	520	40·2	8·7	31·5
	Cr^{+++}	^4F	$^4A_{2g}$	$^4T_{1g}$	1760	780	60·0	13·3	46·7
4	Cr^{++}	^5D	^5E_g	$^5T_{2g}$	1400	620	24·0	7·0	17·0
	Mn^{+++}	^5D	^5E_g	$^5T_{2g}$	2100	930	35·9	10·6	25·3
5	Mn^{++}	^6S	$^6A_{1g}$	$^6A_{1g}$	750	330	0	0	0
	Fe^{+++}	^6S	$^6A_{1g}$	$^6A_{1g}$	1400	620	0	0	0
6	Fe^{++}	^5D	$^5T_{2g}$	^5E_g	1000	440	11·4	7·5	3·9
	•Co^{+++}	^1D	$^1A_{1g}$	^5E_g		780	45	26	19
7	Co^{++}	^4F	$^4T_{1g}$	$^4A_{2g}$	1000	440	17·1	15·0	2·1
8	Ni^{++}	^3F	$^3A_{2g}$	$^3T_{1g}$	860	380	29·3	6·5	22·8
9	Cu^{++}	^2D	^2E_g	$^2T_{2g}$	1300	580	22·2	6·6	15·6
10	Zn^{++}	^1S	$^1A_{1g}$	$^1A_{1g}$	0	0	0	0	0

Table 2.6 Crystal field stabilization energy for transition metal ions.[39]

Under reducing conditions, Ti and Zr solubilities in YAG have been reported to be as high as 5 weight percent (w/o) TiO_2,[6] and 2 w/o ZrO_2[5] respectively, without affecting the optical quality of the crystals. Nd solubilities of up to 1.5 atomic percent (a/o) have been reported for high quality optical crystals.[19]

CHAPTER 3: LITERATURE REVIEW

3.1: Introduction

In this chapter we will review previous work done on the optical and
transport properties of YAG and doped YAG, with emphasis on our particular
systems of interest, Ti:YAG and Zr:YAG. As we will see, despite the voluminous
research done on YAG, much is still not known and controversial, such as the
source of the ultraviolet (UV) absorption in "undoped" YAG. Furthermore, there
has been no systematic quantitative explanation of YAG's electrical and optical
properties in terms of its defect structure to date, nor has any defect structure
other than an acceptor dominated defect structure for YAG been found. This
oversight is unfortunate, as the properties of donor doped YAG may yet prove
very interesting.

3.2: Optical Properties

3.2.1: YAG:

At room temperature, undoped YAG has a transmission window from the
end of the lattice multiphonon bands at 4.2 μm to the beginning of the UV region
at $\approx$300 nm.[32] Consequently YAG is transparent and colorless in the visible
range. YAG's optical bandgap is $\approx$6.6 eV, with the valence band comprised of
filled oxygen 2p orbitals, and the conduction band comprised of empty yttrium 4d
orbitals.[4,32] The UV absorption between 300 nm and the bandedge at 190 nm
varies dramatically from crystal to crystal as seen in Figure 3.1.[32] This
absorption also changes with oxidizing and reducing anneals, as well as with
irradiation of all types, e.g. UV, x-ray, neutron, and γ radiation.[4,49-54]

This UV absorption has traditionally been ascribed to a) trace impurities,
especially of transition metal elements like iron,[32,52,54-55] and b) oxygen vacancy

71
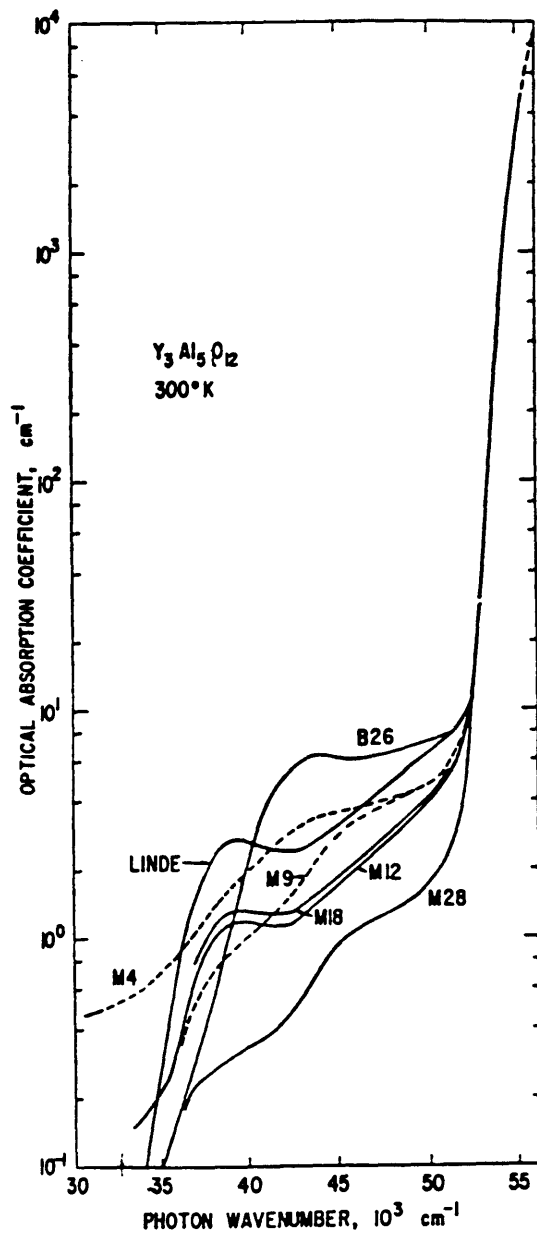
Figure 3.1   The optical-absorption coefficient α vs. photon wave number for several single crystals of $Y_3Al_5O_{12}$ at 300°K in the ultraviolet region.[32]

72

color centers.[4] However, the identification of these trace impurities and their energy levels in YAG, as well as the energy level of the oxygen vacancy in YAG, remain uncertain. For example, Mori places the $V_O^\bullet$ level at greater than 3.7eV below the conduction band, with internal $V_O^\bullet$ transitions at 1, 2, and 3 eV as shown in Figure 3.2 & 3.3.[4] He attributes the UV absorption to charge transfer from the oxygen 2p band to Fe^{+3} impurities with a Fe^{+3} level at 4.9 eV above the valence band (E_4 in Figure 3.3). Rotman, on the other hand, places the $V_O^\bullet$ level at 1 eV below the conduction band, and ascribes part of the UV absorption to internal $V_O^\bullet$ transitions with peaks at 220 and 270 nm as seen in Figure 3.4 & 3.5.[4] It has generally been observed that this UV absorption decreases dramatically with a reducing anneal, and this has often been interpreted in terms of removal of charge transfer bands from oxygen 2p to impurity ions via reduction of the impurity ion's valence.[4,52]

One such impurity that has been extensively investigated is Fe, a common impurity found in YAG crystals. The Fe^{+3} level has been located at ≈ 5 eV above the oxygen 2p band.[52,54] Upon reduction, this band disappears, and a new band at ≈ 300 nm appears as seen in Figure 3.6. Mori and Akhmadullin assign this band to charge transfer from a Fe^{+2} ion to the conduction band.[52,54]

Thus the optical properties of "pure" YAG exhibit considerable variance, especially in the UV range. This no doubt stems from slight differences in the crystal growth conditions, e.g. raw material purity, stoichiometry, etc. Consequently experimental studies of pure YAG may really be detecting "background effects" that reflect differences in processing, and the variance in properties simply reflecting the differences in the "background." Doped YAG, where the doping concentration is high enough to overwhelm any background

73
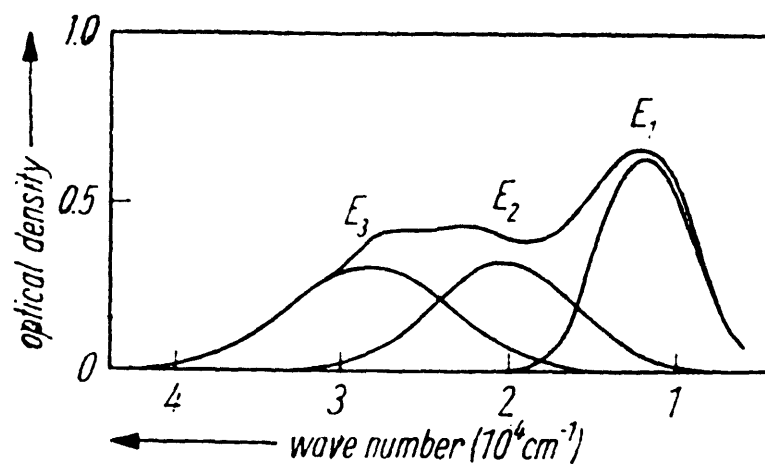
Figure 3.2   YAG optical absorption ascribed to oxygen vacancies.[54]
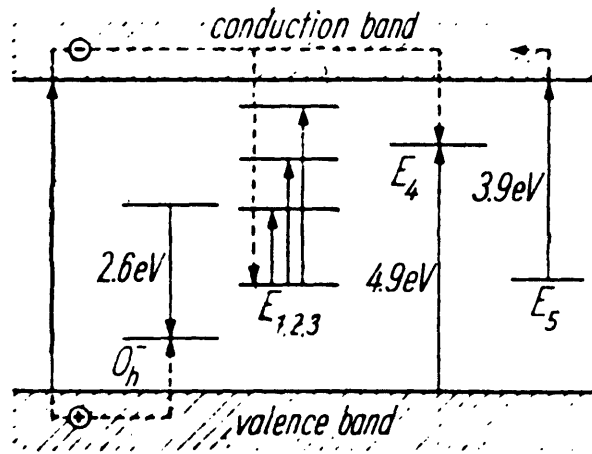
Figure 3.3   Proposed YAG energy diagram for oxygen vacancies and Fe
impurities.[54]
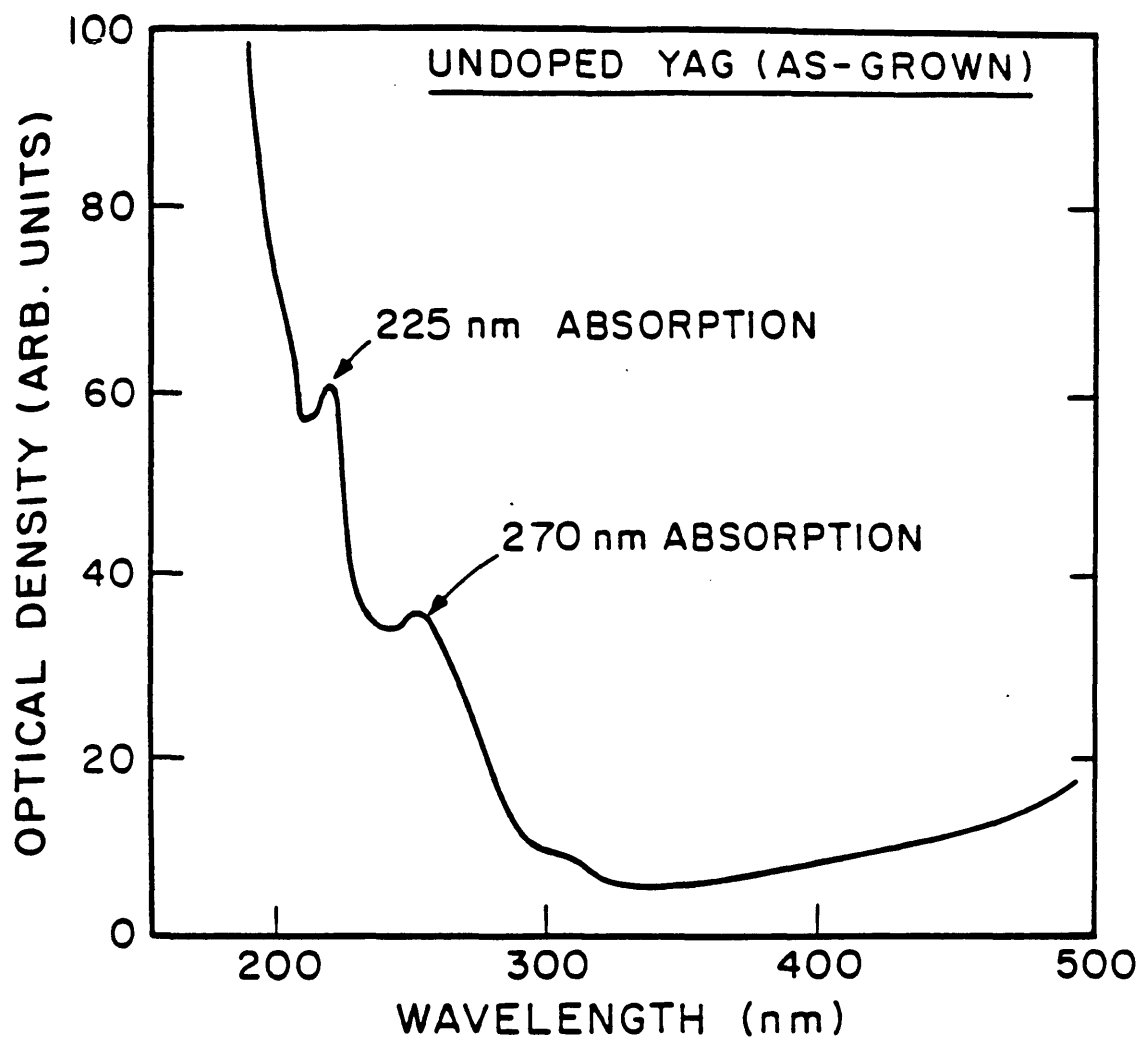
Figure 3.4   YAG optical absorption ascribed to oxygen vacancies.[4]
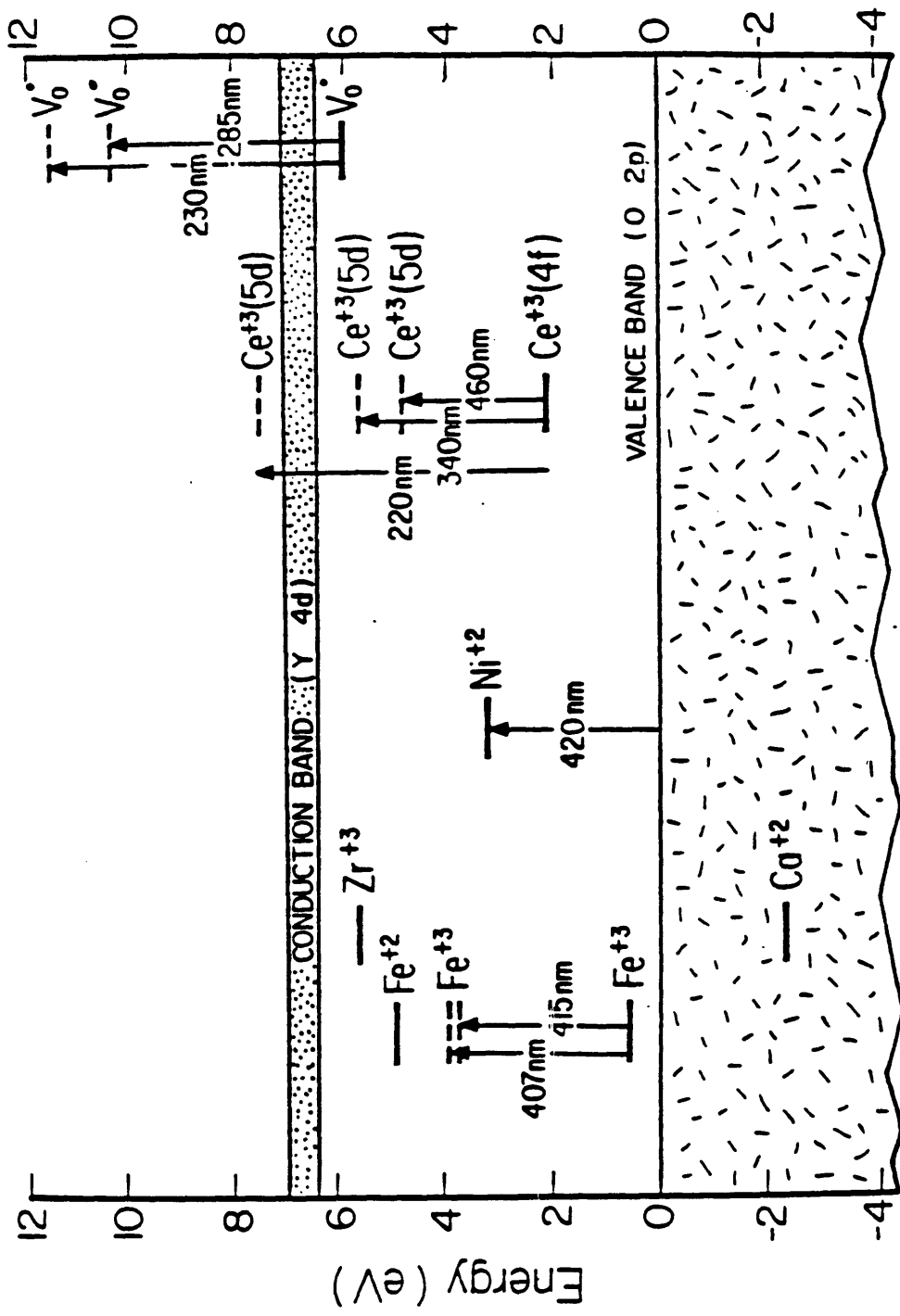
Figure 3.5 Proposed YAG energy diagram for oxygen vacancies and various dopants. [4]

77
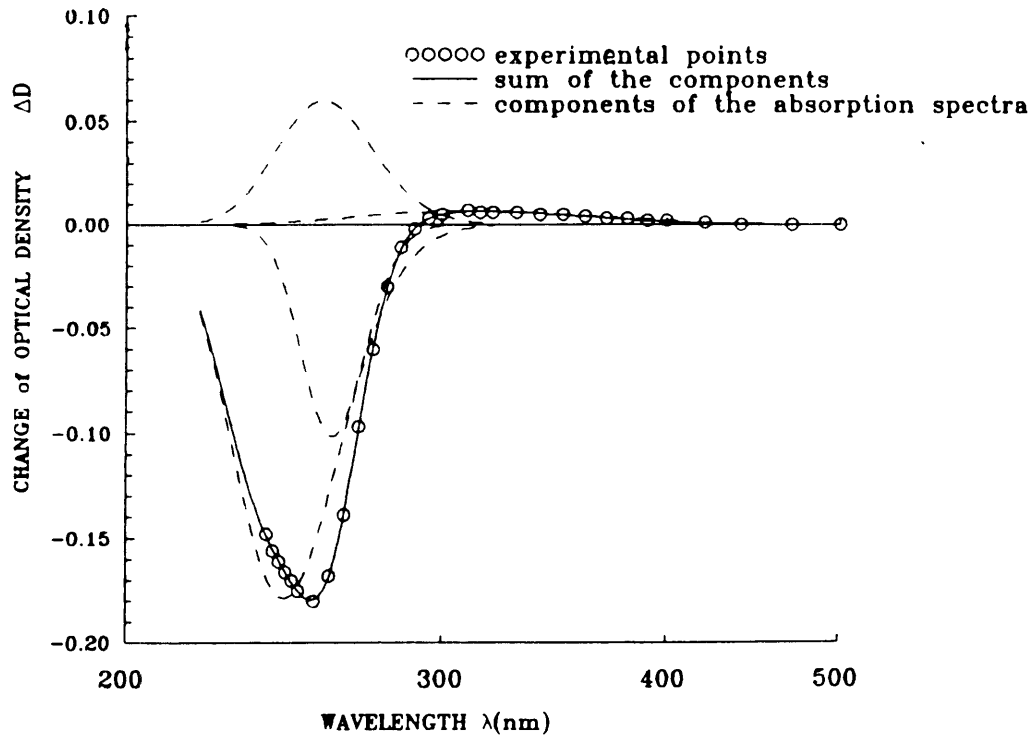
Figure 3.6   Changes of the optical density of a nominally pure YAG after reduction.[52]

effects, is expected to yield more consistent properties, properties which are directly attributable to the system, rather than to background effects. Thus doped YAG results are often more meaningful than those of "pure YAG."

3.2.2: Nd:YAG

When Nd is added to YAG, new absorption bands appear from the UV to the near infra-red (NIR), as shown in Figure 3.7.[19] These bands are due to internal transitions of the three 4f electrons of Nd^{+3}. The f orbitals tend to lie close to the nucleus, and are consequently shielded from interactions with the lattice, such as crystal field effects or vibronic coupling. Thus the f-states tend to be more atom-like with narrow peaks, and transitions between these states are very characteristic of the doping rare-earth ion, irrespective of the particular host.[19,56]

The primary lasing transition is from the $^4F_{3/2}$ level to the $^4I_{11/2}$ level as shown in Figure 3.8.[19] Since the 4f internal transitions are parity-forbidden, the spontaneous radiative lifetime is $\approx$230 μsec at 300° K, compared with typical lifetimes of 10^{-8} sec.[19] This long radiative lifetime greatly facilitates the attainment of a population inversion with a resulting low lasing threshold, as low as 1 mW. Many investigators noted though that radiation induced defects from the pumping source detracted from laser efficiency.[54,57-59] Mori did a systematic study of these defects, and identified oxygen vacancies as the primary defect.[54] He concluded that control of the defect structure of Nd:YAG is important for improving its laser characteristic. As mentioned in Chapter 1, Nd:YAG is best known as a high power solid state laser system, and continuous wave power output of several hundred Watts has been achieved.[19]
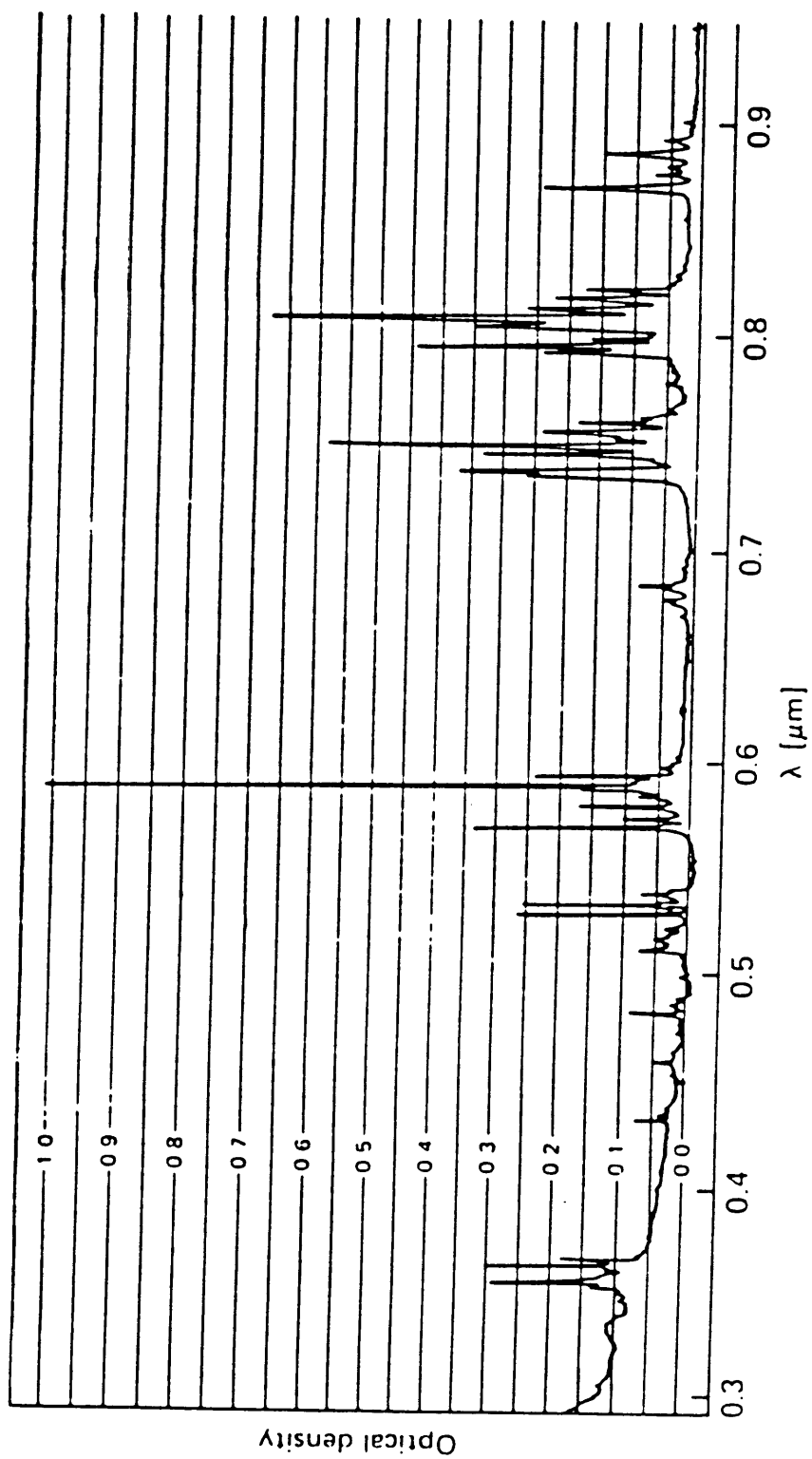
Figure 3.7 Absorption spectrum of Nd:YAG at 300°K. [19]
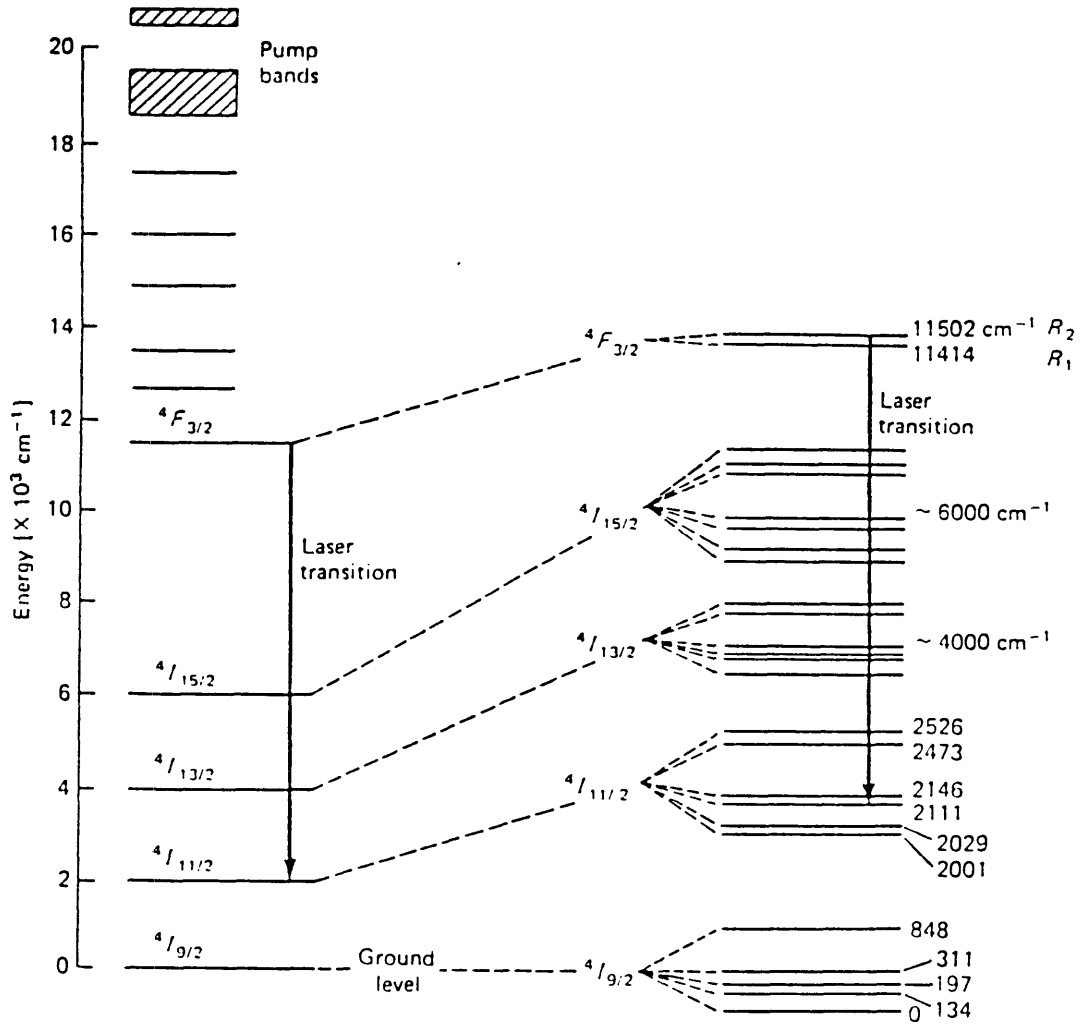
Figure 3.8   Energy level diagram of Nd:YAG.[19]

These are the primary optical properties of interest for our purpose. The interested reader is referred to additional references which review the voluminous research done on the optical properties of Nd:YAG.[19,56]

3.2.3: Ti:Doped Systems:

As discussed in Section 2.1.2, Ti^{+3} has only one d-electron, and consequently its crystal field states are the easiest to calculate. Ti^{+3} tends to enter the octahedral site in a number of hosts, from Ti:sapphire to $Ti:MgAl_2O_4$. Under the action of an octahedral crystal field, its 5-fold degenerate d-orbitals are split into a 3-fold degenerate T_{2g} ground state, and a 2-fold degenerate E_g excited state, as shown in Figure 2.1 & 3.9.[3,11] Thus only one peak should be observed in absorption and emission, and the wavelength of that transition will depend on the magnitude of the crystal field strength, Δ or 10Dq. For oxides, Δ is usually on the order of a few eV, so transitions between crystal field states of Ti^{+3} tend to be in the visible range.[11] The Jahn-Teller effect however, typically splits these crystal field states, ≈ 200 cm^{-1} for the T_{2g} ground state and $\approx 3,000$ cm^{-1} for the E_g excited state in Al_2O_3, as seen in the configuration coordinate diagram in Figure 3.10.[60] The T_{2g} splitting is typically too small to be resolved by room temperature measurements, so two absorption bands (E_{ab}^+ & E_{ab}^- in Figure 3.10) which are often overlapped, are typically seen in Ti:doped systems, as seen in Figure 3.11 & 3.12 for Ti:glass[41] and Ti:YAlO$_3$[61] respectively. Another important point to note is that the minimum energy of the T_{2g} and E_g paraboloids occur at different values of the configuration coordinate, or interatomic distance. This arises because the E_g orbitals have antibonding character while the T_{2g} orbitals have non-bonding character.[11] Consequently the equilibrium interatomic distance for the E_g orbitals are naturally larger than the T_{2g} orbitals. This displacement of the paraboloid minimum for the ground

Figure 3.9   Orgel diagram showing the splitting of a field-free ion D term by a cubic field of magnitude Dq.[11]
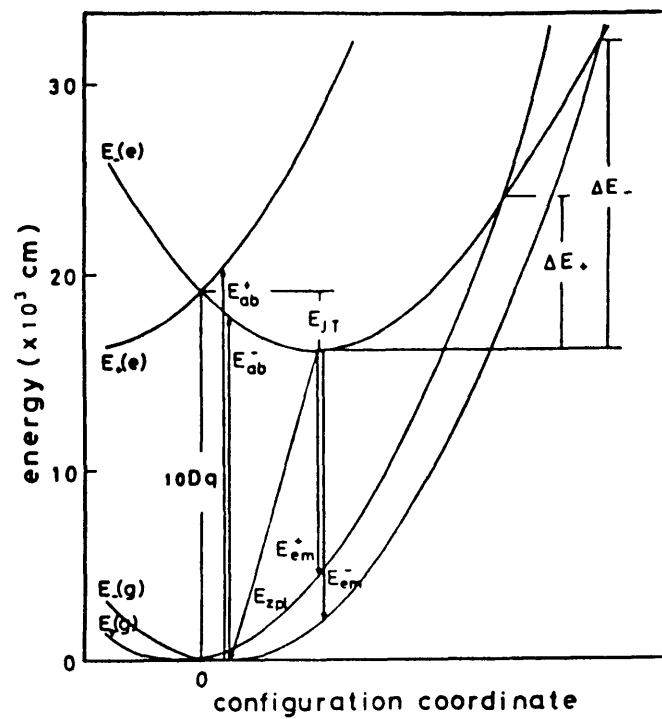
Figure 3.10   Schematic diagram of configuration coordinates of Ti^{+3}.[60]
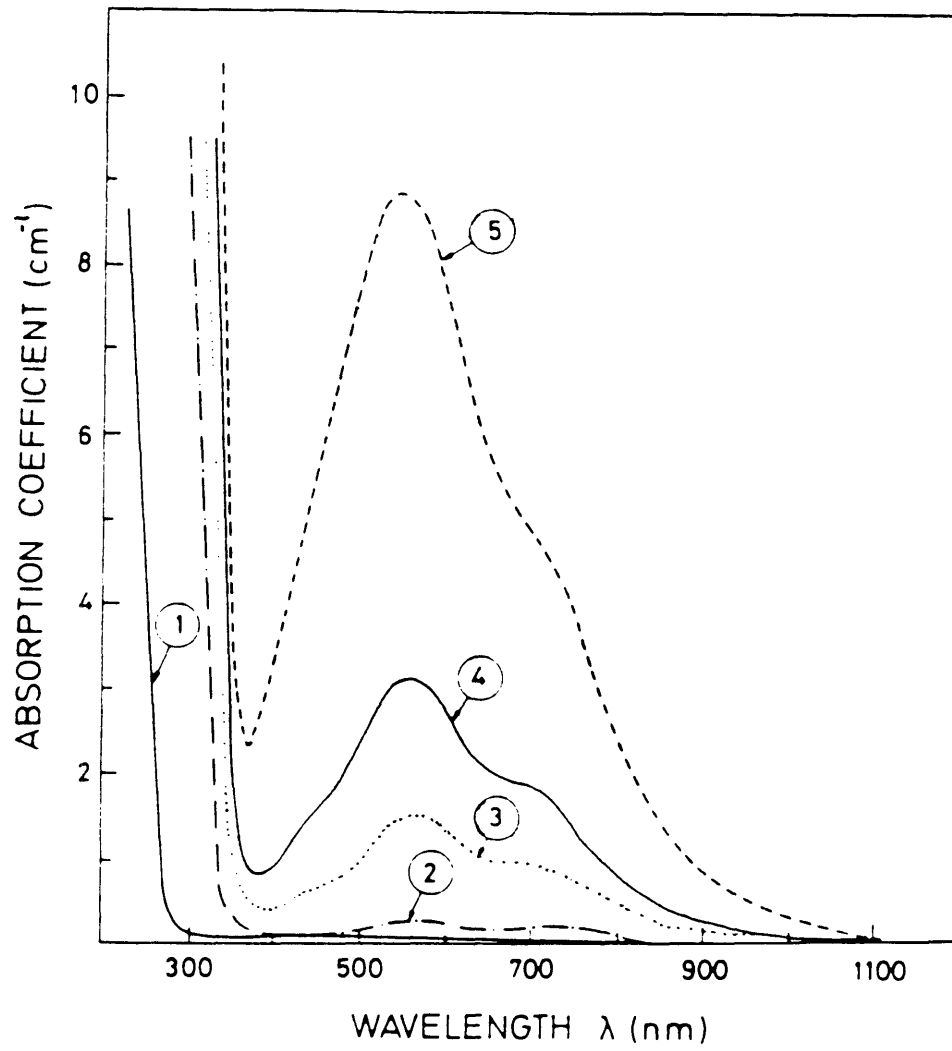
Figure 3.11 Absorption spectra of phosphate glass doped with different TiO$_2$ contents.[41]
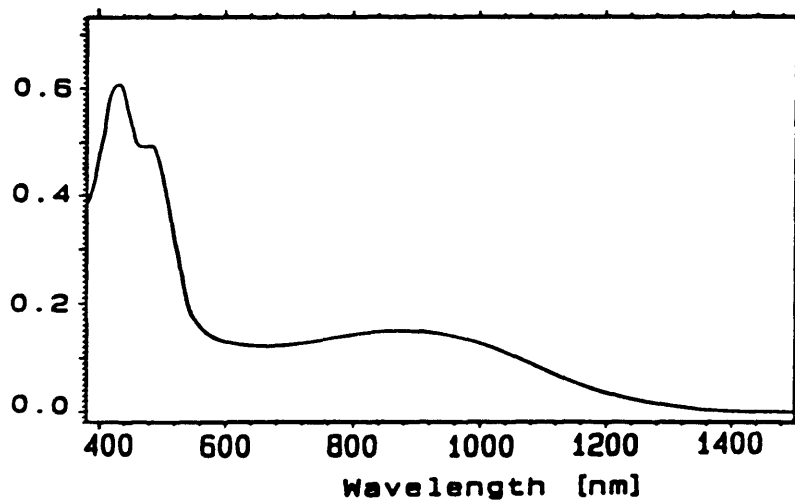
Figure 3.12   Ground-state absorption spectrum of Ti:YAlO$_3$ at 300°K.[61]

state and excited state means that optical transitions between these states occur over a range of vibrational frequencies, resulting in transitions over a range of energies. Consequently both absorption and emission peaks are vibronically-coupled, and quite broad as seen in Figures 3.12 & 3.13 for $Ti:YAlO_3$.[61]

3.2.3.1: Ti:sapphire:

As mentioned in the introduction, Ti:sapphire has received much attention lately because of its utility as a tunable IR laser. The Ti:sapphire laser crystals are usually grown by the Czochralski method in an inert atmosphere like N_2. They typically contain $\approx$0.1 w/o Ti, with those in excess of 0.1 w/o Ti producing crystals of poor optical quality.[62]

The addition of Ti to sapphire results in a number of spectroscopic features as seen in Figure 3.14.[63] The apparent bandedge shifts to between 200-300 nm, a much higher wavelength than that of undoped sapphire at 140 nm.[63] Furthermore, Ti:sapphire now contains optical transitions in the visible region; a double band between 500-550 nm which has been universally assigned to crystal field transitions of the Ti^{+3} ion substituting for aluminum in the octahedral site.[18,63] Typical values of the molar extinction coefficient, $\varepsilon_{max}\approx$140 and the oscillator strength, $f\approx1.9x10^{-4}$ are consistent with this assignment, since the octahedral site in sapphire does not possess a center of inversion.[18,64] Finally, there is a very broad band in the NIR centered at $\approx$800 nm. These features give as-grown Ti:sapphire a pink color.

The UV absorption edge shifts from 200 nm to 300 nm for oxidizing anneals, and thus Albers assigned this absorption to charge transfer from the oxygen 2p band to Ti^{+4}. The remaining absorption between 200 nm and the intrinsic band edge at 140 nm was assigned to charge transfer from the oxygen 2p band to Ti^{+3}.[63,65] Tippins found similar bands in the UV spectra of his
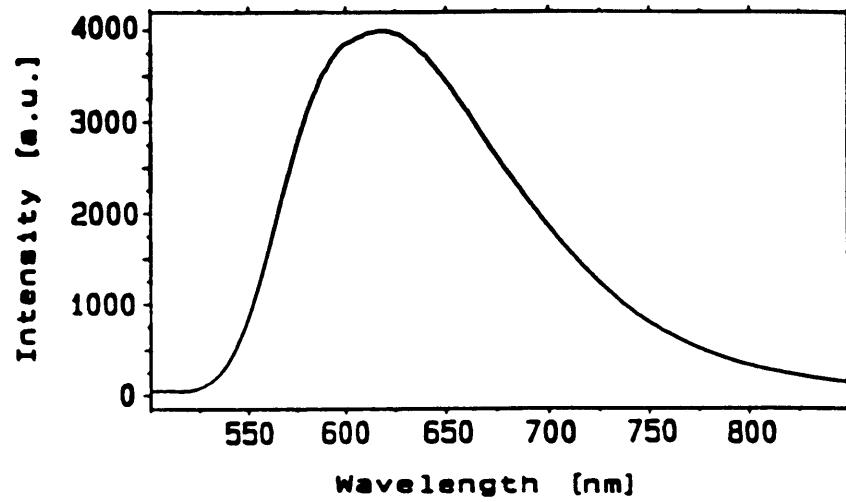
Figure 3.13   300°K fluorescence spectrum of Ti^{+3}:YAlO$_3$ at 488 nm Ar laser excitation.[61]
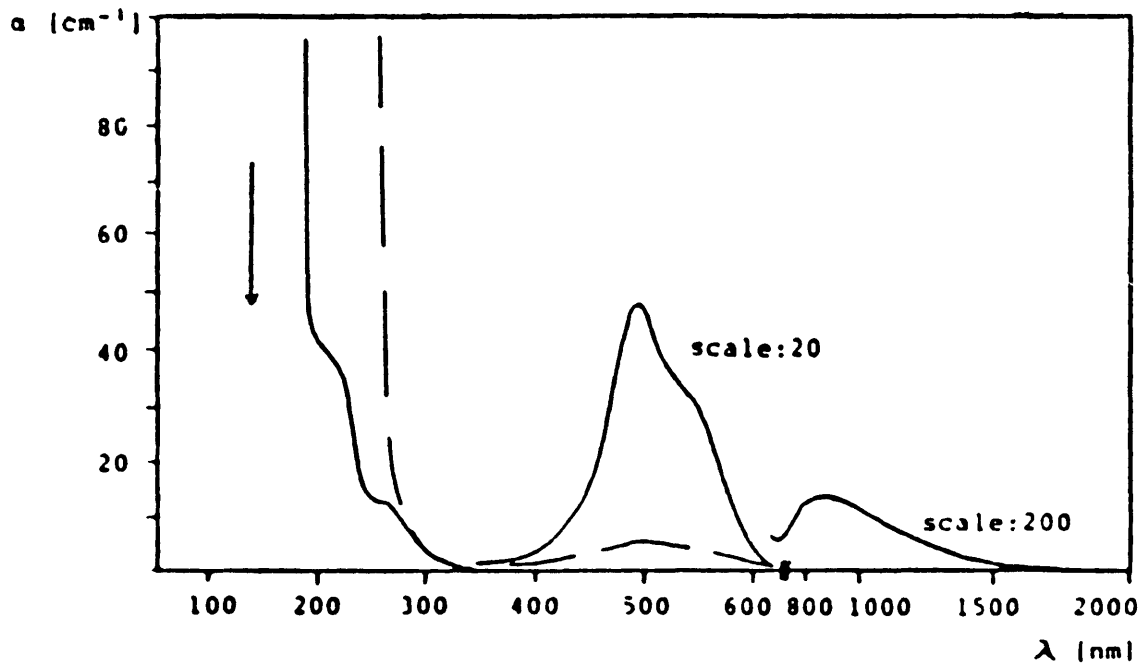
Figure 3.14   Absorption of $Ti^{+3}:Al_2O_3$ at 300°K.[63]

89

as-grown crystal as seen in Figure 3.15, but assigned the band at 4.7 eV

(260 nm) to charge transfer from oxygen to Fe^{+3} impurities, and the band above

6 eV (below 190 nm) as due to charge transfer from oxygen to Ti^{+3}.[23] The

change in the UV absorption with oxidizing and reducing anneals, correlated with

the change in intensity of the Ti^{+3} peaks at $\approx$500 nm as seen in Figure 3.14,

offer compelling evidence that UV absorption between 200-300 nm is directly

associated with the concentration of Ti^{+4}. Since Ti^{+4} has no valence electrons,

intraband transitions within the Ti^{+4} ion are unlikely. Consequently, charge

transfer from the oxygen 2p band to the Ti^{+4} ion is the most probable

mechanism for the 200-300 nm absorption. Furthermore, a two-photon

photoconductivity experiment as seen in Figure 3.16 estimated the position of

the E_g and T_{2g} levels below the conduction band at 2.4 eV$<\Delta E_{Eg}<$ 3.7eV and

4.4 eV$<\Delta E_{T2g}<$5.7 eV respectively.[66] If we assume that the oxygen charge

transfer occurs to a generalized Ti^{+3} level between the E_g and T_{2g} levels as

depicted in Figure 2.1, then this Ti^{+3} level would be between 3.9 and 5.2 eV

below the conduction band. Sapphire's bandgap is $\approx$10 eV[100], which places this

Ti^{+3} level around 5-6 eV above the oxygen 2p valence band, in agreement with

the 200-300 nm absorption assignment for oxygen 2p to Ti^{+4} charge transfer.

An energy diagram for the Ti^{+3} ion in sapphire based on these results is shown

in Figure 3.17. It is interesting to note that a similar behavior and assignment

was observed in Ti:glass, with a peak at $\approx$250 nm as seen in Figure 3.18.[41] This

suggests that the Ti^{+3} level is typically around 5 eV above the oxygen 2p

valence band.

The source of the 800 nm NIR band in Ti:sapphire is still not understood.

Lacovara attributes this absorption to Ti^{+3} on low symmetry sites caused by

adjacent point defects.[62] Powell attributes the absorption to charge transfer

between Fe^{+3} and Ti^{+3}.[67] Moulton suggests that Ti^{+3} to Ti^{+4} charge transfer

WAVELENGTH, Å

0.003 MOLE % Ti^{3+} IN Al$_2$O$_3$
Bi$_2$O$_3$ - PbF$_2$ FLUX-GROWN
t = 0.13 mm

OPTICAL DENSITY

PHOTON ENERGY, eV
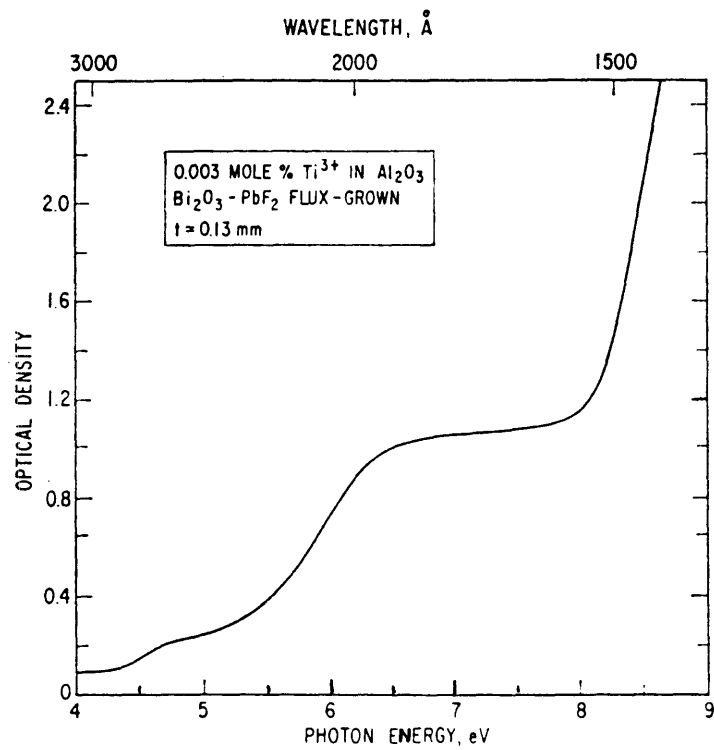
Figure 3.15   Absorption spectrum of Ti^{+3} in Al$_2$O$_3$.[23]

91
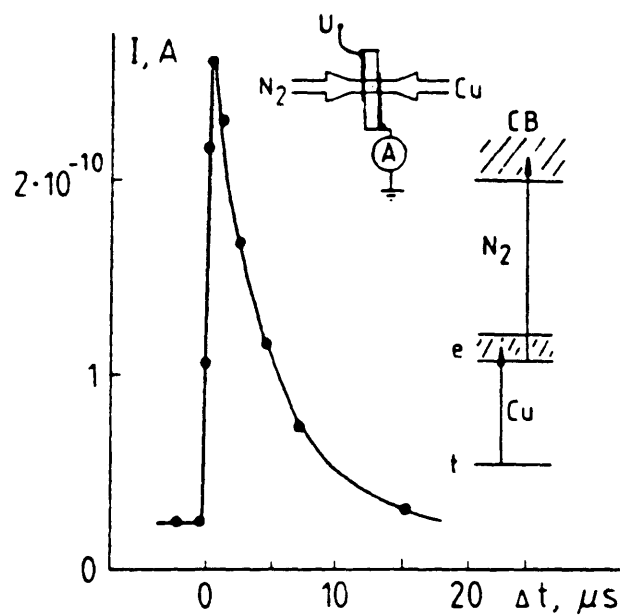
Figure 3.16   The dependence of time-averaged photocurrent in $Al_2O_3:Ti^{+3}$
under excitation with synchronized Cu and N_2 laser pulses on the
delay Δt of N_2 laser pulse relative to Cu laser pulse.[66]

92

Conduction Band (Y4d)

ΔE_e

E_g

$1.5\ eV$

$2.5\ eV$

Ti^{+3}

T_{2g}

$\Delta E_{C.T.}$

$2.4\ eV < \Delta E_e < 3.7\ eV$

Assuming Band Gap is 10 eV

$\Longrightarrow\ 4.8\ eV < \Delta E_{C.T.} < 6.1\ eV$

Valence Band (O2p)
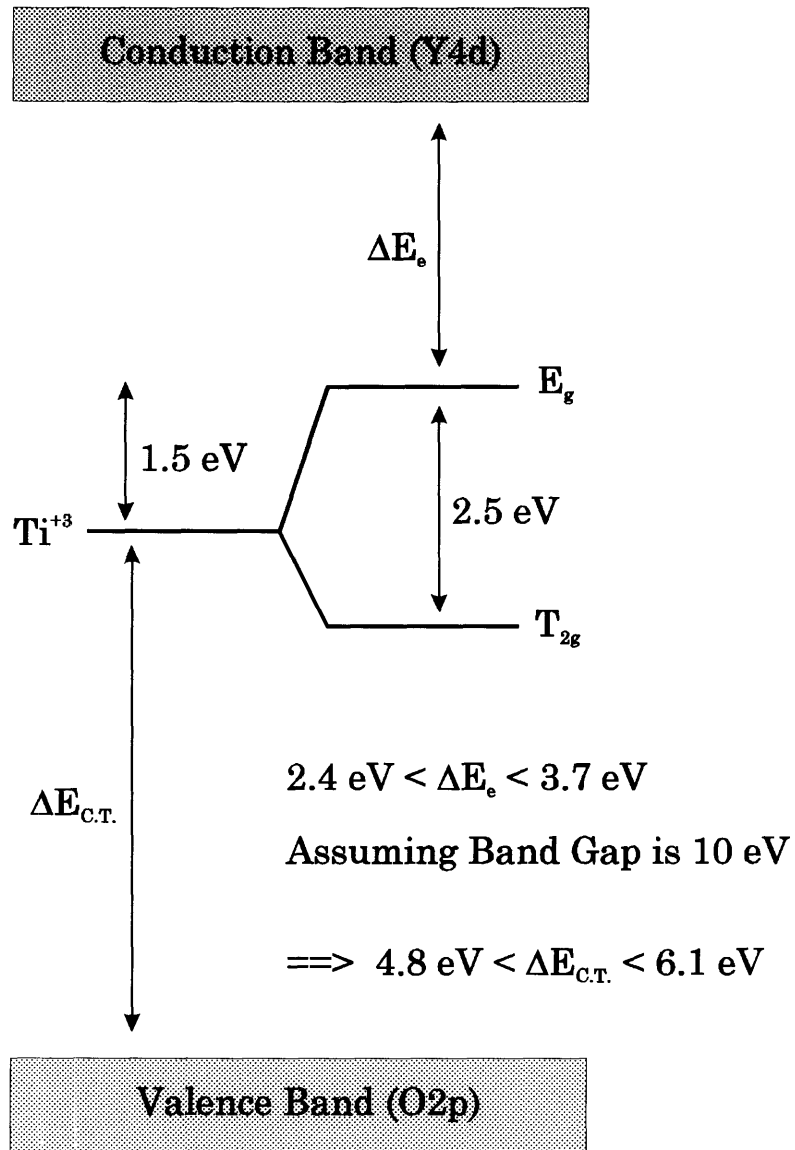
Figure 3.17 Energy band diagram for Ti:sapphire as suggested by the literature survey.[3,18,62-67]
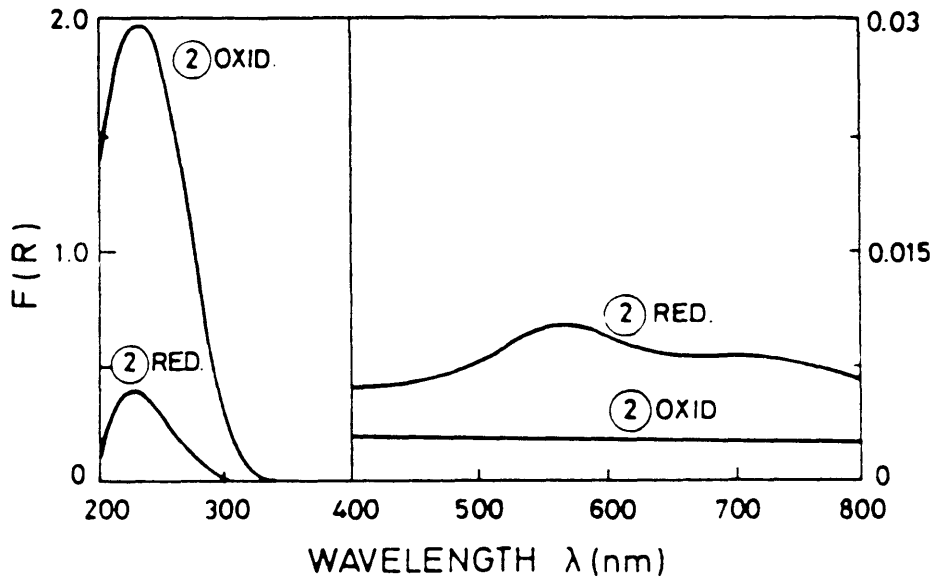
Figure 3.18 Spectra of phosphate glass melted in reducing and oxidizing conditions.[41]

might be another possibility.[18] Active research is still on-going to determine the cause of this absorption and if possible, eliminate it, as it directly reduces the laser efficiency as shown below.

When the absorption bands of the Ti^{+3} ion are pumped, fluorescence is observed at ≈ 750 nm as seen in Figure 3.19.[18] This fluorescence is ascribed to the Stokes-shifted $E_g \text{-->} T_{2g}$ optical relaxation, E_{em} in the configuration diagram of Figure 3.10.[60] It is this fluorescence which leads to lasing in Ti:sapphire lasers, with a tuning range of 660-968 nm. This is also the absorption range of the NIR absorption at 800 nm mention above. Consequently this absorption directly detracts from the laser performance. When the UV band at 200-300 nm is pumped, two fluorescence peaks are observed, as shown in Figure 3.20, the 750 nm peak of Ti^{+3} as before, and a new peak at ≈ 450 nm, a blue emission.[67,68] The origin of this blue emission is unknown, but it is interesting to note that such an emission has also been observed in $Ti:MgAl_2O_4$ and Ti-activated stannates and zirconates when pumped at 200-300 nm. This luminescence has been attributed to a Ti^{+4} octahedral complex.[42,69] (See Figures 3.21 & 3.22) Such an assignment for Ti:sapphire would be consistent with the oxygen 2p to Ti^{+4} charge transfer assignment for the 200-300 nm absorption as discussed earlier. Thus it appears reasonable that the blue emission from sapphire is indeed due to a octahedrally coordinated Ti^{+4}.

3.2.3.2: Ti:YAG:

Ti:YAG crystals have been successfully grown by the Czochralski[6] and Bridgman-Stockbarger[70] methods. Growth is usually carried out in an inert or reducing atmosphere to reduce the Ti ion to a +3 valence and facilitate its incorporation into the YAG lattice. Consequently most of the Ti should be in the octahedral sites as discussed in section 2.4. Growth in air or an oxidizing
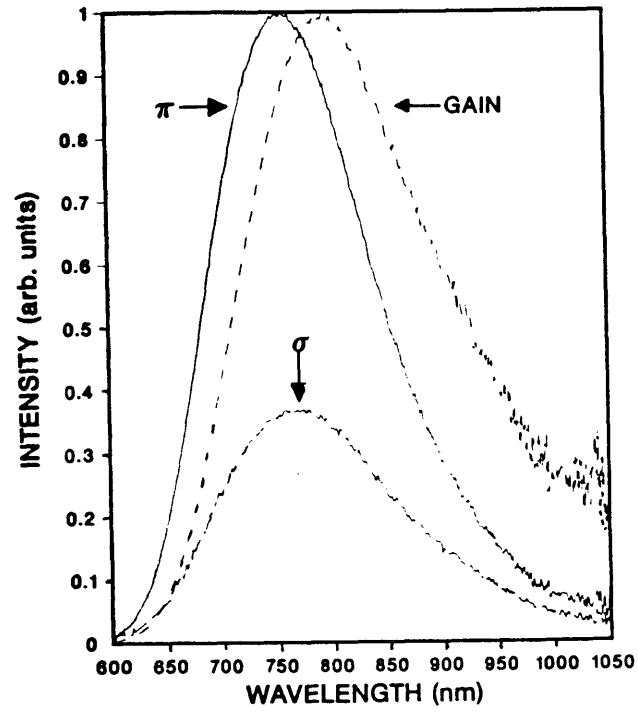
Figure 3.19   Polarized fluorescence spectra and calculated gain line shape for
Ti:Al$_2$O$_3$.[18]
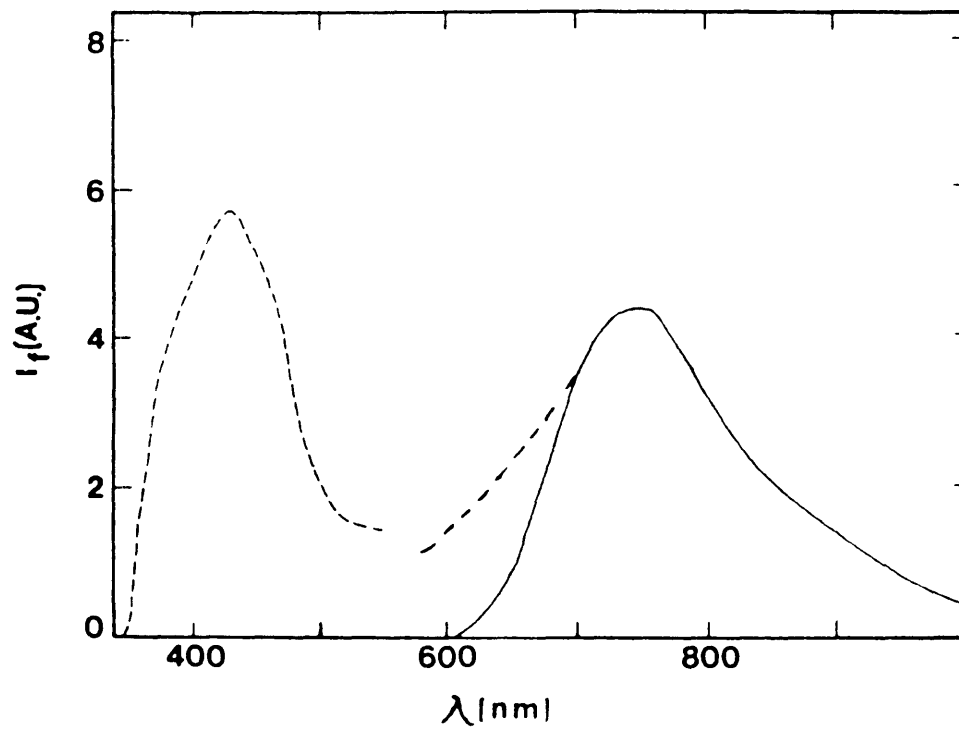
Figure 3.20 Room temperature fluorescence spectra of Al_2O_3:Ti^{+3}. Solid line shows results after excitation at 590 nm. Broken line shows results obtained after excitation at 532 nm.[67]
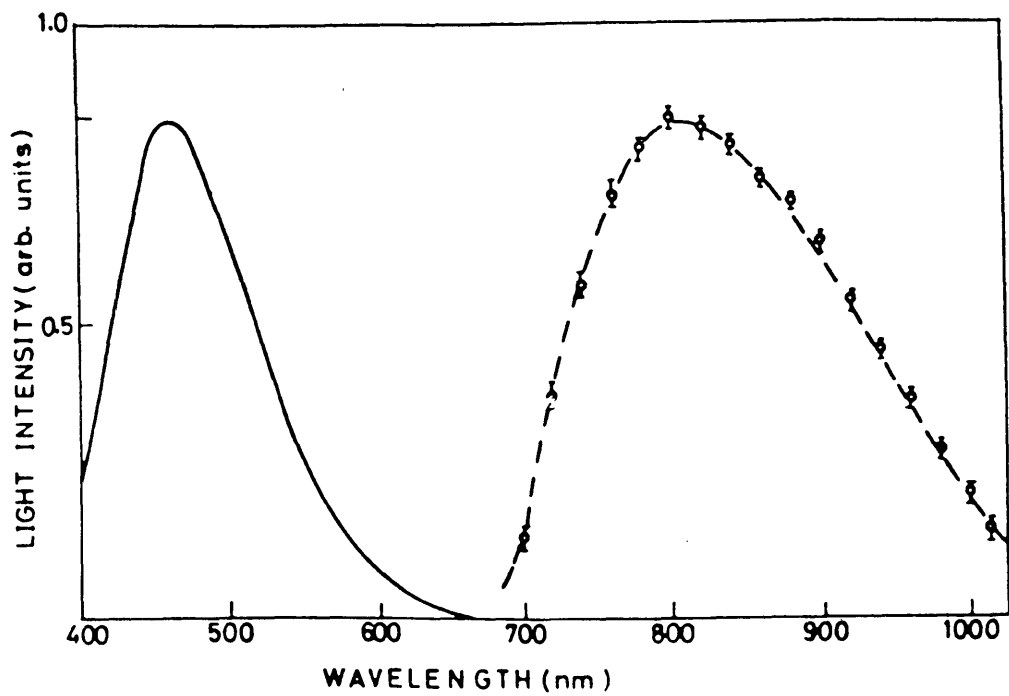
Figure 3.21 MgAl$_2$O$_4$ liquid nitrogen temperature emission spectra obtained
under excitation at 266 nm.[83]
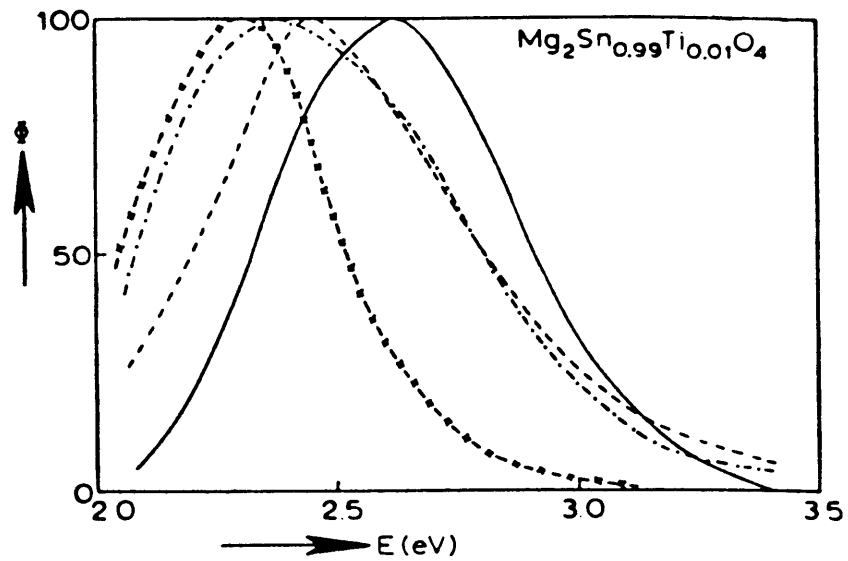
Figure 3.22   Spectral energy distribution of emissions at 5°K in
$Mg_2Sn_{0.99}Ti_{0.01}O_4$. Full line, excited at 4.96 eV. Dashed line,
excited at 4.13 eV. Dash-dotted line, excited at 4.13 eV after firing
in N_2. Dashed-crossed line, 5% excess of SnO_2 excited at 4.13
eV.[69]

atmosphere results in inclusions of yttrium pyrotitanate, $Y_2Ti_2O_7$.[6] As grown Ti:YAG crystals have a brown color whose intensity increases with increasing Ti concentration in the melt and decreasing PO_2 in the growth atmosphere.[6]

The brown color comes from the spectroscopic features that Ti adds to YAG as seen in Figure 3.23 for an as-grown crystal.[40] The apparent band edge is now at 300 nm compared to a band edge of $\approx$200 nm for undoped YAG. Furthermore, Ti:YAG now has three bands in the visible region, at $\approx$400, 500, & 600 nm. The 500 and 600 nm peaks are universally assigned to crystal field transitions of the Ti^{+3} ion substituting for aluminum in the octahedral site.[40,60,66,71] Annealing in an oxidizing environment removes these peaks, presumably changing the Ti from a +3 to a +4 valence. Analogously, a reducing anneal restores these peaks.[6]

The source of the 400 nm peak in uncertain. Karpov noted that the ratio of the optical densities of the 400, 500, & 600 nm peaks remain constant for different growth conditions, suggesting that all three peaks are due to the same center.[72] Most of the other investigators have simply noted its existence without commenting on its source. It is interesting to note that Bausa observed a peak at 450 nm in Ti:glass, and attributed it to charge transfer between Ti^{+3} and Ti^{+4}, as evidenced by a quadratic dependence of the oscillator strength on the Ti concentration, as seen in Figure 3.24.[41]

Similarly, the UV absorption at 300 nm has not been fully investigated, and no explanations published as to its source. The similarity between Ti:YAG and Ti:sapphire though suggests that the absorption may be due to charge transfer from the oxygen 2p band to Ti^{+4}, as in the case for Ti:sapphire. Basun did a two-step photoionization experiment of Ti^{+3} ions in Ti:YAG, similar to the experiment for Ti:sapphire described earlier in Figure 3.16, and concluded that the distance between the conduction band and the E_g state of Ti^{+3}, $\Delta E_e < 2$ eV,
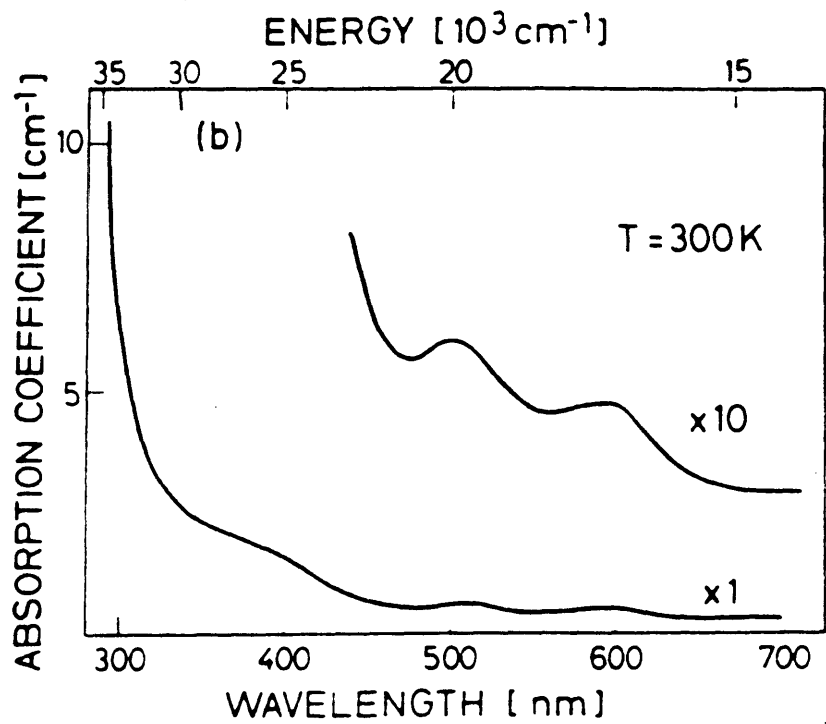
Figure 3.23 Absorption spectra of Ti^{+3}:YAG at room temperature.[40]
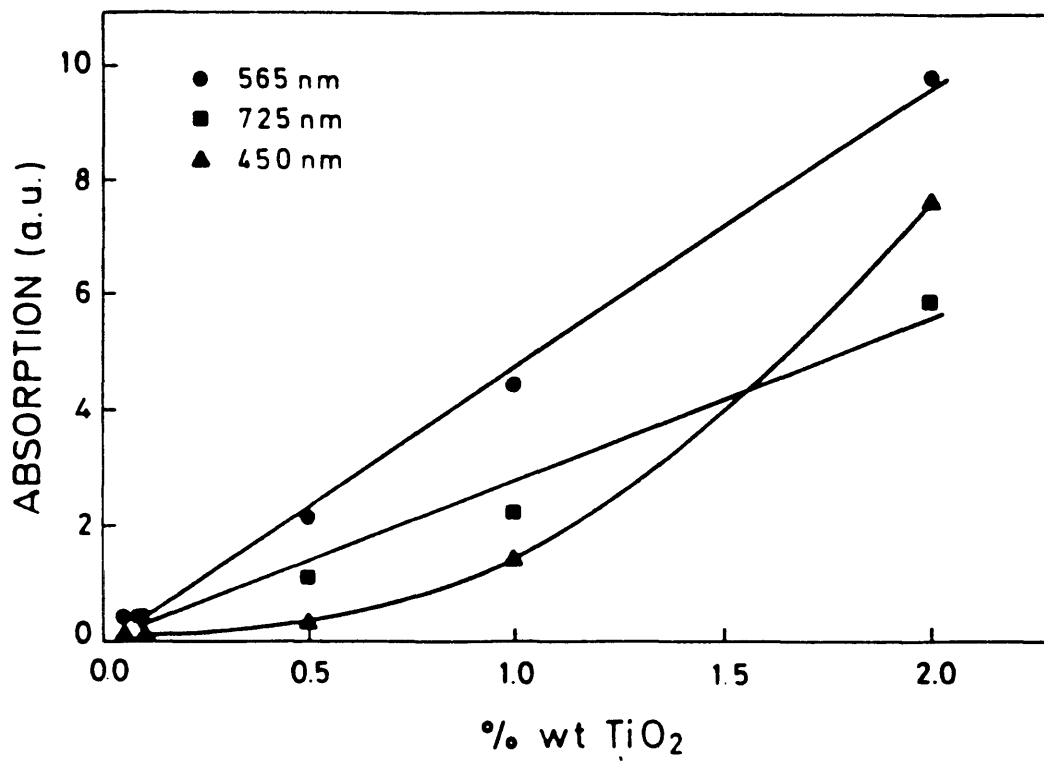
Figure 3.24   Areas of absorption bands versus TiO_2 content in phosphate glass.[41]

i.e. the pumping source used to excite electrons from the T_{2g} state to the E_g state of Ti^{+3}, also excited electrons from the E_g state to the conduction band, with a resulting photoelectric current.[66] If the 500 and 600 nm peaks are indeed due to $T_{2g}-->E_g$ transitions of the Ti^{+3} ion, this implies that the E_g state should lie below the conduction band, i.e. $\Delta E_e > 0$. These two limits define the range for the generalized Ti^{+3} level in YAG, as illustrated in Figure 3.25. These two limits also define the range for the energy of the $O2p-->Ti^{+4}$ charge transfer transition, $\Delta E_{C.T.}$, 3.24 eV$<\Delta E_{C.T.}<$5.24 eV for a optical bandgap of 6.6 eV for YAG.[32] Thus the UV absorption beginning at 300 nm $<==>$ 4.13 eV is within the range of $\Delta E_{C.T.}$, and the $O2p-->Ti^{+4}$ charge transfer may be responsible for the 200-300 nm absorption in Ti:YAG.

When the 500 and 600 nm bands in Ti:YAG are pumped, a fluorescence peak similar to Ti:sapphire at 800 nm is observed, as seen in Figure 3.26.[40] This peak is attributed to the Stokes-shifted $E_g-->T_{2g}$ optical relaxation of Ti^{+3}, as in the case of Ti:sapphire. When the UV band is pumped, a fluorescence peak at 550 nm is observed as seen in Figure 3.27.[73] No assignment was made for this fluorescence peak, but a measurement of the angular dependence of the degree of polarization of this fluorescence suggest that the fluorescence originates from the *edges* of the octahedral and tetrahedral sites, and not their *centers*, i.e. the oxygen part of the YAG lattice.[73]

The 550 nm fluorescence peak in Ti:YAG is analogous to the blue emission of Ti:sapphire,[67,68] $Ti:MgAl_2O_4$,[42] and Ti-activated stannates and zirconates.[69] All fluoresce when pumped in the UV, and in the case of the Ti-activated stannates and zirconates and $Ti:MgAl_2O_4$, this fluorescence is attributed to a Ti^{+4} octahedron complex.[42,69] Such an assignment also seems reasonable in the case of Ti:sapphire, as discussed earlier. If the 200-300 nm absorption in Ti:YAG is also due to charge transfer from the O2p band to the

Conduction Band (Y4d)

ΔE_e

E_g

1.4 eV

2.3 eV

Ti^{+3}

T_{2g}

$\Delta E_{C.T.}$

$0\ eV < \Delta E_e < 2\ eV$

Assuming Band Gap is 6 eV

$\Longrightarrow\ 2.6\ eV < \Delta E_{C.T.} < 4.6\ eV$

Valence Band (O2p)
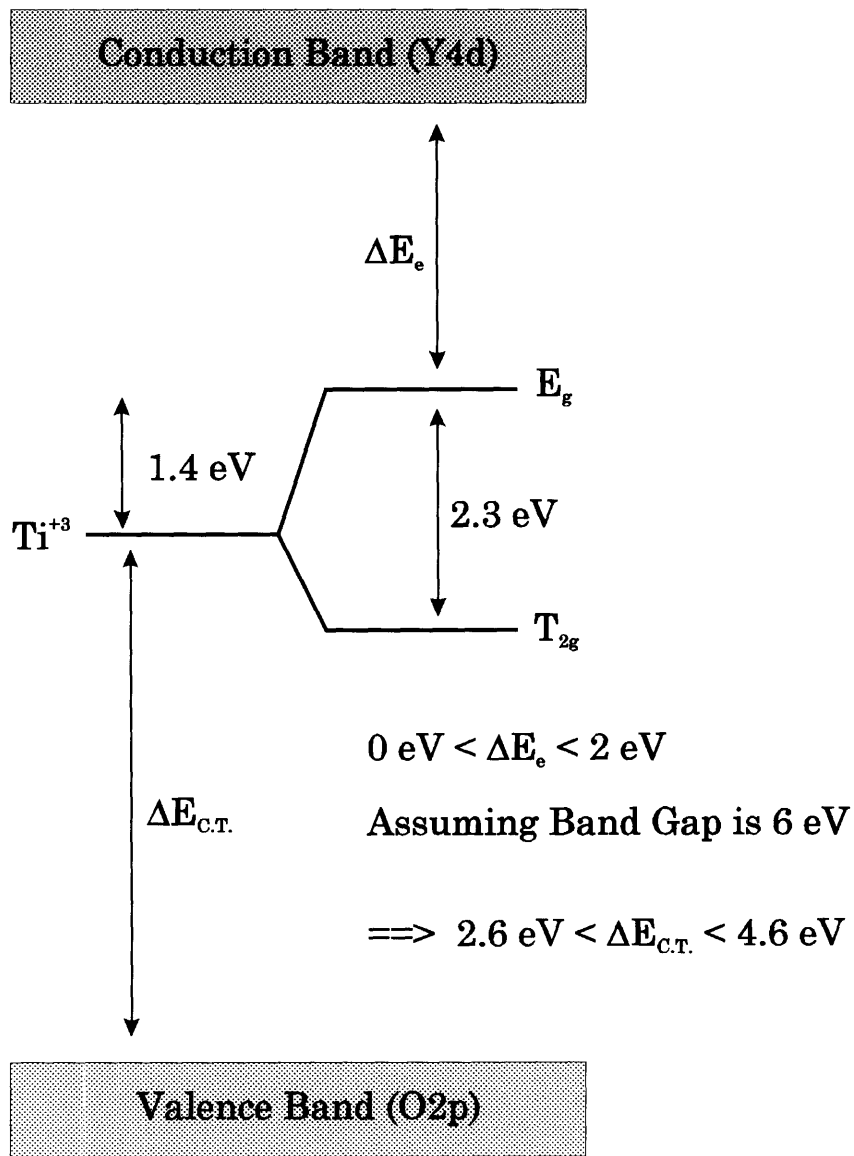
Figure 3.25 Energy band diagram for Ti:YAG as suggested by the literature survey.[3,40,60,66,71]
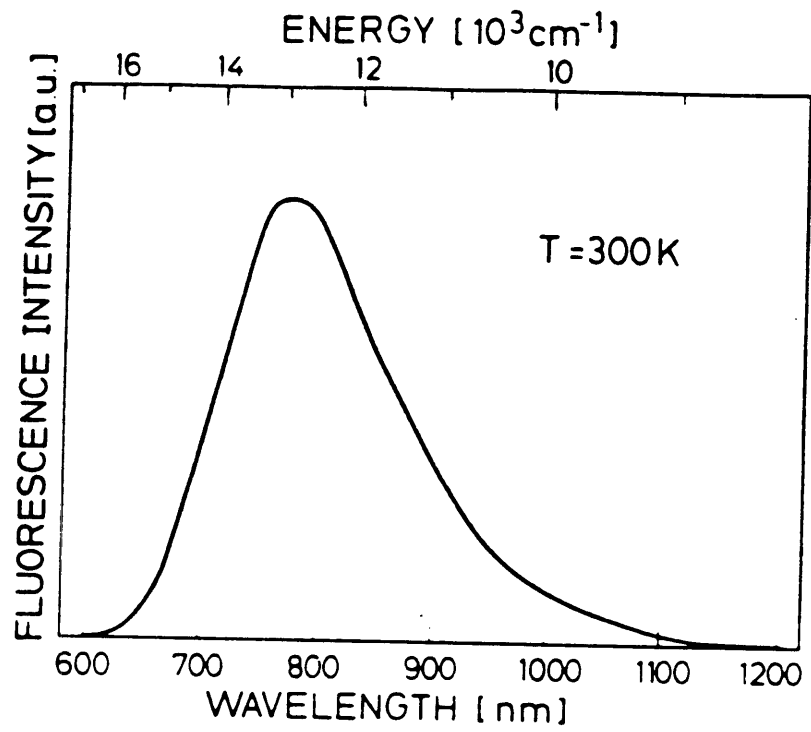
Figure 3.26   Fluorescence spectra of Ti^{+3}:YAG at room temperature.[40]
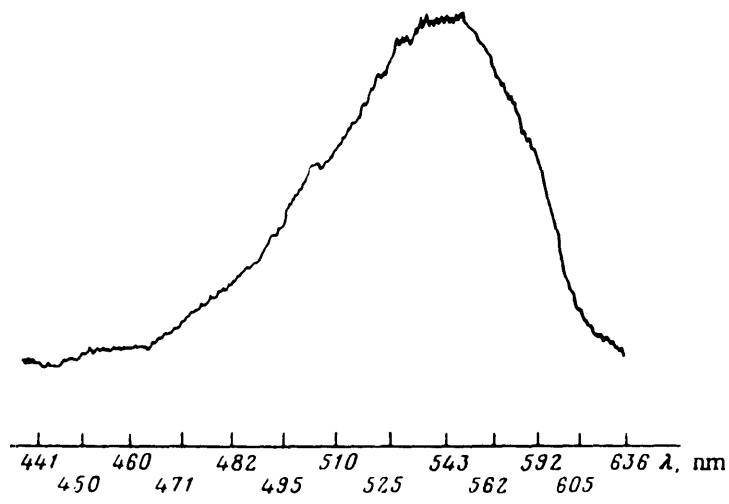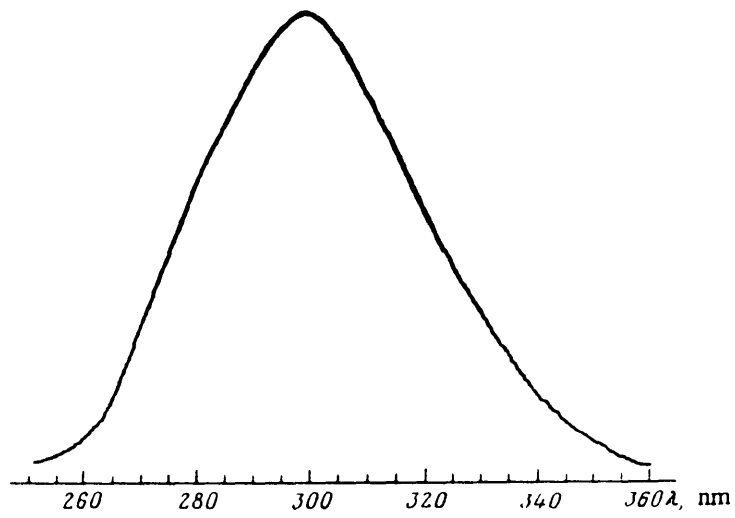
Figure 3.27   (a) Luminescence and (b) excitation spectrum of YAG-Ti crystals.[73]

Ti^{+4} ion, as in the case of Ti:sapphire, Ti:MgAl$_2$O$_4$, and the Ti-activated stannates and zirconates, then it seems reasonable to also assign the 550 nm fluorescence peak in Ti:YAG to a Ti^{+4} octahedron complex. However, in contrast to Ti:sapphire, there is currently no substantive evidence to assign the 200-300 nm absorption in Ti:YAG to charge transfer from the O2p band to Ti^{+4}. A table summarizing the absorption and emission bands in Ti:YAG and Ti:Sapphire is shown in Table 3.1 & 3.2, along with their assignments by previous investigators.

It seems appropriate to conclude this section with a quick comparison of Ti:YAG and Ti:sapphire, especially with regard to their suitability as laser systems. Ti:sapphire is already a proven IR laser system as described earlier. Unfortunately, its low Ti concentration and a small E_g lifetime of 3μsec at 300°K makes the lasing threshold rather high.[62,63] Despite this fact, both pulse and continuous-wave lasing operation have been established.[62,74] High optical quality crystals of Ti:YAG can be grown with a higher Ti concentration than Ti:sapphire.[6,40,71] Furthermore, the symmetry of its distorted octahedral site is C_{3i} versus C_3 for sapphire.[40] The preservation of the inversion symmetry for the octahedral site in YAG means that the parity selection rule is in force, and that the lifetime of the E_g state should be larger in YAG than in sapphire. Indeed, the radiative lifetime of Ti:YAG is 50 μsec vs. 3.9 μsec for Ti:sapphire at 4.2°K, more than an order of magnitude larger.[40,63] Unfortunately by 300°K, this lifetime has dropped to 2 μsec vs. 3 μsec for Ti:sapphire, primarily because of the onset of non-radiative decay mechanisms.[40,60,63] YAG's smaller bandgap also makes excited state absorption a major problem for Ti:YAG, as suggested by Figure 3.25.[66] Despite this limitation, pulsed laser action has been achieved in Ti:YAG.[75]

Absorption & Emission Bands
in Ti:Sapphire

Aborption Bands:

Wavelength:	Literature Assignments:	Intensity: Molar Extinction Coeff.
200-300 nm	$O2p \rightarrow Ti^{+4}$, Ti^{+3} [62,63,65] $O2p \rightarrow Fe^{+3}$ [23]	>140 liters/cm-mole 8000 "
500 & 550 nm	$T_{2g} \rightarrow E_g$ of Ti^{+3} (oct. sites) [18,63,64,67]	140 "
800 nm	Ti^{+3} low symmetry sites [62] Ti^{+3}-Ti^{+4} charge transfer [18,64] $Fe^{+3}+Ti^{+3} \rightarrow Fe^{+2}+Ti^{+4}$ [67]	

Emission Bands:

Wavelength:	Literature Assignments:	Excitation Peaks:
750 nm	$E_g \rightarrow T_{2g}$ of Ti^{+3} (oct. sites) [18,64,60,67]	200-300 nm 500 & 550 nm
450 nm	??	200-300 nm

Table 3.1 Literature survey of absorption and emission bands in Ti:sapphire.
        [18,23,60,62-65,67]

Absorption & Emission Bands
in Ti:YAG

Aborption Bands:

Wavelength:	Literature Assignments:	Intensity: Molar Extinction Coeff.
200-300 nm	??	
400 nm	??	
500 & 600 nm	$T_{2g} \rightarrow E_g$ of Ti^{+3} (oct. sites) [40,60,66,71]	

Emission Bands:

Wavelength:	Literature Assignments:	Excitation Peaks:
800 nm	$E_g \rightarrow T_{2g}$ of Ti^{+3} (oct. sites) [40,60,71]	500 & 600 nm
550	??	200-300 nm

Table 3.2 Literature survey of absorption and emission bands in Ti:YAG.
[40,60,66,71]

3.2.4: Zr:YAG

The optical properties of Zr:YAG deal exclusively with Zr in the +3 valence, as the +4 valence has no valence electrons for optical transitions. Crystals of Zr doped YAG was found to have properties that depended strongly on the growth atmosphere. Crystals grown under a reducing environment had a red color, whose intensity increased with increasing Zr concentration, and decreasing PO_2. The spectra of such a crystal is shown in Figure 3.28.[5] Crystals grown under an oxidizing environment had no red color. Neither did crystals do-doped with compensating ions like Ca^{+2} or Mg^{+2}. Electron spin resonance of colored Zr:YAG suggested the presence of unpaired electrons on the 8-fold dodecahedral site, which was assigned to Zr^{+3} ions substituting for Y.[5] As we discussed in section 2.4, this assignment is reasonable from ion size considerations. The intensity of the optical absorption peaks and the electron spin resonance for Zr^{+3} were found to be well correlated, and the optical absorption spectrum of Figure 3.28 was interpreted in terms of crystal field splitting of the Zr^{+3} ion in a dodecahedral site, as seen in Figure 3.29, with a resulting 10Dq = 2.02 eV.[5] This is in agreement with typical values of crystal field splitting for the octahedral site in YAG, which have 10Dq = 2.03 eV.[76]

The primary difficulty with the above interpretation is the absence of information regarding previous observation of Zr^{+3} in literature. For almost all the oxides in which Zr was a major or minor component, Zr was found in the +4 valence. Only in irradiated $Zr:YPO_4$ and $Zr:Y_2O_3$ at 77°K were Zr found in a +3 valence, as evidenced by electron spin resonance.[77,78] Thus it seems possible that when a large number of electrons are excited into the conduction band by irradiation, some of these electrons can be trapped by a Zr^{+4} ion, changing its valence to Zr^{+3}, and the Zr^{+3} ions are kinetically stable at 77°K. This also suggests that the Zr^{+3} level is below the conduction band of Y_2O_3 and YPO_4.
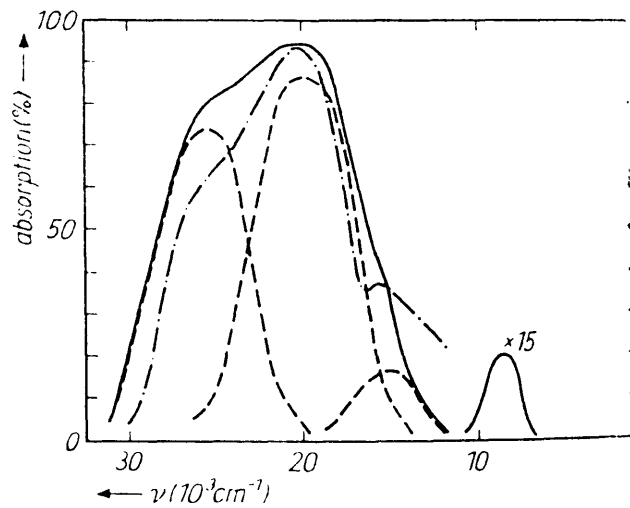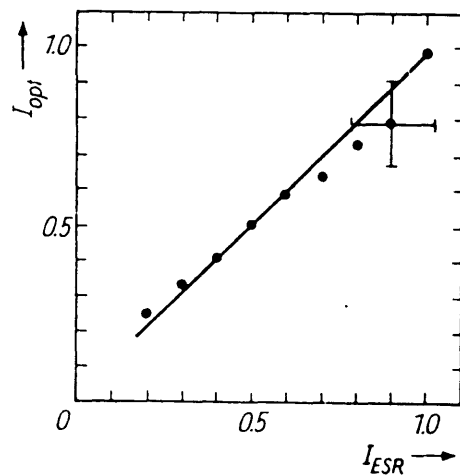
Figure 3.28   (a) Optical absorption spectra of YAG:Zr single crystals, and
(b) correlation of esr and optical absorption intensities.[5]
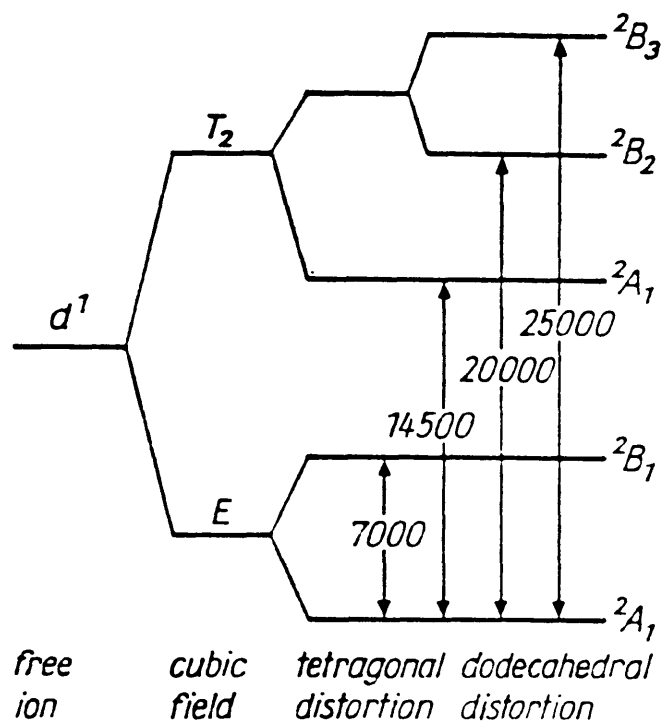
Figure 3.29   Splitting scheme of energy levels of the Zr^{+3} ion in YAG (in cm^{-1}).[5]

Monoclinic ZrO_2 has a bandgap of ≈ 5 eV,[79] while yttria stabilized zirconia has a bandgap of ≈ 4.6 eV.[80] Since the conduction band in both these systems is presumably the Zr 4d band, and the valence band the oxygen 2p band, these bandgaps suggest that the Zr^{+3} level is ≈ 5 eV above the oxygen 2p band in oxides. Since Y_2O_3 has a bandgap of ≈ 5.6 eV,[81] it seems probable that the Zr^{+3} level lies below the Y_2O_3 conduction band, and that Zr^{+4} ions trap electrons irradiated into the conduction band. Similarly, the Zr^{+3} level would also be expected to lie below the conduction band in YAG, which has a optical bandgap of ≈ 6.6 eV.[32] This suggests that under heavily reduced conditions, when electrons start populating the conduction band in significant numbers, Zr^{+4} ions in YAG may start trapping some of these electrons, as in the case of irradiated $Zr:YPO_4$ and $Zr:Y_2O_3$, and that Zr^{+3} ions may indeed be a stable species in Zr:YAG.

3.3: Transport Properties

The transport properties of YAG have been studied by a number of investigators, typically by electrical measurements or by diffusion experiments. Mori did the first transport studies of YAG in 1977 by studying the motion of color fronts in heavily reduced single crystal YAG. He applied an anion diffusion model to the color front motion, and arrived at the following equation:[54]

$$D = 10^{16} \exp\left(\frac{-4.7eV}{kT}\right) \qquad \left[cm^2 / sec\right]$$

Neiman did the first electrical measurements of YAG in 1978 by studying its ionic transference number and electrical conductivity. He found YAG to be a mixed ionic-electronic conductor with an activation energy of ≈ 4 eV, as seen in Figure 3.30.[82] He also concluded that in YAG,

$$D_O >> D_{Al} >> D_Y.$$

113
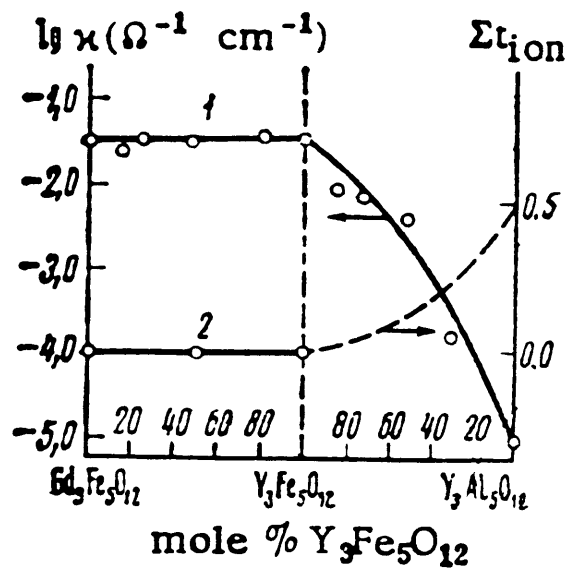
Figure 3.30 Dependence of the electroconductivity (1) and the sum of the ionic transference numbers (2) on the composition of $Me_3E_5O_{12}$ at 1200 °C.[82]

Bates and Garnier did electrical measurements of YAG up to 1000°C, and found

two regions of transport as seen in Figure 3.31, separated by an anomalous

region between 627°C and 727°C.[83] The two regions were independent of PO_2

and had activation energies of 3.4 eV and 2.32 eV for the high and low

temperature regions, respectively. Haneda did systematic studies of oxygen

diffusion in YAG by studying [18]O diffusion, and arrived at the following

expression:[84]

$$D = 5.24 \times 10^{-7} \exp\left(\frac{-3.37 \text{eV}}{kT}\right) \qquad [m^2 / \sec]$$

He also found that for heavily reduced crystals, the oxygen exchange rate was

significantly dependent on the exchange reaction at the specimen surface.

Finally, Rotman and Schuh studied electrical transport in single crystal and

polycrystalline YAG respectively. They also observed that YAG was a mixed

conductor with an n-type electronic activation energy of ≈4 eV and an ionic

activation energy of 2-3 eV as seen in Tables 3.3 & 3.4.[4,25,31,85-88] One should

note that Rotman believes oxygen vacancies to be the ionically conducting

species, whereas Schuh believes that the ionic conductivity is due to aluminum

vacancies. Schuh's interpretation relies heavily on the observation of alumina

inclusions in his ceramic samples fabricated from a stoichiometric starting

composition. Consequently his results may be unique to his samples.[25,88]

3.4: Defect Structure Studies:

To date, only Rotman and Schuh have published defect structure studies

of YAG. Rotman found that most of his samples: Ce:YAG, Ni:YAG, Ni:Zr:YAG,

Ca:YAG, and Fe:YAG had defect structures dominated by inadvertent

background acceptors compensated by oxygen vacancies.[4,31,86] The defect
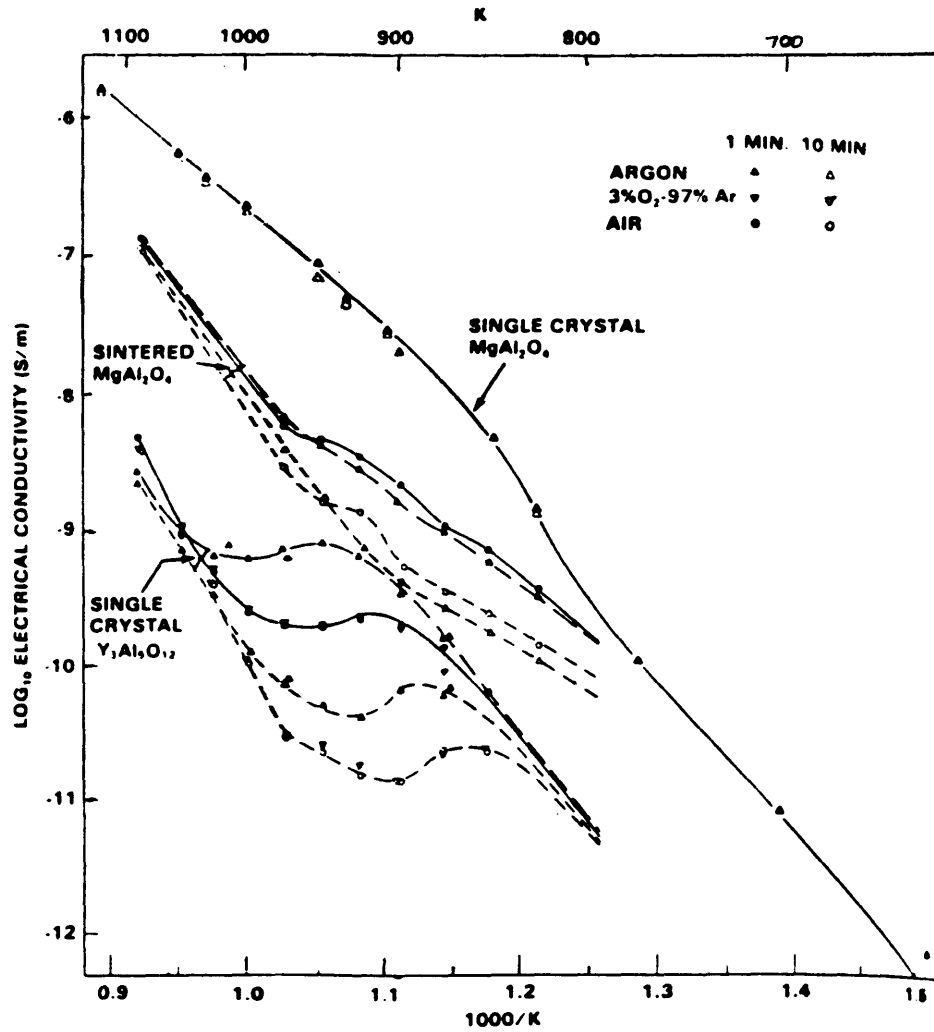
Figure 3.31   Electrical conductivity of YAG showing time and oxygen pressure
anomalies between 900 and 1000°K.[83]

116

Activation Energy for
N-type Conductivity

Investigator:	Crystal:	Activation Energy:
Rotman [4,31]	Ce:YAG (single crystal)	3.9 eV
Rotman [4,86]	Ni:Zr:YAG (single crystal)	3.8 eV
Schuh [25]	YAG (single crystal)	3.7 eV
Schuh [25,87]	Zr:YAG (50 ppm Zr, polycrystalline)	3.4 eV
Schuh [25]	Zr:YAG (500 ppm Zr, polycrystalline)	2.7 eV

Table 3.3   Literature survey of activation energies for n-type conductivity.
[4,25,31,86,87]

Activation Energy for
Ionic Conductivity

Investigator:	Crystal:	Activation Energy:
Rotman [4,31]	Ce:YAG (single crystal)	2.3 eV
Rotman [4]	Ca:YAG (single crystal)	4.0 eV
Rotman [4,86]	Ni:YAG (single crystal)	2.2 eV
Rotman [4,86]	Ni:Zr:YAG (single crystal)	3.0 eV
Rotman [4,85]	Fe:YAG (single crystal)	2.6-2.8 eV
Schuh [25]	YAG (single crystal)	2.1 eV
Schuh [25,88]	Ca:YAG (polycrystalline)	2.7 eV
Schuh [25,87]	Zr:YAG (50 ppm Zr, polycrystalline)	3.0 eV
Schuh [25]	Zr:YAG (500 ppm Zr, polycrystalline)	2.8 eV

Table 3.4 Literature survey of activation energies for ionic conductivity.
[4,25,31,85-88]

model he derived was described in detail in section 2.2. (It is interesting to note that Mori's optical studies of YAG also identified oxygen vacancies as the main crystalline defect detracting from the laser performance of Nd:YAG.[54] See section 3.2.2.) Rotman's conductivity isotherms for Ni:Zr:YAG are shown in Figure 3.32, and their de-convolution in Figure 3.33.[4] The measured Ni and Zr concentrations were very close, and the Ni and Zr were believed to compensate each other. The final defect structure was ultimately controlled by inadvertent background acceptors, following the defect model in Figure 2.6, regime (b).

Schuh in contrast developed a defect model based on aluminum vacancies for his polycrystalline YAG ceramics including Zr:YAG.[25,88] The Zr doping concentration of 50 and 500 ppm Zr represented the first attempt to study donor doped YAG, and his Zr:YAG isotherm is shown in Figure 3.34.[25] Unfortunately the appearance of alumina inclusions in his stoichiometric samples of both acceptor and donor doped ceramics directed a defect model based on aluminum vacancies for all his samples. Consequently his model may not be generally applicable, and we will not consider it further. It is interesting to note though that his one measurement on a single crystal YAG sample had an isotherm very similar to those measured by Rotman as seen in Figure 3.35.[25] He also interpreted the isotherm in terms of Rotman's defect model, a defect structure controlled by inadvertent background acceptors compensated by oxygen vacancies.

Thus we see that to date, a typical YAG conductivity isotherm consists of a PO_2 independent part surrounded by p-type and n-type branches that vary as $PO_2^{\pm 1/4}$ respectively. These isotherms were interpreted in terms of the acceptor dominated defect model in Figure 2.6. Studies of variable-valence Ni:YAG supported this interpretation.[4,85,86] Thus no isotherms have so far been
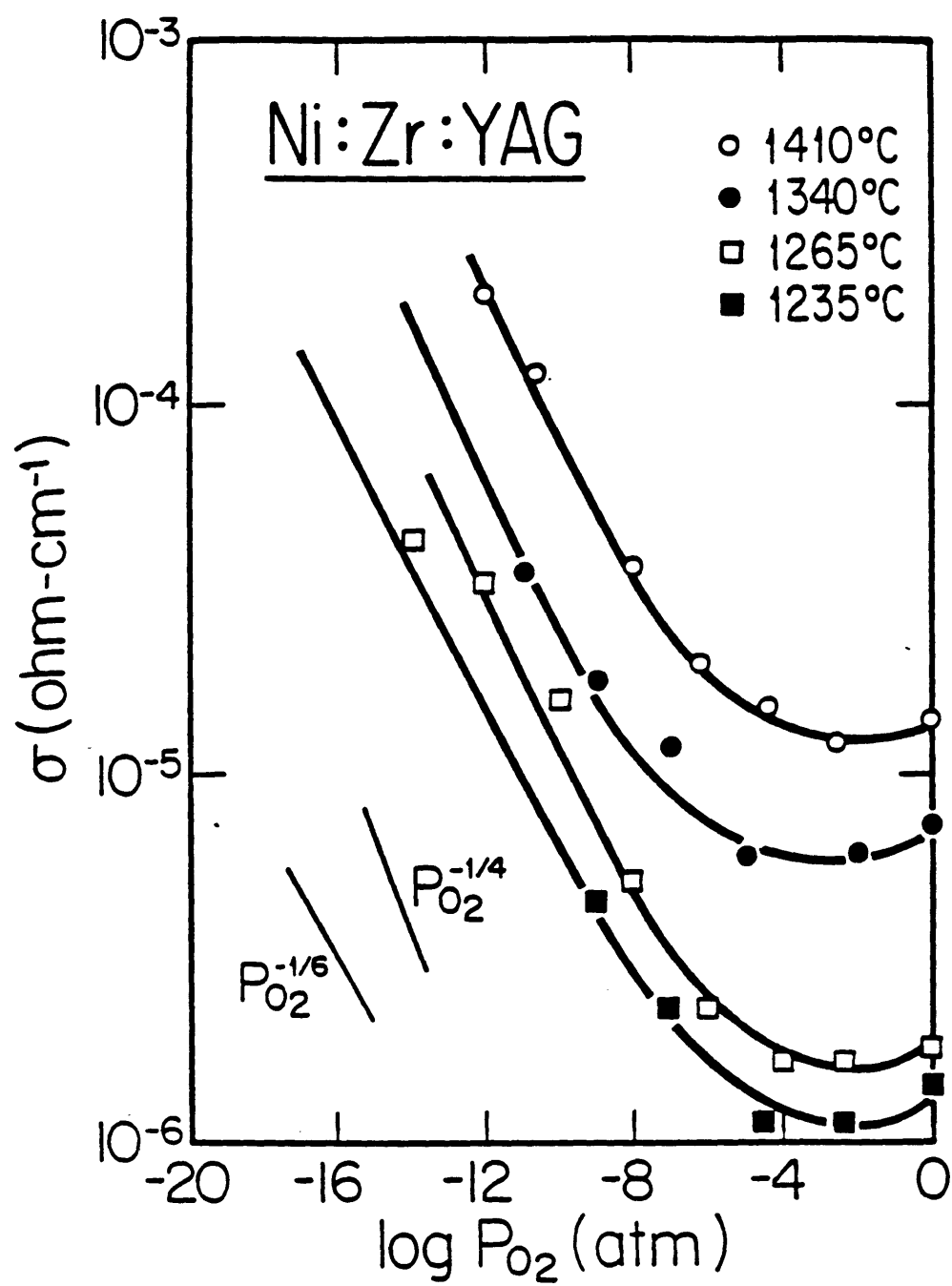
Figure 3.32   Conductivity isotherm for Ni:Zr:YAG.[4,86]
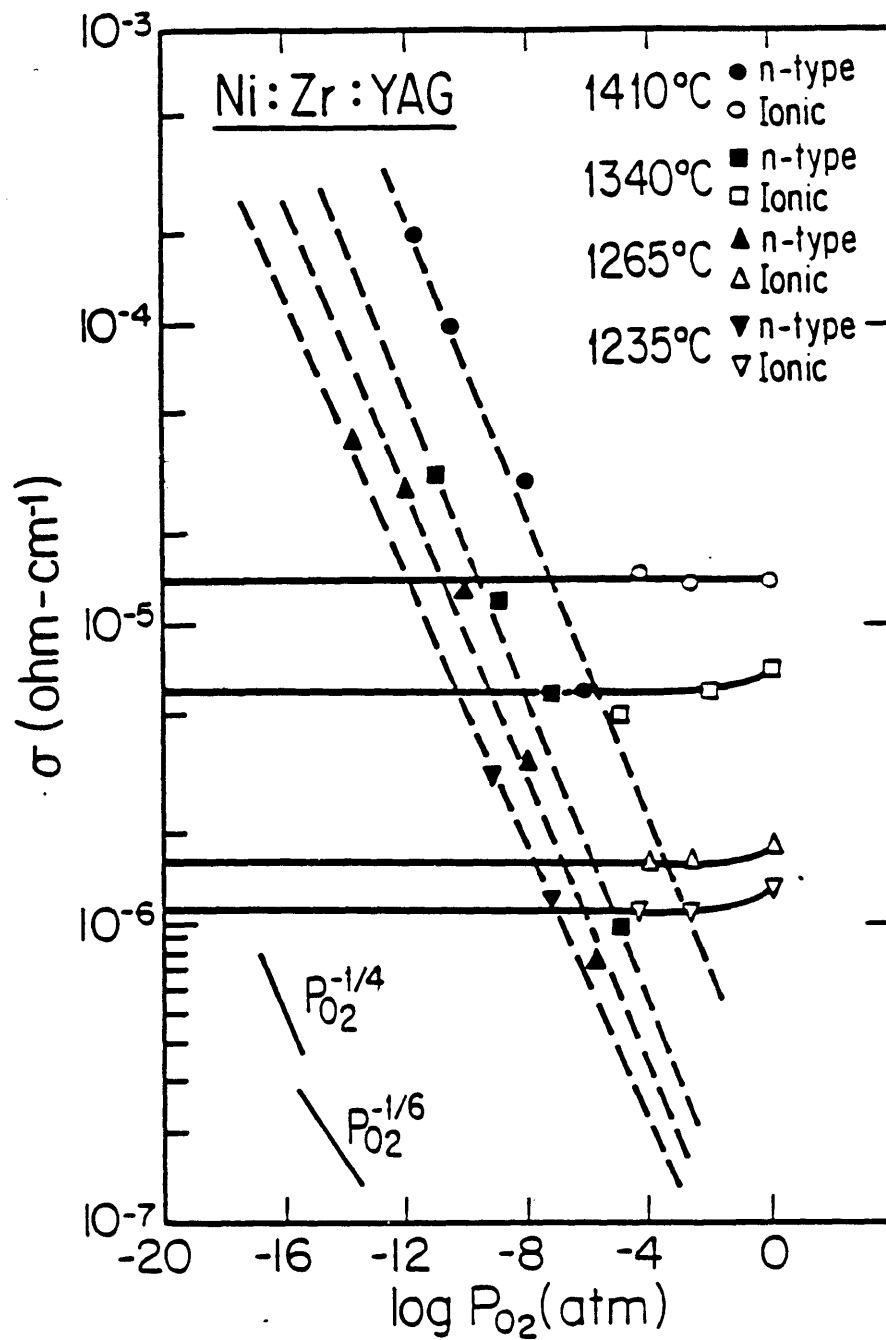
Figure 3.33   Ionic and n-type conductivity components as a function of PO_2 for Ni:Zr:YAG.[4,86]
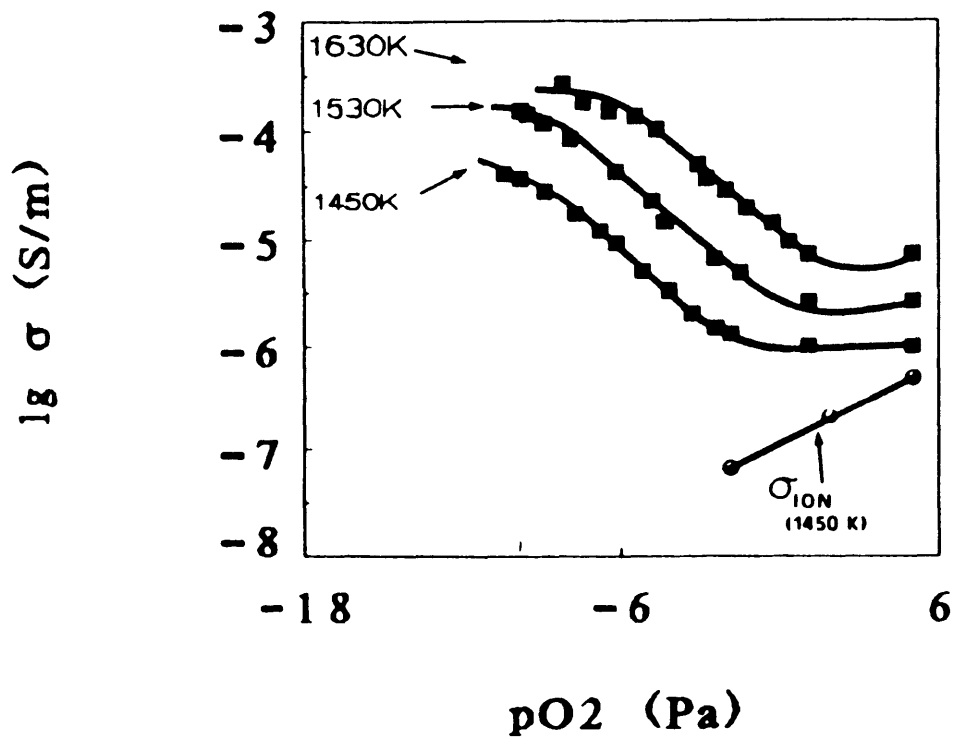
Figure 3.34 Conductivity isotherms of Zr:YAG (50 ppm Zr).[25]
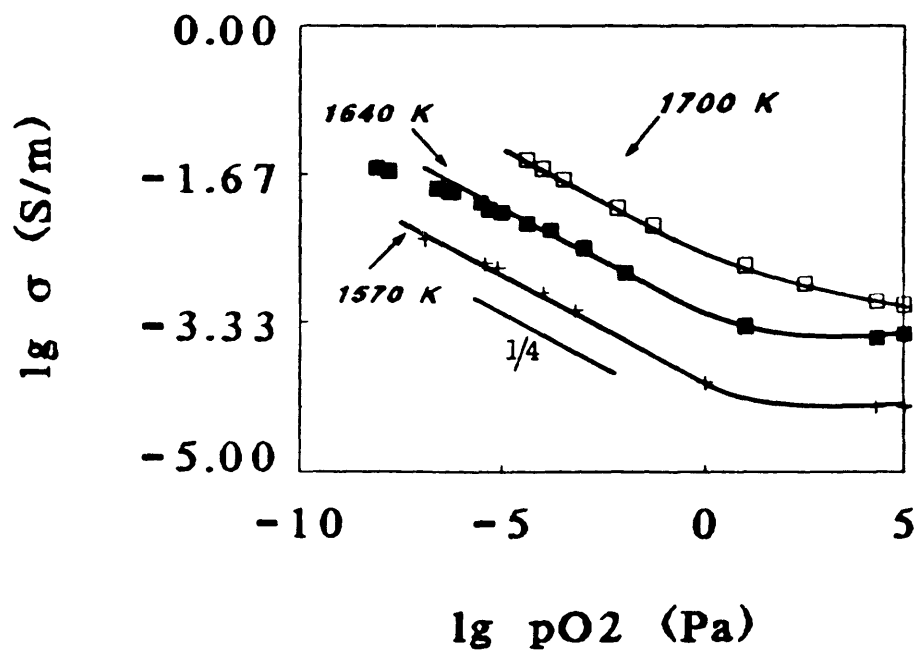
Figure 3.35   Conductivity isotherms of YAG.[25]

123

measured which can be interpreted in terms of an undoped or donor doped

YAG.

CHAPTER 4: EXPERIMENTAL

Chapter 4.1: Introduction:

As described in the introduction, two types of samples were used for our experiments. One type was single crystal YAG fibers grown at MIT using the Laser Heated Floating Zone technique. The other type was YAG boules grown by the Czochralski method. The single crystal fibers provided a much longer path length for optical measurements, since fibers as long as 10 cm long could be grown in a day. Furthermore, since these fibers were grown from ceramic feed, fibers of various dopants and dopant concentrations were readily accessible. Unfortunately their small diameters made coupling of the probe light difficult and irreproducible, so quantitative optical measurements were nearly impossible. These small diameters also posed problems for electrical measurements, since the small cross-sectional area often resulted in high resistances comparable to our alumina sample holders. In contrast, the large single crystal boules grown by the Czochralski method were easy to measure, both optically and electrically. Unfortunately these donated crystals were of a limited composition, and their optical path lengths were generally smaller than the fibers. However by utilizing the strengths of each type of sample, we were able to extract meaningful data for a range of compositions for both Ti:YAG and Zr:YAG. This chapter will cover experimental details of the processing and electrical and optical measurements for these two types of samples. The following chapters will present the results.

4.2: Processing:

4.2.1: Single Crystal Fibers

To make dense ceramic feed rods for growing single crystal fibers, doped and undoped YAG powder was made using a modified Pechini process, as described in Appendix 1. This process has the advantages of excellent control over dopant concentration and near atomic scale mixing of the cations. Furthermore, the only equipment requirements are standard laboratory glassware, hot plates, and a calcining furnace. The major disadvantage of this technique is poor powder characteristics, and low yield, typically ≈ 1 volume percent (v/o) of the starting solutions. YAG, Ti:YAG, and Zr:YAG powders were successfully made with this process. All the powders were single phase. A typical x-ray diffraction pattern is shown in Figure 4.1. An SEM micrograph of representative powders is shown in Figure 4.2. As is clearly evident, the powders have a large size distribution, with the larger particles tending toward a planar shape, and the smaller particles tending to be more spherical. The average particle size is ≈ 0.5 μm. Powder agglomeration is also a major problem. However, spectrochemical analysis of powders with a systematic variation of over three orders of magnitude in doping concentration revealed that doping concentrations were within a factor of two of the starting composition. Since the error associated with spectrochemical analyses is usually a factor of two, the Pechini process provides remarkable control over doping concentrations.

4.2.1.2: Polycrystalline Ceramics

The YAG powders were dried at 110°C overnight to remove residual moisture before pressing. The powders were then pressed at ≈ 4000 psi on a vertical bench press, and then isostatically pressed at 40,000 psi for a few
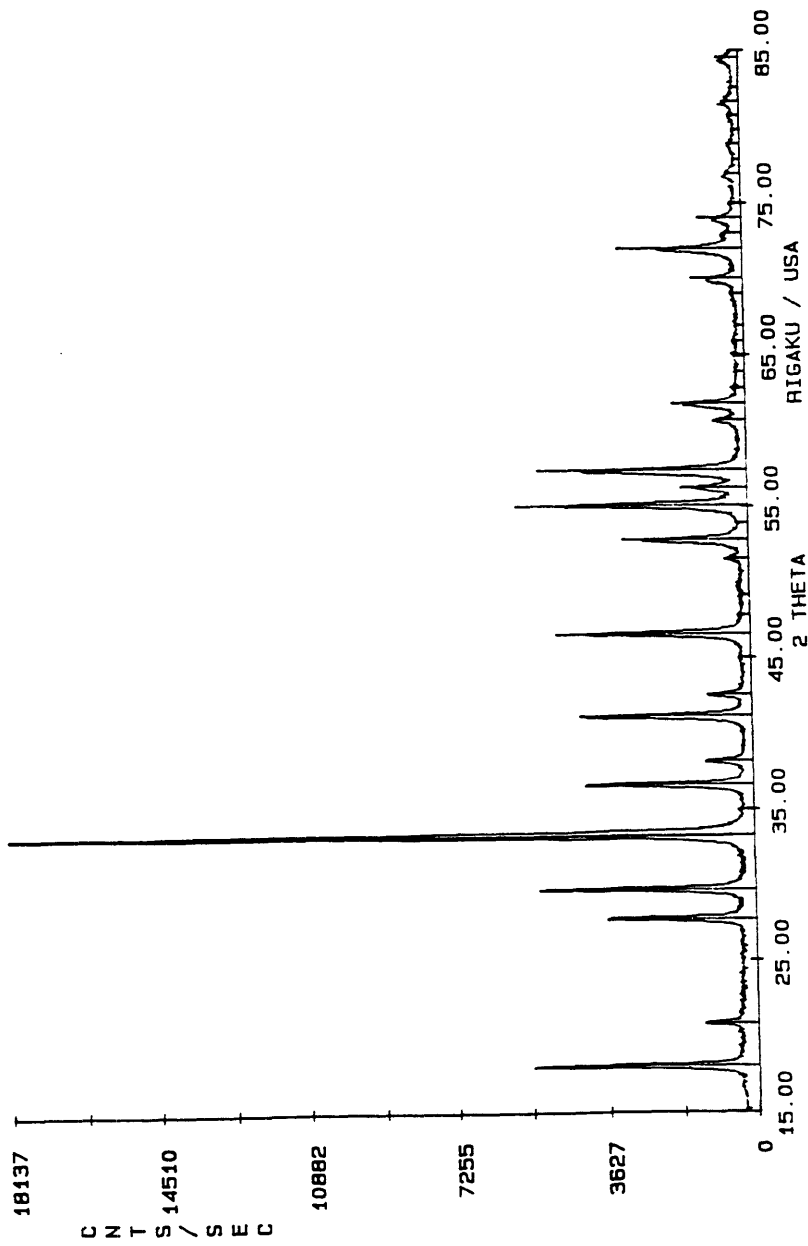
Figure 4.1 X-ray diffraction pattern of YAG powder made from the modified Pechini process.

Figure 4.2   SEM micrograph of YAG powder made from the modified
             Pechini process.

minutes to make pellets. The green strength of these pellets was quite good, and they could be handled readily without crumbling. The pellets were then sintered in vacuum in a graphite furnace at 1800° C for two hours in a powder bed. This sintering temperature was arrived at through a systematic study of the densification rate at various temperatures. Densification rates below 1700°C were negligible. However at 1800°C, the densification rate increased dramatically. This change in densification rate was attributed to liquid phase sintering at 1800°C by the alumina rich eutectic at 1760° C, as seen in the phase diagram in Figure 4.3.[101] Typical pellet densities were ≈95%.

4.2.1.3: Fibers

Small bars were cut from these polycrystalline ceramic pellets and used as feed material for the laser heated floating zone technique as shown in Figure 4.4. Using this technique, Toshihiro Kotani, a member of our laboratory visiting from Sumitomo Electric Industries was able to grow single crystal fibers from 250 μm to 2 mm in diameter, with lengths from 1 to 10 cm.

Ti:YAG fibers with concentrations of y=0.001, 0.01, 0.05, and 0.10 for $Y_3(Al_{1-y}Ti_y)_5O_{12}$ were grown in an atmosphere of Ar+5%H$_2$ gas. These dopant concentrations were determined by inductively coupled plasma (ICP) or microprobe, as seen in Table 4.1. SEM analysis revealed only single phase Ti:YAG, with few physical defects, e.g. bubbles, cracks, etc. Crystals grown under more oxidizing conditions had white precipitates that were identified by their compositions as $Y_2Ti_2O_7$ as measured by microprobe. A micrograph of the precipitates is seen in Figure 4.5. The higher the PO$_2$, the lower the Ti concentrations above which precipitates were found. The as-grown crystals were brown, and the intensity of the brown color increased with increasing Ti concentration and decreasing PO$_2$.
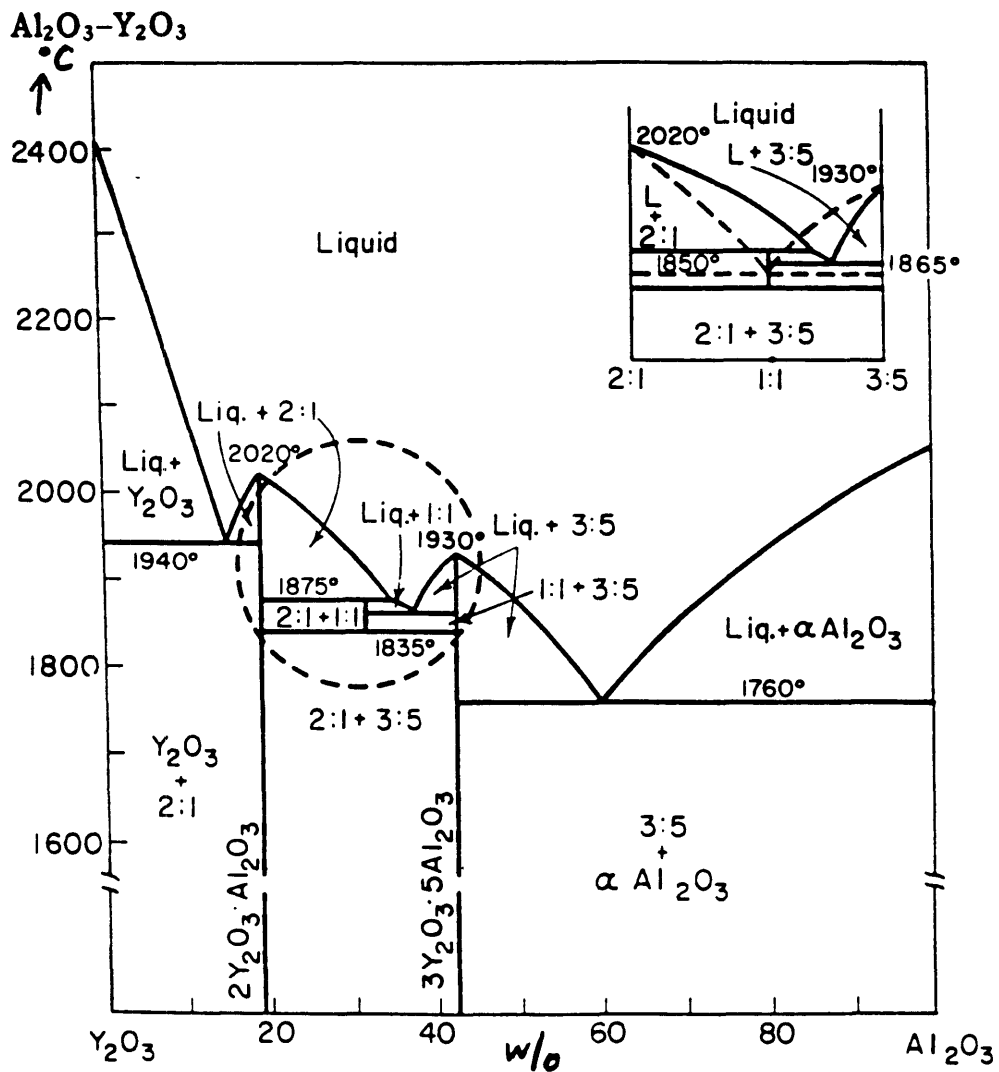
FIG. 2344.—System Al_2O_3-Y_2O_3.

N. A. Toropov, I. A. Bondar, F. Ya. Galakhov, X. S. Nikogosyan, and N. V. Vinogradova, *Izv. Akad. Nauk SSSR, Ser. Khim.*, **No. 7**, 1162 (1964).

Figure 4.3   The Al_2O_3-Y_2O_3 Phase Diagram.[101]

130

SCHEMATIC DIAGRAM OF LHFZ GROWTH APPARATUS

100W, 2-Beam Laser   For Fiber(100-200μm x 30cm Long)

1500W, 4-beam Laser   For 1-10mm Dia. x 20cm Long Crystal
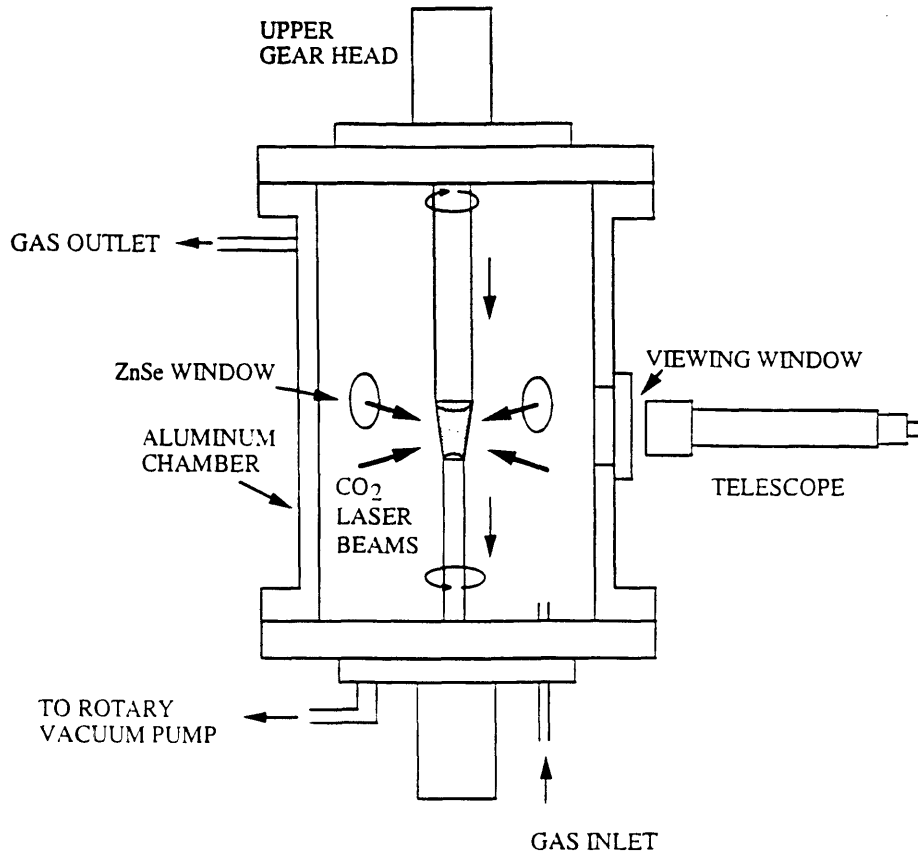
Figure 4.4   Schematic Diagram of the Laser Heated Floating Zone Growth
Apparatus.

Dopant Concentration of Doped YAG Samples

Crystals Grown by the Czochralski Method:

Crystal:	Concentration:	Method of Determination:
Nd:YAG $(Y_{1-x}Nd_x)Al_5O_{12}$	$x=0.01$	Microprobe
Ti:YAG	$x=1.4\times10^{-3}$	ICP

Single Crystal Fibers Grown by the Laser Heated Floating Zone Method:

Crystal:	Concentration:	Method of Determination:
Ti:YAG $Y_3(Al_{1-x}Ti_x)_5O_{12}$	$x=0.0014$	ICP
	$x=0.01, 0.05, 0.10$	Microprobe
Zr:YAG $(Y_{1-x}Zr_x)_3Al_5O_{12}$	$x=0.001$	ICP
	$x<0.001$	Microprobe
	$x=0.004, 0.008$	Microprobe

Table 4.1 Dopant concentration of doped YAG samples.

Figure 4.5   SEM micrograph of $Y_2Ti_2O_7$ precipitates in Ti:YAG single crystal fibers (Backscattered Image).

Zr:YAG fibers with concentrations of x<0.001, x=0.001, 0.004, and 0.008 for $(Y_{1-x}Zr_x)_3Al_5O_{12}$ were grown in an atmosphere of Ar+5%H_2 gas. These doping concentrations were determined by a combination of ICP and microprobe as seen in Table 4.1. SEM analysis revealed only single phase Zr:YAG with few physical defects for x<0.004. For x>0.004, precipitates were observed as seen in Figure 4.6 . These precipitates had a composition of YZr_2O_x as measured by microprobe. Crystals grown under more oxidizing conditions tended to have precipitates at a lower Zr concentration. The as-grown fibers were red, and the intensity of the red color increased with increasing Zr concentration and decreasing PO_2.

4.2.2: Czochralski Crystals:

As mentioned in the introduction, all our crystals grown by the Czochralski method were donated. John Haggerty of MIT generously donated some YAG and Nd:YAG crystals, while Milan Kokta of Union Carbide donated some Ti:YAG crystals. All the crystals were grown in an Ar atmosphere. The as-grown YAG crystal was colorless, the as-grown Ti:YAG brown, and the as-grown Nd:YAG pink. The results of glow discharge mass spectroscopy of the YAG and Ti:YAG crystals are shown in Table 4.2. Microprobe analysis of the Nd:YAG crystal revealed a Nd concentration of x=0.01 for $(Y_{1-x}Nd_x)_3Al_5O_{12}$.

4.3: Electrical Measurements:

High temperature two probe dc and impedance spectroscopy measurements were performed on the samples. The dc measurements

Figure 4.6   SEM micrograph of YZr$_2$O$_x$ precipitates in Zr:YAG single
crystal fibers (Backscattered Image).

Chemical Analysis of YAG and Ti:YAG
Crystals Grown by the Czochralski Process

Element	YAG Impuritites PPM by weight	Ti:YAG Impurities PPM by weight
Na	32	37
Mg	15	10
Si	5.0	26
P	0.9	1
Ca	8.4	14
Ti	4.6	560
V	0.5	0.2
Cr	3.3	1.8
Mn	1.6	0.2
Fe	200	27
Ni	1.9	0.5
Co	<0.1	<0.1
Zn	2.3	13
Ce	<0.1	<0.2

Table 4.2 Chemical analysis of YAG and Ti:YAG crystals grown by the Czochralski process.

were made using a HP4140b picoammeter, and the impedance measurements were made using a HP4192a impedance analyzer. A typical i-v curve and impedance plot for YAG is shown in Figures 4.7 & 4.8. As discussed in section 2.3, the various resistive and reactive responses of the sample can often be modeled by an equivalent circuit of resistors and capacitors. For a single crystal dielectric material such as YAG, a common equivalent circuit is a parallel RC circuit, with possibly another RC circuit for the electrode, as shown in Figure 2.11.[30] A single RC circuit yields a single semicircle in the complex impedance plane, with the low frequency intercept of that semicircle with the real axis being equal to the resistance, the desired quantity. From this resistance, we can determine the conductivity from a knowledge of the geometric length and cross-sectional area of the sample. All the samples we measured exhibited single semicircles as shown in Figure 4.9.

The furnace was an in-house built globar tube furnace with a Eurotherm controller model #818. Oxygen partial pressures, established with CO/CO_2 gas mixtures, were monitored with a yttria stabilized zirconia cell, and calibrated with an in-situ TiO_2 sensor. The furnace controller, thermocouples, zirconia cell, and measuring equipment were all controlled and monitored with a computer. Automated measurements were made every hour. Achievement of "equilibrium" was arbitrarily defined as three consecutive measurements whose values differed by less than 2%.

The Czochralski grown crystals were cut into thin plates for electrical measurements, typically 1 mm thick by ≈ 1 cm^2 area. These crystals were wedged into slots in alumina rods with platinum (Pt) foil as shown in Figure 4.9. This foil was then spot welded to Pt leads that were fed through the alumina rods, with only one lead per sample fed through the same alumina rod to

137
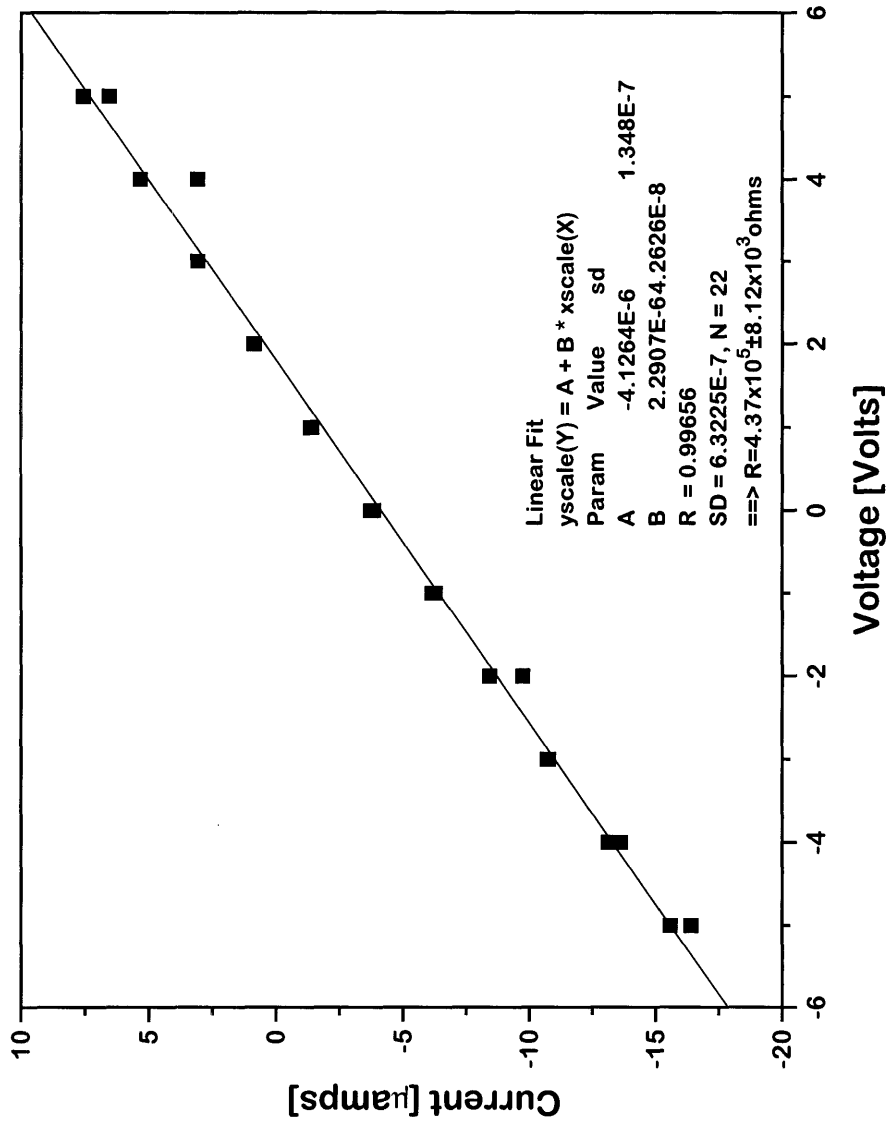
Figure 4.7 Typical 2 probe I-V characteristics of a YAG sample.
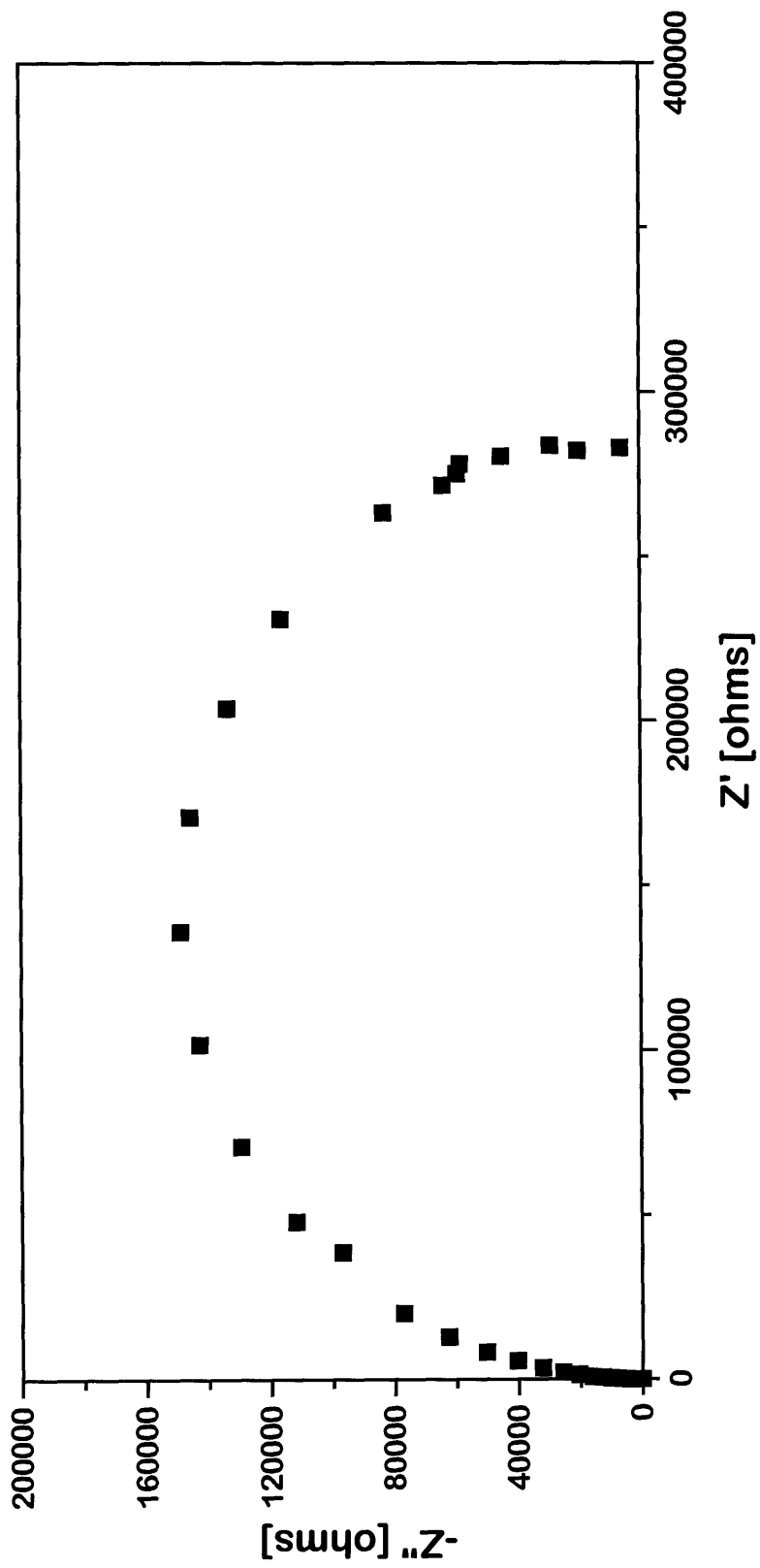
Figure 4.8 Typical 2 probe impedance plot of a YAG sample.
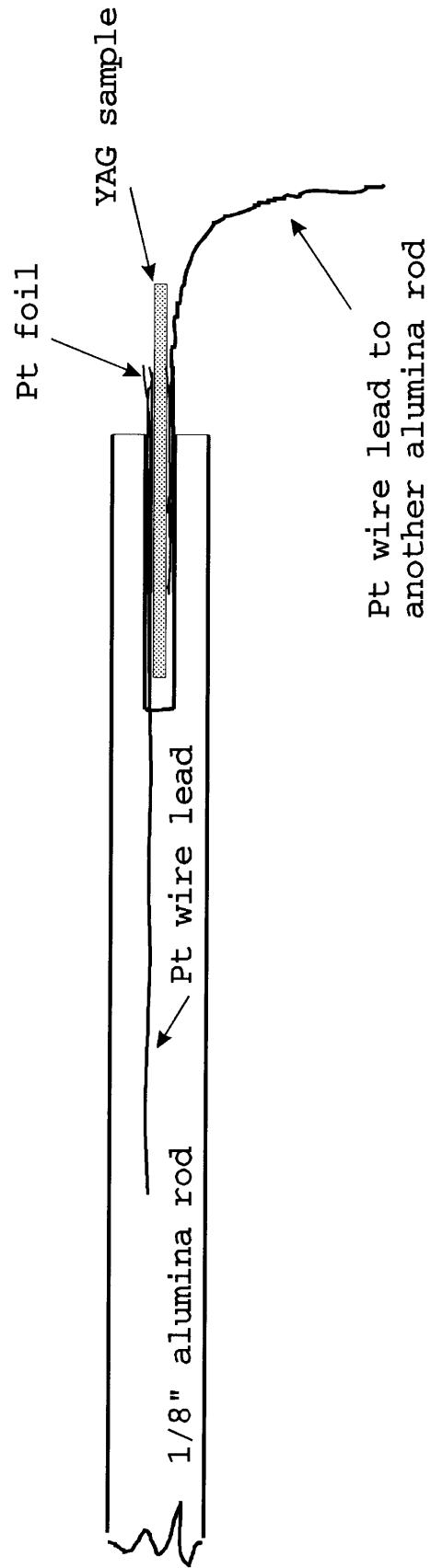
Figure 4.9 Electrical measurement sample holder for YAG crystals grown by the Czochralski method.

eliminate potential parallel electrical pathways through the alumina. Electrodes consisted of sputtered Pt followed by painting with Pt ink 6926 from Engelhard. The resistance of the sample holder without any samples was measured for calibration.

The YAG fibers were cut into thin disks typically 0.5 mm thick by 1.0 mm in diameter. Pt ink electrodes were used to sinter thin strips of Pt foil to the disks as leads. The disk and foil setup was then rigidly attached to a flattened alumina rod with alumina cement as shown in Figure 4.10. Pt wire fed through the alumina was then spot welded to the foil as before. Again, only one lead per sample was fed through the same alumina rod. This resistance of the sample holder without any samples attached was also measured for calibration.

4.4: Optical Measurements:

Samples for optical measurements were polished with diamond paste of successively smaller grit sizes. The final polish was done with 0.25 μm diamond particles. If the samples were annealed, optical measurements were made immediately after the anneal, re-polished, and measured again. These two measurements were almost always identical, suggesting that thermal etching of the YAG single crystal polished surfaces was minimal.

To establish the same defect structure as the high temperature electrical measurements, optical samples were annealed under the same temperature and PO_2 conditions as the electrical samples, and then quenched. Quenching was achieved by withdrawing the alumina crucible containing the samples from the hot zone of the furnace. To maintain the gas flow conditions of the anneal during the quench, the crucible was suspended with Pt wire from an alumina rod which extended out of the furnace tube. This rod was sealed with silicone gaskets to

Pt wire lead to
another alumina rod

Pt foil

YAG sample

alumina cement

Pt wire lead
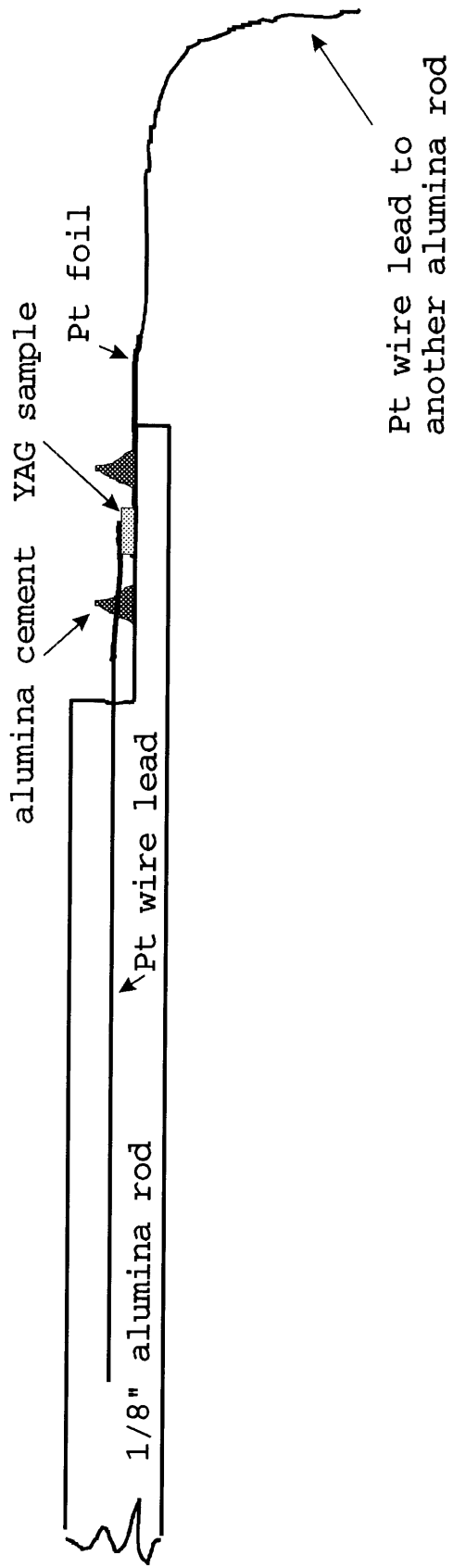
1/8" alumina rod

Figure 4.10 Electrical measurement sample holder for YAG single crystal fibers.

the furnace endcaps. Estimated quench rates associated with withdrawing this alumina rod and crucible was ≈70°C/minute.

The optical transmission of Czochralski grown crystals was measured with a Perkin-Elmer Lambda 19 spectrophotometer. All measurements were calibrated with a standard YAG sample for reference, to remove day to day instrument fluctuations. The optical transmission of the YAG fibers was measured with a specially designed fiber attachment for the Lambda 19. A schematic of this attachment is seen in Figure 4.11. With this attachment we were able to measure fibers from 250 μm to 2 mm in diameter, with lengths of up to 40 cm. This was accomplished by using pairs of parabolic mirrors to transmit and focus the light as shown in Figure 4.11. The incident light was focused onto one polished end of the fiber, and collected out the other polished end. To permit semi-quantitative measurements, the fiber accessory itself without any fibers was calibrated before every measurement.

Excitation and emission spectra were measured at GTE Labs by Roger Hunt. A SPEX 1902 spectrophotometer with a xenon arc lamp and computer controlled double monochromator was used for these measurements.
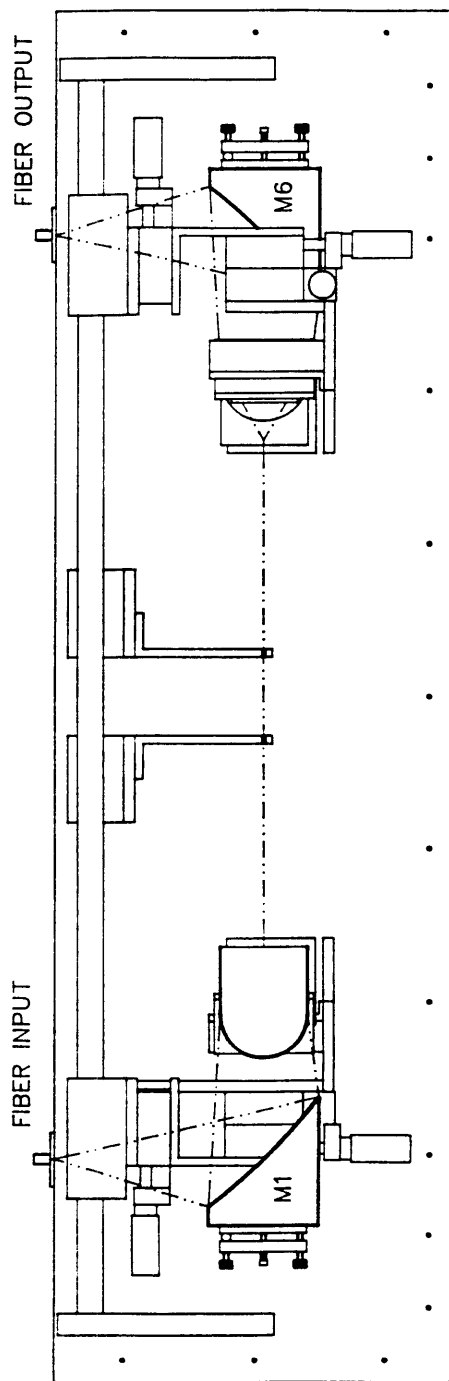
Figure 4.11 Top view of the fiber accessory used to measure single crystal YAG fibers with the Perkin-Elmer Lambda 19 spectrophotometer. (Dashed lines represent the light path.)

144

CHAPTER 5: EXPERIMENTAL MEASUREMENTS OF YAG AND Nd:YAG

5.1: Introduction:

Experimental measurements were first performed on YAG and Nd:YAG to establish a set of references for the undoped and isovalently doped crystals. As mentioned in chapter 4, both these crystals were grown by the Czochralski method. Consequently their electrical and optical properties were easier to measure because of the larger size of these crystals. Changes in defect structure were induced by high temperature anneals under oxidizing and reducing conditions, and these changes were monitored by their effect on the electrical and optical properties. Oxygen partial pressures were controlled by O_2/Ar and CO/CO_2 gas mixtures, and correlations between electrical and optical measurements were made by quenching a sample for optical measurement from the temperature and PO_2 where the high temperature electrical measurements were made.

5.2: Results:

5.2.1: Electrical:

The electrical conductivity of YAG & Nd:YAG measured as a function of PO_2 for a series of isotherms is shown in Figures 5.1 & 5.2 respectively. Both crystals exhibit an n-type like behavior at reduced PO_2's and a trend towards PO_2 independence under oxidizing conditions. If these isotherms are caused by a defect structure similar to those measured by Rotman[4,31], then we would expect the isotherm to consist of branches of electronic conductivity with a $|1/4|$ slope separated by a region of ionic conductivity which is PO_2 independent,
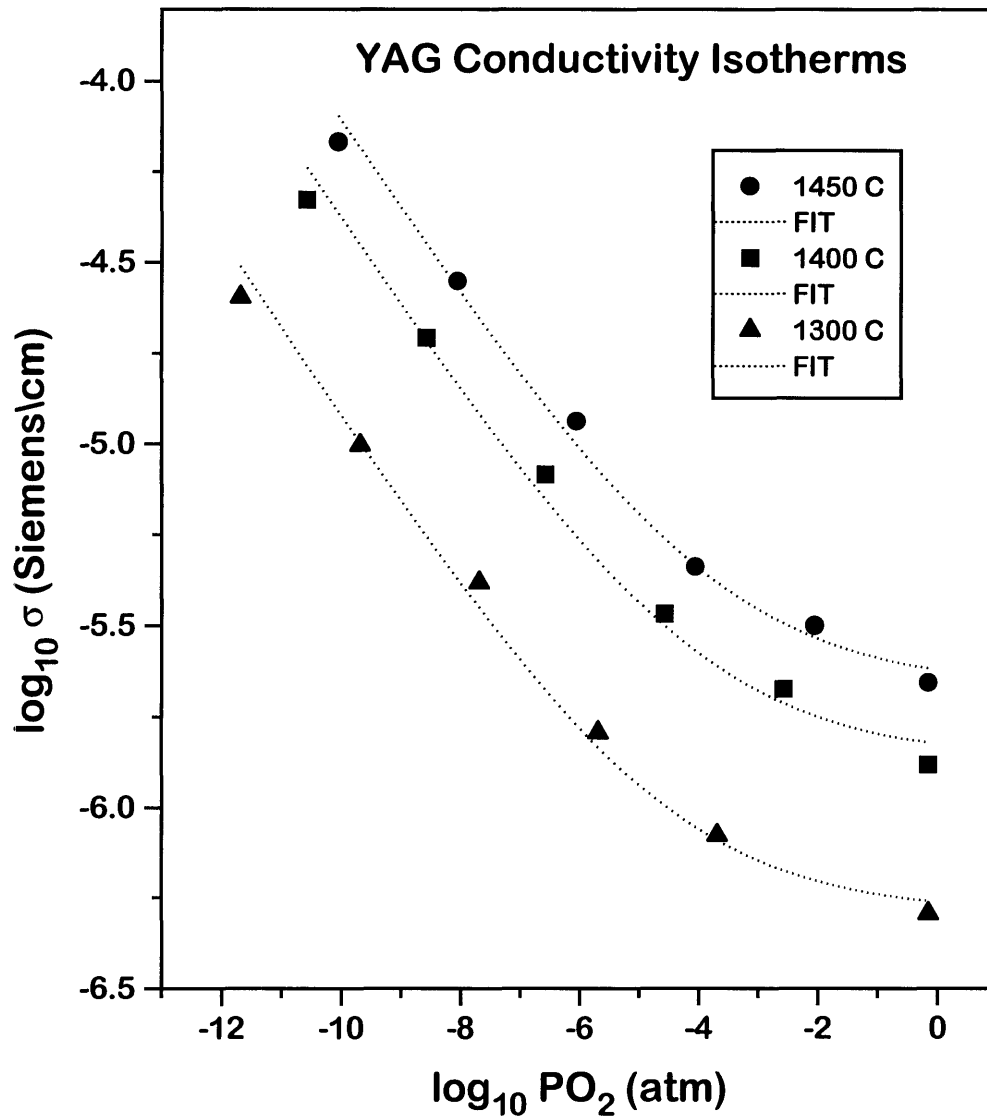
Figure 5.1 YAG conductivity isotherms fitted by an equation assuming a PO_2 independent part and a PO_2 dependent part that varies as $PO_2^{-1/4}$.

Nd:YAG Conductivity Isotherms
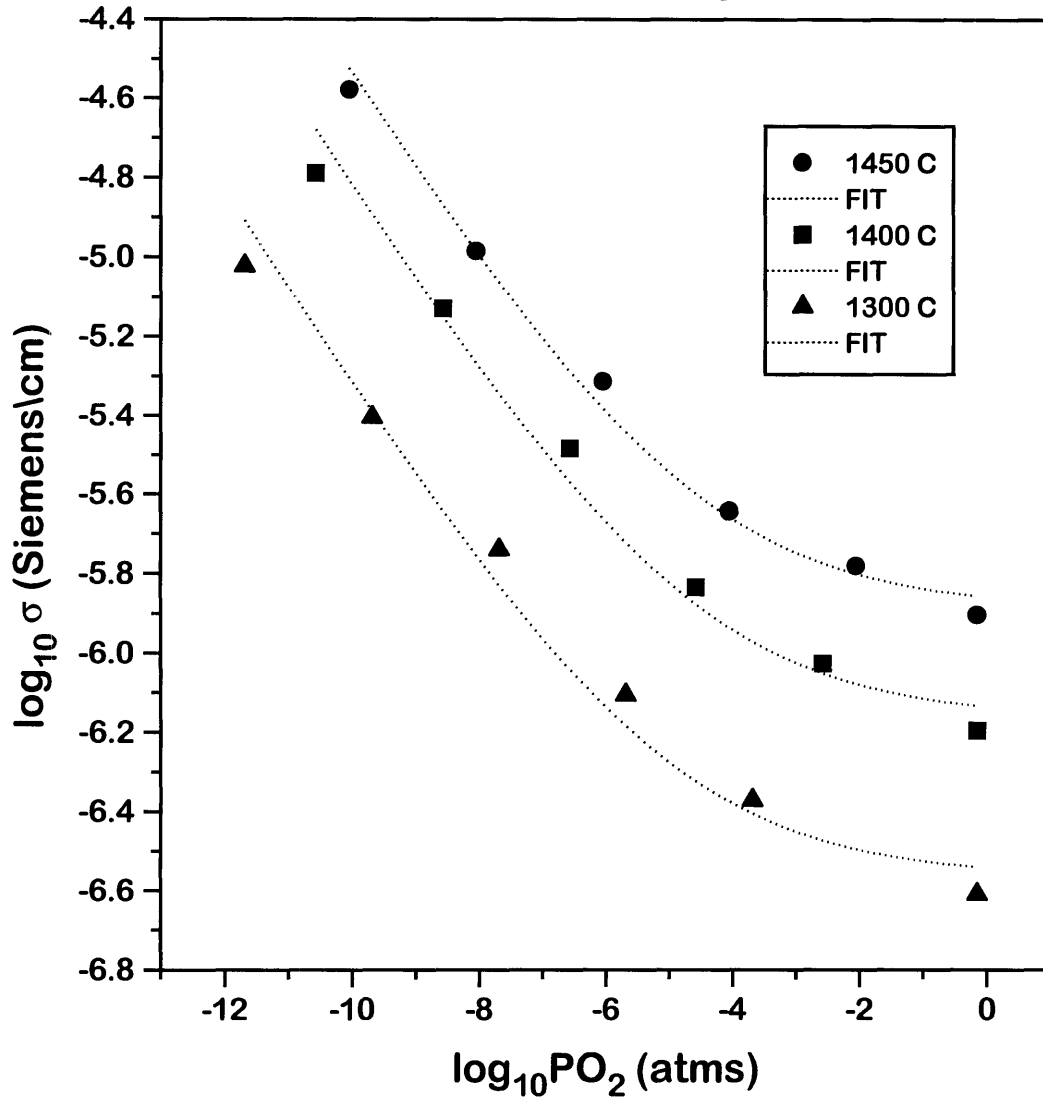
Figure 5.2 Nd:YAG conductivity isotherms fitted by an equation assuming a PO_2 independent part and a PO_2 dependent part that varies as $PO_2^{-1/4}$.

as shown in Figure 2.6. The lines connecting the data points are a best fit of this model. As seen in Figures 5.1 & 5.2, the model fits the data quite well. Using the fitting parameters of this model, we can generate de-convoluted isotherms as shown in Figures 5.3 & 5.4. Activation energies of the n-type electronic branch and the PO_2 independent ionic segment can then be calculated from these de-convoluted isotherms as shown in Figures 5.5 & 5.6 for YAG and Nd:YAG respectively. N-type activation energies are 3.0 and 2.9 eV for YAG and Nd:YAG respectively. The PO_2 independent ionic activation energies are 2.3 and 2.5 eV for YAG and Nd:YAG respectively.

5.2.2: Optical:

The spectra of the as-grown YAG and Nd:YAG crystals are shown in Figures 5.7 & 5.8 respectively. Undoped YAG has the expected flat transmission window for $\approx$300 nm < λ < 3200 nm, with absorption increasing rapidly as one approaches YAG's band edge at $\approx$ 200 nm. Nd:YAG has the typical spectra of the 4f electronic transitions of Nd^{+3} as seen in Figure 3.7. The spectra of oxidized and reduced YAG and Nd:YAG are shown in Figures 5.9 & 5.10 respectively. As seen in Figure 5.9 for YAG, the band centered at $\approx$250 nm decreases with reduction and increases with oxidation, while the band at $\approx$310 nm increases with reduction and decreases with oxidation. These spectra are similar to those observed by Mori[54] and Akhmadullin[52] for undoped YAG, and has been attributed to iron impurities as described in section 3.2.1. For Nd:YAG on the other hand, the reduced and oxidized spectra are essentially identical with the as-grown crystal. However, a difference spectra as

148
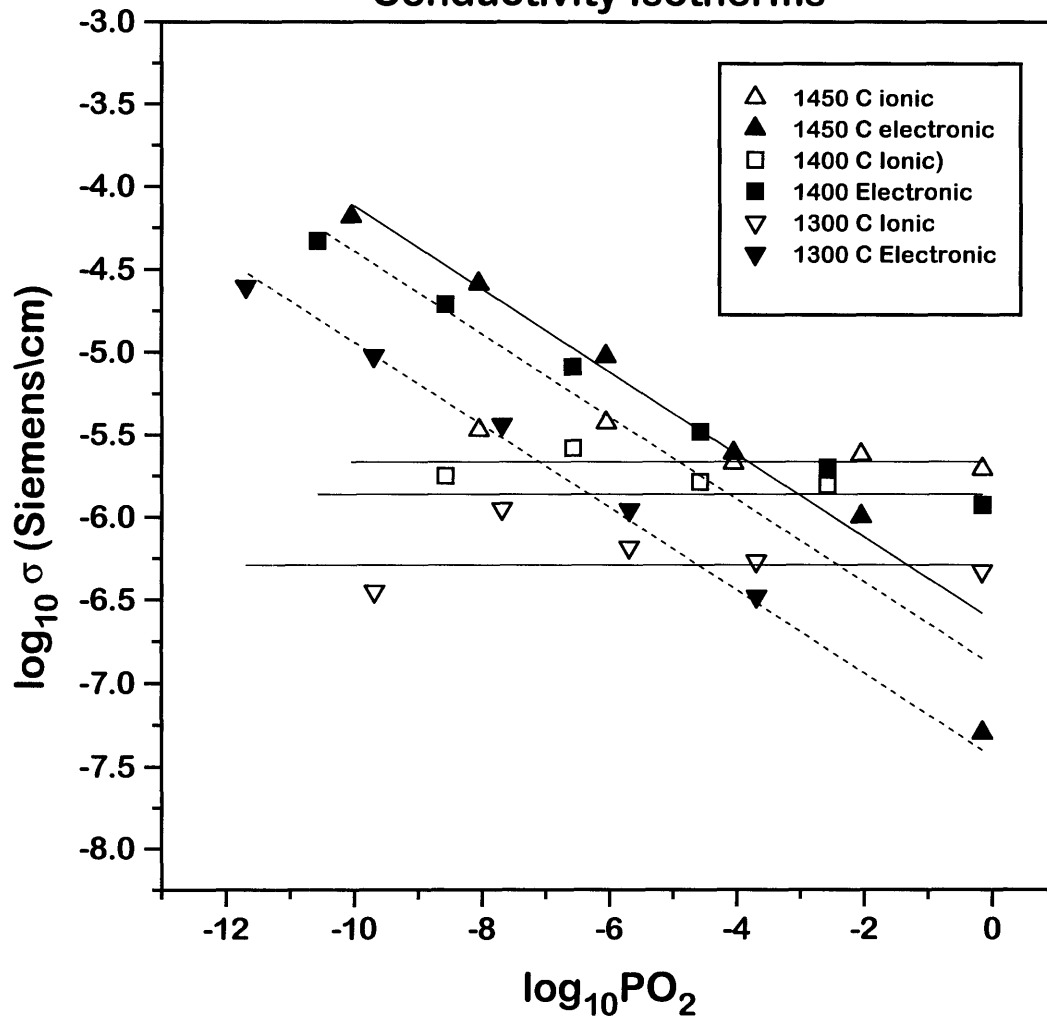
Figure 5.3 Component analysis of the YAG conductivity isotherms.
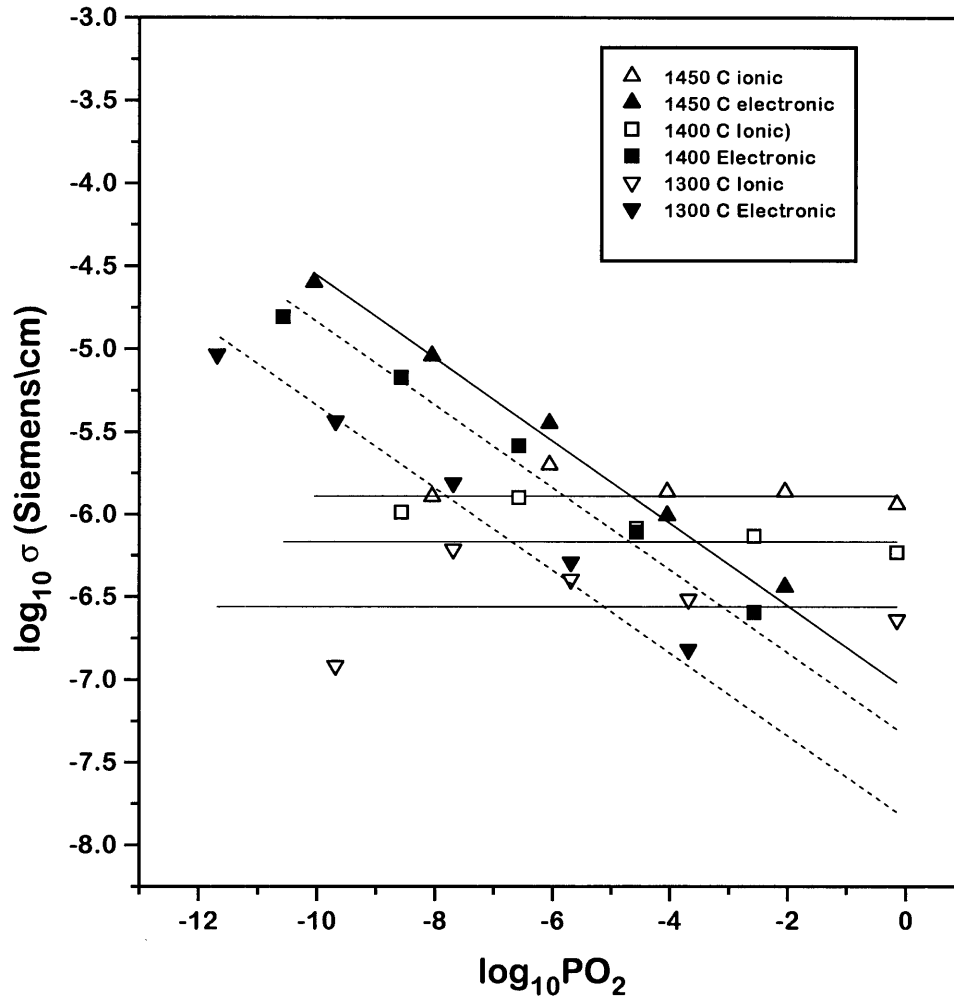
Figure 5.4 Component analysis of the Nd:YAG conductivity isotherms.
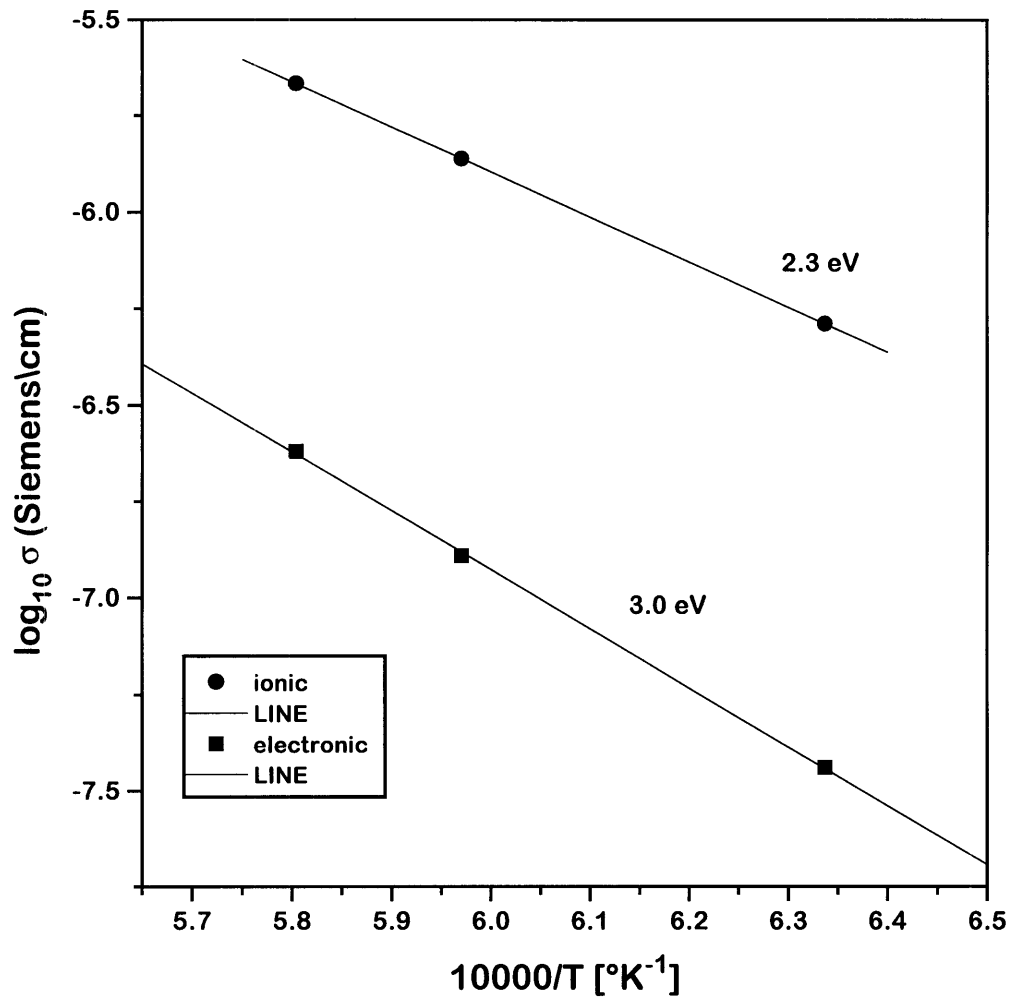
Figure 5.5 Activation energy of YAG conductivity components.
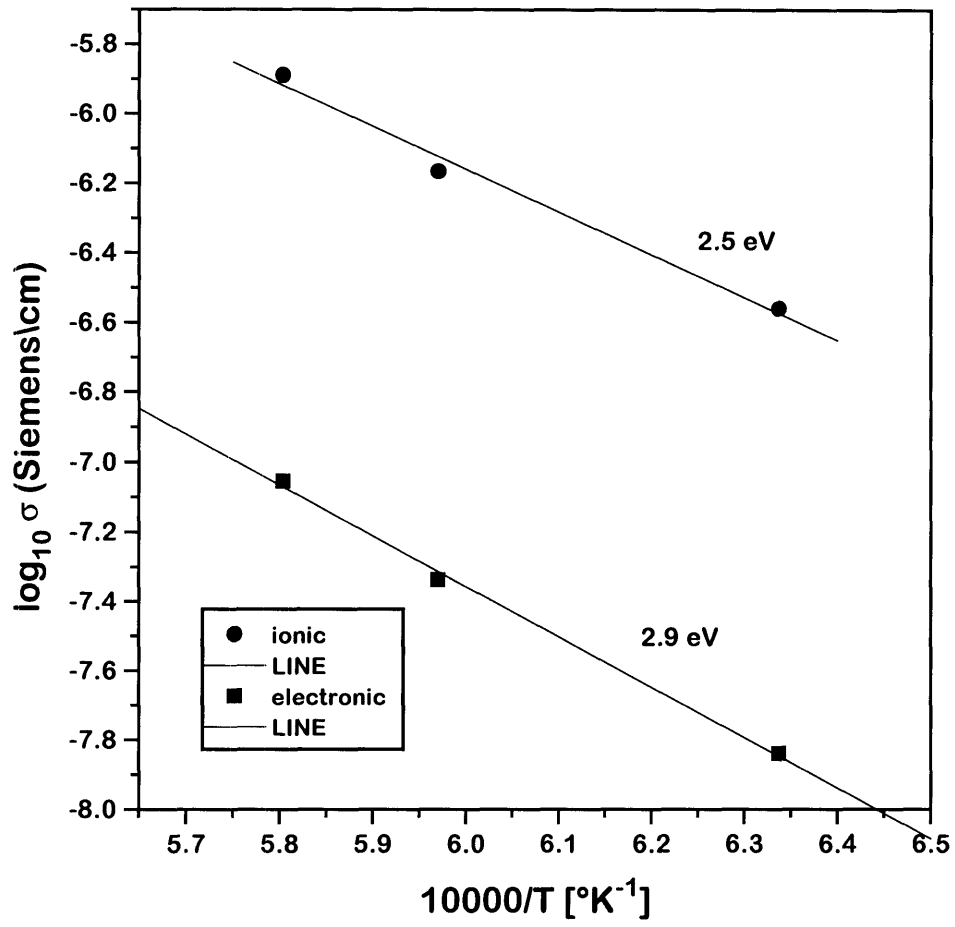
Figure 5.6 Activation energy of Nd:YAG conductivity components.
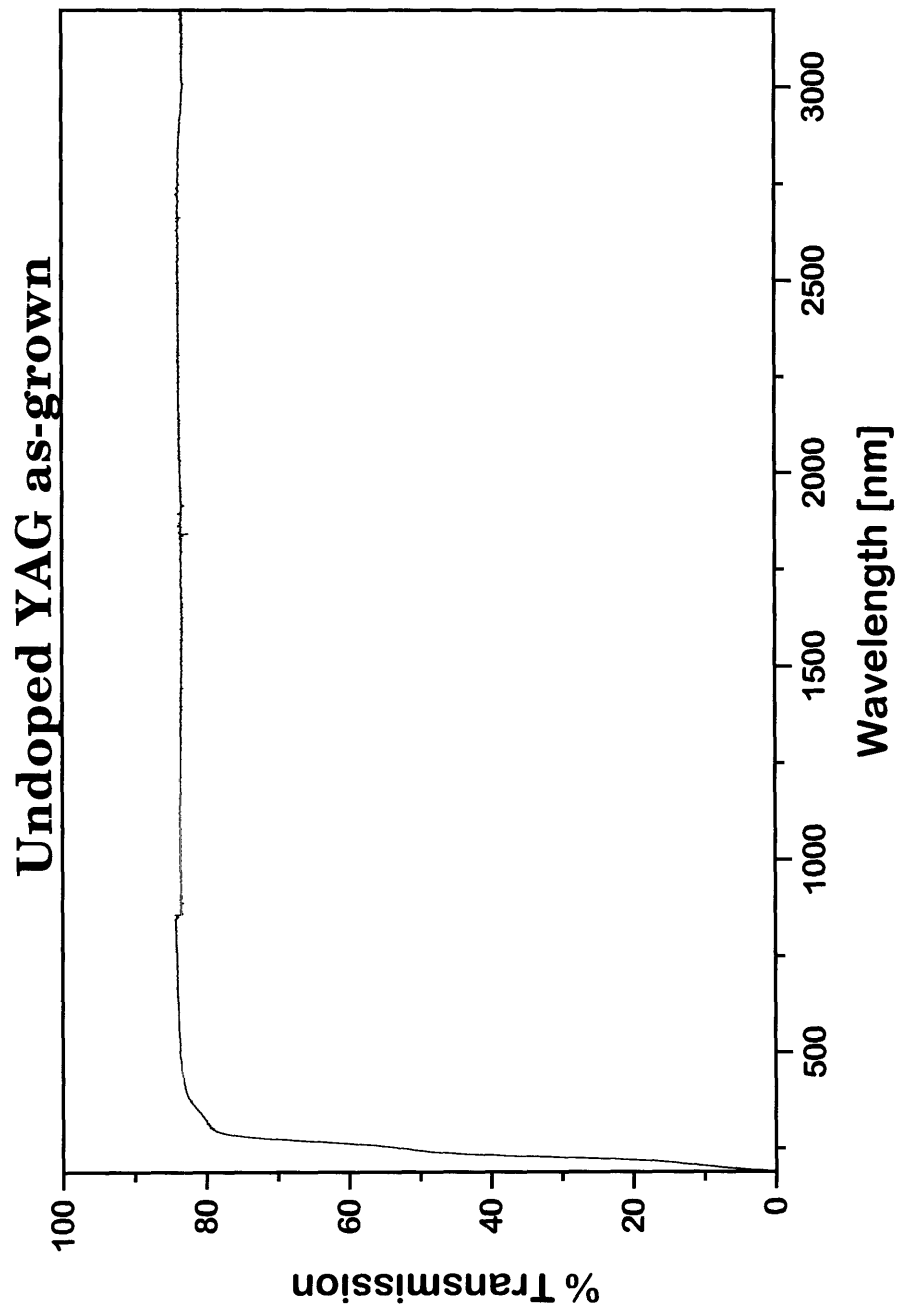
Figure 5.7 Transmission spectrum of as-grown YAG.

Nd:YAG Absorption Spectra
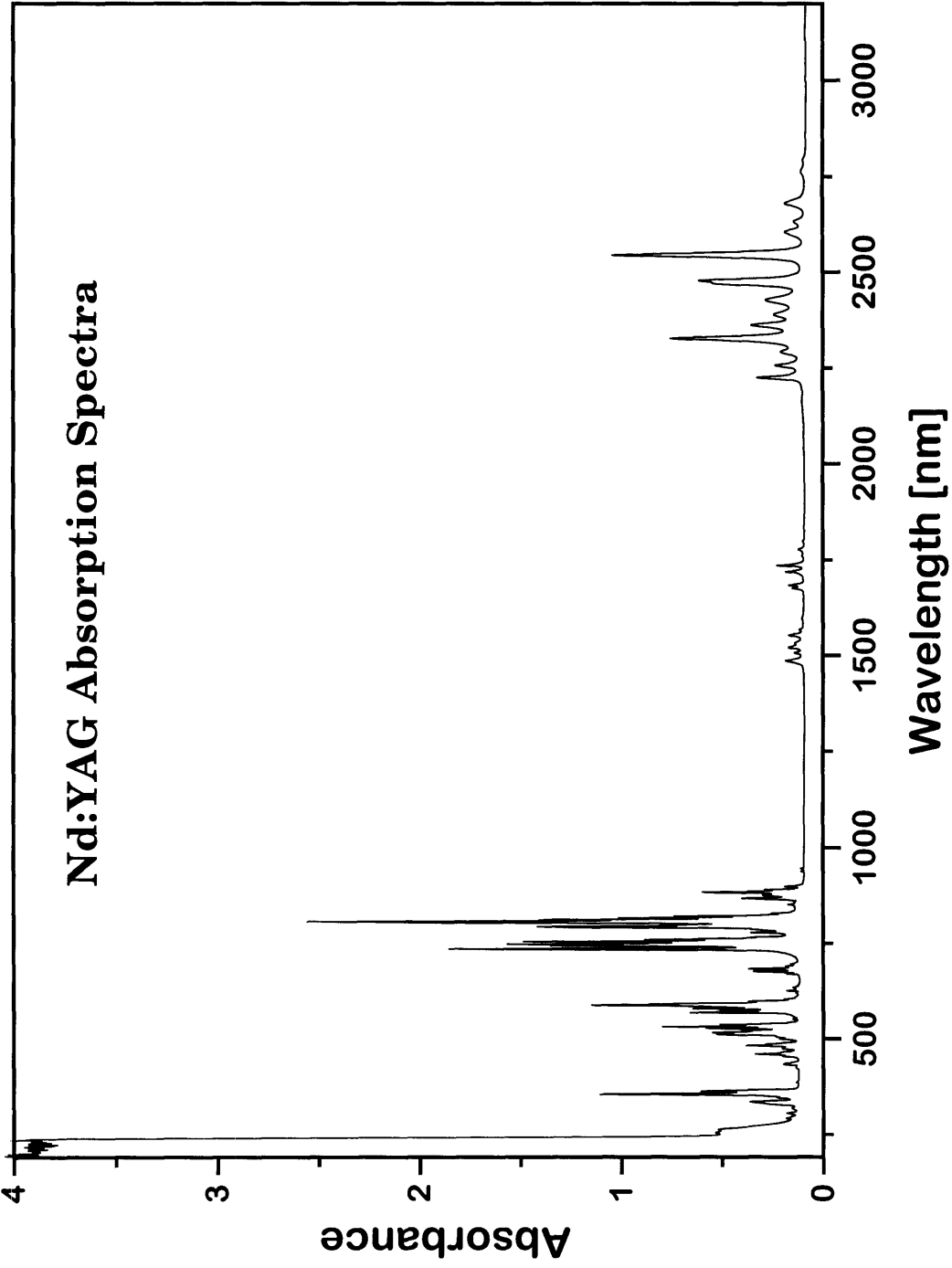
Figure 5.8 Absorption spectrum of as-grown Nd:YAG.
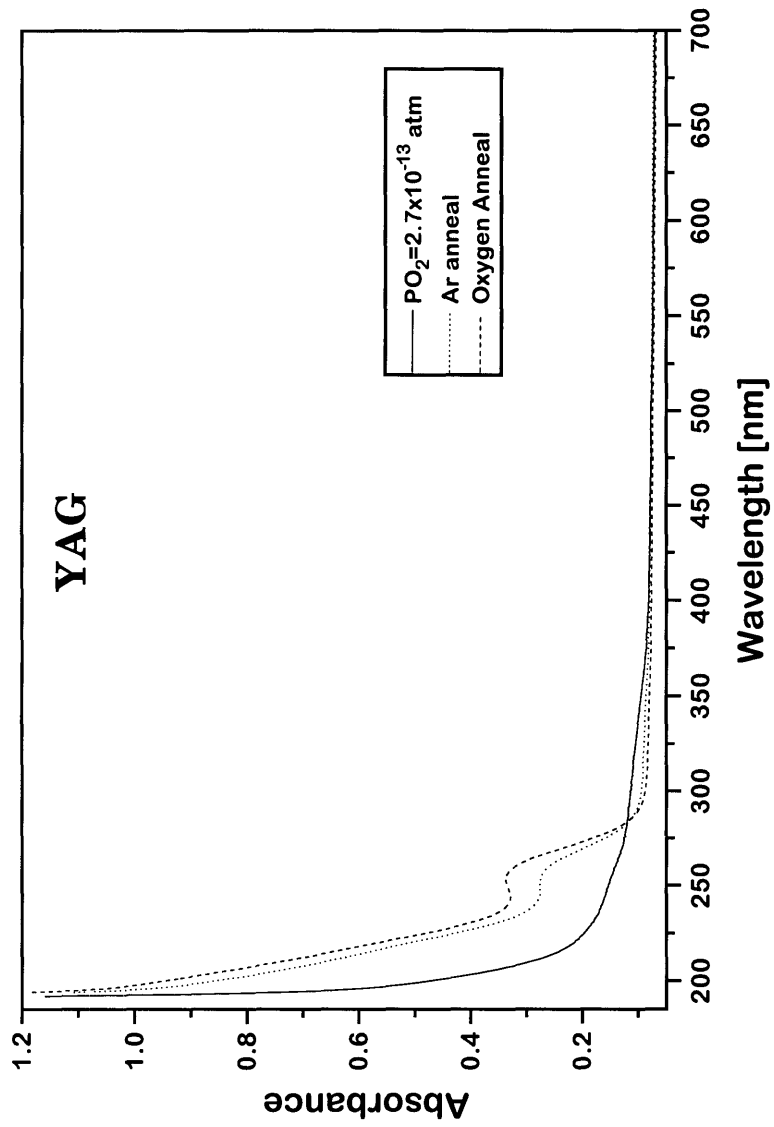
Figure 5.9 Absorption spectra of YAG after oxidizing and reducing anneals.
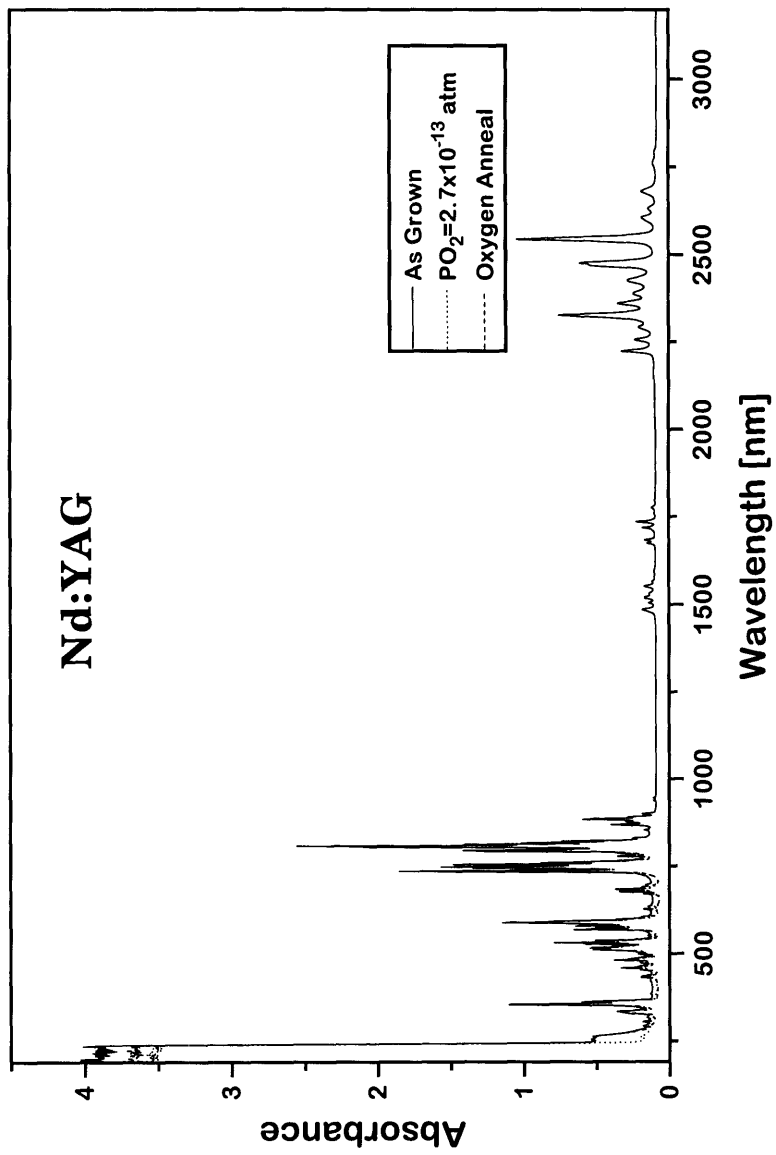
Figure 5.10 Absorption spectra of Nd:YAG after oxidizing and reducing anneals.

shown in Figure 5.11 reveals the same pattern as observed above for YAG, a peak at ≈250 nm that increases with oxidation, and a peak at ≈310 nm that increases with reduction.

5.3: Discussion:

The good fit between our measured isotherm and the defect model of Figure 2.6 as seen in Figure 5.1 & 5.2 suggests that both our YAG and Nd:YAG crystals have defect structures controlled by background acceptors which are compensated by oxygen vacancies. This is the same defect structure observed by Rotman[4,31] for most of his doped and undoped YAG samples, as mentioned in section 3.4. Thus it seems that we have verified Rotman's defect model. The one difficulty lies in the activation energies. N-type and ionic activation energies measured by Rotman[4,31,85,86] and Schuh[25,87,88] are listed in Tables 3.3 & 3.4 respectively. For our YAG crystal, the n-type and ionic activation energies are 3.0 and 2.3 eV respectively, while for our Nd:YAG crystal they are 2.9 and 2.5 eV respectively. Our ionic activation energies are comparable to those measured by Rotman and Schuh, and are attributed to the migration energy of oxygen vacancies compensating the background acceptors.[4,25] In contrast, our n-type activation energies are significantly less than those measured by Rotman and Schuh, as seen in Table 3.2.

We can rationalize this difference if we assume that iron is involved in our redox reaction. (Fe was not listed as an impurity in Rotman's samples which exhibited an n-type conductivity branch.[4,31]) Rotman's[4,31] n-type activation energy of 3.9 eV resulted in a reduction enthalpy of 7.8 eV for the following reduction reaction (See Table 2.2):

$$O_o \rightarrow V_o^{\bullet\bullet} + 2e' + \frac{1}{2}O_2 \qquad K_R = [V_o^{\bullet\bullet}]n^2 PO_2^{1/2} \qquad \Delta H_R = 7.8 \text{ eV}$$
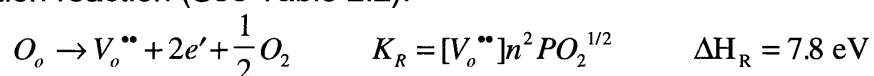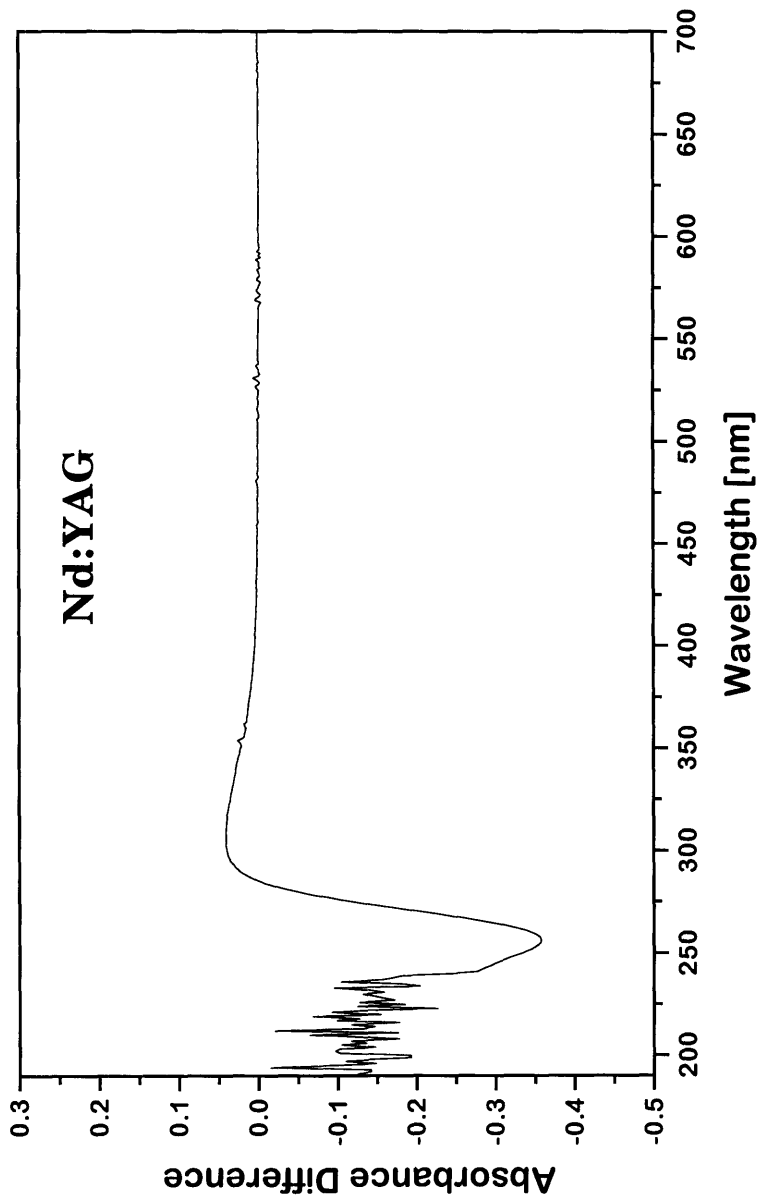
Figure 5.11 Difference spectra of Nd:YAG, absorption spectra of reduced crystal minus absorption spectra of oxidized crystal.

If the reduction process in our samples involves the reduction of Fe^{+3} to Fe^{+2}, then the pertinent reduction equation for our sample is:

$$O_O \rightarrow V_O^{\bullet\bullet} + 2e' + \frac{1}{2}O_2 \qquad K_R = \left[V_O^{\bullet\bullet}\right]n^2 PO_2^{1/2} \qquad \Delta H_R = 7.8\ eV$$

$$2Fe^x{}_{Al} + 2e' \rightarrow 2Fe'_{Al} \qquad K_i = \frac{\left[Fe'_{Al}\right]^2}{\left[Fe^x{}_{Al}\right]^2 n^2} \qquad 2\Delta H_i$$

$$------------------$$

$$2Fe^x{}_{Al} + O_O \rightarrow V_O^{\bullet\bullet} + 2Fe'_{Al} + \frac{1}{2}O \qquad K_{R2} = \frac{\left[Fe'_{Al}\right]^2\left[V_O^{\bullet\bullet}\right]PO_2^{1/2}}{\left[Fe^x{}_{Al}\right]^2} \qquad \Delta H_{R2} = \Delta H_R + 2\Delta H_i$$
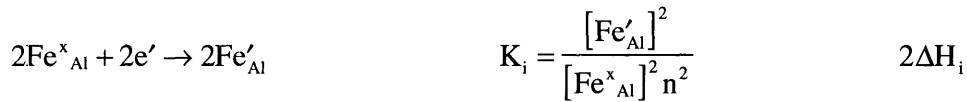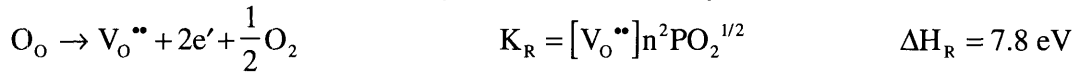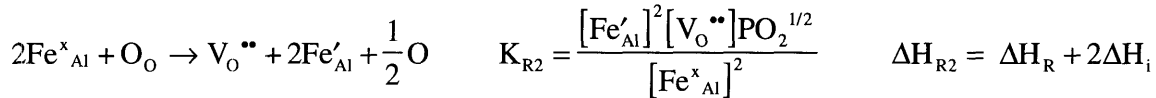
As mentioned in section 3.2.1, an absorption band at ≈ 5 eV has been observed in a number of undoped YAG samples, and has been attributed to a charge transfer process from the oxygen 2p band to Fe^{+3}.[52,54] Since YAG has a thermal bandgap of ≈ 6 eV,[4,31] this implies that the Fe^{+2} level is ≈ 1 eV below the conduction band, or that for the above equation, $\Delta H_i \approx -1$ eV. This in turn suggests that $\Delta H_{R2} \approx 5.8$ eV, and that the n-type activation energy for this redox reaction is 2.9 eV as we in fact observed.

The optical properties of YAG and Nd:YAG are consistent with the above explanation. As seen in Figures 5.9 & 5.11, a peak in the same position as the charge transfer process from oxygen to Fe^{+3} is observed in our spectra at ≈ 250 nm.[4,52,54] In addition to YAG, similar charge transfer peaks have been observed in $Fe:Al_2O_3$[23,89] and Fe:YGG.[99] The observation that the intensity of this peak increases with oxidation, and decreases with reduction is consistent with this charge transfer assignment. A reducing anneal would change Fe^{+3} to Fe^{+2} and remove this band as observed. Chemical analysis does indeed reveal Fe as the primary impurity in the YAG sample, as seen in Table 4.1. Microprobe analysis of the Nd:YAG sample did not reveal any Fe, but that simply implies that the Fe concentration is less that ≈ 200 ppm. If we assume that an O_2 anneal

fixes all the Fe in the +3 valence, we can calculate the molar extinction coefficient and oscillator strength for the peak:[10,11]

$$A = 0.8 = \varepsilon_{max}cl \qquad\qquad c = concentration = 200ppm = 1.63x10^{-2} moles / liter$$
$$===> \varepsilon_{max} = 164\ liter / cm - mole \qquad l = crystal\ thickness = 0.3\ cm$$

$$f = 4.6x10^{-9}\varepsilon_{max}\Delta v \qquad\qquad \Delta v = 1.01x10^4\ cm^{-1}$$
$$===> f = 7.6x10^{-3}$$

This value of ε_{max} and f is at the low end of charge transfer processes, as described in section 2.1.3. However, these values represent the minimum values, since we assumed that all the Fe was in the +3 valence. If some of the Fe was actually in the +2 valence, then ε_{max} and f would be larger. It's interesting to note that Akhmadullin's[52] values for ε_{max} and f were of the same order of magnitude as the ones we calculated above. Finally, a luminescence experiment was done as shown in Figure 5.12. Pumping at 240 nm results in the characteristic 800 nm emission of Fe^{+3} for the as-grown YAG.[4] For the reduced YAG, no luminescence was observed.

Thus the electrical and optical measurements of our YAG and Nd:YAG crystals are consistent with an acceptor dominated defect structure where Fe impurities play a significant role for the minority electronic carriers. Our n-type conductivity isotherms correspond to regime (b) of the defect model shown in Figure 2.6. Detailed quantitative correlations between these electrical and optical properties, guided by our defect model in Figure 2.6 will allow us to estimate the position of the Fe^{+2} and Nd^{+2} ground state in the YAG bandgap. As seen in Figure 2.6, at a particular PO_2, the "stoichiometric" PO_2: $PO_{2,s}$, n=p, and at that PO_2 the Fermi level is at midgap. For $PO_2<PO_{2,s}$, n>p and
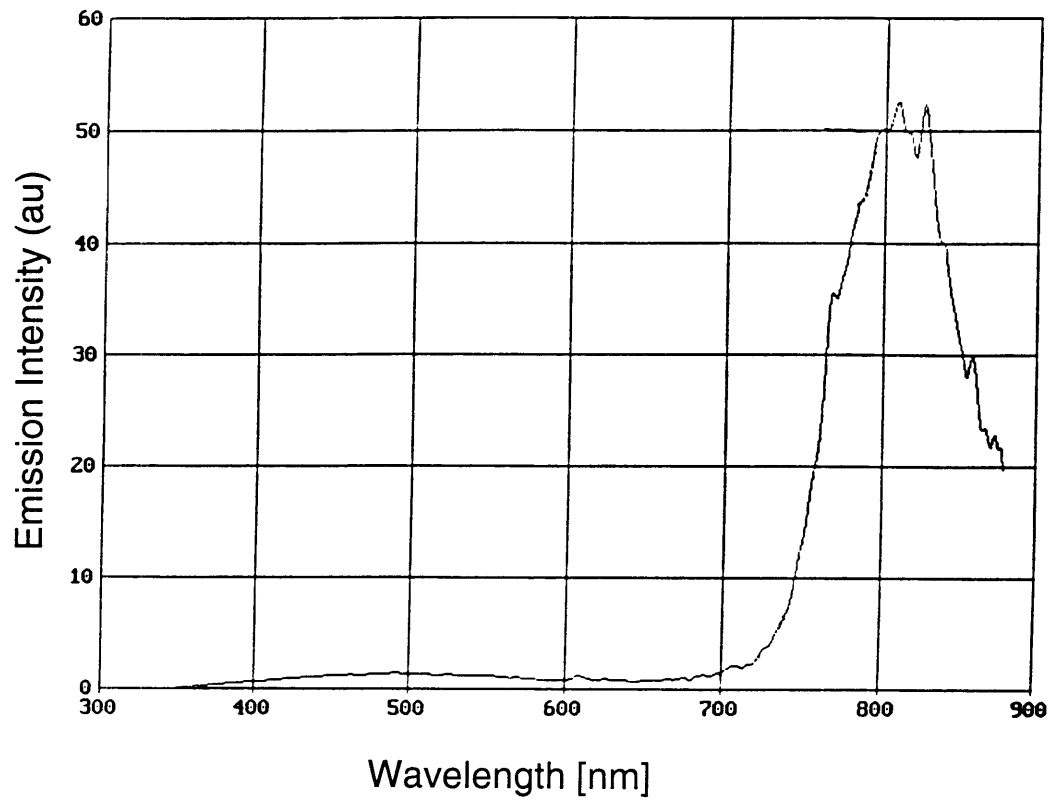
Figure 5.12   Fluorescence spectrum of YAG pumped at 240 nm.

the Fermi level is above midgap. Similarly for $PO_2 > PO_{2,s}$, $n < p$ and the Fermi level is below midgap. By comparing our measured conductivity isotherms in Figure 5.1 & 5.2 with the schematic isotherm in regime (b) of Figure 2.6, we see that the Fermi level is probably above midgap, even for the most oxidizing PO_2 in our measurements, an O_2 anneal. Thus the Fermi level, $E_f \geq E_g/2$ after an O_2 anneal, where E_g is the YAG bandgap. Using the defect model as a guide, we can estimate the Fermi level shift for the range of PO_2's covered in our conductivity measurements. As seen in regime (b), of Figure 2.6 and Table 2.2, $n \alpha PO_2^{-1/4}$. For our conductivity measurements, PO_2 varies from roughly 1 atm to 10^{-12} atm. Thus n varies by three orders of magnitude over this PO_2 range, and this corresponds to a Fermi level shift upward of ≈ 1 eV relative to an O_2 anneal at 1400°C as shown below:

$$n = N_c \exp\left(\frac{E_f - E_c}{kT}\right)$$ N_c = Effective Density of States in Conduction Band

$$===> \quad 2.3\log\frac{n}{N_c} = \frac{E_f - E_c}{kT}$$ E_f = Energy of Fermi Level

E_c = Energy of Conduction Band Level

$$\therefore \text{ If } \quad n_2(PO_2 \approx 1 \text{ atm}) = 10^{-3} \, n_1(PO_2 \approx 10^{-12} \text{ atm})$$

$$===> \quad \Delta E_f \approx 2.3kT\log(10^3) \approx 1 \text{ eV at } T = 1673° \text{ K}$$

Since the thermal bandgap in YAG is ≈ 6 eV,[4,31] this implies that at 1400° C, $PO_2 \approx 10^{-12}$ atm, the Fermi level $E_f \geq (E_g/2) + 1\text{eV} \approx 4$ eV above the oxygen 2p valence band. Similarly, an anneal in Ar gas with $PO_2 \approx 10^{-4}$ atm shifts the Fermi level upward by $\approx 1/3$ eV relative to an oxygen anneal, so after such an anneal, $E_f \geq 3.3$ eV above the oxygen 2p valence band. From Figure 5.9, we see that the charge transfer peak from oxygen 2p to Fe^{+3} disappears after an anneal at 1400°C, $PO_2 \approx 10^{-12}$ atm. However, a significant amount of this peak is still present after a 1400°C anneal in Ar gas, with $PO_2 \approx 10^{-4}$ atm. This suggests that

the Fe^{+2} level is significantly higher than 3.3 eV above the oxygen 2p valence band, and is consistent with our earlier assignment of $\approx$5 eV above the valence band to explain our measured n-type activation energies. This analysis also allows us to comment on the location of the $V_o^{\bullet\bullet}$ level. Our model requires that the $V_o^{\bullet\bullet}$ level be above the Fe^{+2} level. This suggests that the $V_o^{\bullet\bullet}$ level is greater than 5 eV above the oxygen 2p valence band. From Figure 5.10, we see that peaks associated with the 4f electronic transitions of Nd^{+3} are unchanged by both oxidizing and reducing anneals. This suggests that the Nd^{+2} level is significantly higher than 4 eV above the valence band, and may even be in the conduction band.

This analysis also allows us to comment on the 310 nm peak observed in our samples after a reducing anneal. Mori,[54] Masumoto,[53] and Akhmadullin[52] assign this peak to charge transfer from Fe^{+2} to the conduction band as seen in Figure 5.13.[52] We disagree with this assignment. Our electrical and optical measurements suggest that the ground state of the Fe^{+2} level is at most probably 1-2 eV below the conduction band, and not 4-5 eV as suggested by these investigators: 313 nm ==> 4 eV, 258 nm ==> 5 eV. We propose that the 310 nm band is more likely a charge transfer process between Fe^{+3} and Fe^{+2}. As the crystal is reduced, Fe^{+2} ions are produced, and Fe^{+3} to Fe^{+2} charge transfer then becomes a viable process. In yttrium iron garnets, such charge transfer processes can only occur for $\lambda < \approx$370 nm, as no evidence for their presence has been observed for λ>370 nm,[90] so our 310 nm band is consistent with this condition. Our explanation however requires that the Fe ions are
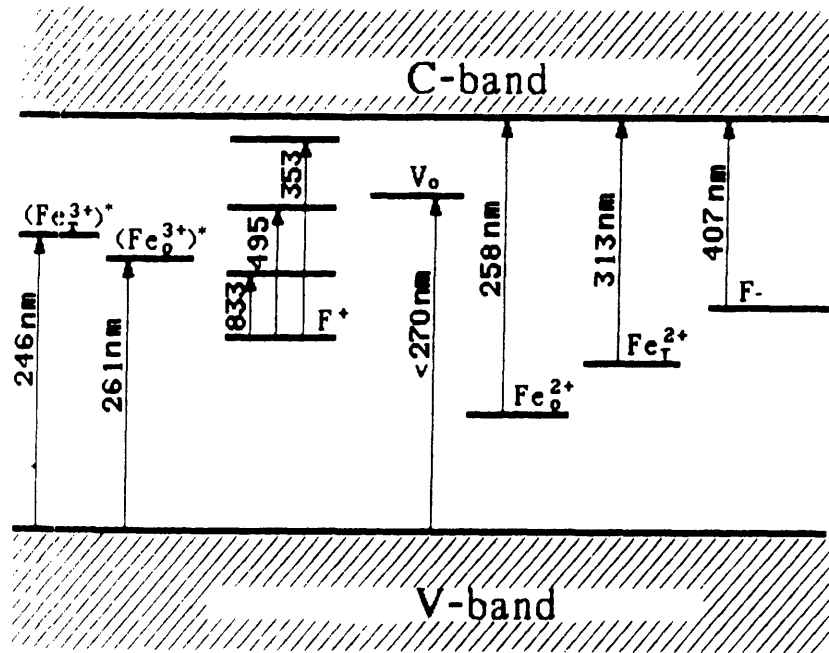
Figure 5.13 Proposed energy band diagram for Fe impurities in YAG with assignments for the 250 and 313 nm absorption.[52]

164

paired, as charge transfer processes are extremely unlikely between atoms more than two interatomic distances apart, and the concentration of Fe in our samples is small. Such pairing of Fe impurity ions have been observed in sapphire.[91] Thus by quantitatively correlating the electrical and optical properties, we have been able to gain a much deeper insight into the position of the Fe^{+2} impurity level in the YAG bandgap, as well as the relative position of the $V_o^{\bullet\bullet}$ and Nd^{+2} levels.

5.4: Conclusion:

Electrical conductivity isotherms of YAG and Nd:YAG exhibit n-type like behavior that is consistent with a defect structure controlled by background acceptors and compensated by oxygen vacancies. Derived activation energies are ≈2.9 eV for the n-type electronic branch, and ≈2.4 eV for the PO_2 independent ionic branch. Fe impurities were found to play a significant role in the redox reaction of both crystals. Fe impurities were also found to play a role in the optical properties, inducing an absorption band at 250 nm assigned to charge transfer from oxygen 2p to Fe^{+3}, and a band at 310 nm assigned to charge transfer between Fe^{+3} and Fe^{+2}. Quantitative correlations of the electrical and optical properties suggest that the Fe^{+2} level is 5 eV above the oxygen 2p valence band, the $V_o^{\bullet\bullet}$ level is higher than 5 eV above the valence band, and the Nd^{+2} level is much higher than 5 eV above the valence band.

CHAPTER 6: EXPERIMENTAL MEASUREMENTS OF Ti:YAG

6.1: Introduction:

Electrical and optical measurements were performed on the Ti:YAG crystals next. As described earlier, Ti is the simplest of the transition metal dopants to study in YAG with this technique, since Ti^{+3} has only one d-electron, and Ti^{+4} has no d-electrons, greatly simplifying the optical analysis. Furthermore, we were interested in the defect structure of donor doped YAG, and the ability of Ti to have a +4 valence makes Ti:YAG a potential system to study a donor controlled defect structure.

High temperature anneals of the Ti:YAG fibers at all $PO_2 > 10^{-12}$ atm and $T \approx 1400°C$ resulted in precipitation of $Y_2Ti_2O_7$, similar to the precipitates observed when the fibers were grown under oxidizing conditions. The density of the precipitates increased dramatically with increasing Ti doping concentration and increasing PO_2, so that precipitates in the $Y_3(Al_{0.9}Ti_{0.1})_5O_{12}$ fiber after an O_2 anneal changed the fiber appearance from a transparent single crystal to an opaque polycrystalline ceramic. Only at 1550°C and $PO_2 = 8 \times 10^{-14}$ atm were we able to suppress the bulk precipitation in $Y_3(Al_{0.9}Ti_{0.1})_5O_{12}$. Even then, precipitates of $Y_2Ti_2O_7$ still occurred at the surface. This precipitation reaction presented a major problem. High temperature electrical measurements become extremely difficult for $T \geq 1500°C$. Above this temperature, surface and gas conduction contribute significantly to the total conduction.[92] As we were not set up to handle these type of measurements, and as precipitation would probably still occur under oxidizing conditions even at these temperatures, we decided to complete the bulk of our electrical and optical measurements on the Ti:YAG crystal grown by the Czochralski method. This crystal had a much lower Ti concentration, and precipitate densities did not exceed 1.4 volume percent (v/o),

even for anneals that lasted three months. From this precipitation density and the composition of the precipitates, we estimated that the Ti concentration in the bulk of the samples decreased by $\approx 10\%$ because of the $Y_2Ti_2O_7$ precipitation.

6.2: Results:

6.2.1: Electrical:

The conductivity isotherms of Ti:YAG are shown in Figure 6.1. The isotherms appear n-type at the more reducing PO_2's, with a slope of $\approx -1/4$, and begin to flatten out at the more oxidizing PO_2's. This isotherm is well fitted by an equation assuming a PO_2 independent part and a PO_2 dependent part with a slope of -1/4. Separating these components, we can de-convolute the isotherm as seen in Figure 6.2. Activation energies for these two parts can then be calculated as seen in Figure 6.3, with 4.7 eV for the n-type PO_2 dependent part, and 3.2 eV for the PO_2 independent part.

6.2.2: Optical

The optical spectra of the as-grown Ti:YAG is shown in Figure 6.4, overlapped with the spectra of an undoped YAG for comparison. Similar to spectra obtained by other investigators,[6,40] our as-grown Ti:YAG has a band edge at ≈ 300 nm compared with 200 nm for undoped YAG, and now has three peaks in the visible at ≈ 400, 500, & 600 nm. As described earlier, the source of the absorption in the UV and at 400 nm is unknown, whereas the peaks at 500 and 600 nm have been assigned to transitions between the crystal field states $T_{2g} \rightarrow E_g$ of Ti^{+3} ions in an octahedral site[40,60,66,71]. The two peaks result from Jahn-Teller splitting of the excited E_g state.

The spectra of oxidized (PO_2=1 atm) and reduced (PO_2=2.7x10^{-13} atm)
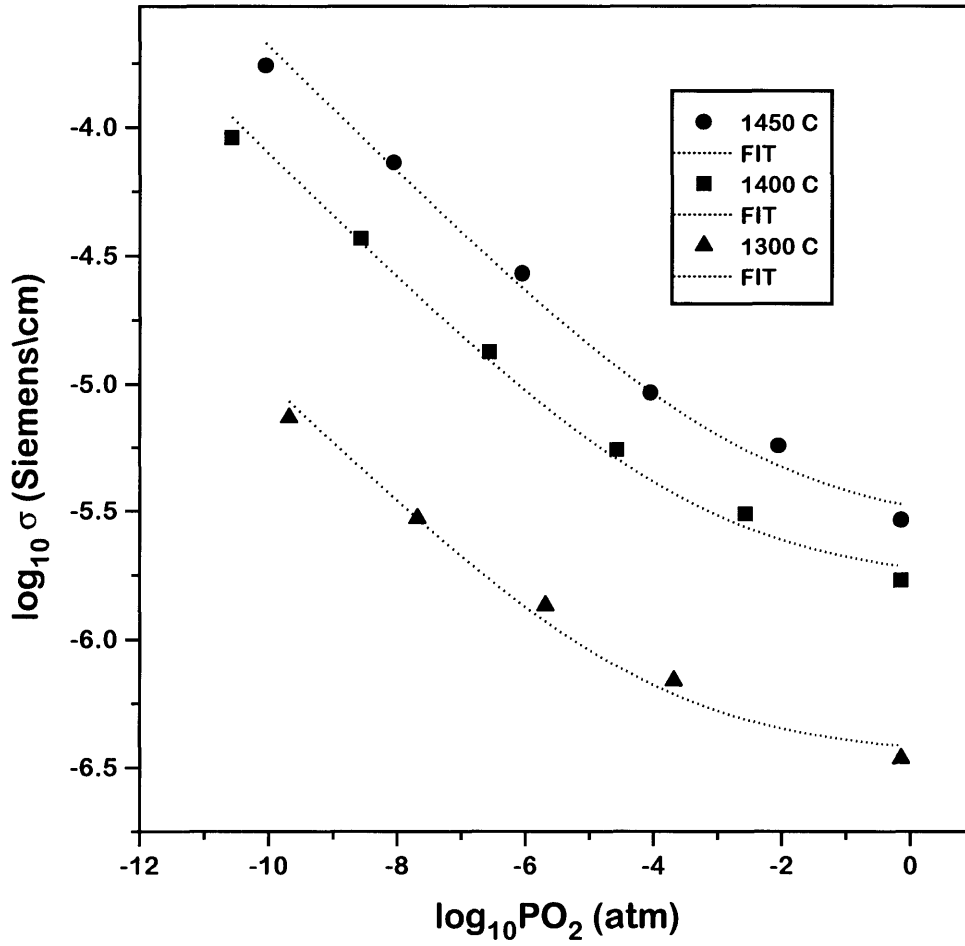
Figure 6.1 Ti:YAG conductivity isotherms fitted by an equation assuming a PO_2 independent part and a PO_2 dependent part that varies as $PO_2^{-1/4}$.
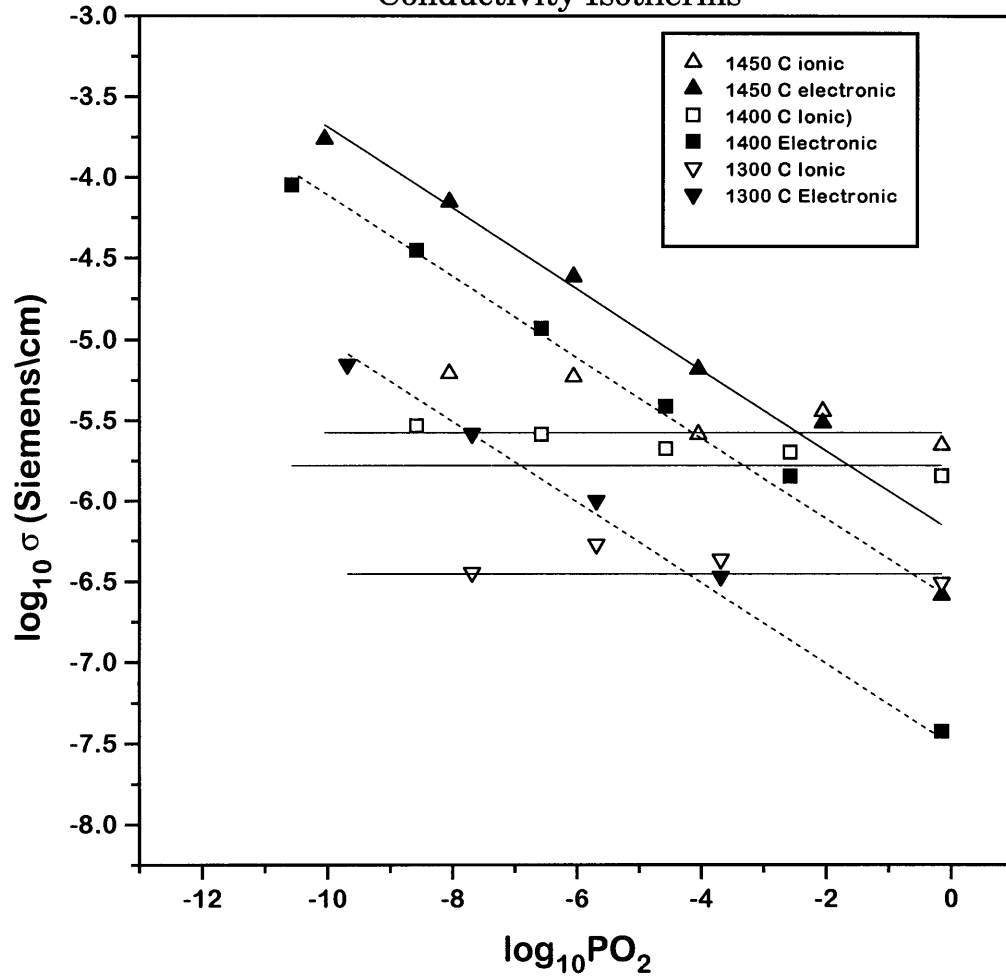
Figure 6.2 Component analysis of the Ti:YAG conductivity isotherms.
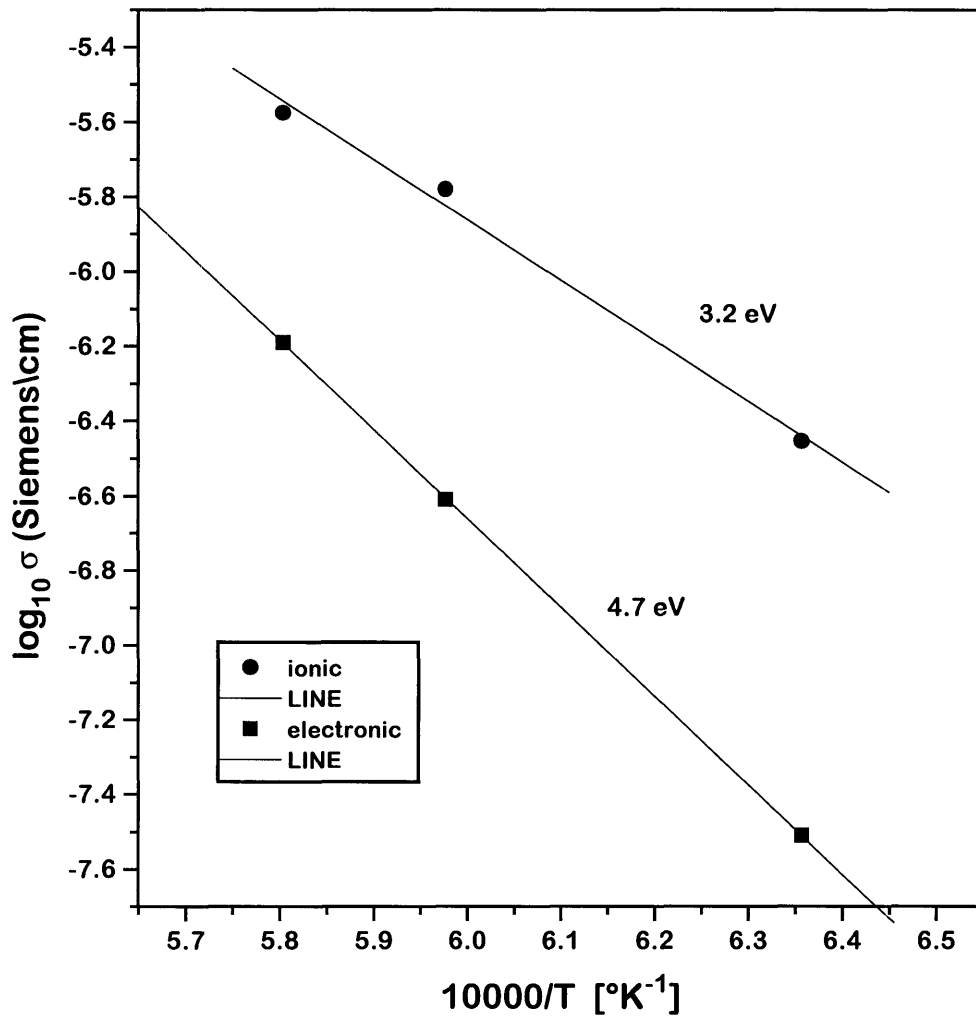
Figure 6.3 Activation energy of the Ti:YAG conductivity components.
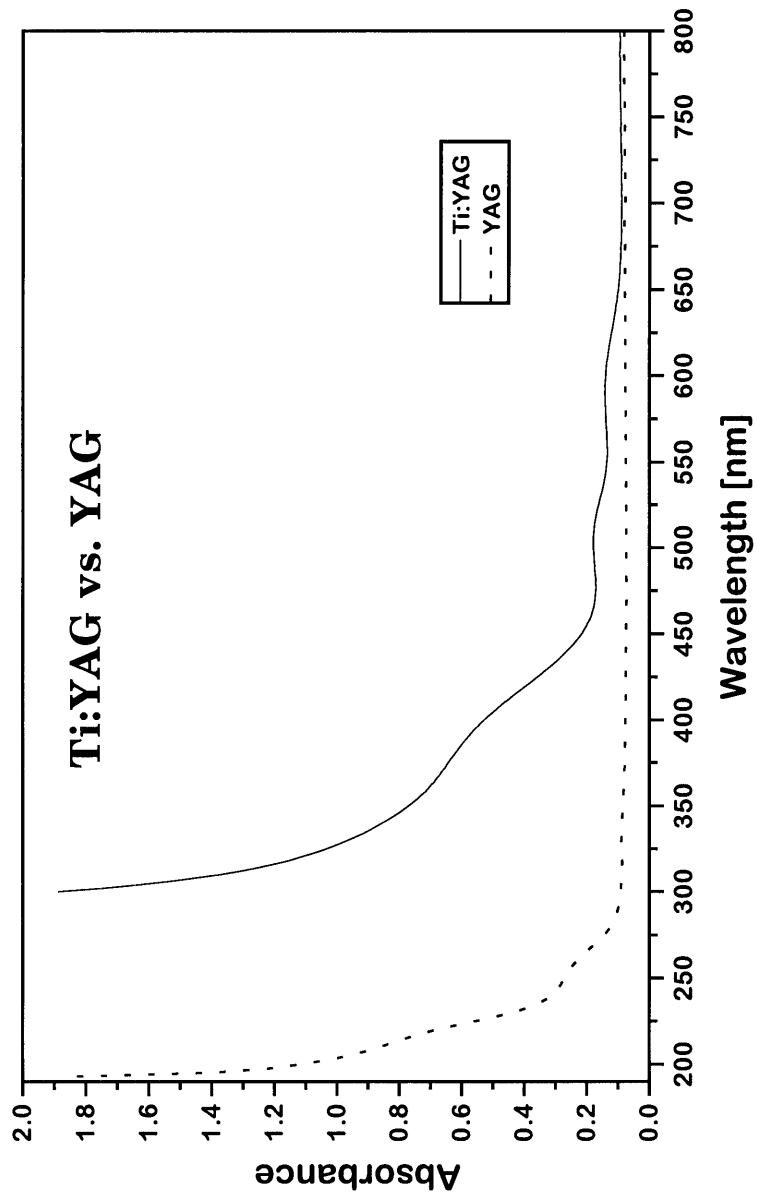
Figure 6.4 Absorption spectrum of as-grown Ti:YAG.

Ti:YAG is shown in Figure 6.5. As clearly evident, the 400, 500, and 600 nm peaks disappear with an O_2 anneal, and re-appear with a reducing anneal. Clearly we are able to change the Ti valence from +3 to +4 with an oxidizing anneal, and reverse it with a reducing anneal, as was observed by Karpov.[6] The effective band edge at 300 nm does not seem to be much affected by these anneals, as shown in Figure 6.6. However, a more reducing anneal in H_2 with an effective PO_2 of $\approx 10^{-20}$ atm dramatically reduced the UV absorption as seen in Figure 6.7. An oxidizing anneal brings the UV absorption back, as well as removing the 400, 500, and 600 nm peaks as before. When the UV band is pumped after an oxidizing anneal, a fluorescence is observed as shown in Figure 6.8. The excitation spectrum for this fluorescence is seen in Figure 6.9. As seen in Figure 6.9, there appears to be an excitation peak at $\approx$ 270 nm.

6.3: Discussion:

A conductivity isotherm as shown in Figure 6.1 can arise from both a donor dominated defect structure (regime "c" of Figure 2.7), or an acceptor dominated defect structure (regime "b" of Figure 2.6), as discussed in Section 2.2. Fortunately, our ability to change the Ti valence as evidenced by the optical measurements allows us to distinguish between these two cases as shown below.

For both the donor dominated and the acceptor dominated case, the ionic defects are constant over regimes "c" and "b" respectively, these defects being fixed by a constant acceptor and donor concentration. The n-type -1/4 power law in both cases is due to the increasing concentration of electrons in the conduction band as the crystal is reduced. As seen in Figure 6.5, anneals under the highest and lowest PO_2 of the 1400°C conductivity isotherm induce dramatic changes in the concentration of Ti^{+3}, as witnessed by the change in area of the

Ti:YAG
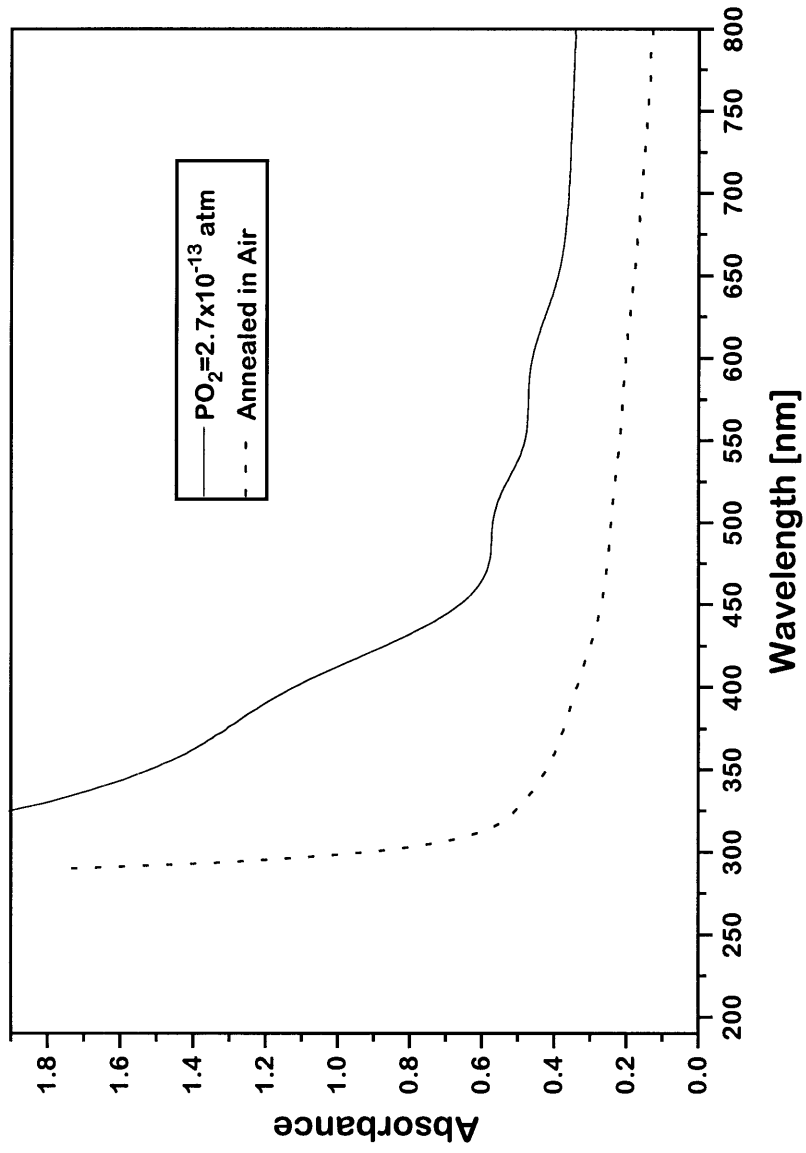
Figure 6.5 Absorption spectra of oxidized and reduced Ti:YAG.

TIYAG AS RECEIVED

CO/CO2,N2   TIYAG23
N2   TIYAG17
AS RECEIVED   TIYAG16
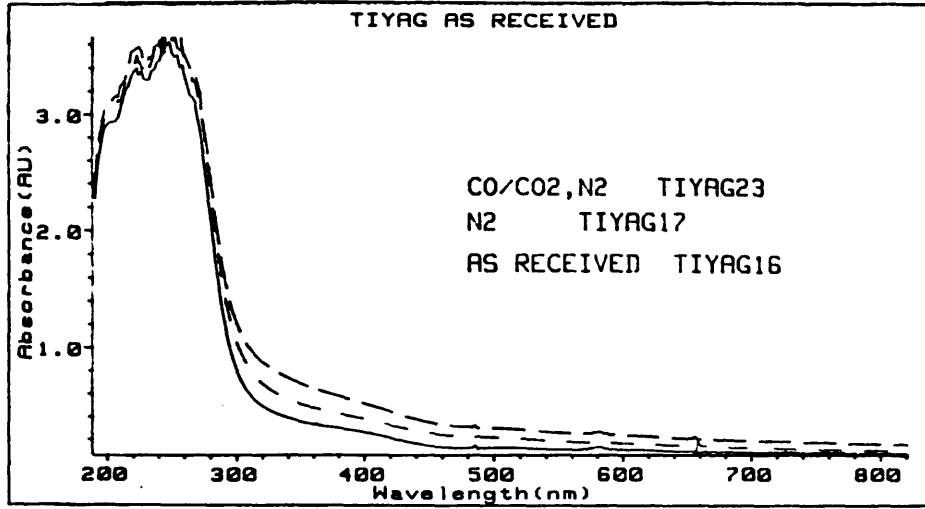
Figure 6.6   Absorption spectra of oxidized and reduced Ti:YAG.
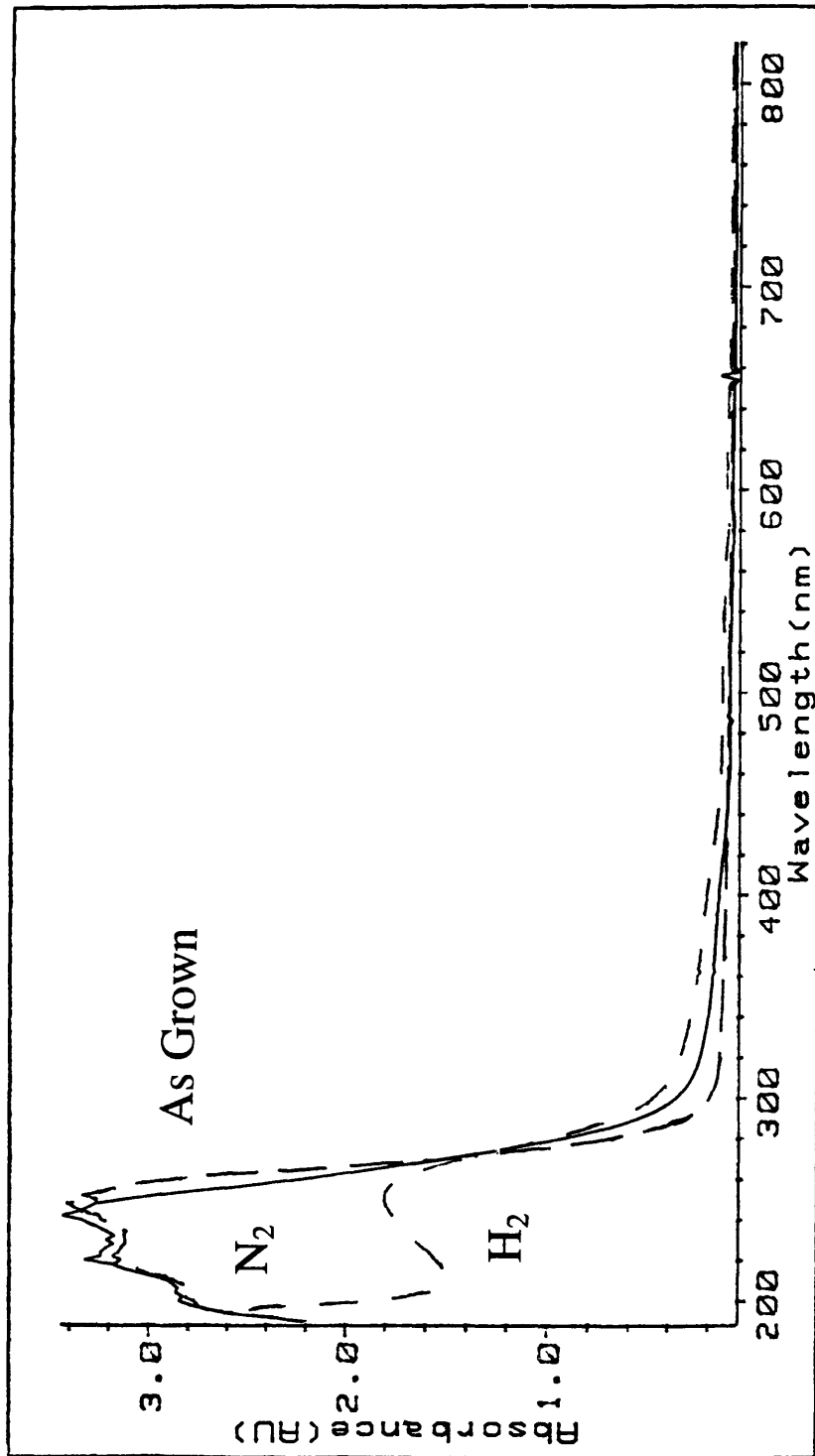
Figure 6.7 Absorption spectra of oxidized and reduced Ti:YAG.

175
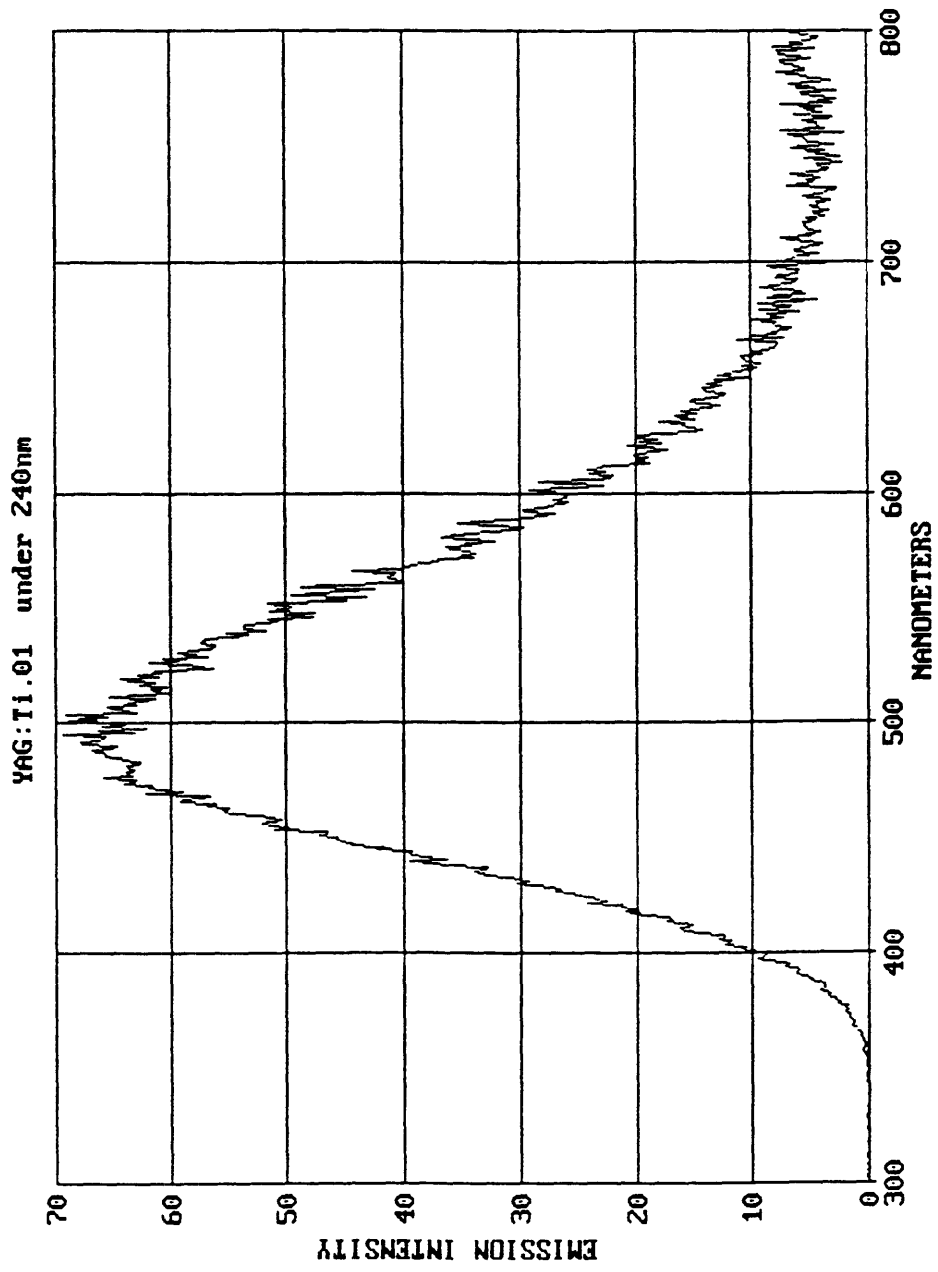
Figure 6.8 Flourescence spectrum of Ti:YAG when pumped between 200-300 nm.

176
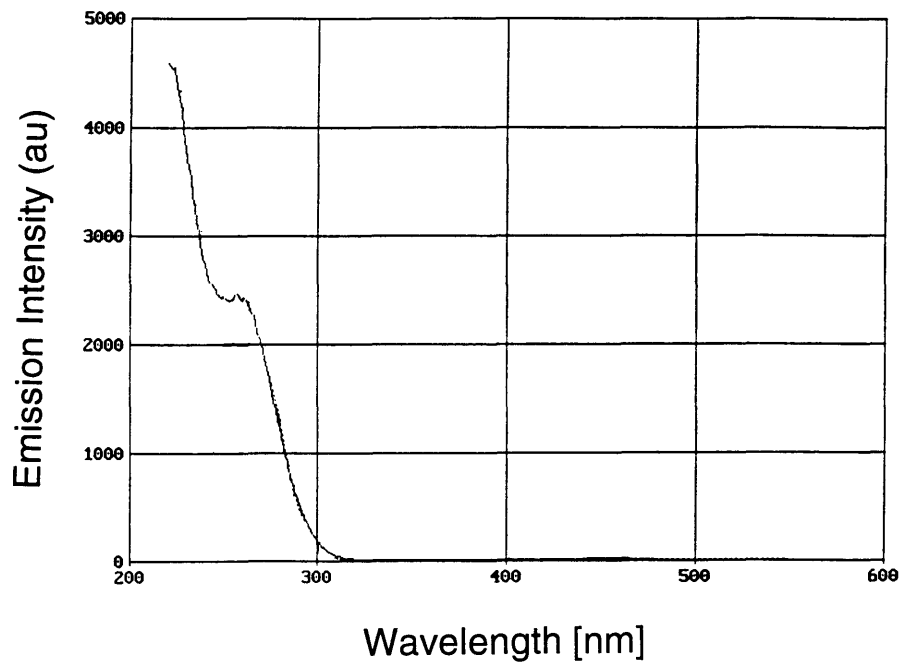
Figure 6.9   Excitation spectrum for the 500 nm emission in Ti:YAG.

500 and 600 nm peaks. We find that these peak areas grow to a limiting maximum with reducing anneals, so that by the lowest PO_2 of our isotherms, the peak areas have essentially saturated. This suggest that most of the Ti is present as Ti^{+3} after such an anneal. After an O_2 anneal, these same peak areas are roughly one tenth of the areas after the lowest PO_2 anneal. This implies that most of the Ti is now Ti^{+4}, and that the donor concentration, $[Ti^{+4}]$ has changed by roughly an order of magnitude over the PO_2 range of our conductivity measurement. This clearly rules out the fixed valence donor dominated defect model, and suggests that the appropriate defect model is the fixed valence acceptor dominated defect model, where the concentration of background acceptors is much greater than the concentration of Ti, so that the valence changes of Ti have a negligible effect on the defect structure. Another relevant defect model to consider is the variable valence donor dominated defect model, as seen in Figure 2.8. However such a model cannot yield a n-type branch with a -1/4 power law dependence over a PO_2 range where the donor concentration is changing by a factor of ≈ 10. Thus the most appropriate model is an acceptor dominated defect model as shown in Figure 2.6, where our conductivity isotherm lies to the reducing half of regime "b".

Our value of the ionic activation energy at 3.2 eV is slightly higher than those measured by other investigators, as seen in Table 3.4. However, this difference is small compared to the range of values listed in Table 3.4, which range from 2.2 to 3.0 eV. Thus our value may be considered comparable to those measured before. Our activation energy for the n branch at 4.7 eV however, is larger than those measured by other investigators, which are typically ≈ 3.9 eV, as seen in Table 3.3. It may be that Ti ions are providing trapping states for these electrons, and restricting their mobility. At a Ti concentration of 560 ppm, this would correspond to a trap every 3.5 nm if the Ti

ions were uniformly distributed. Some evidence for this reduction in electron mobility can be seen by comparing Rotman's conductivity isotherm for Ce:YAG in Figure 2.13[31] and our conductivity isotherm for Ti:YAG in Figure 6.1. At 1300°C, the minimum in Rotman's conductivity isotherm occurs at $PO_2 \approx 10^{-6}$ atm$\equiv PO_{2,s}$, while in ours, the minimum is at $PO_2 \geq 1$ atm $\equiv PO_{2,s}$. For the sake of comparison, let us assume that our minimum occurs at $PO_2 = 1$ atm. As we described in section 5.3, this minimum is related to the point where n=p in Figure 2.6, and the Fermi level is at midgap. Consequently the concentration of n and p at this point is a function of temperature only, and is equal to the concentration of intrinsic electronic defects at that temperature, n_o (i.e. $n=p=n_o$). Thus at the minimum of the 1300°C conductivity isotherms, both Rotman's Ce:YAG sample and our Ti:YAG sample have the same concentration of electrons, $n=n_o$. For $PO_2 < PO_{2,s}$, the electron concentration will increase as $PO_2^{-1/4}$ as seen in regime (b) of Figure 2.6 & Table 2.2. This implies that at $PO_2 \approx 10^{-6}$ atm, our electron concentration will be one and a half orders of magnitude or ≈ 32 times larger than n_o, and 32 times larger than Rotman's electron concentration. If we compare the de-convoluted isotherms in Figure 2.14 and Figure 6.2, we see that our electronic conductivity is only 4 times higher than Rotman's electronic conductivity at 1300°C for a given PO_2. A reduction in electron mobility for our Ti:YAG samples relative to Rotman's Ce:YAG samples might explain some of this difference.

Let us now focus on the optical properties. The dramatic reduction of the UV absorption at 300 nm with a reducing anneal as seen in Figure 6.7 strongly supports charge transfer from the oxygen 2p band to Ti^{+4} as the source of this absorption. Similar absorption and assignments have been made for Ti:sapphire,[63,65] Ti:MgAl$_2$O$_4$,[42] and Ti-activated stannates and zirconates,[69] as mentioned in the literature review. This assignment is also consistent with the

energy diagram of Figure 3.25 in Section 3.2.3.2. The fluorescence peak observed when this band is pumped is analogous to the fluorescence peak observed for these other Ti doped systems when pumped in the UV, and further supports this assignment.[42,67-69] This fluorescence center has been ascribed to a Ti^{+4} octahedron as described earlier.[42,69] Karpov's work on the polarization dependence of this fluorescence revealed that this fluorescence originates from the *edges* of the octahedral and tetrahedral sites in YAG, and not their centers, further supporting the notion of a charge transfer process responsible for the UV absorption and subsequent fluorescence.[73] In fact, the 270 nm peak in the excitation spectrum of Figure 6.9 suggests that the generalized Ti^{+3} level is ≈ 4.6 eV above the oxygen 2p band, specifying the position of the generalized Ti^{+3} level in the YAG energy diagram of Figure 3.25 in Section 3.2.3.2. This energy is within the range suggested earlier from the literature review,[66] and is comparable to the position of the Ti^{+3} level in Ti:sapphire at 5 eV above the oxygen 2p band.[63,65]

Let us now consider the optical properties of Ti:YAG in the visible range. As discussed in the literature review, Bantien,[40] Albers,[71,93] and Yamaga[60] have assigned the 500 and 600 nm peaks to the crystal field transitions of the Ti^{+3} ion in an octahedral site. Similar transitions have been observed in a number of Ti doped systems, and the magnitude of the crystal field splitting is comparable to those measured for other ions in the octahedral site of YAG. For example, 10Dq for Cr^{+3} is ≈ 2.0 eV[76] while a fit to the 500 and 600 nm peaks of Ti:YAG yield 10Dq$\approx$2.3 eV.[60] Furthermore, the magnitude of the molar extinction coefficient and oscillator strengths for these two peaks are in the range of those expected for forbidden d-d transitions, as shown below:[18,41,42,61]

From Table 4.2, we know that the Ti concentration is 560 ppm by weight. This concentration translates into a molar concentration of 5.32×10^{-2} moles

of Ti/liter. The 500 and 600 nm peaks of the as-grown crystal in Figure 6.4 have absorbances of 0.024 and 0.023, and half widths Δv of 1.5×10^3 cm^{-1} and 1.6×10^3cm^{-1} respectively, after removal of the background. Our crystal is 0.6 cm thick, so the molar extinction coefficients are:[10,11]

$$\varepsilon_{max} = \frac{A_{max}}{cl}$$

A = Absorbance

c = Concentration [moles / liter]

l = thickness [cm]

= 0.75 for the 500 nm peak

= 0.72 for the 600 nm peak

The resulting oscillator strengths are:

$$f = 4.32 \times 10^{-9} \int \varepsilon \, dv \approx 4.6 \times 10^{-9} \varepsilon_{max} \Delta v$$

= 5.2×10^{-6} for the 500 nm peak

= 5.3×10^{-6} for the 600 nm peak

These values are in the range of oscillator strengths expected for d-d transitions in an octahedral site containing a center of inversion.[10,11] They represent a lower limit since not all of the Ti is in the +3 valence for the as-grown crystal. An anneal in log $PO_2 \approx$ -12.57 at 1400°C actually increased the oscillator strength of the 500 nm peak by 14% with respect to the as-grown crystal.

The presence of the 400 nm peak presents a problem with this interpretation of the 500 and 600 nm peaks. As we discussed in the literature review, no assignments have been proposed for this peak, although many investigators have noted its existence.[6,40] Furthermore, the ratios of the absorbance for the 400, 500, and 600 nm peaks were found to remain constant after various oxidizing and reducing anneals, collaborating Karpov's results for crystals grown under different conditions.[6] This suggests that the 400 nm peak

is also associated with d-d transitions of the Ti^{+3} ion. I propose that this absorption as well as the absorption of the 500 and 600 nm peaks are primarily due to Ti^{+3} in the 8-fold *dodecahedral* site. I base this proposal on two key observations. First, three peaks for Ti^{+3} in an octahedral site can only occur for a tetragonally distorted octahedral site.[11] To account for these three peaks in Ti:YAG at 400, 500, and 600 nm, the distortion would have to be severe, as illustrated in Figure 6.10,[3] so that the T_{2g} ground state is now split by ≈ 2.1 eV to explain the 600 nm absorption. A distortion of this magnitude is unlikely, and has not been observed in the spectra of other dopants believed to enter the octahedral site in YAG, such as Cr:YAG.[76] Furthermore, structural refinement studies of YAG have not revealed any distortion of this magnitude for the octahedral site.[27,33] Second, three peaks with these same approximate positions have been observed in another transitional metal dopant with only 1-d electron, Zr^{+3}:YAG as discussed in section 3.2.4.[5] Electron spin resonance (esr) has confirmed that Zr^{+3} enters the dodecahedral sites, and correlations between these optical peaks and the esr signal suggest that d-d transitions of Zr^{+3} in the dodecahedral site are responsible for these peaks. As discussed in section 2.4, Ti^{+3} should prefer the octahedral sites. However, since the dodecahedral site has no center of inversion, d-d transitions would be ≈ 100 times stronger in this site, so even if only a fraction of the Ti^{+3} were to enter the dodecahedral sites, the signal from these optical transitions would swamp out those from Ti^{+3} in octahedral sites. There is also evidence for three peaks in other Ti:garnets, such as Ti:GSAG as seen in Figure 6.11. The oscillator strength of these three peaks are comparable to those calculated for the Ti:YAG peaks above.

It may be possible though given the breadth of the peaks at 400, 500, and 600 nm, that some of the signal may be due to Ti^{+3} on octahedral sites. As stated earlier, crystal field splitting of Ti^{+3} levels in an octahedral site would yield
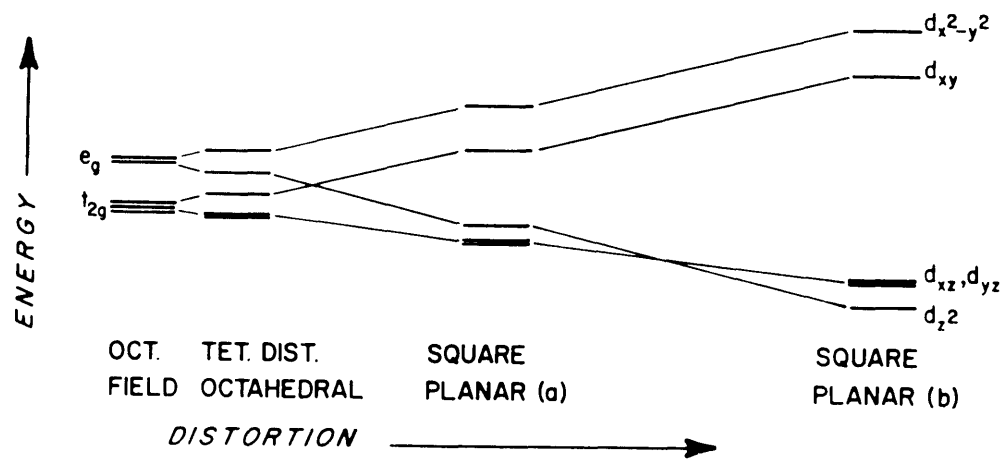
Figure 6.10   Splitting of the five d-orbitals with a tetrahedral distortion from an octahedral symmetry.[3]

absorption peaks in the same vicinity. This is in contrast to crystal field splitting of Ti^{+3} levels in a tetrahedral site. Unlike crystal field strengths of dodecahedral and octahedral sites which are about the same magnitude $((8/9)\Delta_{octahedral}=\Delta_{dodecahedral})$, the crystal field strength of the tetrahedral site is roughly one half that of the octahedral site, $(4/9)\Delta_{octahedral}=\Delta_{tetrahedral}$.[3] Consequently, all crystal field transitions of Ti in a tetrahedral site should be in the NIR. It should be mentioned that we did attempt to look for peaks in the NIR. However, optical measurements of very thick crystals, as well as the heavily doped Ti:YAG single crystal fibers revealed no peaks. Such peaks may still be present, but just too weak to see.

It is interesting to note that Ti has been found in 8-fold coordination in Ti doped ZrO_2 as well as disorderd pyrochlores with the flourite structure.[94] Examples of these disordered pyrochlores include $Gd_2(Zr_{0.3}Ti_{0.7})_2O_7$ and $Y_2(Zr_{0.3}Ti_{0.7})_2O_7$.[29,95] In the case of $Gd_2(Zr_{0.3}Ti_{0.7})_2O_7$, the bandgap is 4.1 eV.[29] This suggests that the Ti^{+3} level in 8-fold coordination is $\approx$ 4 eV above the oxygen 2p valence band. In contrast, Ti in 6-fold coordination as in rutile and $Ba_{0.03}Sr_{0.97}TiO_3$ have bandgaps of 3.1.[96,97] This suggests that the Ti^{+3} level in 6-fold coordination is typically $\approx$ 3 eV above the oxygen 2p valence band. Thus the Ti^{+3} level in octahedral sites seem to be at a lower energy than the Ti^{+3} level in dodecahedral sites, typically around 0.5-1.0 eV difference. For the three defect models relevant to this system: the fixed valence acceptor controlled (See Figure 2.6), the fixed valence donor controlled (See Figure 2.7), and the variable valence donor controlled defect model (See Figure 2.8), a n-type isotherm as we observed in Figure 6.1 can only occur when n>p, i.e. the Fermi Level is above midgap throughout the conductivity measurements and increases as the PO_2 of the anneal decreases. For a thermal bandgap of 6 eV in YAG,[4,31] this means that if the Ti^{+3} level for octahedral sites is indeed at

Ti:GSAG
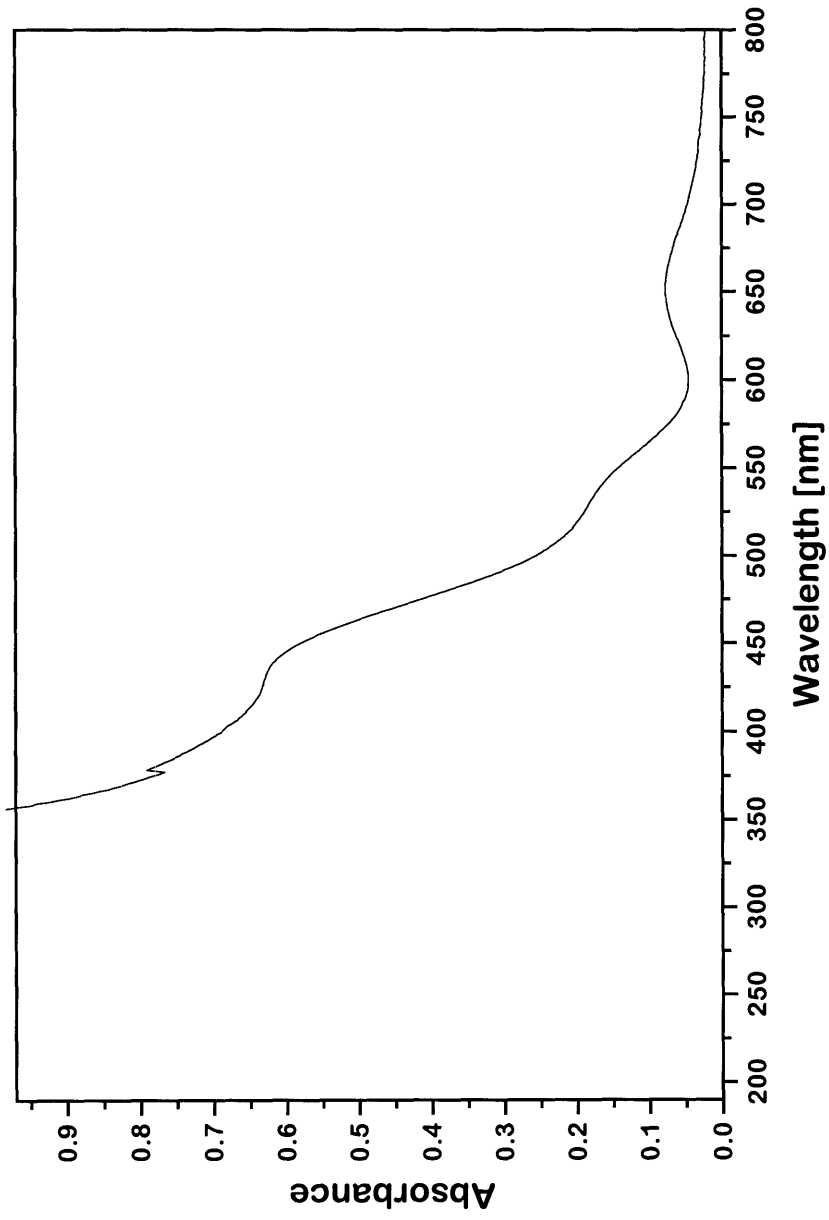
Figure 6.11 Absorption spectrum of Ti:GSAG.

3 eV above the oxygen 2p level as suggested above, then the majority of these ions will remain +3 throughout the PO_2 range of our conductivity measurements. Since most of the Ti is on octahedral sites as mentioned in section 2.4, this means that most of the Ti is essentially isovalent with the host throughout our conductivity measurements, and the only potential Ti donors are the small fraction of Ti ions sitting on the dodecahedral sites, the same ions we are detecting with our optical measurements. This explains why the Ti:YAG crystal with a Ti concentration of 560 ppm by weight has a defect structure controlled by inadvertent background acceptors, as found in chapter 5 for YAG and Nd:YAG. The majority of the Ti ions are deep level donors, whose levels are so deep that they don't affect the defect structure for the range of temperatures and PO_2 measured. Thus although we are measuring only a fraction of the Ti ions with our optical measurements, we are in fact measuring the Ti ions that directly affect the defect structure, and all the previous analysis we did earlier remains valid. Furthermore, we have now demonstrated that it is important to utilize shallow donors if one intends to study donor controlled defect structures.

We conclude this section by quantitatively correlating the electrical and optical measurements, and demonstrating the complementary power of these measurements. Incorporating Ti into the acceptor dominated defect model derived in section 2.6 allows us to quantitatively predict the PO_2 dependence of the Ti^{+3} concentration as shown below:

For an acceptor dominated defect structure, the Brouwer approximation for the regime of interest is $2[V_o^{\bullet\bullet}]=[A']$ where $[A']$ is the concentration of background acceptors and is constant. The relevant defect reactions are:

$$\varnothing \rightarrow e' + h^{\bullet} \qquad\qquad K_e = np$$

$$O_o \rightarrow V_o^{\bullet\bullet} + 2e' + \frac{1}{2}O_2 \qquad\qquad K_r = [V_o^{\bullet\bullet}]n^2 PO_2^{1/2}$$

$$\text{with } [V_o^{\bullet\bullet}] = \frac{[A']}{2} = \text{constant} \equiv C, \qquad K_r = Cn^2 PO_2^{1/2}$$

$$\Longrightarrow \quad n = \frac{K_r^{1/2}}{C^{1/2}PO_2^{1/4}}$$

Ti doping adds the additional equations of:

$$Ti^x_Y \rightarrow Ti^{\bullet}_Y + e' \qquad\qquad K_i = \frac{[Ti^{\bullet}_Y]n}{[Ti^x_Y]}$$

$$[Ti^{\bullet}_Y] + [Ti^x_Y] = [Ti_Y]_{total}$$

$$\Longrightarrow \quad K_i = \frac{[Ti^{\bullet}_Y]K_r^{1/2}}{[Ti^x_Y]C^{1/2}PO_2^{1/4}} = \frac{\{[Ti_Y]_{total} - [Ti^x_Y]\}K_r^{1/2}}{[Ti^x_Y]C^{1/2}PO_2^{1/4}}$$

$$\therefore \quad \frac{1}{4}\log PO_2 = \log\left\{\frac{[Ti_Y]_{total} - [Ti^x_Y]}{[Ti^x_Y]}\right\} + \log\left\{\frac{K_r^{1/2}}{K_i C^{1/2}}\right\}$$

$$\Longrightarrow \quad \log PO_2 = 4\log\left\{\frac{[Ti_Y]_{total} - [Ti^x_Y]}{[Ti^x_Y]}\right\} + \text{constant} \qquad\qquad 6(a)$$

at a given temperature, where Ti_Y refers now only to Ti on dodecahedral sites. Since the 400, 500, and 600 nm peaks are a measure of $[Ti_Y^x]$, a plot of the log of the area under these peaks vs. log PO_2 should follow the schematic curve shown in Figure 6.12. To test this prediction, two crystals 6 mm and 12 mm thick were measured after successive equilibration anneals at 1400°C in log PO_2's of -12.6, -8.6, -4.6, -2.6, and -0.70. After each equilibration anneal, the samples were quenched from high temperature as described in the

Section 4.4. The areas under the 400, 500, and 600 nm peaks were measured, and the integrity of the Gaussian peak fit tested by checking that the area of the 12 mm crystal was two times that of the 6 mm crystal. For all the measurements, the integrity of the gaussian peak fit was verified. The resulting 400, 500, and 600 nm peaks for the 12 mm crystal are shown in Figure 6.13. The peak areas versus PO_2 are shown in Figure 6.14, fitted by equation 6(a). As seen in Figure 6.14, the fit is reasonably good. We observed that at low PO_2's, equilibration was difficult to achieve, supporting Haneda's observation that the oxygen exchange rate for *reduced* YAG was significantly dependent upon the exchange reaction at the sample surface, in addition to the normal oxygen diffusion rate.[84] Thus we have more confidence that the data points taken under oxidizing conditions were equilibrated. If we focus on these points, we see that the defect model predicts a -1/4 power law dependence as shown below: Under oxidizing conditions where almost all of the Ti is in the +4 valence state, we would expect:

$$K_i = \frac{[Ti^{\bullet}_Y]n}{[Ti^x_Y]} = \frac{[Ti_Y]_{total} K_r^{1/2}}{[Ti^x_Y]C^{1/2}PO_2^{1/4}}$$

$$==> \quad [Ti^x_Y] = \frac{[Ti_Y]_{total} K_r^{1/2}}{K_i C^{1/2}PO_2^{1/4}} \quad \propto \quad PO_2^{-1/4} \qquad \qquad 6(b)$$

A plot of the peak areas vs. PO_2 is shown in Figure 6.15 for the oxidizing anneals. As evident, all three peaks follow the -1/4 power law, verifying the prediction of the defect model, and supporting our conclusion that the Ti:YAG crystals are acceptor controlled, despite a Ti doping level of 560 ppm by weight as seen in Table 4.2.

Furthermore, detailed quantitative correlations between the electrical and optical properties allows us to estimate the position of the Ti^{+3} level in the YAG bandgap for Ti ions in the dodecahedral site, as was done earlier for the Fe^{+2}
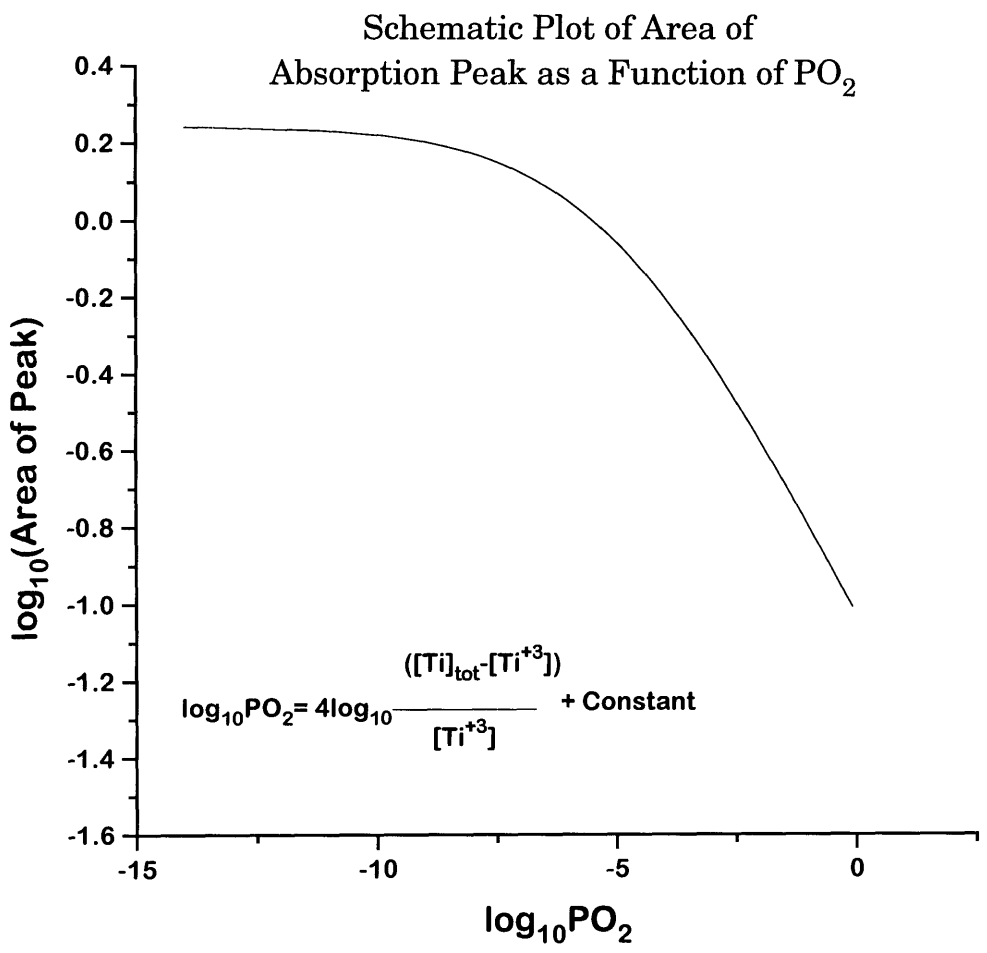
Figure 6.12 Schematic absorption of area of absorption peak of Ti^{+3} as a function of PO_2, after equation 6(a).
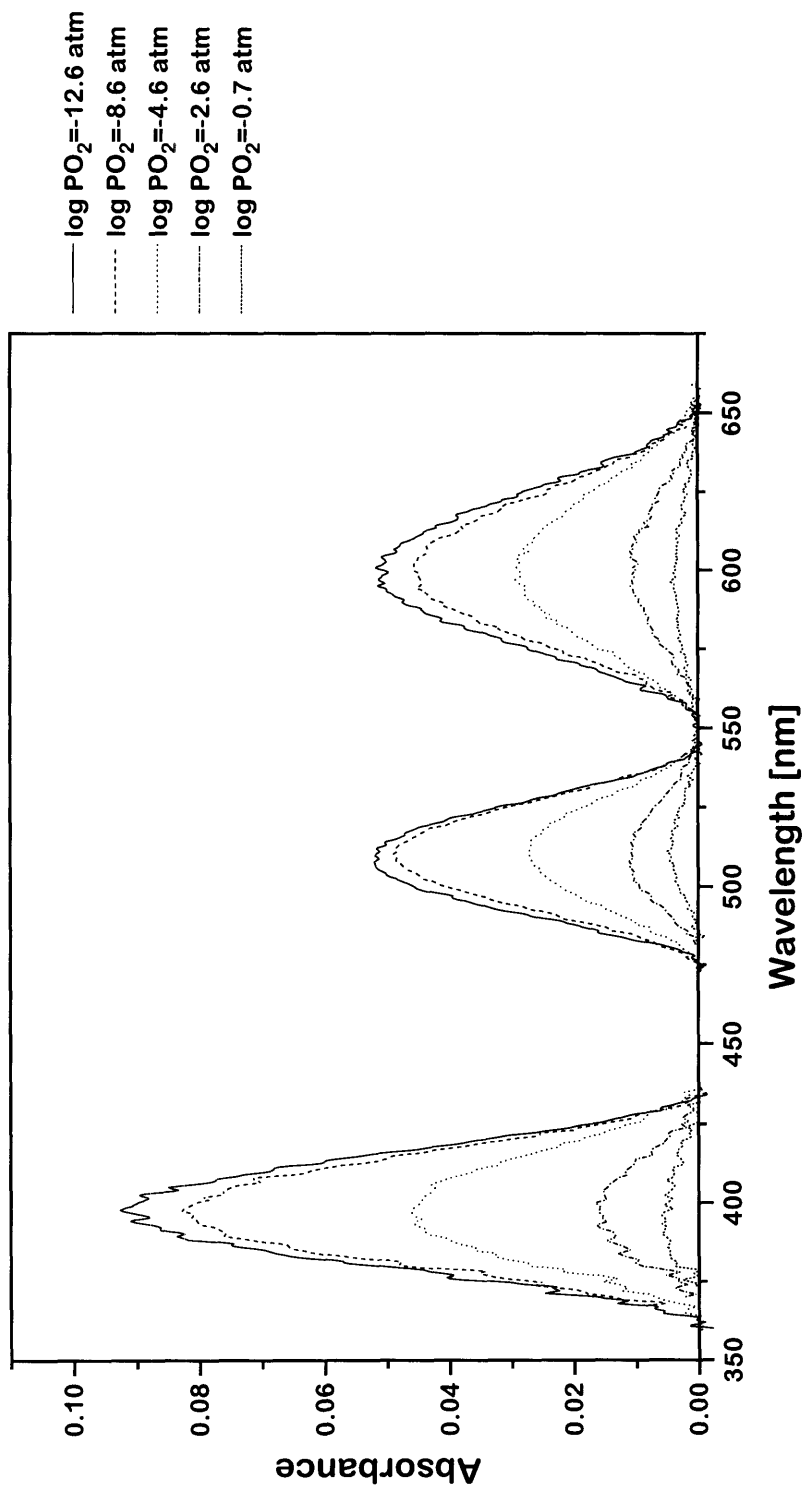
Figure 6.13 Ti:YAG absorption peaks as a function of PO_2.

Area of Absorption Peaks as a Function of PO_2

Fit to:

$$\log_{10} PO_2 = 4\log_{10} \frac{([Ti]_{tot} - [Ti^{+3}])}{[Ti^{+3}]} + \text{Constant}$$

Legend:
- ▲ 400 nm peak
- ■ 500 nm peak
- ● 600 nm peak
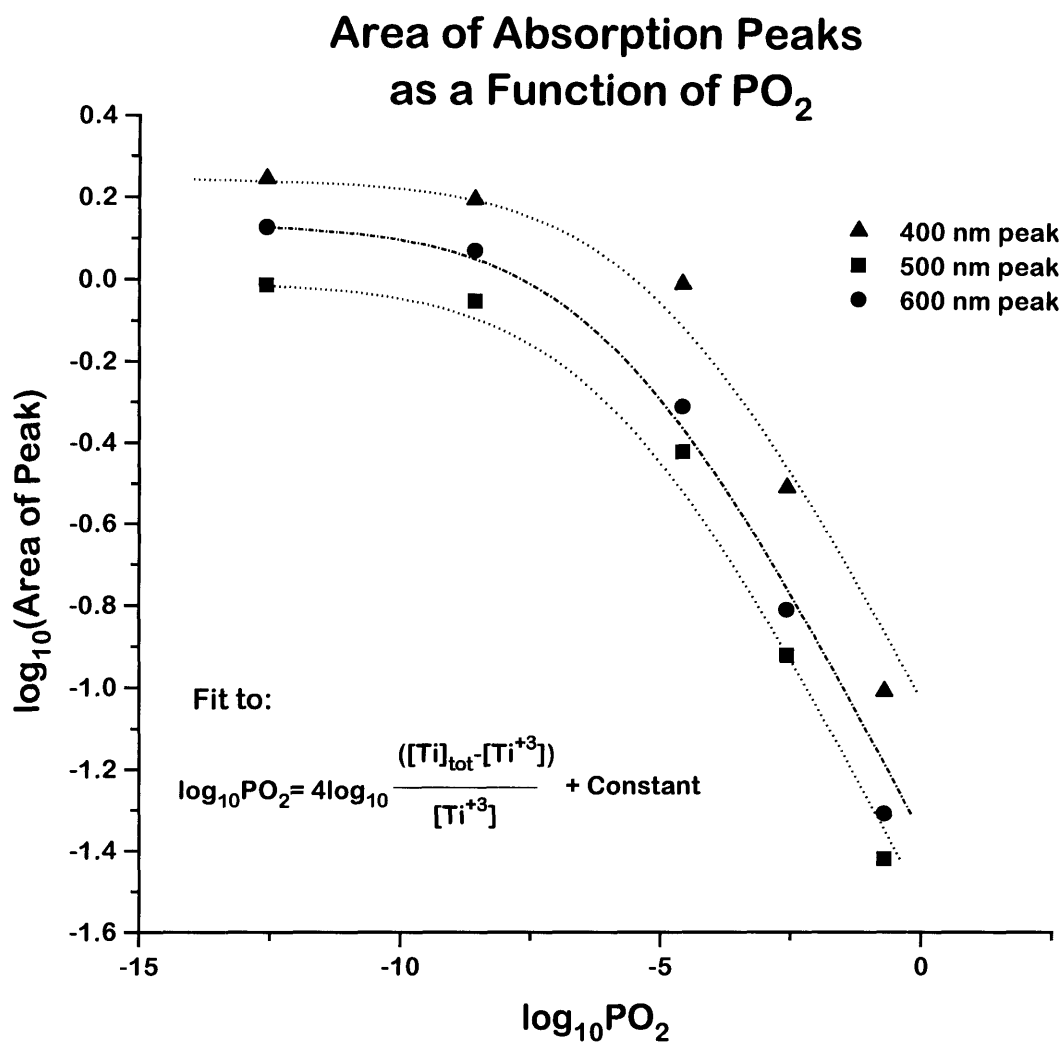
Figure 6.14 Area of Ti:YAG absorption peaks as a function of PO_2, fitted by equation 6(a).

191

level in section 5.3. Since the area under the 400, 500, and 600 nm peaks begin to saturate for reducing anneals approaching PO_2^{-12} atm, this implies that the Fermi Level has risen above this Ti^{+3} level during the course of our conductivity measurements. The saturation seems to start at $PO_2 \approx 10^{-8}$ atm at 1400°C, as seen in Figure 6.14. As discussed above, the Fermi Level is actually above midgap for all anneals in our conductivity measurements, even for the O_2 anneal. However, if we assume that the Fermi Level was at midgap for the O_2 anneal, then an anneal at $PO_2 = 10^{-8}$ would induce an upward shift of ≈ 0.66 eV as described earlier in section 5.3 for an acceptor controlled defect structure, and the Ti^{+3} level should be ≈ 3.66 eV above the oxygen 2p band, for Ti^{+3} ions in the dodecahedral site. This value is close to the value of the bandgap of $Gd_2(Zr_{0.3}Ti_{0.7})_2O_7$ at 4.1 eV, where the Ti^{+4} ions also sit in 8-fold-like sites, and the conduction band represents the Ti^{+3} levels.[29] Since the Fermi Level is actually above midgap for the O_2 anneal as mentioned above, the agreement is even closer. This agreement further supports our interpretation that Ti^{+3} ions on dodecahedral sites are responsible for the 400, 500, and 600 nm peaks in Ti:YAG.

6.4: Conclusion:

Under reducing atmospheres, the solubility of Ti in YAG can approach 10%, resulting in $Y_3(Al_{0.9}Ti_{0.1})_5O_{12}$ for crystals grown from the melt. However, high temperature anneals at 1400°C resulted in precipitation of $Y_2Ti_2O_7$. The precipitation density increased with increasing Ti concentration and increasing PO_2 of the anneal. Electrical conductivity isotherms of Ti:YAG exhibit n-type behavior that is consistent with a defect structure controlled by background acceptors and compensated by oxygen vacancies. Derived activation energies are ≈ 4.7 eV for the n-type electronic branch, and 3.2 eV for the PO_2 independent

PO$_2$ Dependence of the Area Under the 400, 500, & 600 nm Peaks in Ti:YAG

- ■ 500 nm Peak
- ● 600 nm Peak
- ▲ 400 nm

Linear Regression:
yscale(Y) = A + B * xscale(X)

400 nm

Param	Value	sd
A	-0.89605	0.00479
B	-0.2523	0.00157

500 nm

A	-1.20592	0.04483
B	-0.25301	0.01468

600 nm

A	-1.00137	0.01269
B	-0.24666	0.00416

x-axis: $\log_{10}PO_2$

y-axis: $\log_{10}$(Integrated Area of Peak)
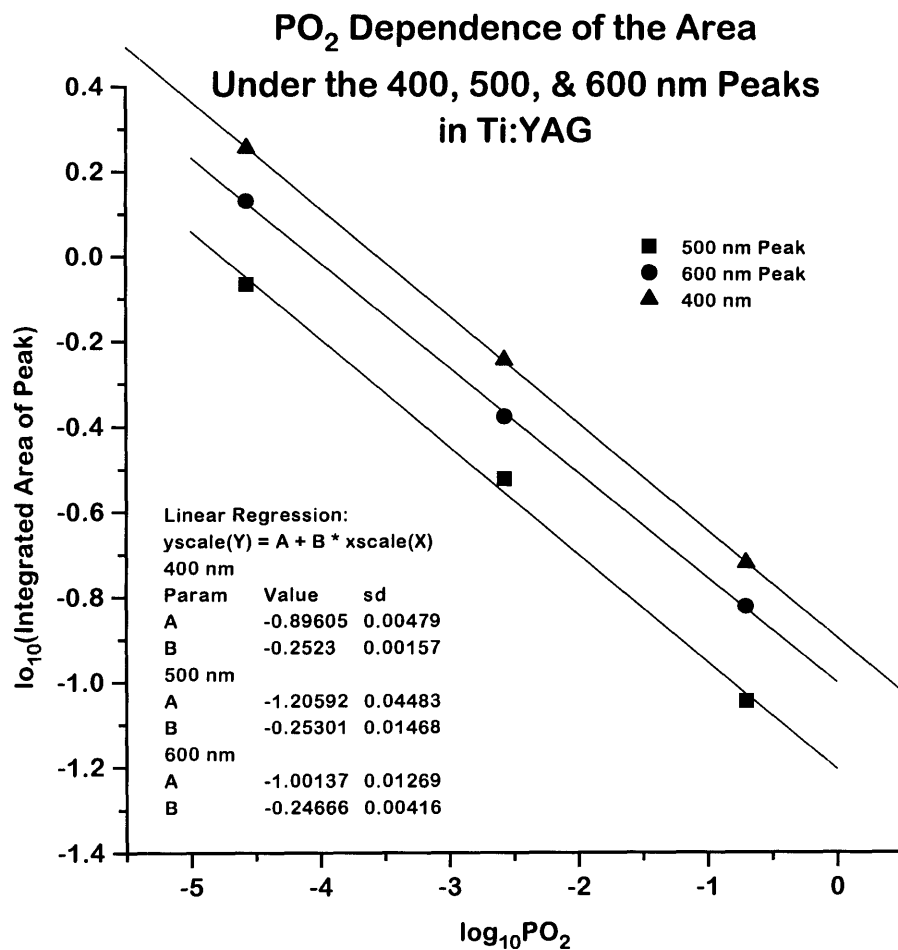
Figure 6.15 Area of Ti:YAG absorption peaks as a function of PO$_2$, fitted by equation 6(b).

ionic branch. Ti doping induced optical peaks at 400, 500, and 600 nm in YAG, as well as producing an effective band edge at $\approx$300 nm. Oxidation removed the optical peaks, while reduction restored them. Severe reducing anneals were required to move the band edge back to that of undoped YAG at $\approx$200 nm. The optical peaks were attributed to Ti^{+3} on dodecahedral sites, while the UV absorption was attributed to charge transfer from the oxygen 2p valence band to the Ti^{+4}. Quantitative correlations of the electrical and optical properties places the Ti^{+3} level of the octahedral and dodecahedral site at $\approx$3 and $\approx$3.7 eV, respectively above the oxygen 2p valence band.

CHAPTER 7: EXPERIMENTAL MEASUREMENTS OF Zr:YAG

7.1: Introduction:

Electrical and optical measurements were next made on Zr:YAG single crystal fibers. As discussed in section 4.1, electrical and optical measurements of fibers were difficult because of their small size. This small size resulted in large resistances, even at 1400°C. However, higher temperatures were avoided because of the fragile nature of the electrodes. Below 1400°C, the sample resistance quickly exceeded the measurement range of our instruments. Consequently we were confined to a narrow temperature range for our electrical measurements. Furthermore, the sample resistance was often of the same order as our alumina sample holders, so careful calibration of the sample holder was required, and under oxidizing conditions where the resistance of the sample holder was comparable to that of the sample, the data was discarded.

The optical measurements also had problems. The small fibers made coupling of the probe light difficult, so quantitative comparisons of spectra taken before and after an anneal was difficult. However, semi-quantitative measurements of a given spectra were possible.

Fibers of two different concentrations were measured, one with $x<1000$ppm, and one with $x\approx3000$ppm for $(Y_{1-x}Zr_x)_3Al_5O_{12}$. Zirconium is typically found in the $+4$ valence, and thus Zr doping at a concentration of $x\approx3000$ ppm represents the first study of donor doped YAG at this high a concentration of donors. As we will see, the defect structure of this sample may be the first YAG sample that is not dominated by background acceptors.

7.2: Results:

7.2.1: Electrical:

The conductivity isotherms of Zr:YAG are shown in Figure 7.1 & 7.2. The isotherms appear n-type, with slopes of $\approx$-1/6 and $\approx$-1/4 for the heavily and lightly doped Zr:YAG sample respectively, as seen from the fitted lines. From these fitted lines, we calculated an activation energy for each PO_2 condition measured, at each temperature. We then averaged these activation energies, obtaining 4.1 and 3.9 eV for the heavily and lightly doped Zr:YAG respectively, as shown in Figure 7.3(a)&(b). As seen by these figures, the final averaged activation energy is very close to those obtained for each PO_2. Thus, although only two isotherms were measured for the heavily doped Zr:YAG sample, this value of the activation energy actually represents several data points taken over several orders of magnitude of PO_2, so we have a high confidence level in its validity.

7.2.2: Optical:

As grown Zr:YAG had a red color whose intensity increased with increasing Zr concentration and decreasing PO_2 of the growth chamber. The optical spectra of an as-grown Zr:YAG fiber is shown in Figure 7.4. High temperature anneals at 1400°C at PO_2=2.7x10^{-13} lead to a significant reduction in intensity of all the peaks, as shown in Figure 7.5. The higher the PO_2 of the anneal, the smaller the peaks. An analysis of the peak areas revealed that an anneal at 1400°C and PO_2=2.7x10^{-13} atm results in a peak area on the order of one tenth of the as-grown peak area.

Oxidizing and reducing anneals of Zr:YAG did not result in any precipitation in the fibers. However, the fiber surfaces did appear less transparent after each anneal, possibly due to surface precipitates or thermal etching.

Figure 7.1 Conductivity isotherms of heavily doped Zr:YAG.
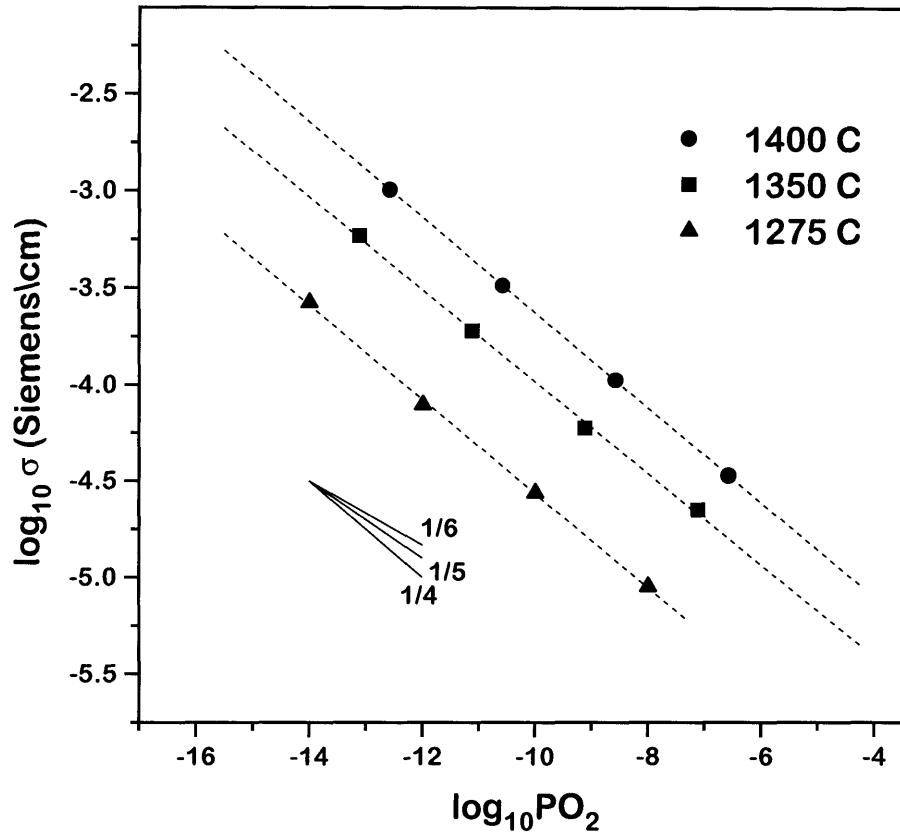
Figure 7.2 Conductivity isotherms of lightly doped Zr:YAG.
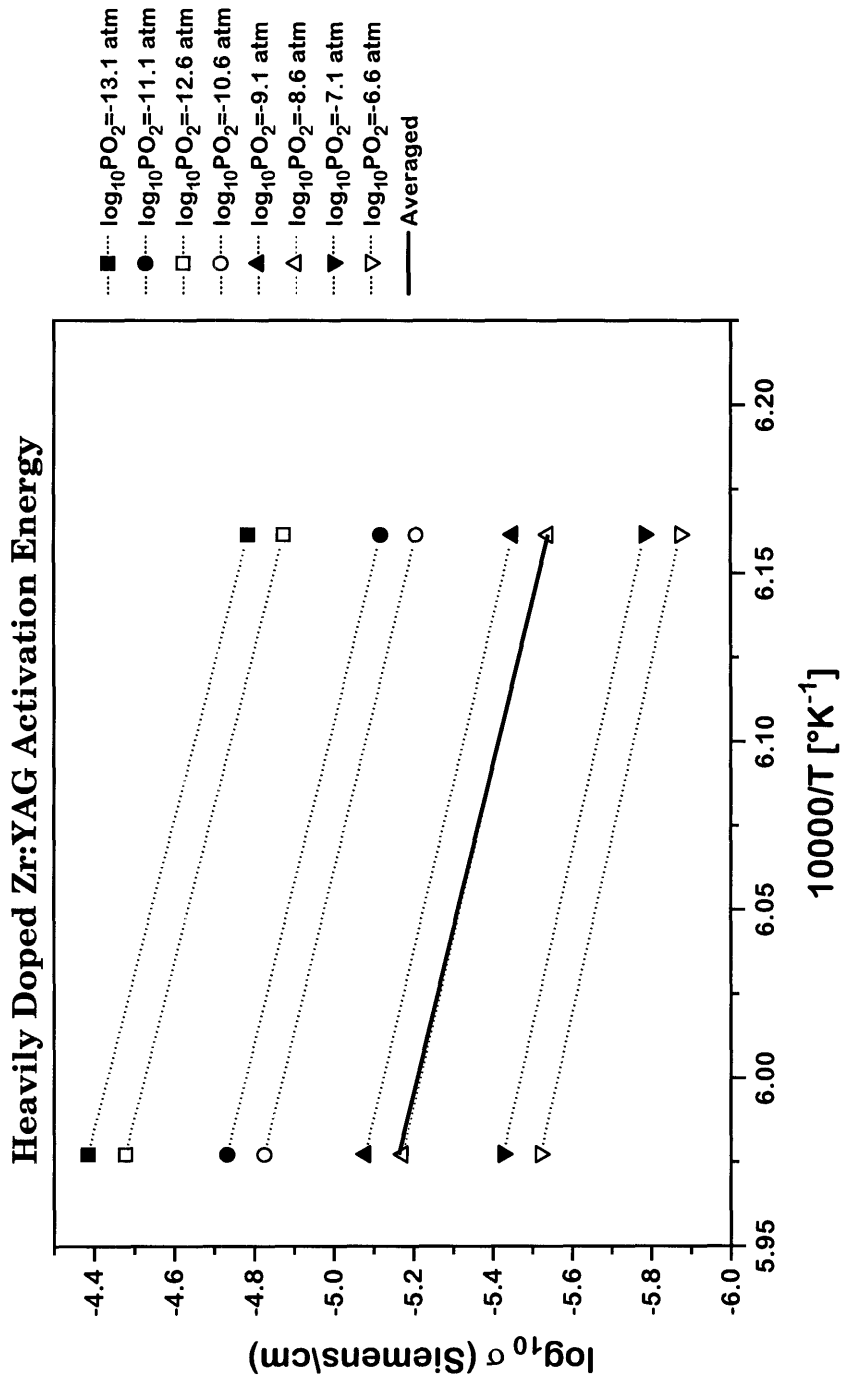
Figure 7.3(a) Activation energy of heavily doped Zr:YAG.
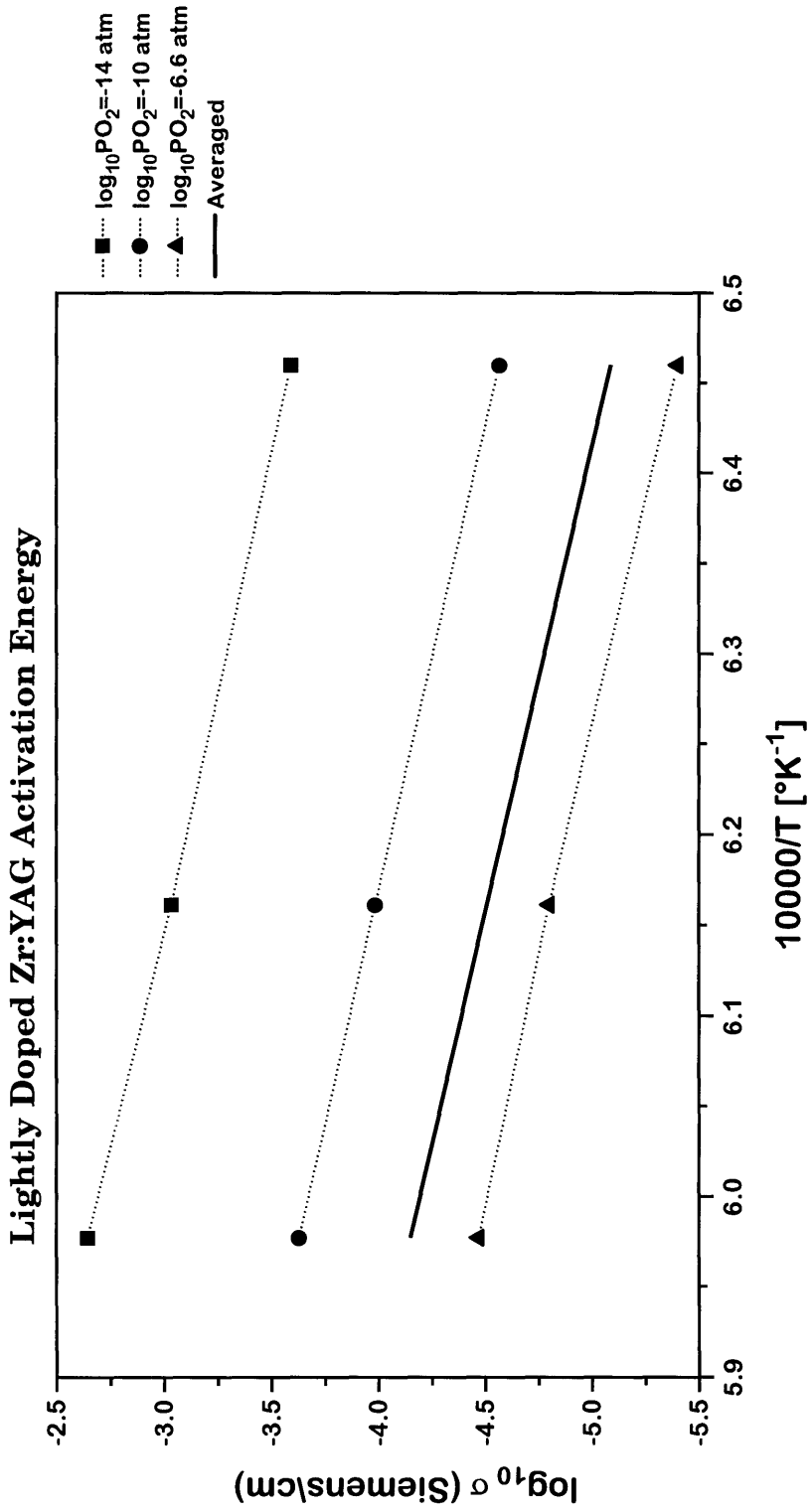
Figure 7.3(b) Activation energy of lightly doped Zr:YAG.

200
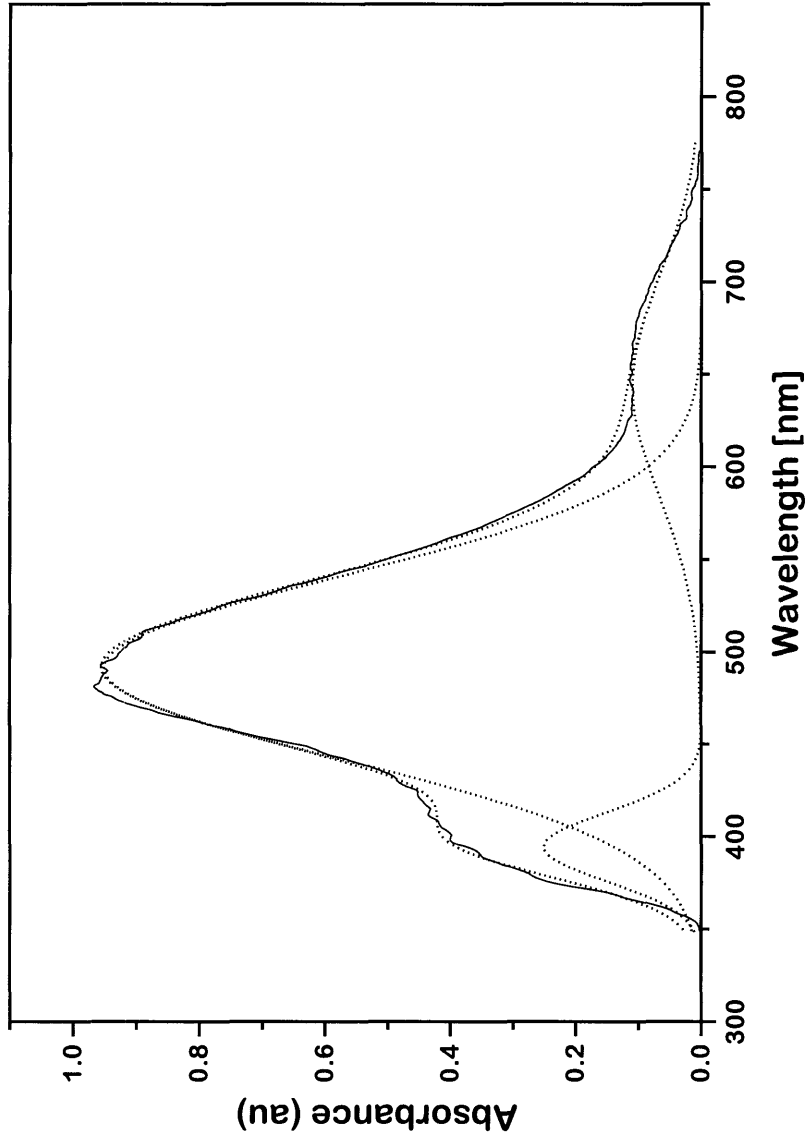
Zr:YAG

Figure 7.4 Absorption spectrum of as-grown Zr:YAG.

Zr:YAG
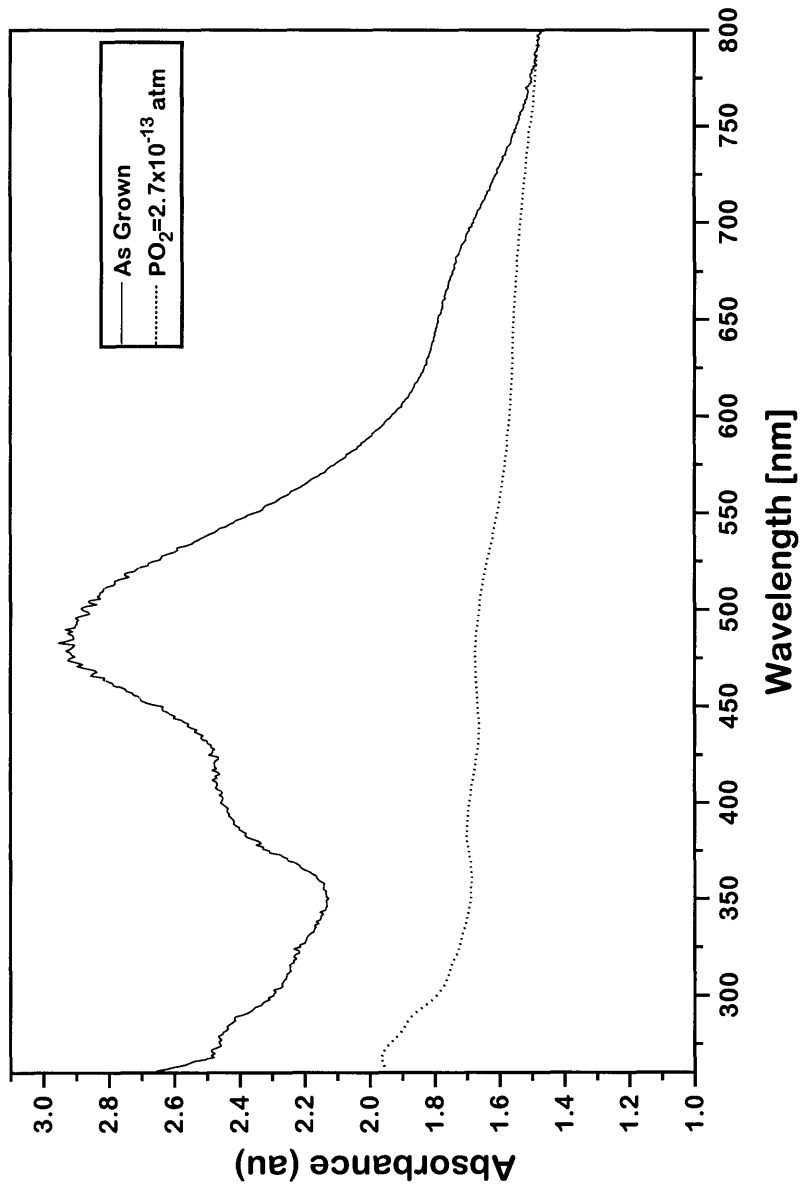
Figure 7.5 Absorption spectrum of reduced Zr:YAG.

202

7.3: Discussion:

Our measured spectra of Zr:YAG is nearly identical with those reported by Asatryan.[5] (Figure 3.28.) The spectra can be de-convoluted into three Gaussian peaks at 394, 491, and 643 nm as shown in Figure 7.4 and also reported by Asatryan.[5] Similarly, we found that the intensity of these peaks increased with increasing Zr concentration and decreasing PO_2, all consistent with their assignment of the optical peaks to Zr^{+3} ions in dodecahedral sites. If their assignment is correct, then we seem to be changing the Zr ion valence with oxidizing and reducing anneals as shown in Figure 7.5. The small magnitude of these optical peaks even after our most reducing anneal suggests that the optical center responsible for these peaks is not easy to stabilize. This observation further supports the Zr^{+3} assignment, since Zr^{+3} ions are indeed very rare, as evidenced by the lack of literature on its properties. The magnitudes of the molar extinction coefficient and oscillator strength for these peaks are consistent with this assignment as shown below for the 491 nm peak. The Zr concentration was measured by microprobe, and if we assume that all the Zr is present as Zr^{+3}, then:

$$A_{500} = \varepsilon_{max} cl = 0.96 \qquad\qquad c = 20.7 \times 10^{-2} \, moles/liter, \qquad l = 3.5 \, cm$$
$$===> \quad \varepsilon_{max} = 11.91$$

$$f = 4.6 \times 10^{-9} \varepsilon_{max} \Delta v \qquad\qquad \Delta v = 4890 \, cm^{-1}$$
$$===> \quad f = 2.67 \times 10^{-4}$$

These values are of the magnitude expected for forbidden d-d transitions as described in section 2.1.3. The challenge now is to develop a defect model that

explains the isotherms of Figure 7.1 & 7.2 in terms of changes in the Zr concentration and Zr valence.

The optical spectra of Figure 7.5 suggests that most of the Zr ions are in the +4 valence for the range of PO_2's used in our conductivity measurements. An anneal at the lowest PO_2 of the 1400°C conductivity isotherm leads to a significant reduction of the optical peaks attributed to the Zr^{+3} ion, compared to the as-grown crystal. If most of the Zr ions are in the +4 valence throughout our conductivity measurements, then our defect model must account for the following observations for the conductivity isotherm:

> i) the more heavily doped Zr sample has a -1/6 slope, while the lightly doped Zr sample has a -1/4 slope,
>
> ii) the magnitude of the conductivity at a given temperature and PO_2 is larger in the lightly doped Zr sample, and
>
> iii) the activation energy of the heavily doped Zr sample is 4.1eV, while that of the lightly doped Zr sample is 3.9 eV.

Let us start by considering that these two samples represent different regimes of the same defect structure. As seen in Figure 2.7, a donor dominated defect structure is clearly not appropriate. Such a defect structure cannot account for observations (ii) or (iii) above. Moreover, from Table 2.3, such a defect model requires that the activation energies of the two samples be related by the following equation:

$$2E_a(\text{Lightly doped Zr:YAG})=3E_a(\text{Heavily doped Zr:YAG})=\Delta H_r$$

The measured activation energies of 3.9 eV and 4.1eV for the light and heavily doped Zr:YAG respectively, clearly do not satisfy this equation. For similar reasons, a compensated or acceptor doped defect structure as seen in Figure 2.5 & Figure 2.6 is not appropriate either. Thus we are force to conclude that these two samples have different defect structures. The obvious candidates are

204

that the lightly doped sample is acceptor dominated and the heavily doped sample compensated, or that the lightly doped sample is compensated and the heavily doped sample donor dominated. Unfortunately, neither of these scenarios can account for observations (ii) & (iii) above either. Thus we must develop a new defect model.

Conductivity isotherms of pyrochlore ceramic samples made by the Pechini process reveal that compensation of background acceptors typically occur when donor concentrations approach 0.1-1%. This suggests that our heavily doped Zr:YAG sample with a Zr concentration of $\approx$3000 ppm has a compensated defect structure, while the lightly doped Zr:YAG sample has an acceptor dominated defect structure. Thus the defect model for the lightly doped Zr:YAG is Figure 2.6, where the measured isotherm is the reduced half of regime (b), and the -1/4 slope comes from the increasing electronic contribution to the total conductivity, arising from the increasing concentration of "n" as the sample is reduced. The total Zr concentration is much less than the background acceptor concentration, so the change in valence of Zr has a negligible effect on the defect structure.

Furthermore, detailed quantitative correlations of the electrical and optical properties allows us to estimate the location of the Zr^{+3} level in the YAG bandgap, as was done earlier for the Fe^{+2} level in section 5.3 and the Ti^{+3} level in section 6.3. Again the Fermi Level is probably above midgap for all the conductivity measurements, even those in O_2 which had a resistance comparable to the sample holder. Then an anneal in $PO_2 \approx 10^{-12}$ atm at 1400°C would shift the Fermi Level up by 1 eV as discussed earlier. For a thermal bandgap of 6 eV in YAG, [4,31] this places the Fermi Level at $\approx$4 eV above the oxygen 2p valence band after such an anneal. However, the optical spectra in Figure 7.5 indicates that there is very little Zr^{+3} after such an anneal. Thus the

Zr^{+3} level must be significantly higher than the Fermi Level after such an anneal, or significantly higher than 4 eV above the oxygen 2p valence band. This conclusion is consistent with the location of the Zr^{+3} level as estimated from the bandgap of ZrO_2. As discussed in section 3.2.4, such an estimate places the Zr^{+3} level at 5 eV above the oxygen 2p valence band.

Now for the -1/6 slope of the heavily doped Zr:YAG sample. Another method of getting a -1/6 slope for a compensated defect structure other than the electronic one in regime (a) of Figure 2.5 is an ionic one, where the -1/6 slope arises from a change in the valence state of a dopant, as in the Ni:YAG case measured by Rotman.[4,86] If we assume that Zr^{+4} ions compensate the background acceptors, then as Zr goes to a +3 valence with reducing anneals, oxygen vacancies must now compensate the background acceptors, and consequently the oxygen vacancy concentration will increase as we go to more and more reducing gases. The relevant defect reactions are:

$$O_o \rightarrow V_o^{\bullet\bullet} + 2e' + \frac{1}{2}O_2 \qquad\qquad K_r = \left[V_o^{\bullet\bullet}\right]n^2 PO_2^{1/2} \qquad (a)$$

$$Zr_Y^x \rightarrow Zr_Y^{\bullet} + e' \qquad\qquad K_z = \frac{\left[Zr_Y^{\bullet}\right]n}{\left[Zr_Y^x\right]} \qquad (b)$$

$$\left[Zr_Y^x\right] + \left[Zr_Y^{\bullet}\right] = \left[Zr_Y\right]_{tot} \qquad (c)$$
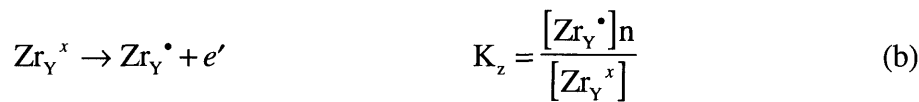
and the relevant Brouwer approximation of the electroneutrality equation is:

$$\left[A'\right] = \left[Zr_Y^{\bullet}\right] + 2\left[V_o^{\bullet\bullet}\right] \qquad (d)$$

From the optical measurements we know that $[Zr_Y^{\bullet}] \approx [Zr_Y]_{tot}$ throughout the PO_2 range of the conductivity measurements. Furthermore for the compensated case,

$$[Zr_Y]_{tot} = [A'] \tag{e}$$

Equations (c), (d), and (e) imply:

$$[Zr_Y^x] = [Zr_Y]_{tot} - [Zr_Y^\bullet] = 2[V_O^{\bullet\bullet}] \tag{f}$$

From equations (a) and (e) we know:

$$n = \frac{K_r^{1/2}}{[V_O^{\bullet\bullet}]^{1/2} PO_2^{1/4}}$$

$$K_z = \frac{[Zr_Y^\bullet]n}{[Zr_Y^x]} = \frac{[Zr_Y^\bullet]K_r^{1/2}}{[Zr_Y^x][V_O^{\bullet\bullet}]^{1/2} PO_2^{1/4}}$$

===>

$$K_z PO_2^{1/4}[Zr_Y^x][V_O^{\bullet\bullet}]^{1/2} = [Zr_Y^\bullet]K_r^{1/2} \approx [Zr_Y]_{tot} K_r^{1/2} \approx [A']K_r^{1/2} \tag{g}$$

From equations (f) & (g):

$$K_z PO_2^{1/4}[Zr_Y^x][V_O^{\bullet\bullet}]^{1/2} = K_z PO_2^{1/4} 2[V_O^{\bullet\bullet}]^{3/2} = [A']K_r^{1/2}$$

$$===> \quad [V_O^{\bullet\bullet}]^{3/2} = \frac{[A']K_r^{1/2}}{2K_z PO_2^{1/4}}$$

$$==> \quad [V_O^{\bullet\bullet}] = \frac{[A']^{2/3} K_r^{1/3}}{2^{2/3} K_z^{2/3} PO_2^{1/6}} \propto PO_2^{-1/6}$$

The activation energy and PO_2 dependence of the remaining components throughout the PO_2 range are shown in Table 7.1, and our derived defect model is drawn in Figure 7.6.

Thus both observation (i) and (ii) for the conductivity isotherms above are satisfied. The lower magnitude of the conductivity for the heavily doped Zr:YAG

Defect Model for Variable Valence Donor Compensating an Acceptor Controlled Defect Structure where Oxidation Occurs over Regime (c) & (d)
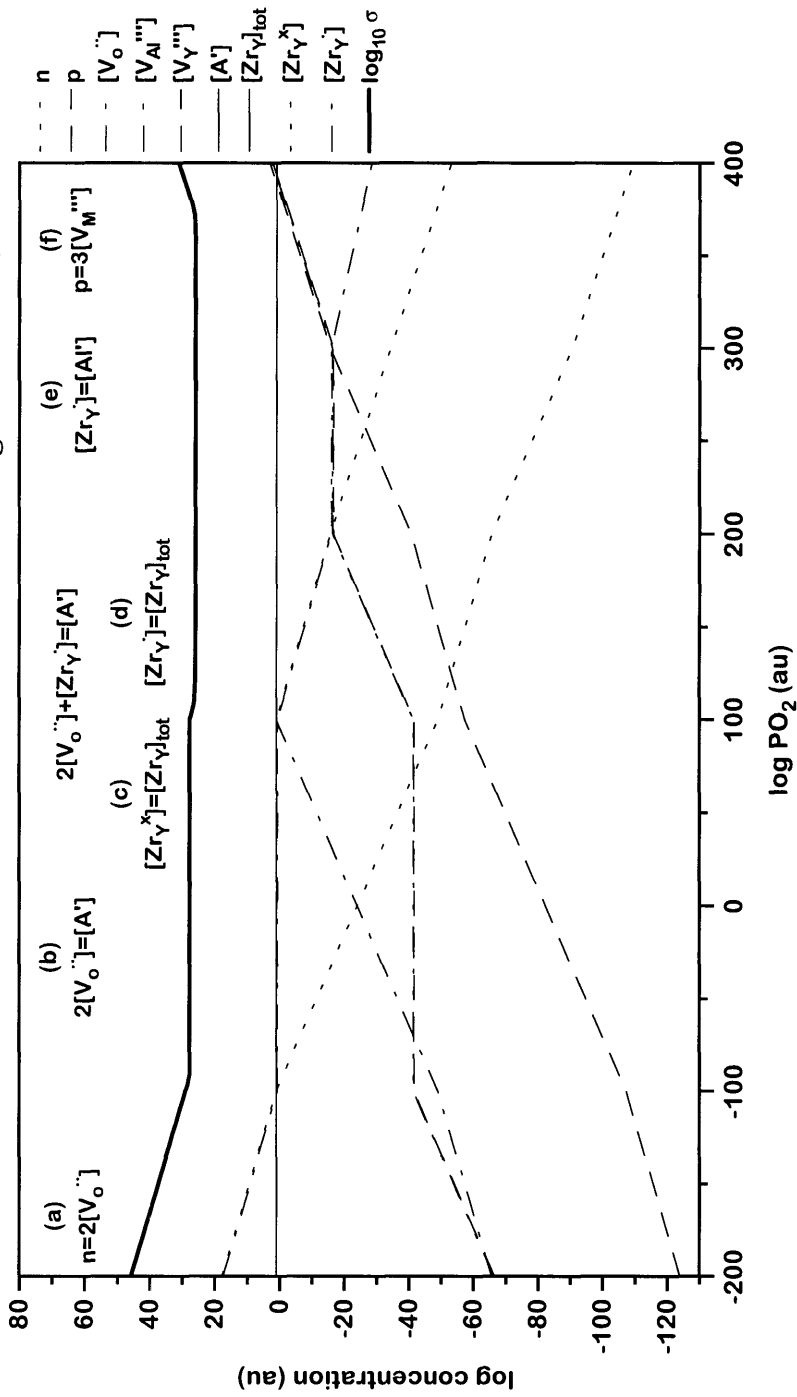
Figure 7.6   Schematic representation of the defect concentrations as a function of PO_2 for the defect model of acceptor doped YAG compensated by a variable valence donor.

Temperature & PO₂ Dependence for Compensated Defect Structure with Variable Valence Donor

Defect	Regime (a) $n = 2[V_O^{\bullet\bullet}]$		Regime (b) $2[V_O^{\bullet\bullet}] = 3[V_M''']$		Regime (c) $[Zr_Y^{\bullet}] + 2[V_O^{\bullet\bullet}] = [A']$ $[Zr_Y^x] \approx [Zr_Y]_{total}$	
	PO₂ Dep.	Activation Energy	PO₂ Dep.	Activation Energy	PO₂ Dep.	Activation Energy
$[V_{Al}''']$	$PO_2^{1/4}$	$\dfrac{\Delta H_r}{2} - \dfrac{\Delta H_s}{8}$	None	$-\dfrac{\Delta H_s}{20}$	None	$\dfrac{-\Delta H_s}{8}$
$[V_Y''']$	$PO_2^{1/4}$	$\dfrac{\Delta H_r}{2} - \dfrac{\Delta H_s}{8}$	None	$-\dfrac{\Delta H_s}{20}$	None	$\dfrac{-\Delta H_s}{8}$
$[V_O^{\bullet\bullet}]$	$PO_2^{-1/6}$	$-\dfrac{\Delta H_r}{3}$	None	$-\dfrac{\Delta H_s}{20}$	None	None
n	$PO_2^{-1/6}$	$-\dfrac{\Delta H_r}{3}$	$PO_2^{-1/4}$	$-\dfrac{\Delta H_r}{2}$	$PO_2^{-1/4}$	$-\dfrac{\Delta H_r}{2}$
p	$PO_2^{1/6}$	$\dfrac{\Delta H_r}{3} - E_g$	$PO_2^{1/4}$	$\dfrac{\Delta H_r}{2} - E_g$	$PO_2^{1/4}$	$\dfrac{\Delta H_r}{2} - E_g$
$[Zr_Y^{\bullet}]$	$PO_2^{1/6}$	$\dfrac{\Delta H_r}{3} - \Delta H_i$	$PO_2^{1/4}$	$-\Delta H_i + \dfrac{-\Delta H_s}{40} + \dfrac{\Delta H_r}{2}$	$PO_2^{1/4}$	$\dfrac{\Delta H_r}{2} - \Delta H_z$
$[Zr_Y^x]$	None	None	None	None	None	None

Defect	Regime (d) $[Zr^\bullet_Y] + 2[V_o^{\bullet\bullet}] = [A']$ $[Zr^\bullet_Y] \approx [Zr_Y]_{total}$		Regime (e) $[Zr^\bullet_Y] = [A']$		Regime (f) $p = 3[V_M''']$	
	PO$_2$ Dep.	Activation Energy	PO$_2$ Dep.	Activation Energy	PO$_2$ Depend ence	Activation Energy
$[V_{Al}''']$	$PO_2^{1/4}$	$\frac{-\Delta H_s}{8} + \frac{\Delta H_r}{2}$	None	$-\frac{\Delta H_s}{20}$	$PO_2^{3/16}$	$\frac{3\Delta H_r}{8} - \frac{\Delta H_s}{32} - \frac{3E_g}{4}$
$[V_Y''']$	$PO_2^{1/4}$	$\frac{-\Delta H_s}{8} + \frac{\Delta H_r}{2}$	None	$-\frac{\Delta H_s}{20}$	$PO_2^{3/16}$	$\frac{3\Delta H_r}{8} - \frac{\Delta H_s}{32} - \frac{3E_g}{4}$
$[V_o^{\bullet\bullet}]$	$PO_2^{-1/6}$	$\frac{-\Delta H_r}{3} + \frac{2\Delta H_z}{3}$	None	$-\frac{\Delta H_s}{20}$	$PO_2^{-1/8}$	$\frac{\Delta H_r}{4} - \frac{\Delta H_s}{16} - \frac{E_g}{2}$
n	$PO_2^{-1/6}$	$\frac{-\Delta H_r}{3} + \frac{-\Delta H_z}{3}$	$PO_2^{-1/4}$	$\frac{\Delta H_s}{40} + \frac{-\Delta H_r}{2}$	$PO_2^{-3/16}$	$-\frac{3\Delta H_r}{8} + \frac{\Delta H_s}{32} - \frac{E_g}{4}$
p	$PO_2^{1/6}$	$\frac{\Delta H_r}{3} + \frac{\Delta H_z}{3} - E_g$	$PO_2^{1/4}$	$-\frac{\Delta H_s}{40} + \frac{\Delta H_r}{2} - E_g$	$PO_2^{3/16}$	$\frac{3\Delta H_r}{8} - \frac{\Delta H_s}{32} - \frac{3E_g}{4}$
$[Zr^\bullet_Y]$	None	None	None	None	None	None
$[Zr^x_Y]$	$PO_2^{-1/6}$	$\frac{-\Delta H_r}{3} + \frac{2\Delta H_z}{3}$	$PO_2^{-1/4}$	$\Delta H_z + \frac{\Delta H_s}{40} + \frac{-\Delta H_r}{2}$	$PO_2^{-3/16}$	$-\Delta H_i + \frac{\Delta H_s}{32} + \frac{-3\Delta H_r}{8} - \frac{E_g}{4}$

Table 7.1 Temperature and PO2 dependence of defects for the defect model of acceptor doped YAG compensated by a variable valence donor in Figure 7.6.

sample is due to a low oxygen vacancy concentration and a low ionic mobility, versus electronic conduction for the lightly doped Zr:YAG sample. Finally, observation (iii) can be rationalized. For the lightly doped Zr:YAG sample, the n-type activation energy of 3.9 eV is equal to one half of the redox enthalpy as seen in Table 2.2. This value is very close to other measured activation energies for the same defect model as seen in Table 3.3. For the heavily doped Zr:YAG sample, our defect model assigns the activation energy to:

$$E_a = \frac{\Delta H_r}{3} - \frac{2\Delta H_z}{3} + \Delta E_{migration}$$

We know from Rotman's work that $\Delta H_r \approx 7.8$ eV, and $\Delta E_{migration} \approx 2.2$ to 3 eV for oxygen vacancies as seen in Table 3.4.[4,86,98] ΔH_z can be estimated from the bandgap of ZrO_2 and quantitative correlations of the electrical and optical properties as discussed above. These estimations place the Zr^{+3} level at 5 eV above the oxygen 2p valence band. For a thermal bandgap of 6 eV in YAG,[4,31] this implies that $\Delta H_z \approx 1$ eV. Thus $E_a \approx 4.1$-4.9 eV, which is in the range of our measured activation energy at 4.1 eV. Thus our derived defect model also accounts for observation (iii) of the conductivity isotherms. Consequently this defect model is consistent with all the features of the conductivity isotherms in Figure 7.2, and we believe is the appropriate defect model for the heavily doped Zr:YAG sample. These conductivity measurements of the heavily doped Zr:YAG sample are the first measurements of a YAG sample whose defect structure is not dominated by background acceptors.

7.4: Conclusions:

The optical properties of Zr:YAG single crystal fibers were measured. Zr induces absorption peaks at 394, 491, and 643 nm. These peaks were found to

increase with increasing Zr concentration, and decreasing PO_2. These peaks were assigned to d-d transitions between crystal field states of Zr^{+3} in a dodecahedral site. Lightly doped Zr:YAG had a defect structure controlled by background acceptors compensated by oxygen vacancies. Its n-type activation energy was 3.9 eV. Heavily doped Zr:YAG fibers were found to have an extrinsically compensated defect structure. Its n-type activation energy was 4.1 eV. Quantitative correlations of the electrical and optical properties suggest that the Zr^{+3} level is at 5 eV above the oxygen 2p valence band.

CHAPTER 8: CONCLUSION

Single phase undoped, Ti doped, and Zr doped YAG powders were successfully made with the Pechini process. These powders were successfully processed into dense ceramics with greater than 99% theoretical density by sintering at 1800°C for 2 hours in vacuum. The densification mechanism is believed to be liquid phase sintering of an alumina rich eutectic at 1760°C. These ceramics were successfully used as feed material for growing single crystal fibers by the laser heated floating zone technique. In a reducing environment of Ar+5% H_2, Ti solubilities of up to 10% and Zr solubilities of up to 1% were successfully incorporated into the YAG structure without precipitation. At higher solubilities or higher PO_2's, $Y_2Ti_2O_7$ precipitates were observed in the Ti:YAG fibers, and YZr_2Ox precipitates were observed in the Zr:YAG fibers.

Electrical measurements were done on YAG, Nd:YAG, Ti:YAG, and Zr:YAG samples. All the conductivity isotherms were n-type, and all the isotherms except those for the heavily doped Zr:YAG could be fit by an equation involving an n-type component that varied at $PO_2^{-1/4}$ and a ionic component that was PO_2 independent. The heavily doped Zr:YAG sample in contrast, had a n-type like component which varied as $PO_2^{-1/6}$. Activation energies for these components in the various samples are shown in Table 8.1 and 8.2. The ionic activation energy varies by ≈ 1 eV for the three systems studied. This is comparable to the variation reported in the literature, as seen in Table 3.4. The reason for this variation is unclear, and it would be interesting to explore this issue further. The n-type activation energy varies by ≈ 2 eV for the four systems studied. This differs from literature where the variation is only ≈ 1 eV. The reason for this variation is also unclear. The reduction of the Fe impurities in our

213

Ionic Activation Energies

YAG	2.3 eV
Nd:YAG	2.5 eV
Ti:YAG	3.2 eV

Table 8.1 Ionic activation energies in YAG.

N-Type Activation Energies

YAG	3.0 eV
Nd:YAG	2.9 eV
Ti:YAG	4.7 eV
Lightly Doped Zr:YAG	3.9 eV
Heavily Doped Zr:YAG	4.1 eV

Table 8.2 N-type activation energies in YAG.

undoped YAG, and the restriction of the electronic mobility in our Ti:YAG may explain some of this variation, but more work is clearly needed before we can understand this difference.

Optical measurements were done on YAG, Nd:YAG, Ti:YAG, and Zr:YAG samples. The YAG sample had peaks at 250 and 310 nm. The 250 nm peak was found to increase with oxidizing anneals and decrease with reducing anneals, while the 310 nm peak was found to do just the opposite. The 250 nm peak was attributed to charge transfer from the oxygen 2p valence band to Fe^{+3} impurities. The 310 nm peak was attributed to charge transfer between Fe^{+3} and Fe^{+2} ions. The Nd:YAG sample had peaks throughout the UV, VIS, and NIR, and all the peaks were attributed to the three 4-f electrons of Nd^{+3}. These peaks were unchanged by oxidizing and reducing anneals. However, a difference spectra revealed the same peaks as observed in the YAG sample above, with the same PO_2 dependencies. The Ti:YAG sample had peaks at 400, 500, and 600 nm, along with intense UV absorption that shifted the effective bandedge to 300 nm, from 200 nm for undoped YAG. The three peaks in the visible were found to decrease with oxidizing anneals and increase with reducing anneals, while the UV absorption was found to be unaffected, except for extremely reducing anneals where the UV absorption decreased dramatically. All these absorption peaks increase with increasing Ti concentration. The 400, 500, and 600 nm peaks were attributed to crystal field transitions of the Ti^{+3} ion in the 8-fold dodecahedral site, while the UV absorption was attributed to charge transfer from oxygen 2p to Ti^{+4}. The Zr:YAG sample had peaks at 394, 491, and 643 nm. All three peaks increased with increasing Zr concentration and decreasing PO_2. These peaks were attributed to crystal field transitions of Zr^{+3} ions in the 8-fold dodecahedral site.

Quantitative correlations of the electrical and optical properties of all the samples except the heavily doped Zr:YAG sample were found to be consistent with a defect structure controlled by inadvertent background acceptors and compensated by oxygen vacancies. The heavily doped Zr:YAG sample was found to have a defect structure where the Zr^{+4} ions compensated the background acceptors. This compensation suggests that the concentration of background acceptors is typically $\approx 0.3\%$. Thus to study donor controlled defect structures in YAG, the concentration of shallow donors must be $>>0.3\%$. Finally, quantitative correlations of electrical and optical measurements also suggest the location of the $V_O^{\bullet\bullet}$, Fe^{+2}, Ti^{+3}, and Zr^{+3} levels in the YAG bandgap, as illustrated in Figure 8.1. Following convention, the energy level is labeled with the valence that the ion would have if that level was occupied.
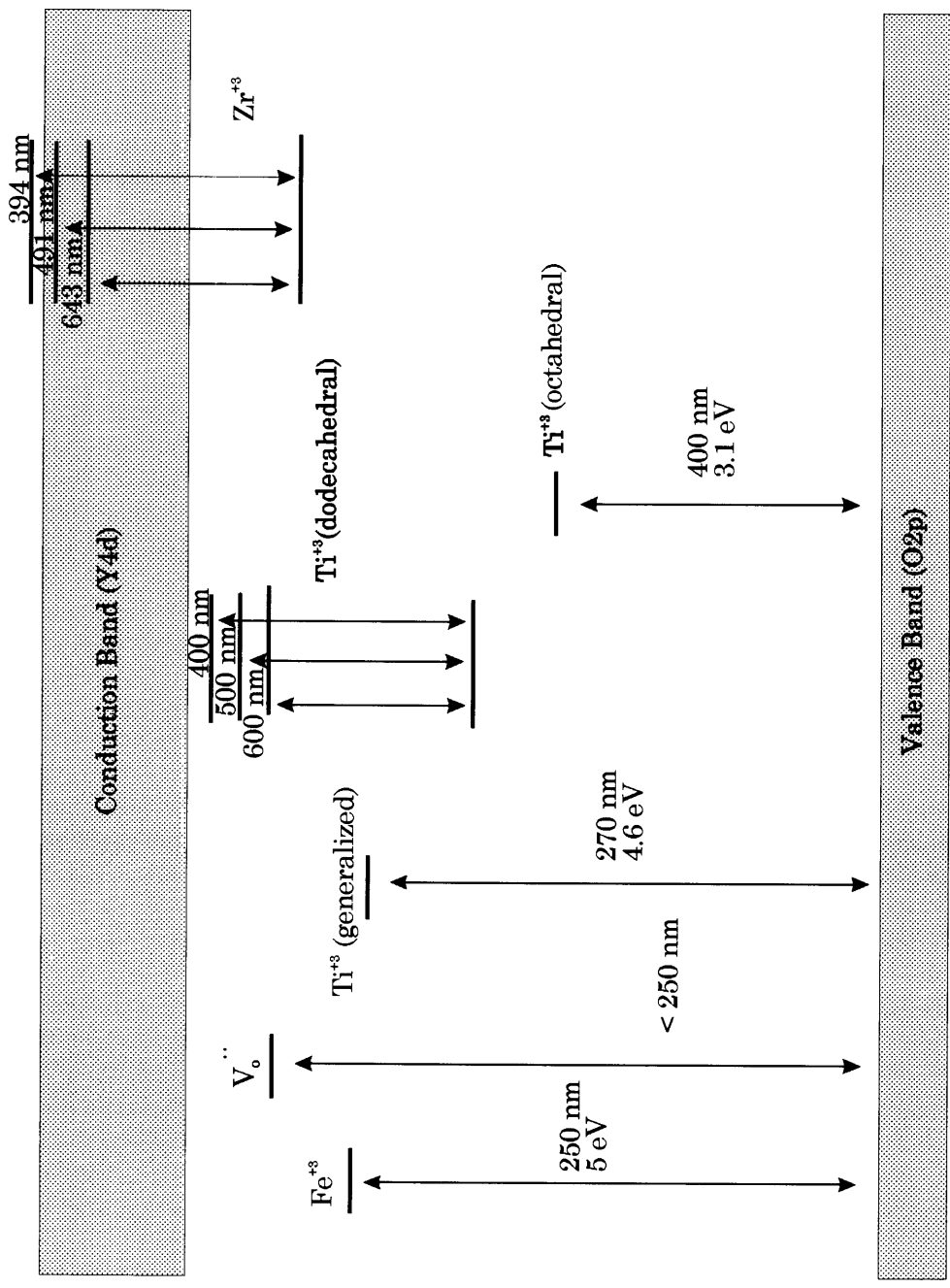
Figure 8.1 Energy band diagram for YAG.

Chapter 9: Future Work

The short term future work should be to explicitly verify the models developed in this thesis. Specifically, esr experiments should be done on Ti:YAG to verify the presence of Ti^{+3} on the 8-fold dodecahedral sites, and quantitative correlations of the intensity of the esr signal with the intensity of the 400, 500, and 600 nm optical absorption peaks should be made to conclusively demonstrate that Ti^{+3} ions on these sites are responsible for the optical properties. Another interesting experiment would be to pump Ti:YAG at 400 nm to see what the fluorescence spectrum looks like, and see if it changes when pumped at 500 and 600 nm.

For the Zr:YAG samples, short term future work should involve a transference measurement, to verify that the lightly doped Zr:YAG sample is indeed electronically conducting, and that the heavily doped Zr:YAG sample is indeed ionically conducting. Another interesting experiment would be to pump the optical absorption bands of Zr:YAG and see what the fluorescence spectrum looks like.

Long term future work should involve searching for an effective donor in YAG, one that would induce a donor controlled defect structure. This defect structure may yield some interesting transport and optical properties. Such a donor should be a shallow donor, as well as one with a high solubility in the YAG structure. Possible donors included Hf, Si, and Ta.

APPENDIX 1

Modified Pechini Process:

The Pechini process utilizes the ability of citric acid to form polybasic chelates with a number of metal cations, among them Y, Al, Ti, and Zr. The chelates can undergo polyesterization when heated with a polyhydroxl alcohol, thereby locking the cations in the same intimately mixed state as the solution. The organics are then burned off to form the oxide powder.

A typical process following a recipe developed by Peter Moon,[29] involves dissolving a metal salt such as $Y(NO_3)_3$ in distilled water and precipitating out $Y(OH_3)_3$ by adding ammonia (NH_4OH). The precipitate is filtered and washed, and then dissolved in a solution of citric acid and ethylene glycol. This solution is then assayed to determine the Y concentration.

Citric acid solutions of Y and Al, as well as any dopants are then mixed together in the appropriate ratios for the desired composition. The mixed solution is then dried into a hard resin, and the resin ashed in a box furnace in flowing O_2 at $\approx 600°C$. The amorphous ash is then calcined to the oxide phase at $\approx 900°C$. The final powder characteristics (e.g. size, size distribution, shape, etc.) are largely determined by the characteristics of the ash.

References

1) Moon, P.K. <u>Sol. State Ionics</u>, **28-30**, 1988, p.470.

2) Moon, P.K. <u>Mat. Res. Soc. Proc</u>. **135**, Pittsburgh, PA, (1989), pp. 149-163.

3) Nassau, K., <u>The Physics & Chemistry of Color</u>, John Wiley & Sons, 1983.

4) Rotman, S. PhD Thesis, MIT, 1985.

5) Asatryan, H.R. "Single Crystal Growth and Investigation of Optical and ESR Absorption Spectra of Zirconium-Doped YAG," <u>Phys. Stat. Sol. (B)</u>, **135**, 1986, 343-352.

6) Karpov, I.I. "Conditions of Growth of Yttrium-Aluminum Garnet Crystals with Added Titanium," <u>Sov. Phys. Crystallogr.</u> **23**(6) 1978, 710-713.

7) Karplus, M. <u>Atoms & Molecules</u>, Benjamin/Cummings Publishing Company, 1970.10) Atkins, P.W. <u>Physical Chemistry</u>, 2nd Edition, Oxford University Press, 1982.

8) Eisberg, R.M. <u>Fundamentals of Modern Physics</u>, John Wiley & Sons, New York, 1967.

9) DeKock, R.L. <u>Chemical Structure & Bonding</u>, University Science Books, 1989.

10) Atkins, P.W. <u>Physical Chemistry</u>, 2nd Edition, Oxford University Press, 1982.

11) Dunn, T.M. "The Visible and Ultra-Violet Spectra of Complex Compounds in Modern Coordination Chemistry," <u>Modern Coordination Chemistry</u>, ed. by Lewis & Wilkins, Interscience Publishers, New York, 1960, 229-300.

12) Lever, A.B.P., <u>Inorganic Electronic Spectroscopy</u>, Elsevier Publishing Company, 1968.

13) Ballhausen, C.J. <u>Introduction to Ligand Field Theory</u>, McGraw-Hill Company, Inc. 1962.

14) Dunn, T.M., <u>Some Aspects of Crystal Field Theory</u>, Harper & Row Publishers, 1965.

15) Tanabe, Y. "On the Absorption Spectra of Complex Ions. I," <u>J. Phys. Soc. Jap.</u> **9**(5) 1954, p. 753.

16) Tanabe, Y. "On the Absorption Spectra of Complex Ions. II," <u>J. Phys. Soc. Jap.</u> **9**(5) 1954, pp.766-779.

17) Liehr, A.D. "Inherent Configurational Instability of Octahedral Inorganic Complexes in E_g Electronic States," Annals of Physics, **3**(1958), pp. 304-319.

18) Moulton, P.F. "Spectroscopic and Laser Characteristics of Ti:Al_2O_3," J. Opt. Soc. Am. B, **3** (1) 1986, 125-133.

19) Koechner, W. Solid-State Laser Engineering, Springer-Verlag, 1992.

20) Saleh, B.E.A. Fundamentals of Photonics, John Wiley & Sons, Inc. 1991.

21) Mead, A. "Absorption Spectra in Aqueous Solution of Co-ordination Compounds of Chromium and Cobalt," Tran. Faraday Soc., **30** (1934), pp. 1052-1058.

22) Moffitt, W. "Quantum Theory," Ann. Rev. Phys. Chem., **7** (1956), pp. 107-136.

23) Tippins, H.H. "Charge-Transfer Spectra of Transition-Metal Ions in Corundum," Phys. Rev. B, **1** (1) 1970, 126-135.

24) Kingery, W.D., Introduction to Ceramics, 2nd Ed. John Wiley & Sons, New York, 1976.

25) Schuh, L. PhD Thesis, Technische Universiteit, Eindhoven, The Netherlands, 1989.

26) Schuh, L. "Computer Modelling Studies of Defect Structures and Migration Mechanisms in Yttrium Aluminium Garnet," J. European Ceramic Soc. **7** (1991) 67-74.

27) Geller, S. "Crystal Chemistry of the Garnets," Zeitschrift fur Kristallographic, Bd. 125, S. 1-47 (1967).

28) Kittel, C., Introduction to Solid State Physics, 5th Ed. John Wiley & Sons, New York, 1976.

29) Moon, P. PhD Thesis, MIT, 1988.

30) Macdonald, J.R., Impedance Spectroscopy, John Wiley & Sons, New York, 1987.

31) Rotman, S.R. "Defect-Property Correlations in Garnet Crystals: The Electrical Conductivity and Defect Structure of Luminescent Cerium-Doped Yttrium Aluminum Garnet," J. Appl. Phys. **57**(6) 1985, pp. 1951-1955.

32) Slack, G.A. "Optical Absorption of $Y_3Al_5O_{12}$ from 10 to 55,000 cm^{-1} Wave Numbers," Phys. Rev. **177** (3) 1969, 1308-1314.

33) Euler, F. "Oxygen Coordinates of Compounds with Garnet Structure," Acta Cryst., **19** (1965), pp. 971-978.

34) Novak, G.A. "The Crystal Chemistry of the Silicate Garnets," <u>Am. Min.</u>, **56** (1971), pp. 791-825.

35) Wang, F.F.Y. "Physical and Chemical Properties of Garnets," <u>Treatise on Materials Science and Technology</u> II, ed. by H. Herman, Academic Press, 1973, pp. 279-384.

36) Gibbs, G.V. "Refinement of the Crystal Structure of Synthetic Pyrope," <u>Am. Min.</u>, **50** (1965), pp. 2023-2039.

37) Shannon & Prewitt, Acta Cryst., **B25** (1969) p. 925-946.

38) Shannon & Prewitt, Acta Cryst., **B26** (1970) p. 1046-1048.

39) McClure, D.S., "The Distribution of Transition Metal Cations in Spinels," <u>J. Phys. Chem. Sol.</u>, **3**, 1957, 311-317.

40) Bantien, F. "Optical Transitions in Titanium Doped YAG," <u>J. Lum.</u> **36** (1987), pp. 363-?.

41) Bausa, L.E. "Characterization of Titanium Induced Optical Absorption Bands in Phosphate Glasses," <u>J. Non-Cryst. Sol.</u> **127** (1991), 267-272.

42) Bausa, L.E. "Laser-Excited Luminescence in Ti_Doped $MgAl_2O_4$ Spinel," <u>J. Appl. Phys.</u> **68**(2) 1990, 736-740.

43) Geller. S. "Substitution of Ti^{4+}, Cr^{3+}, and Ru^{4+} Ions in Yttrium Iron Garnet," <u>J. Appl. Phys.</u> **36** (1965) pp. 321-322.

44) Espinosa, G.P. "A Crystal Chemical Study of Titanium(IV) and Chromium(III) Substituted Yttrium Iron and Gallium Garnets," <u>Inorg. Chem.</u> **3**(6) 1964, pp. 848-850.

45) Moon, P.K. "Intrinsic Fast Oxygen Ionic Conductivity in the $Gd_2(Zr_xTi_{1-x})_2O_7$ and $Y_2(Zr_xTi_{1-x})O_7$ Pyrochlore Systems," <u>Mat. Res. Soc. Symp.</u> **135** (1989), pp. 149-163.

46) Yamamura, H. "Preparation of $Pb(Zr,Ti)O_3$ by Oxalate Method in Ethanol Solution (Part 1)," <u>Yogyo- Kyokai-Shi</u> **94**(5) 1986, pp. 470-475.

47) Mill, B.V. "New Compounds with Structures of the Garnet Type," <u>Izv. Akad. Nauk SSSR Neorg. Mater.</u> **2**(10) 1966, pp. 1861-1864.

48) Geller, S. "Crystal Chemical and Magnetic Studies of Garnet Systems $\{YCa_2\}[M_2^{4+}](Fe_3)O_{12}$-$\{Y_3\}[Fe_2](Fe_3)O_{12}$, M = Zr or Hf," <u>J. Phys. Chem. Solids</u> **13** (1960) pp. 28-32.

49) Kvapil, J. "O^- Centre Formation in YAG Crystals Doped with Rare Earth Ions," <u>Kristall und Technik</u> **10**(2) 1975, 161-165.

50) Kvapil, J. "O^- Centre Formation in YAG Crystals Doped with Iron Group Ions," <u>Kristall und Technik</u> **10**(5) 1975, 529-534.

51) Bernhardt, HJ. "Bound Polarons in YAG Crystals," Phy. Stat. Sol. (b) **87**, 1978, 213-219.

52) Akhmadullin, I. Sh. "Thermo- and Phytoinduced Defects in Y3Al5O12 Crystals," Nuclear Instruments and Methods in Physics Research **B65** (1992) pp. 270-274.

53) Masumoto, T. "Effects of Oxygen Pressure on Optical Absorption of YAG," Jap. Journ. Appl. Phys. **24**, 1985, 546-551.

54) Mori, K. "Transient Colour Centres Caused by UV Light Irradiation in Yttrium Aluminium Garnet Crystals," Phys. Stat. Sol. A **42** (1977) 375-384.

55) Willis, J.B. "Assessment and Control of Imperfections in Crystals for Laser Devices," J. Cryst. Growth **3,4** (1968) pp. 236-240.

56) Kaminskii, A.A. Laser Crystals, Springer-Verlag, 1990.

57) Albers, P. "The Influence of Site Symmetry on the Spectroscopic Properties of Laser Ions," Acta Crystll. Supplement A **40** (1984) C150.

58) Kvapil, J. "Transient Absorption and Laser Output of YAG:Nd," Czech. J. Phys. B **31**, 1981, pp.644-651.

59) Zeidler, G. IEEE J. Quant. Elect. **4,** (1968), p. 1016.

60) Yamaga, M. "Radiative and Non-Radiative Decays From the Excited State of Ti^{+3} Ions in Oxide Crystals," Appl. Phys. **B51**, (1990) pp. 329-335.

61) Wegner, T. "Excited State Absorption of Ti^{3+}:YALO$_3$," Appl. Phys. B, **49** (1989), pp. 275-278.

62) Lacovara, P. "Growth, Spectroscopy, and Lasing of Titanium-Doped Sapphire," IEEE J. Quantum Elec. **QE-21** (10) 1985 pp. 1614-1618.

63) Albers, P. "Continuous Wave Tunable Laser Operation of Ti^{+3}-Doped Sapphire at 300 K," Tunable Solid State Lasers II ed. by Budgor et.al., Springer-Verlag, 1986, 208-211.

64) Sanchez, A. "Crystal Growth, Spectroscopy, and Laser Characteristics of Ti:Al$_2$O$_3$," IEEE J. Quant. Elect. **24**(6) 1988, pp995-1002.

65) Bessonova, T.S. "Effect of Heat Treatment and Irradiation on Absorption Spectra of Ti and Si Corundum," Opt. Spectrosc. **41**(1) 1976, pp. 87-88.

66) Basun, S.A. "Photoelectric Studies of Two-Step Photoionization of Ti^{+3} Ions in Oxide Crystals," J. Lum. **53**(1992), pp. 28-31.

67) Powell, R.C. "Growth, Characterization, and Optical Spectroscopy of Al$_2$O$_3$:Ti^{+3}," J. Appl. Phys. **58**(6) 1985, pp. 2331-2336.

68) Lupei, A. "Spectroscopy of Ti^{+3}:α-Al$_2$O$_3$," Optics Comm., **59**(1) 1986, pp. 36-38.

69) Macke, A.J.H. "Investigations on the Luminescence of Titanium-Activated Stannates and Zirconates," J. Sol. State Chem., **18** (1976), pp. 337-346.

70) Peshev. P. "Growth and Spectral Characteristics of $Y_3Al_5O_{12}:Ti^{3+}$ Single Crystals," Mat. Res. Bull. **23** (1988) pp. 1193-1198.

71) Albers, P. "Laser Relevant Spectroscopic Properties of Ti^{+3} - Doped Sapphire and YAG," Cleo 1986.

72) Karpov, I.I. "Color Centers in Titanium-Activated Yttrium-Aluminum Garnet Crystals," Sov. Phys. Crystallogr. **23**(5) 1978, 609-610.

73) Karpov, I.I. "Use of Polarized Luminescence to Investigate Luminescence in Yttrium-Aluminum Garnet Crystals with Added Titanium," Sov. Phys. Crystallogr. **23**(6) 1978, 688-690.

74) Bair, C.H. "Injection Controlled Titanium-Doped Sapphire Laser Using a Pulsed Dye Laser," Tuneable Solid State Lasers II ed. Budgor, Esterowitz, Springer-Verlag 1986, 247-250.

75) Driscoll, T.A. Digest of Technical Papers, Conference on Lasers and Electro Optics, 1986, San Francisco, CA p. 106.

76) Wood, D.L. "Crystal-Field Spectra of $d^{3,7}$ Ions. III. Spectrum of Cr^{+3} in Octahedral Crystal Fields," J. Chem. Phys. **39**(4) 1963, pp.890-898.

77) Samatov, M. V. "Paramagnetic Impurtiy Centers in Single Crystals of Synthetic Xenotime," Izvestiya Akademii Nauk SSSR, Neorganicheskie Materialy, **18** (11) 1982, pp. 1866-1868.

78) Vainer, V.S. "Electron Spin Resonance Spectrum of Zr^{+3} Ions," Sov. Phys, Solid State **20**(9) 1978, pp1628-1629.

79) Bandoraitis, J.G. "Optical Energy Gaps in the Monoclinic Oxides of Hafnium And Zirconium and Their Solid Solutions," J. Phys. Chem. **69**(10) 1965 pp. 3666-3667.

80) Wachsman, E.D. "Spectroscopic Investigation of Oxygen Vacancies in Solid Oxide Electrolytes," Sol. State Ionics Conf., Hakone, Japan, January, 1990.

81) Nigara, Y. Jap. J. Appl. Phys., **7** (1968), pp. 404.

82) Neiman, A.Y. "Nature of Defect Formation in Complex Oxides of the Composition $Me_3^{III}E_5^{III}O_{12}$ with a Garnet Structure," Dok. Akad. Nauk SSSR **240** (4) 1978, 876.

83) Bates, J.L. "Electrical Conductivity of $MgAl_2O_4$ and $Y_3Al_5O_{12}$," J. Am. Ceram. Soc., **64**, October 1981, C138-C141.

84) Haneda, H. "Oxygen Diffusion in Single Crystal Yttrium Aluminum Garnet," J. Crystal Growth **68** (1984) 581-588.

85) Rotman, S.R. "Defect-Property Correlations in Garnet Crystals. V. Energy Transfer in Luminescent Yttrium Aluminum-Yttrium Iron Garnet Solid Solutions," J. Appl. Phys. **66** (7) 1989, 3207.

86) Rotman, S.R. "Defect-Property Correlations in Garnet Crystals. III. The Electrical Conductivity and Defect Structure of Luminescent Nickel-Doped Yttrium Aluminum Garnet," J. Appl. Phys., **62** (4) 1987, 1305-1312.

87) Schuh, L. "Electrical Conductivity Study of Defects in Zirconium Doped Yttrium Aluminum Garnet Ceramics," Science of Ceramics, 14 Shelton, Stoke-on Trent, 1988, pp. 973-978.

88) Schuh, L. "Electrical Transport and Defect Properties of Ca- and Mg-Doped Yttrium Aluminum Garnet Ceramics," J. Appl. Phys., **66**, (6), 1989, 2627-2632.

89) Blum, J.B. "Temperature Dependence of the Iron Acceptor Level in Aluminum Oxide," J. Am. Cer. Soc. **65** (8) 1982, pp. 379-382.

90) Scott, G.B. "Absorption Spectra of $Y_3Fe_5O_{12}$ (YIG) and $Y_3Ga_5O_{12}:Fe^{3+}$," Phys. Rev. B **10** (3) 1974, pp. 971-986.

91) Ferguson, J. "The Origins of the Colours of Yellow, Green and Blue Sapphire," Chem. Phys. Lett. **10**(3) 1971, pp. 262-265.

92) Mohopatra, S.K. "Defect Structure of Alpha-Al_2O_3 Doped with Titanium," J. Am. Cer. Soc. **60** (9-10) 1977 pp. 381-387.

93) Albers, P. PhD Thesis, Hamburg University, 1985.

94) Swider, K.E. "Investigation of the Electronic Conduction Mechanism in Yttria Stabilized Zirconia-Titania," Proceedings of the First International Symposium on Ionic and Mixed Conducting Ceramics," ed. by Ramanarayanan, T.A., 1991.

95) Hereman-Goemanns, C., PhD Thesis, MIT, 1993.

96) Gupta, V.P. "Optoelectronic Properties of Rutile (TiO2)," J. Phys. Chem. Solids **41** 1980, pp. 591-594.

97) Choi, B.M. "Defect Structure and Electrical Properties of Single-Crystal $Ba_{0.03}Sr_{0.97}TiO_3$," J. Am. Ceram. Soc., **71**(4) 1988, pp. 201-205.

98) Rotman, S.R. "Defect-Property Correlations in Garnet Crystals. IV. The Optical Properties of Nickel-Doped Yttrium Aluminum Garnet," J. Appl. Phys., **66** (3) 1989, 1366-1369.

99) Lacklison, D.E. Sol. State Comm. **14**, (1974), p. 861.

100) Arakawa, E.T., J. Phys. Chem. Solids, **29** (1968) pp. 735.

101) Toropov, I.A., Izv. Akad. Nauk. SSSR, Ser. Khim., No. 7 (1964) pp. 1162.